

DIVERSITY OF STRUCTURAL TYPES AND MOLECULAR NANOMAGNETISM IN
IRON AND MANGANESE CLUSTERS

By

RASHMI BAGAI

A DISSERTATION PRESENTED TO THE GRADUATE SCHOOL
OF THE UNIVERSITY OF FLORIDA IN PARTIAL FULFILLMENT
OF THE REQUIREMENTS FOR THE DEGREE OF
DOCTOR OF PHILOSOPHY

UNIVERSITY OF FLORIDA

2008

© 2008 Rashmi Bagai

To mummi, papa, and Shammi, for their infinite unconditional love

ACKNOWLEDGMENTS

Undertaking and completing this dissertation has been an extraordinary journey for me. It is my pleasure to thank the many people who have encouraged and supported me and made the completion of this work possible.

First and foremost, I would like to thank my mentor and research advisor, Prof. George Christou, for his guidance and help over the last 5 years. His constant encouragement, insightful advice and confidence in my abilities as a chemist have been invaluable in attaining my goal. His impact on my scientific writing skills is enormous. I deeply appreciate the freedom that I enjoyed while working under him, nicely balanced by much-needed guidance and support. Most importantly I would like to thank him for always having the time to sit and talk about research. He was always open to my ideas, yet quick to point out weaknesses and incompleteness in my arguments. Without his support, this dissertation would have been impossible. I walk away from his lab infinitely more knowledgeable about crystal growth, magnetochemistry, and a lifelong experience. I wear the title of “Christou group Alumnus” with pride.

I would also like to thank the other members of my committee, Prof. Stephen Hill, Prof. Lisa McElwee-White, Prof. Michael J. Scott and Prof. Daniel R. Talham for their insightful discussions and comments. I would like to express my gratitude to Dr. Khalil A. Abboud and his staff at the UFCXC for not only solving my crystal structures but most importantly for giving me the rough structures asap. I would also like to acknowledge Dr. Wolfgang Wernsdorfer for providing essential single crystal measurements on Fe_9 and $\text{Mn}_{10}\text{Dy}_2$ compounds below 1.8 K using his micro-SQUID apparatus and answering all my questions to help bring these results together. Many thanks to Prof. Stephen Hill, and Saiti Datta at the UF Physics Department for the HFEPR measurements. Their patience as they taught me the fundamentals, from

understanding a HFEPR experiment to interpreting the terms in a spin Hamiltonian of a SMM, was exceptional.

I would like to thank the entire Christou group, past and present, for their friendship, laughs and all the positive and negative interactions which have helped me in some way or the other. I appreciate the friendship and help of all my seniors Jon, Nicole, Abhu, Dolos and Alina who helped me get started in the lab. Special thanks go to Nicole for her sincere help and for always cheering me up. My juniors Chris, Antonio, Taketo, Arpita, Shreya, Jennifer also deserve special mention for the all fun talking. I would also like to acknowledge our postdoc Tasos (Dr. A. J. Tasiopoulos) for helping me in my first project and Muralee (Dr. M. Murugesu) for introducing me to madras curry paste. Watching Harris (Dr. T. C. Stamatatos) getting new clusters everyday has been very inspiring. During the last five years I had the pleasure of working with two great undergraduates – Sarah Nam and Matthew Daniels. Sincere thanks go for the efficient secretaries of Prof. Christou, Sondra and Melinda. Without them, the little things that make everything run smoothly would never get done. A special thanks goes out to Soma, Rumi, Parul, Arpita, Shreya and Ozge for their warm friendship.

Finally, I must thank my family, which has been an integral part of my existence. I am forever indebted to my parents and my brother Shammi for their constant pride, encouragement, never-ending love, and unwavering confidence in me and for always being there for me. Papa and mummi's philosophy of "work is worship" and "time is money" have helped me become who I am today and where I am today. Thanks shammi for being my greatest critique and best brother in the world. I would like to thank my in-laws for accepting me like a daughter and for all their warmth, love and affection. "Thanks" just seems too insignificant of a word to express

my gratefulness. I feel that my gratitude can not be expressed in words alone. I am grateful for having such a wonderful, loving family and cannot wait to go back.

Last but not least, I would like to thank one very special person, my husband Ranjan. The understanding ear with which he listens to me day and night is commendable. His patience and perfectionism in chemistry and cooking has helped me grow as a person. His love and support carried me through the roughest times. Without him, life would be meaningless. Thanks Ranjan for helping me finish this journey so that we may begin another. I thank you for the daily experience of helping, sharing, complaining, joking and all the things that make life what it is.

The chain of my gratitude would be incomplete if I forget to thank the first cause of this chain, 'Thou Formless One'. My deepest and sincere gratitude for inspiring and guiding this humble being.

TABLE OF CONTENTS

	<u>page</u>
ACKNOWLEDGMENTS	4
LIST OF TABLES	11
LIST OF FIGURES	13
LIST OF ABBREVIATIONS.....	18
ABSTRACT.....	19
CHAPTER	
1 GENERAL INTRODUCTION	22
2 LIGAND-INDUCED DISTORTION OF A TETRANUCLEAR MANGANESE BUTTERFLY COMPLEX	34
2.1 Introduction.....	34
2.2 Experimental Section	35
2.2.1 Syntheses.....	35
2.2.2 X-ray Crystallography.....	37
2.3 Results and Discussion.....	39
2.3.1 Syntheses.....	39
2.3.2 Description of Structures	40
2.3.2.1 Structure of $[\text{Mn}_4\text{O}_2(\text{O}_2\text{CR})_5(\text{salpro})]$ (R = Me (2-1), Bu ^t (2-3))	40
2.3.2.2 Structure of $\text{NMe}_4[\text{Mn}(\text{O}_2\text{CPh})_2(\text{salproH})]$ (2-4)	42
2.3.3 Magnetochemistry.....	43
2.4 Conclusions.....	47
3 ROLE OF MIXED-LIGAND AND MIXED-SOLVENT SYSTEM: ROUTE TO Mn_4 AND Mn_{25}	54
3.1 Introduction.....	54
3.2 Experimental Section	55
3.2.1 Syntheses.....	55
3.2.2 X-ray Crystallography.....	56
3.3 Results and Discussion.....	57
3.3.1 Syntheses.....	57
3.3.2 Description of Structures	59
3.3.2.1 Structure of $[\text{Mn}_4(\text{hmp})_4(\text{pdmH})_2(\text{MeCN})_4](\text{ClO}_4)_4$ (3-1)	59
3.3.2.2 Structure of $[\text{Mn}_{25}\text{O}_{18}(\text{OH})_2(\text{hmp})_6(\text{pdm})_8(\text{pdmH})_2(\text{L})_2](\text{ClO}_4)_6$ (3-2)	60
3.3.3 Magnetochemistry.....	61
3.3.3.1 Dc Studies.....	61

3.3.3.2	Ac Studies	63
3.4	Conclusions	64
4	DIVERSITY OF STRUCTURAL TYPES IN POLYNUCLEAR IRON CHEMISTRY WITH A (N,N,O)-TRIDENTATE LIGAND	70
4.1	Introduction	70
4.2	Experimental Section	71
4.2.1	Syntheses	71
4.2.2	X-ray Crystallography	74
4.3	Results and Discussion	75
4.3.1	Syntheses	75
4.3.2	Description of Structures	77
4.3.2.1	Structure of $[\text{Fe}_7\text{O}_4(\text{O}_2\text{CPh})_{11}(\text{dmem})_2]$ (4-1)	77
4.3.2.2	Structure of $[\text{Fe}_7\text{O}_4(\text{O}_2\text{CMe})_{11}(\text{dmem})_2]$ (4-2)	78
4.3.2.3	Structure of $[\text{Fe}_6\text{O}_2(\text{OH})_4(\text{O}_2\text{CBu}^t)_8(\text{dmem})_2]$ (4-3)	79
4.3.2.4	Structure of $[\text{Fe}_3\text{O}(\text{O}_2\text{CBu}^t)_2(\text{N}_3)_3(\text{dmem})_2]$ (4-4)	79
4.3.3	Magnetochemistry of Complexes 4-1 to 4-4	80
4.3.3.1	Dc Studies	80
4.3.3.2	Rationalization of the Ground State Spin of 4-1 and 4-3	82
4.3.3.3	Determination of the Exchange Interactions in 4-4	83
4.3.4	High-Frequency EPR Spectroscopy	85
4.4	Conclusions	89
5	A NEW N, N, O CHELATE FOR TRANSITION METAL CLUSTER CHEMISTRY: Fe_5 AND Fe_6 CLUSTERS FROM THE USE OF 6-HYDROXYMETHYL-2, 2' BIPYRIDINE	99
5.1	Introduction	99
5.2	Experimental Section	100
5.2.1	Syntheses	100
5.2.2	X-ray Crystallography	102
5.3	Results and Discussion	104
5.3.1	Syntheses	104
5.3.2	Description of Structures	105
5.3.2.1	Structure of $[\text{Fe}_5\text{O}_2(\text{OH})(\text{O}_2\text{CMe})_5(\text{hmbp})_3](\text{ClO}_4)_2$ (5-1)	105
5.3.2.2	Structure of $[\text{Fe}_6\text{O}_2(\text{OH})_2(\text{O}_2\text{CPh})_6(\text{hmbp})_4](\text{NO}_3)_2$ (5-2)	106
5.3.3	agnetochemistry of Complexes 5-1 to 5-4	107
5.3.3.1	Dc Studies	107
5.3.3.2	Rationalization of the Ground State Spin	109
5.4	Conclusions	111
6	NEW STRUCTURAL TYPES IN POLYNUCLEAR IRON CLUSTERS INCORPORATING O,N,N,O LIGAND: A SNAKE LIKE CHAIN AND A SUPRAMOLECULAR DIMER OF SMMs	117
6.1	Introduction	117

6.2	Experimental Section	119
6.2.1	Syntheses	119
6.2.2	X-ray Crystallography	120
6.3	Results and Discussion	123
6.3.1	Syntheses	123
6.3.2	Description of Structures	124
6.3.2.1	Structure of $[\text{Fe}_{18}\text{O}_8(\text{OH})_2(\text{O}_2\text{CBu}^t)_{28}(\text{heen})_4]$ (6-1)	124
6.3.2.2	Structure of $[\text{Fe}_9\text{O}_4(\text{OH})_4(\text{O}_2\text{CPh})_{13}(\text{heenH})_2]$ (6-2)	125
6.3.2.3	Structure of $[\text{Fe}_7\text{O}_3(\text{OMe})_3(\text{MeOH})_1(\text{heen})_3\text{Cl}_{4.5}(\text{H}_2\text{O})_{1.5}]\text{Cl}_{1.25}[\text{FeCl}_4]_{1/4}$ (6-3)	126
6.3.2.4	Structure of $[\text{Fe}_6\text{O}_2(\text{O}_2\text{CPh})_5(\text{heen})_3(\text{heenH})](\text{ClO}_4)_2$ (6-4)	127
6.3.3	Magnetochemistry of complexes 6-1 to 6-4	128
6.3.3.1	Dc Studies	128
6.3.3.2	Ac Studies	131
6.3.3.3	Single-Crystal Hysteresis Studies	131
6.4	Conclusions	132
7	UNUSUAL STRUCTURAL TYPES IN Mn AND Fe CHEMISTRY FROM THE USE OF <i>N,N,N',N'</i> TETRAKIS (2-HYDROXYETHYL)ETHYLENEDIAMINE	142
7.1	Introduction	142
7.2	Experimental Section	143
7.2.1	Syntheses	143
7.2.2	X-ray Crystallography	146
7.3	Results and Discussion	149
7.3.1	Syntheses	149
7.3.2	Description of Structures	153
7.3.2.1	Structure of $[\text{Mn}_8\text{O}_3(\text{OH})(\text{OMe})(\text{O}_2\text{CPh})_7(\text{edte})(\text{edteH}_2)](\text{O}_2\text{CPh})$ (7-1)	153
7.3.2.2	Structure of $[\text{Mn}_{12}\text{O}_4(\text{OH})_2(\text{edte})_4\text{Cl}_6(\text{H}_2\text{O})_2]$ (7-2)	155
7.3.2.3	Structure of $[\text{Mn}_{20}\text{O}_8(\text{OH})_4(\text{O}_2\text{CMe})_6(\text{edte})_6](\text{ClO}_4)_2$ (7-3)	157
7.3.2.4	Structure of $[\text{Fe}_5\text{O}_2(\text{O}_2\text{CPh})_7(\text{edte})(\text{H}_2\text{O})]$ (7-4)	158
7.3.2.5	Structure of $[\text{Fe}_6\text{O}_2(\text{O}_2\text{CBu}^t)_8(\text{edteH})_2]$ (7-5)	159
7.3.2.6	Structure of $[\text{Fe}_{12}\text{O}_4(\text{OH})_2(\text{O}_2\text{CMe})_6(\text{edte})_4(\text{H}_2\text{O})_2](\text{ClO}_4)_4$ (7-6)	160
7.3.3	Magnetochemistry	161
7.3.3.1	Dc Studies on 7-1 to 7-3	161
7.3.3.2	Dc Studies on 7-4 to 7-8	163
7.3.3.3	Ac Studies on 7-1 to 7-5	165
7.3.3.4	Rationalization of the Ground State Spin of 7-4 and 7-5	167
7.4	Conclusions	168
8	SINGLE-MOLECULE MAGNETISM AND MAGNETOSTRUCTURAL CORRELATION WITHIN A FAMILY OF $[\text{Mn}^{\text{III}}_{10}\text{Ln}^{\text{III}}_2]$ COMPLEXES	184
8.1	Introduction	184
8.2	Experimental Section	186
8.2.1	Syntheses	186

8.2.2	X-ray Crystallography.....	189
8.3	Results and Discussion.....	190
8.3.1	Syntheses.....	190
8.3.2	Description of Structures	191
8.3.3	Magnetochemistry.....	193
8.3.3.1	Complexes 8-9 (Mn ₁₀ Y ₂) and 8-4 (Mn ₁₀ Gd ₂).....	193
8.3.3.2	Comparison of 8-9 (Mn ₁₀ Y ₂) with 8-4 (Mn ₁₀ Gd ₂), 8-5 (Mn ₁₀ Tb ₂), 8-6 (Mn ₁₀ Dy ₂), 8-7 (Mn ₁₀ Ho ₂), and 8-8 (Mn ₁₀ Er ₂)	195
8.3.3.3	Comparison of 8-9 (Mn ₁₀ Y ₂) with 8-1 (Mn ₁₀ Pr ₂), 8-2 (Mn ₁₀ Nd ₂), 8-3 (Mn ₁₀ Sm ₂)	198
8.3.3.4	Out-of-Phase ac Susceptibility Signals and Magnetization Hysteresis Loops.....	199
8.4	Conclusions.....	202
9	A FOURTH ISOLATED OXIDATION LEVEL OF THE [Mn ₁₂ O ₁₂ (O ₂ CR) ₁₆ (H ₂ O) ₄] FAMILY OF SINGLE MOLECULE MAGNETS.....	212
9.1	Introduction.....	212
9.2	Experimental Section.....	214
9.2.1	Syntheses.....	214
9.3	Results and Discussion.....	215
9.3.1	Syntheses.....	215
9.3.2	Magnetochemistry.....	218
9.3.2.1	Dc Studies.....	218
9.3.2.2	Comparison of the Magnetic Properties of the [Mn ₁₂] ^Z (z = 0 - 3) Family	219
9.3.2.3	Ac Studies.....	222
9.4	Conclusions.....	224
APPENDIX		
A	BOND DISTANCES AND ANGLES.....	233
B	LIST OF COMPOUNDS.....	256
C	PHYSICAL MEASUREMENTS	258
D	VAN VLECK EQUATIONS	259
LIST OF REFERENCES.....		266
BIOGRAPHICAL SKETCH		284

LIST OF TABLES

<u>Table</u>	<u>page</u>
2-1 Crystallographic Data for 2-1 ·MeCN, 2-3 ·MeOH·2CH ₂ Cl ₂ ·C ₇ H ₁₆ and 2-4 ·CH ₂ Cl ₂	47
2-2 Bond-valence sums for the Mn atoms of complexes 2-1 , 2-3 and 2-4	48
2-3 Comparison of core parameters of selected [Mn ₄ O ₂] ⁸⁺ complexes (Å, °).....	48
2-4 Comparison of exchange parameters in [Mn ₄ O ₂] ⁸⁺ complexes	48
2-5 Spin states of 2-1 ·CH ₂ Cl ₂ in the S _T , S _A , S _B > format	49
3-1 Crystallographic Data for 3-1 and 3-2 ·8MeCN·4MeOH	65
3-2 Bond-valence sums for the Mn atoms of complex 3-2	65
3-3 Bond-valence sums for the O atoms of complex 3-2	65
4-1 Crystallographic data for 4-1 ·4MeCN, 4-2 ·MeCN, 4-3 ·2MeCN and 4-4 ·CH ₂ Cl ₂	91
5-1 Crystallographic Data for 5-1 ·5MeCN and 5-2 ·3MeCN·H ₂ O.	112
6-1 Crystallographic data for 6-1 ·4C ₅ H ₁₂ ·4CH ₂ Cl ₂ , 6-2 ·9MeCN, 6-3 ·2MeOH·½H ₂ O and 6-4 ·2EtOH·2H ₂ O.....	134
7-1 Crystallographic Data for 7-1 ·2CH ₂ Cl ₂ ·MeOH, 7-2 ·6MeCN·½H ₂ O and 7-3 ·10MeOH..	169
7-2 Crystallographic Data for 7-4 ·CH ₂ Cl ₂ , 7-5 ·2CHCl ₃ , 7-6 ·MeCN and 7-7	170
7-3 Bond-valence sums for the Mn atoms of complex 7-1 and 7-3	170
7-4 Bond-valence sums for the O atoms of complex 7-1	171
7-5 Bond-valence sums for the Mn and O atoms of complex 7-2	171
7-6 Bond-valence sums for the O atoms of complex 7-5 and 7-6	172
7-7 Selected Fe-O distances and Fe-O-Fe angles for 7-5	172
8-1 Crystallographic data for 8-4 ·3MeCN·MeOH, 8-6 ·3MeCN·MeOH and 8-9 ·4MeCN.....	204
8-2 Bond-valence sums for the Mn atoms of complex 8-4 , 8-6 and 8-9	204
9-1 Magnetism Data for [Mn ₁₂] ^{Z-} (z = 0 - 3) Complexes 9-1 to 9-5	226
A-1 Selected interatomic distances (Å) and angles (°) for 2-1 ·MeCN.....	233

A-2	Selected interatomic distances (Å) and angles (°) for 2-3 ·MeOH·2CH ₂ Cl ₂ ·C ₇ H ₁₆	234
A-3	Selected interatomic distances (Å) and angles (°) for 2-4 ·CH ₂ Cl ₂	235
A-4	Selected interatomic distances (Å) and angles (°) for 3-1	236
A-5	Selected interatomic distances (Å) and angles (°) for 3-2 ·8MeCN·4MeOH.....	237
A-6	Selected interatomic distances (Å) and angles (°) for 4-1 ·4MeCN.....	238
A-7	Selected interatomic distances (Å) and angles (°) for 4-2 ·MeCN.....	239
A-8	Selected interatomic distances (Å) and angles (°) for 4-3 ·2MeCN.....	240
A-9	Selected interatomic distances (Å) and angles (°) for 4-4 ·2CH ₂ Cl ₂	241
A-10	Selected interatomic distances (Å) and angles (°) for 5-1 ·5MeCN.....	242
A-11	Selected interatomic distances (Å) and angles (°) for 5-2 ·3MeCN·H ₂ O.....	243
A-12	Selected interatomic distances (Å) and angles (°) for 6-1 ·4C ₃ H ₁₂ ·4CH ₂ Cl ₂	244
A-13	Selected interatomic distances (Å) and angles (°) for 6-2 ·9MeCN.....	245
A-14	Selected interatomic distances (Å) and angles (°) for 6-3 ·6MeOH·H ₂ O	246
A-15	Selected interatomic distances (Å) and angles (°) for 6-4 ·2EtOH·1.5H ₂ O	247
A-16	Selected interatomic distances (Å) and angles (°) for 7-1 ·2CH ₂ Cl ₂ ·MeOH.....	248
A-17	Selected interatomic distances (Å) and angles (°) for 7-2 ·6MeCN·½H ₂ O.....	249
A-18	Selected interatomic distances (Å) and angles (°) for 7-3 ·10MeOH.....	250
A-19	Selected interatomic distances (Å) and angles (°) for 7-5 ·2CHCl ₃	251
A-20	Selected interatomic distances (Å) and angles (°) for 7-6 ·4MeCN.....	252
A-21	Selected interatomic distances (Å) and angles (°) for 8-4 ·3MeCN·MeOH.....	253
A-22	Selected interatomic distances (Å) and angles (°) for 8-6 ·3MeCN·MeOH.....	254
A-23	Selected interatomic distances (Å) and angles (°) for 8-9 ·4MeCN.....	255

LIST OF FIGURES

<u>Figure</u>	<u>page</u>
1-1	Representations of magnetic dipole arrangements in paramagnetic, ferromagnetic, antiferromagnetic, and ferrimagnetic materials31
1-2	Schematic diagram of a hysteresis curve for a typical ferromagnet.31
1-3	Schematic representation of a multidomain ferromagnetic particle in the unmagnetized state.....31
1-4	Representation of the $[\text{Mn}_{12}\text{O}_{12}]^{16+}$ core and $[\text{Mn}_{12}\text{O}_{12}(\text{O}_2\text{CMe})_{16}(\text{H}_2\text{O})_4]$ complex with peripheral ligation.32
1-5	Representative plots of the potential energy versus orientation of the m_s vector along the z axis and the m_s sublevels for a Mn_{12} complex.32
1-6	Magnetization hysteresis loops for a typical $[\text{Mn}_{12}\text{O}_{12}(\text{O}_2\text{CR})_{16}(\text{H}_2\text{O})_4]$ complex.33
1-7	Representation of the change in energy of the m_s sublevels as a function of the applied magnetic field.....33
2-1	Structure of SalproH_350
2-2	Labeled representation of the structure of 2-1 and 2-350
2-3	Comparison of the cores of 2-1 and 2-3 with that of the normal butterfly complexes.51
2-4	Labeled representation of the structure of 2-451
2-5	Plots of $\chi_M T$ vs T for complexes 2-1 · CH_2Cl_2 , 2-2 · CH_2Cl_2 and 2-3 · $\frac{1}{2}\text{CH}_2\text{Cl}_2$52
2-6	The core of 2-1 defining the pairwise exchange interactions and rationalization of ground state spin of 2-153
2-7	$\chi_M T$ vs. T and reduced magnetization ($M/N\mu_B$) vs H/T plots for 2-4 · $\frac{1}{2}\text{CH}_2\text{Cl}_2$53
2-8	Two-dimensional contour plot of the fitting-error surface vs D and g for 2-4 · $\frac{1}{2}\text{CH}_2\text{Cl}_2$53
3-1	Structure of ligands: 2-hydroxymethyl pyridine (hmpH), 2,6-pyridine dimethanol (pdmH ₂), 6-hydroxymethyl 2-pyridine carboxylic acid (L).66
3-2	Labeled representation of the structure of 3-166
3-3	Structure of the cation of 3-266
3-4	Centrosymmetric core of 3-2 and its three types of constituent layers.....67

3-5	Plots of $\chi_M T$ vs T for complex 3-1	67
3-6	The core of 3-1 defining the pairwise exchange interactions.	68
3-7	Plot of reduced magnetization ($M/N\mu_B$) vs H/T and two-dimensional contour plot of the fitting error surface vs D and g for complex 3-1	68
3-8	Plot of in-phase ($\chi_M' T$) and out-of-phase (χ_M'') ac susceptibility data for complex 3-1	69
3-9	$\chi_M T$ vs T and reduced magnetization ($M/N\mu_B$) vs H/T plots for complex 3-2 ·3H ₂ O.....	69
3-10	Plot of $\chi_M' T$ vs T (in-phase) ac susceptibility data for 3-2 ·3H ₂ O.	69
4-1	Structure of ligands: mdaH ₂ and dmemH.	91
4-2	Labeled representation of the structure of 4-1 and 4-2	92
4-3	Comparison of cores of 4-1 , 4-2 and 4-3	92
4-4	Labeled representation of the structures of 4-3 and 4-4	93
4-5	Plots of $\chi_M T$ vs T for complexes 4-1 , 4-2 , 4-3 and 4-4	93
4-6	Plot of reduced magnetization ($M/N\mu_B$) vs H/T for complex 4-1 ·½MeCN.....	94
4-7	Two-dimensional contour plot of the fitting error surface vs D and g for 4-1 ·½MeCN.....	94
4-8	Plot of reduced magnetization ($M/N\mu_B$) vs H/T and two-dimensional contour plot of the fitting error surface vs D and g for 4-2 ·2MeCN	95
4-9	Plot of reduced magnetization ($M/N\mu_B$) vs H/T and two-dimensional contour plot of the fitting error surface vs D and g for 4-3	95
4-10	Rationalization of the ground state spin of 4-1 and 4-3	96
4-11	Plot of reduced magnetization ($M/N\mu_B$) vs H/T and two-dimensional contour plot of the fitting error surface vs D and g for 4-4 ·½CH ₂ Cl ₂	96
4-12	Core of 4-4 defining the pairwise exchange interactions and the rationalization of its ground state spin	97
4-13	HFEPR peak positions for 4-3 ·2MeCN from angle-dependent studies and frequency dependence for 4-3 ·2MeCN.....	97
4-14	Simulated Zeeman diagram for a spin $S = 5$ and $5/2$ system with $D < 0$ and $D > 0$	98
4-15	Temperature dependent spectra and easy-plane peak positions for 4-1 ·4MeCN plotted versus frequency	98

5-1	Structure of ligands: dmemH and hmbpH.....	112
5-2	Synthetic scheme for hmbpH.....	112
5-3	Labeled representation of the structure of 5-1	113
5-4	Labeled representation of the structure of 5-2	113
5-5	Plots of $\chi_M T$ vs T for complexes 5-1 , 5-2 ·H ₂ O, 5-3 ·H ₂ O and 5-4 ·H ₂ O.....	114
5-6	Plot of reduced magnetization ($M/N\mu_B$) vs H/T and two-dimensional contour plot of the fitting error surface vs D and g for 5-1	114
5-7	Plot of reduced magnetization ($M/N\mu_B$) vs H/T and two-dimensional contour plot of the fitting error surface vs D and g for 5-2 ·H ₂ O, 5-3 ·H ₂ O and 5-4 ·H ₂ O.....	115
5-8	Rationalization of spin ground state of complex 5-1 and 5-2	116
6-1	Structure of chelates: dmemH, heenH ₂	134
6-2	Labeled representation of the structure of 6-1	135
6-3	Labeled representation of the structure of 6-2	135
6-4	[Fe ₉] ₂ dimer showing intermolecular and intramolecular hydrogen-bonding, and the resultant ON and OFF state with respect to the coupling of the two molecules.....	136
6-5	Labeled representation of the structure of 6-3	137
6-6	Labeled representation of the cation of 6-4	137
6-7	Plot of $\chi_M T$ vs T for complexes 6-1 to 6-4	138
6-8	Spin alignments at the Fe atoms of 6-1 rationalizing its ground state spin.....	138
6-9	Plot of reduced magnetization ($M/N\mu_B$) vs H/T and two-dimensional contour plot of the r.m.s. error vs D and g for the fit for 6-2	139
6-10	Plot of reduced magnetization ($M/N\mu_B$) vs H/T for 6-3 and 6-4	139
6-11	Two-dimensional contour plot of the r.m.s. error vs D and g for the fit for complexes 6-3 and 6-4	140
6-12	Plot of the in-phase ($\chi_M' T$) and out-of-phase (χ_M'') ac susceptibility data for 6-2	140
6-13	Plot of in-phase ac susceptibility data for 6-3 and 6-4	141
6-14	Single-crystal magnetization (M) vs dc field (H) hysteresis loops for 6-2	141

7-1	Structure of ligands.....	172
7-2	Labeled representation of the cation of 7-1	173
7-3	Crystallographically established coordination modes of edte^{4-} and edteH_2^{2-} found in complexes 7-1 to 7-3	173
7-4	Labeled representation of the structure of 7-2	174
7-5	The structure of the cation of 7-3	175
7-6	Labeled representation of the core of 7-3	176
7-7	Labeled representation of the structure of 7-4	177
7-8	Crystallographically established coordination modes of edte^{4-} and edteH^{3-} found in complexes 7-4 to 7-6	177
7-9	Labeled representation of the structure of 7-5	177
7-10	Labeled representation of the cation of 7-6	178
7-11	Labeled representation of the cation of 7-7	179
7-12	Plots of $\chi_M T$ vs T for complexes 7-1 ·2H ₂ O, 7-2 and 7-3 ·5H ₂ O	179
7-13	Plots of reduced magnetization ($M/N\mu_B$) vs H/T for 7-1 ·2H ₂ O and 7-2	180
7-14	Two-dimensional contour plot of the r.m.s. error surface vs D and g for the magnetization fit for 7-1 ·2H ₂ O and 7-2	180
7-15	Plots of reduced magnetization ($M/N\mu_B$) vs H/T and two-dimensional contour plot of the r.m.s. error surface vs D and g for the magnetization fit for 7-3 ·5H ₂ O.	181
7-16	Plots of $\chi_M T$ vs T for complexes 7-4 to 7-8	181
7-17	Plot of reduced magnetization ($M/N\mu_B$) vs H/T for 7-4 and 7-5 ·2CHCl ₃ ·4H ₂ O	182
7-18	Two-dimensional contour plot of the fitting error surface vs D and g for complexes 7-4 and 7-5 ·2CHCl ₃ ·4H ₂ O	182
7-19	Plot of $\chi_M' T$ vs. T for complexes 7-1 – 7-5	183
7-20	Spin alignments at the Fe atoms of 7-5 rationalizing its $S = 5$ ground state.....	183
8-1	Labeled structures of 8-4 , 8-6 , and 8-9	205
8-2	Centrosymmetric core of 8-6 emphasizing the ABCBA layer structure..	206

8-3	Plot of $\chi_M T$ vs T and $\chi_M' T$ vs T for complexes 8-4 and 8-9	206
8-4	Plot of reduced magnetization ($M/N\mu_B$) vs H/T for 8-9 and 8-4	207
8-5	Two-dimensional contour plot of the error surface for the D vs g fit for 8-9 and 8-4	207
8-6	Plots of dc $\chi_M T$ vs T for $\text{Gd}(\text{NO}_3)_3$ and $\text{Dy}(\text{NO}_3)_3$	208
8-7	Plots of $\chi_M T$ vs T for 8-9 , 8-5 and 8-6	208
8-8	Plots of $\chi_M T$ vs T for 8-9 , 8-7 and 8-8	208
8-9	Plots of $\chi_M T$ vs T for 8-1 , 8-2 , 8-3 and 8-9	209
8-10	Plots of out-of-phase χ_M'' vs T ac susceptibility data for 8-9 and 8-4	209
8-11	Plots of out-of-phase χ_M'' vs T ac susceptibility data for 8-1 and 8-2	209
8-12	Plots of in-phase, $\chi_M' T$ vs T , and out-of-phase χ_M'' vs T ac susceptibility data for 8-5 , 8-6 and 8-7	210
8-13	Plot of relaxation rate vs reciprocal temperature for 8-5 – 8-7	210
8-14	Magnetization vs. time decay plots in zero dc field and τ vs $1/T$ plot for 8-6	211
8-15	Single-crystal magnetization vs dc field hysteresis loops for 8-6 ·3MeCN·MeOH.....	211
9-1	Cyclic voltammogram and differential pulse voltammogram for 9-1	226
9-2	Proposed structural core of 9-2 – 9-4	227
9-3	Plot of $\chi_M T$ vs T for 9-2 – 9-5	228
9-4	Plot of reduced magnetization ($M/N\mu_B$) vs H/T for 9-4 and 9-5	228
9-5	Plot of reduced magnetization ($M/N\mu_B$) vs H/T for 9-2 and 9-3	229
9-6	Two-dimensional contour plot of the error surface for the D vs g fit and D vs E fit for complex 9-4	229
9-7	Plot of the in-phase ($\chi_M' T$) and out-of-phase (χ_M'') ac susceptibility data for 9-4	230
9-8	Plot of the in-phase ($\chi_M' T$) and out-of-phase (χ_M'') ac susceptibility data for 9-5	230
9-9	χ_M'' vs T plots for vacuum-dried complexes $[\text{Mn}_{12}]^{z-}$ ($z = 0-3$).....	231
9-10	Comparison of the χ_M'' vs T plots for vacuum-dried complexes $[\text{Mn}_{12}]^{z-}$ ($z = 0-3$).....	232

LIST OF ABBREVIATIONS

Bu'	tertiary butyl
BVS	bond valence sum
CV	cyclic voltammogram
dmemH:	2-{[2-(dimethylamino)ethyl]-methylamino} ethanol
DPV	differential pulse voltammogram
edteH ₄	<i>N,N,N',N'</i> -tetrakis(2-hydroxyethyl)ethylenediamine
heenH ₂	<i>N,N'</i> -bis(2-hydroxyethyl)ethylenediamine
HFEPR	high Frequency electron paramagnetic resonance
hmbpH	6-hydroxymethyl-2,2'-bipyridine
hmpH:	2-hydroxymethyl pyridine
L	6-hydroxymethyl-2-pyridine carboxylic acid
pdmH ₂ :	2,6-pyridine dimethanol
PS II	photosystem II
Py	pyridine
salproH ₃	1,3-bis(salicylideneamino)-2-propanol
TIP	temperature independent paramagnetism
ZFS	zero-field splitting

Abstract of Dissertation Presented to the Graduate School
of the University of Florida in Partial Fulfillment of the
Requirements for the Degree of Doctor of Philosophy

DIVERSITY OF STRUCTURAL TYPES AND MOLECULAR NANOMAGNETISM IN
IRON AND MANGANESE CLUSTERS

By

Rashmi Bagai

May 2008

Chair: George Christou
Major: Chemistry

The primary reason for the current interest in high nuclearity manganese and iron-oxo clusters is because of their relevance in molecular magnetism and bio-inorganic chemistry. A particularly appealing area in molecular magnetism is that of molecules which show slow relaxation of magnetization at low temperatures, behaving as tiny magnets, and thus known as single molecule magnets (SMMs). One of the first SMM to be synthesized was $[\text{Mn}_{12}\text{O}_{12}(\text{O}_2\text{CMe})_{16}(\text{H}_2\text{O})_4]$ (Mn_{12}), which now serves as the “drosophila” of molecular magnetism. The various modifications of the Mn_{12} family of SMMs have permitted advances in our knowledge and understanding of Mn_{12} complexes and the SMM phenomenon in general. For the first time, Mn_{12} family of SMMs has been extended to a fourth isolated member by the successful isolation and characterization of $[\text{Mn}_{12}]^{3-}$ complexes with $S = 17/2$ ground-state spin and $D = -0.24(1) \text{ cm}^{-1}$. When studied by ac susceptibility techniques, the $[\text{Mn}_{12}]^{3-}$ complexes exhibit frequency-dependent out-of-phase signals indicating them to be SMMs, albeit with smaller barriers than the other Mn_{12} oxidation levels. The $[\text{Mn}_{12}]^{3-}$ complexes represent a fourth isolated oxidation level of the Mn_{12} family of SMMs, by far the largest range of oxidation levels yet encountered within single-molecule magnetism.

Towards the synthesis of polynuclear molecular clusters, various alcohol-based ligands have been explored. Among them is a family of ligands incorporating one, two and four hydroxyethyl arms on ethylenediamine backbone. Use of *dmemH* (2- $\{[2-(\text{dimethylamino})\text{ethyl}]-\text{methylamino}\}$ ethanol) has led to two new Fe_7 clusters and one Fe_6 cluster, depending on the identity of the carboxylate employed. Unlike *dmemH*, use of *hmbpH* (6-hydroxymethyl-2,2'-bipyridine), one that amalgamates the chelating property of bipyridine and *hmpH* (hydroxymethyl pyridine), resulted in Fe_6 cluster irrespective of the carboxylate employed. These contrasting results from flexible *dmemH* and rigid *hmbpH* underline the exquisite sensitivity of the reaction product on a variety of reaction conditions and reagents used. The magnetochemical characterization of these clusters emphasize how ground state spin values of significant magnitude can result from spin-frustration effects even though all the pair wise exchange interactions are antiferromagnetic.

The use of *heenH*₂ (*N,N'*-bis(2-hydroxyethyl)ethylenediamine) has provided an entry into new cluster types, including a discrete Fe_{18} molecular chain with an unusual double-headed serpentine structure and a Fe_9 SMM, both having unprecedented structures in Fe chemistry. Fe_{18} represents the highest nuclearity, chain-like metal-containing molecule to be yet discovered, and Fe_9 SMM contains a mixture of ON and OFF dimers with respect to the quantum-mechanical coupling through the hydrogen-bond.

The initial use of *edteH*₄ (*N,N,N',N'*-tetrakis(2-hydroxyethyl)ethylenediamine) in Mn and Fe chemistry has resulted in novel complexes of high nuclearity and architectural beauty ranging from Mn_8 to Mn_{20} and Fe_5 to Fe_{12} . The complexes all possess rare or novel core topologies. The combined results demonstrate the ligating flexibility of alkoxide containing chelates and their usefulness in the synthesis of a variety of Fe_x and Mn_x molecular clusters.

A family of tetranuclear Mn clusters has been synthesized using Schiff-base ligand, salproH₃ (1,3-bis(salicylideneamino)-2-propanol). The structure of these is much more closed than the previously reported butterfly-like complexes as a result of the alkoxide oxygen of salpro bridging the two wingtip Mn atoms. Fitting of the dc magnetic susceptibility data revealed that the various exchange parameters are all antiferromagnetic, and the core thus experiences spin frustration effects.

Use of hmpH and pdmH₂ (2,6-pyridine dimethanol) has resulted in an aesthetically pleasing Mn₂₅ with a ground-state spin of 65/2, which is the second highest in Mn chemistry. Achieving high spin ground state is one of the elusive goals in the search for obtaining superior SMMs. A family of isostructural heterometallic Mn-Ln clusters with a [Mn^{III}₁₀Ln^{III}₂] core (Ln = Pr, Nd, Sm, Gd, Tb, Dy, Ho and Er) has been synthesized as well as the [Mn^{III}₁₀Y^{III}₂] analog with diamagnetic Y^{III} to assist the magnetic studies of the nature of Mn···Ln exchange interactions. Complexes containing Tb, Dy and Ho exhibit strong frequency-dependent out-of-phase ac susceptibility signals characteristic of SMMs which was confirmed for the Dy complex by the observation of magnetization hysteresis.

CHAPTER 1 GENERAL INTRODUCTION

Magnetism has been known to humans for millennia. What is magnetism? This question has fascinated people ever since Thales of Miletus (about 634-546 BC) first described the phenomenon as the attraction of iron by “lodestone.”¹ Over the last 2500 years, magnetism has played an important role in the development of civilization, we have not only extensively used the phenomenon for navigation, power production and “high tech” applications but we have also come a long way in exploring its origin. Today we more specifically associate lodestone with the spinel magnetite, Fe_3O_4 , which is magnetically aligned in nature, most likely by the earth’s magnetic field during the cooling process of hot lava.

One of the most fundamental ideas in magnetism is the concept of a magnetic field. A magnetic field is produced whenever there is an electrical charge in motion, specifically the spin and orbital angular momenta of electrons within atoms of a material. Thus the essential component of any magnetic material is the presence of an unpaired electron and how they interact with each other determines the magnetic behavior of all magnets.² The different types of magnetic materials are usually classified on the basis of their susceptibility (χ). A magnetic susceptibility is merely the quantitative measure of the response of a material to an applied magnetic field. Substances were first classified as diamagnetic or paramagnetic by Michael Faraday in 1845, but it was not until many years later that these phenomena came to be understood in terms of electronic structure.³ Diamagnetism is an underlying property of all matter and arises from the interaction of paired electrons with the magnetic field while paramagnetism is a property exhibited by substances containing unpaired electrons. Diamagnets are slightly repelled by a magnetic field and χ for these is small negative (-10^{-5}) and paramagnets are attracted into an applied field and χ for these is small positive (10^{-3} to 10^{-5}). Diamagnetic

susceptibilities are independent of field and temperature while paramagnetic susceptibility varies inversely with temperature, $\chi = C/T$, where C is Curie constant.⁴ Upon bringing the spins closer together, spin-coupling enables a tendency toward parallel ($\uparrow\uparrow$) or antiparallel ($\uparrow\downarrow$) alignment. This behavior can be modeled as a function of temperature by the Curie-Weiss expression, $\chi = C/(T-\theta)$, where θ is proportional to the strength of coupling between adjacent spins. Pairwise ferromagnetic coupling ($\uparrow\uparrow$) can lead to long-range ferromagnetic order, whereas antiferromagnetic order may arise from pairwise antiferromagnetic coupling ($\uparrow\downarrow$) as shown in Figure 1-1. The ferromagnetic solids are the most widely recognized magnetic materials with χ ranging from 50 to 10,000. Examples of these materials are iron, cobalt, nickel and several rare earth metals and their alloys.⁵ Ferrimagnets (e.g. magnetite, Fe_3O_4) arise from antiferromagnetic coupling, which does not lead to complete cancellation, and thus they have a net magnetic moment (Figure 1-1). Ferro-, antiferro- and ferrimagnetic ordering occurs below a critical temperature, T_c . Below T_c , the magnetic moments for ferro- and ferrimagnets align in small domains. In the absence an applied magnetic field, despite the nature of interactions, a net zero magnetization is thermodynamically favored, as different domains have their net magnetizations randomly oriented. A useful property of these materials is that when an external field is applied to them, the magnetic fields of the individual domains tend to line up in the direction of the external field. At some particular value of the field, no domains are present as all the spins are aligned and net magnetization is at its saturation point. The system will remain in that situation unless enough energy is given to overcome the energy barrier for domain formation. This property can be monitored in a plot of magnetization vs applied field called hysteresis loop (Figure 1-2).² Because an additional field is required to reverse the direction of magnetization, magnetic storage of information is possible in ferromagnetic and ferrimagnetic materials.

In addition to the ferri- and ferromagnetic behavior, other magnetic-ordering phenomena, such as metamagnetism, canted ferromagnetism, and spin-glass behavior may occur.⁶ The transformation from an antiferromagnetic state to a high moment state is called metamagnetism. A canted antiferromagnet (or weak ferromagnet) results from the relative canting of antiferromagnetically coupled spins that lead to a net moment. A spin glass occurs when local spatial correlations with neighboring spins exist, but long-range order does not. The spin alignment for a spin glass is that of paramagnet; however, unlike paramagnets, for which spin directions vary with time, the spin orientations of a spin glass remain fixed or vary only very slowly with time.⁷

As throughout history, today's magnetism research remains closely tied to applications. It is therefore no surprise that some of the forefront research areas in magnetism today are driven by the "smaller and faster" mantra of advanced technology. Future of the magnetic data storage and memory technology is concerned with cramming information into smaller and smaller bits and manipulating these bits faster and faster. Thus, the need to develop magnetic particles of nanoscale dimensions is unavoidable. The synthesis of such nanomagnets can be accomplished by fragmentation of bulk ferromagnets or ferrimagnets, for example, crystals of magnetite can be broken down such that each fragment is smaller in size than a single domain (20-200 nm); these subdomain nanoscale magnetic particles with varying sizes are called superparamagnets (Figure 1-3).⁸ The magnetic moments within one superparamagnetic particle are ferromagnetically aligned due to short range order. These clusters are thermally unstable, i.e., their magnetic moments (represented by moment vectors) experience thermal fluctuations with great ease, as is the case with paramagnetic species due to lack of long-range ordering. In other words, even though the temperature is below the Curie or Neel temperature and the thermal energy is not

sufficient to overcome the coupling forces between neighboring atoms, the thermal energy is sufficient to change the direction of magnetization of the entire crystallite. The resulting fluctuations in the direction of magnetization cause the magnetic moment to average to zero. When cooled below a critical blocking temperature (T_B), superparamagnetic systems experience a very slow relaxation time, their net magnetic moments align parallel to the applied field and appear to behave as if they had an apparent “bulk-like” ferromagnetic behavior.⁸ This aspect will result in hysteresis of “apparent” ferromagnetic behavior. But this approach unfortunately gives a distribution of particle sizes, and this complicates detailed study of these systems, making difficult, for example, an accurate assessment of variation of properties as a function of particle size.⁹

One approach being investigated for new magnets is based on molecules as building blocks also called bottom-up approach. Molecule-based magnets present several attributes unavailable in conventional metal and metal-oxide magnets. These properties include low density, mechanical flexibility, low temperature processability, high magnetic susceptibility, biocompatibility and several other desirable characteristics.¹⁰ This strategy has the advantage that a single particle size can be ensured, that organic ligands on the periphery can be chosen or systematically altered to ensure crystallinity and solubility in a variety of solvents, and that X-ray crystallographic and various spectroscopic and physicochemical studies can be readily performed in solution and/or solid state.^{6,11}

Worldwide interest in molecule-based magnets has arisen for both fundamental scientific and technological reasons. Molecular magnetic materials have been added to the library of magnetism only at the end of twentieth century. The first molecule-based magnet, reported in 1967 was that of $[\text{Fe}^{\text{III}}(\text{S}_2\text{CNET}_2)_2\text{Cl}]$ molecules, which orders at 2.46 K.⁴ Subsequently, there

was very little published activity in this area until 1987 when Miller *et al.* characterized a ferromagnetic transition in the organometallic donor acceptor salt, $[\text{Fe}(\text{C}_5\text{Me}_5)_2][\text{TCNE}]$. The $\frac{1}{2}$ spins associated with both donor and acceptor units are strongly coupled along the chains in a ferromagnetic fashion resulting in bulk ferromagnetic properties with a spontaneous magnetization below $T_c = 4.8 \text{ K}$.⁷ Since then, plethora of molecule-based magnets exhibiting a wide variety of bonding and structural motifs have been synthesized. These include molecules with extended bonding within chains (1D), within layers (2D), and within 3D network structures. Molecule-based magnets include materials with spins only in organic moieties (in p orbitals), and those with spins both on metal ions and organic moieties and those materials with spins on metal ions with exchange pathways provided by organic moieties that do not contain spin.¹⁰

A big breakthrough in molecule-based systems was the discovery of zero-dimensional (isolated molecules) nanoscale magnets now called Single Molecule Magnets (SMMs). One of the first SMM to be synthesized was $[\text{Mn}_{12}\text{O}_{12}(\text{O}_2\text{CMe})_{16}(\text{H}_2\text{O})_4]$ (Mn_{12}),¹² which by now serves as the “drosophila” of molecular magnetism (Figure 1-4).¹³ The ease of preparation, stability, high ground state spin, high magnetic anisotropy coupled with its highly crystalline nature and high symmetry space group, which simplifies the spin Hamiltonian by precluding second-order transverse (rhombic) terms, has made Mn_{12} the favorite for detailed study within the chemistry and physics communities by a myriad of techniques.¹⁴ Structurally, the family of Mn_{12} molecules contain an external crown of eight Mn^{III} ions ($S = 2$), which are ferromagnetically coupled and an inner core of four Mn^{IV} ions ($S = 3/2$), also ferromagnetically coupled. The crown and core are antiferromagnetically coupled to produce a total spin of $S = 10$.¹⁵ Remarkably, a negative axial zero-field splitting (ZFS), D , leads to a loss in the degeneracy of the associated m_s levels, such that $m_s = +10$ and $m_s = -10$ are lowest in energy (Figure 1-5). Thus there exists an energy barrier

for the conversion of “spin up” to “spin down”. The slow relaxation of magnetization, which is at the origin of the interesting behavior, is due to the presence of an energy barrier to be overcome in the reversal of the magnetic moment. The energy barrier is proportional to $S^2|D|$ for integer spin and $(S^2-1/4)|D|$ for half-integer spin system.¹³

A unique feature of Mn_{12} is that slow relaxation of magnetization gives rise to hysteresis cycle, similar to that observed in bulk magnets, but of molecular origin (Figure 1-6). The magnet-like behavior of Mn_{12} has sparked the idea that information might one day be stored as the direction of magnetization in individual molecules.¹⁶ The most information that can be stored on hard drives and other devices currently is 3 billion bits, or 3 gigabits, in 1 cm^2 area of a cobalt-based magnetic material. The much smaller size of SMMs means that one can get 30 trillion of them into 1 cm^2 , and thus a storage density of 30 trillion bits, or 30 terabits, is feasible. This is 10,000 times greater than the current best by computer manufacturers.¹⁷ One of the research challenges now is to find better SMMs that function at higher temperatures. The second appealing feature of Mn_{12} is that relaxation of its magnetization shows clear quantum effects, which is manifested in the step-like hysteresis loop (Figure 1-6).¹⁸ The observed steps correspond to an increase in the relaxation rate of magnetization that occurs when there is an energy coincidence of m_s sublevels on the opposite sides of the potential energy barrier. For these critical field values, $H = nD/g\mu_B$, at which steps occur, quantum tunneling of magnetization (QTM)¹⁹ is allowed, resulting in an increase in the relaxation rate of the molecule. Thus the relaxation of the magnetization of an SMM occurs not just by thermal activation over the energy barrier, but also by QTM through the energy barrier (Figure 1-7). A transverse component contained in the Hamiltonian of the molecule must be present to promote tunneling through the energy barrier; such transverse components can be provided in three ways 1) by low symmetry

components of the crystal field 2) by a magnetic field provided by magnetic nuclei 3) by a magnetic field provided by neighboring molecules.¹⁹ Although tunneling provides a route for rapid reversal of magnetization and, hence, a less attractive memory storage device but, these features can be used to develop new classes of quantum computers in which quantum coherence is used to store information. The SMM phenomenon is not unique to Mn₁₂, the family of SMM compounds has been extended to various other metals including Fe, V, Co, Ni and combinations of 3d with 4d, 5d, 4f paramagnetic ions, and homometallic Ln^{III} species.^{9,13,20-23} In order to be considered for real applications, the challenge that falls within the domain of inorganic chemistry is to synthesize molecules with higher spin-reversal barriers, capable of storing information at more practical temperatures.

In order to observe SMM behavior from a molecular compound, it is necessary to have a high spin ground state, S , and a large negative ZFS of the ground state and negligible interactions between molecules. The combination of these properties can lead to energy barrier so that, at low temperatures, the system can be trapped in one of the high-spin energy wells. In principle, large spin can be achieved using a small number of ions if the individual components have a large spin and ZFS of clusters is determined by single ion anisotropy and spin-spin interactions which can be both magnetic dipolar and exchange in nature.²⁰ Two ions with $S = 5/2$ ferromagnetically coupled can have a ground state with $S = 5$, while it is necessary to assemble a cluster of ten $S = 1/2$ ions in order to achieve the same result. This is the reason why ions with large spin such as high spin Fe^{III} and Mn^{III} have been largely used for the preparation of SMMs.^{13,22}

In addition to their relevance in magnetochemistry, Mn and Fe are two of the most important elements in biochemistry.²⁴⁻²⁷ The ability to exist in different oxidation states makes manganese well suited as the active site for redox reactions in a number of metalloproteins and

enzymes.²⁸ The most important of which is the water-oxidizing complex of PS II. This reaction is responsible for the generation of almost all the oxygen for this planet.²⁹ The relevance of Fe in geology and biochemistry is even larger than that of Mn. Iron is the fourth most abundant element in the earth's crust. In addition to its availability, iron also possesses chemical properties such as Lewis acidity and redox capability that allows it to perform diverse set of metabolic functions. Iron storage protein ferritin can store upto 4500 iron atoms.³⁰ In addition, ferritin is also considered as a nanosize magnetic particle and has been investigated for quantum tunneling effects of magnetization.³¹ The work presented in this thesis focuses on the synthesis and characterization of new complexes of Mn and Fe, stimulated by the search for inorganic models of important metalloproteins and by the remarkable magnetic properties that these complexes display.

In order to design clusters, it is necessary to have available both connecting blocks, which provide efficient bridges and determine the growth of the cluster, and terminal blocks, which stop the growth of the cluster at a finite size. The bridging blocks must not only provide the right connection between metal ions but also provide efficient exchange pathways thus assuring strong magnetic coupling. In the design and synthesis of polynuclear molecular clusters, the choice of appropriate ligand is the most important step. The ligand (from the latin word ligare, to bind) is any molecular moiety that has at least one donor atom i.e. an atom with a non-binding electron pair. A ligand is called mono-, bi-, tri- etc, dentate if it possesses one, two, three etc donor atoms. Commonly employed are the polydentate ligands that possess more than one donor atom. If the different donor atoms coordinate the same metal ion it is called a chelating ligand. An important class of polydentate ligands is constituted by polyalcohols since this functionality is an excellent bridging group and fosters higher nuclearity product formation on deprotonation.³² In this work

we decided to explore the possibility of creating new structural types using a variety of alcohol based ligands:

- 1) a pentadentate Schiff-base ligand,
- 2) bi- and tridentate ligands containing one and two hydroxymethyl arms on pyridine backbone,
- 3) tri-, tetra- and hexadentate ligands incorporating one, two and four hydroxyethyl arms on ethylenediamine backbone.

The layout of the thesis is as follows. Chapters 2 to 7 are organized according to the types of ligands used. In Chapter 2, a Schiff-based ligand (salproH₃) has been used to synthesize tetranuclear Mn clusters and magnetic interactions between different spin centers have been determined. Chapter 3 is devoted to the ‘mixed-ligand approach’ where synthesis of a high nuclearity, high spin complex has been achieved using hmpH and pdmH₂. In Chapter 4 and 5, a flexible and a rigid N,N,O based ligand, dmemH and hmbpH respectively, is employed for the synthesis of Fe₅, Fe₆ and Fe₇ clusters. Chapter 6 explores the potential of O,N,N,O based ligand, heenH₂, which has led to the largest molecular chain complex, Fe₁₈, and also provides insight into the micro SQUID measurements of a supramolecular Fe₉ dimer. Denticity of ligand is further extended in Chapter 7, which employs O,O,N,N,O,O based ligand, edteH₄, for the preparation of novel Mn_x and Fe_x clusters. Synthesis and magnetostructural correlation of a family of heterometallic Mn-Ln SMMs is the theme of Chapter 8. The chemical reduction of [Mn₁₂O₁₂(O₂CCHCl₂)₁₆(H₂O)₄] forming one-, two- and three- electron reduced complexes with identical peripheral ligation is detailed in Chapter 9.

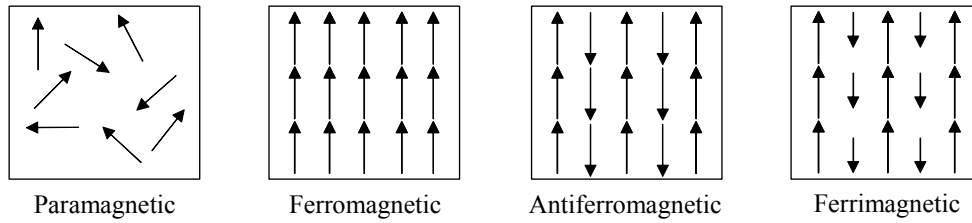


Figure 1-1. Representations of magnetic dipole arrangements in 1) paramagnetic, 2) ferromagnetic, 3) antiferromagnetic, and 4) ferrimagnetic materials.

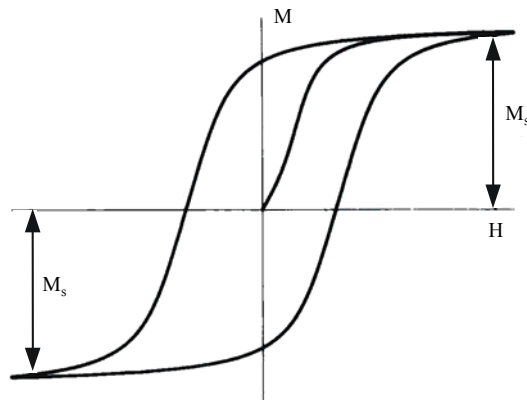


Figure 1-2. Schematic diagram of a hysteresis curve for a typical ferromagnet showing magnetization (M) as a function of the applied magnetic field (H). Saturation magnetization is indicated by M_s .

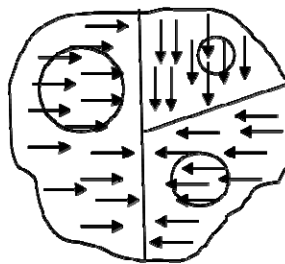


Figure 1-3. Schematic representation of a multidomain ferromagnetic particle in the unmagnetized state. Each of the three domains with net moments remain randomized in this state. Circles of varying sizes represent the subdomain superparamagnetic clusters.

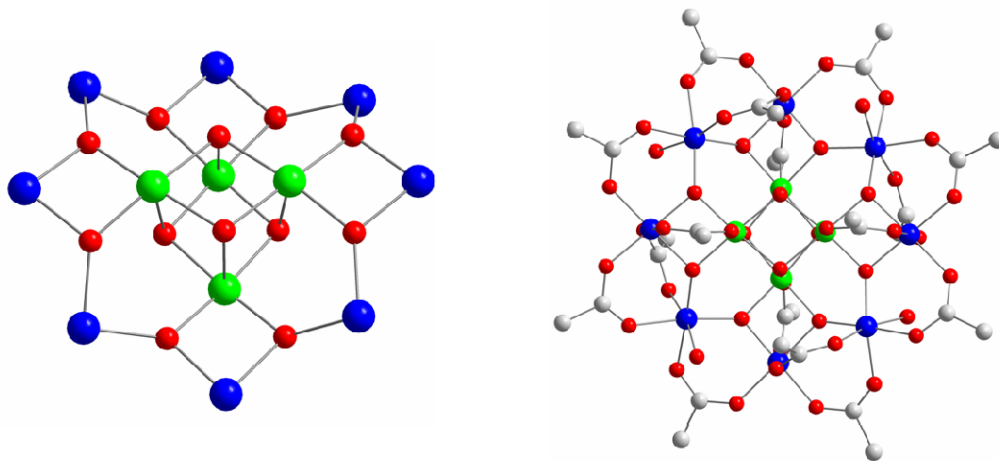


Figure 1-4. (left) Representation of the $[\text{Mn}_{12}\text{O}_{12}]^{16+}$ core. (right) $[\text{Mn}_{12}\text{O}_{12}(\text{O}_2\text{CMe})_{16}(\text{H}_2\text{O})_4]$ complex with peripheral ligation. Color Code: Mn^{IV} , green; Mn^{III} , blue; O, red; C, grey.

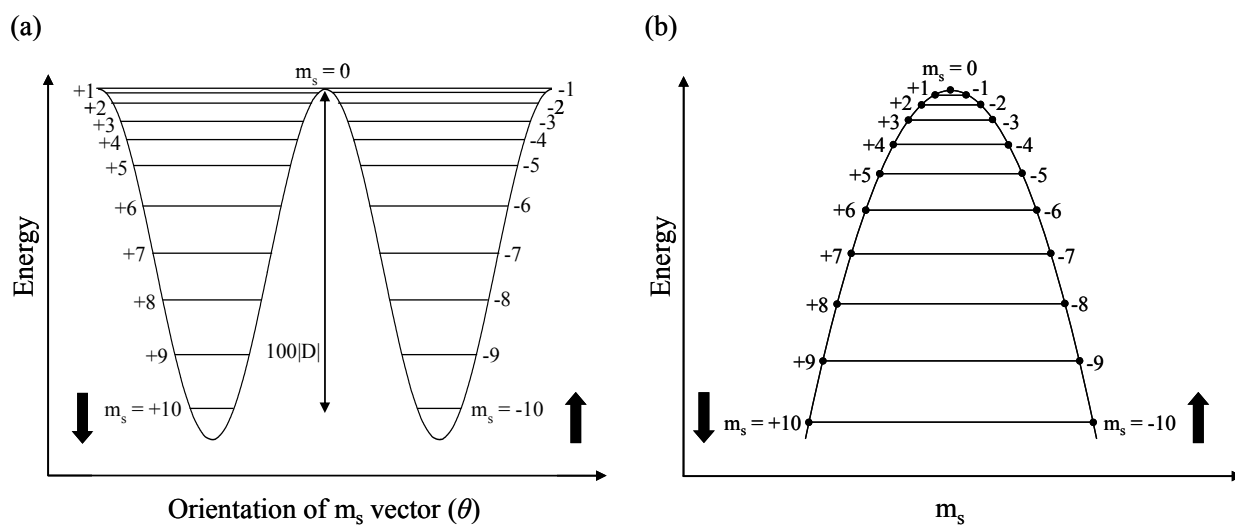


Figure 1-5. Representative plots of the potential energy versus a) the orientation of the m_s vector (θ) along the z axis and b) the m_s sublevels for a Mn_{12} complex with an $S = 10$ ground state, experiencing zero-field splitting.

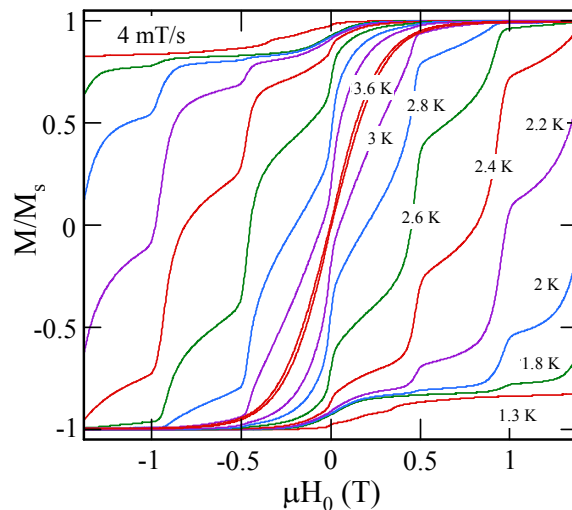


Figure 1-6. Magnetization hysteresis loops for a typical $[\text{Mn}_{12}\text{O}_{12}(\text{O}_2\text{CR})_{16}(\text{H}_2\text{O})_4]$ complex in the 1.3-3.6 K temperature range at 4 mT/s field sweep rate, M is normalized to its saturation value, M_s .

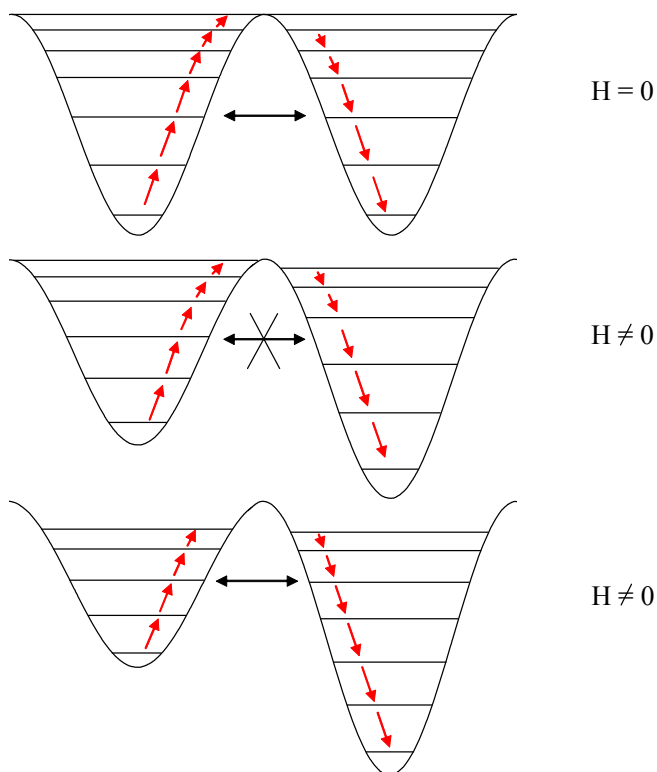


Figure 1-7. Representation of the change in energy of the m_s sublevels as the magnetic field is swept from zero to a non-zero value. Resonant magnetization tunneling occurs when the m_s sublevels are aligned between the two halves of the diagram.

CHAPTER 2 LIGAND-INDUCED DISTORTION OF A TETRANUCLEAR MANGANESE BUTTERFLY COMPLEX

2.1 Introduction

Manganese cluster chemistry has been receiving a great deal of attention for two main reasons: (i) the occurrence of this metal in a variety of manganese-containing biomolecules, the most important of which is the water oxidizing complex (WOC) in the photosynthetic apparatus of green plants and cyanobacteria. This contains an oxide-bridged Mn₄ unit and is responsible for essentially all the oxygen gas on this planet.³³ This has stimulated the search for tetranuclear Mn complexes with oxide bridges that can serve as models for the WOC.²⁹ (ii) High nuclearity Mn clusters often display large ground state spin (*S*) states as a result of ferromagnetic exchange interactions and/or spin frustration effects.^{34,35} If such molecules with large *S* values also possess significant magnetoanisotropy of the Ising (easy-axis) type, then they have the potential to be single-molecule magnets (SMMs).¹³ These are individual molecules that possess a significant barrier (*vs kT*) to magnetization relaxation and thus exhibit the ability to function as magnets below their blocking temperature (*T_B*).

Our group has had a strong interest over many years in the development of synthesis methodologies to oxide-bridged Mn clusters, primarily with carboxylate ligands. One synthetic strategy that has proven particularly useful has been the use of the preformed clusters of general formula [Mn₃O(O₂CR)₆(py)₃]^{0,+} as starting materials in reactions with a variety of co-reagents.³⁶⁻³⁸ A wide range of the latter have been employed, almost always bidentate or higher denticity chelates, and often ones that also contain potentially bridging alkoxide groups. Such reactions have often caused higher-nuclearity products to form, both homo- and mixed-valent.³⁶⁻³⁸ The present work represents an extension of this approach. As part of our continuing search for new preparative routes to high nuclearity Mn clusters, we have investigated the reactivity of the

pentadentate Schiff-base ligand 1,3-bis(salicylideneamino)-2-propanol (salproH₃, Figure 2-1). This group has been used previously by others in Mn chemistry and had afforded mononuclear, dinuclear and polymeric complexes.³⁹⁻⁴² With this precedent, we believed that salproH₃ might prove a route to more new Mn compounds under appropriate reaction conditions, and decided to investigate its reactions with the [Mn₃O(O₂CR)₆(py)₃] complexes. It was obvious that pentadentate salproH₃ cannot bind to these Mn₃ species without resulting in a serious structural perturbation, and a possible nuclearity change. Indeed, as will be described below, these reactions have yielded new types of Mn₄ complexes with a core structure that is distinctly different from those seen before. Additionally, a mononuclear complex has also been obtained. The syntheses, structures and magnetochemical properties of these complexes are the subject of this chapter.⁴³

2.2 Experimental Section

2.2.1 Syntheses

All preparations were performed under aerobic conditions using reagents and solvents as received. The compound salproH₃ was synthesized using the reported procedure.⁴⁴

[Mn₃O(O₂CMe)₆(py)₃]·py, [Mn₁₂O₁₂(O₂CMe)₁₆(H₂O)₄], [Mn₃O(O₂CEt)₆(py)₃]·py, [Mn₃O(O₂CBu')₆(py)₃] and [Mn₃O(O₂CPh)₆(py)₂(H₂O)] were synthesized as reported elsewhere.^{12,45}

[Mn₄O₂(O₂CMe)₅(salpro)] (2-1). Method A. To a stirred solution of salproH₃ (0.05 g, 0.17 mmol) in CH₂Cl₂/MeOH (3/2 mL) was added triethylamine (0.08 mL, 0.55 mmol) followed by the addition of a solution of complex [Mn₃O(O₂CMe)₆(py)₃]·py (0.22 g, 0.25 mmol) in CH₂Cl₂ (10 mL). This solution was left under magnetic stirring for 30 minutes and then filtered through a medium frit. The brown filtrate was left undisturbed to evaporate slowly, giving X-ray quality crystals that grew slowly over five days. These were collected by filtration, washed with

CH₂Cl₂ and dried *in vacuo*. Yield 56%. Anal. Calcd (Found) for **2-1**·CH₂Cl₂

(C₂₈H₃₂Mn₄N₂O₁₅Cl₂): C, 36.27 (36.82); H, 3.48 (3.64); N, 3.02 (2.97). IR (KBr, cm⁻¹): 3446br, 1625s, 1568s, 1445s, 1394s, 1297m, 1153m, 1092w, 1026m, 759m, 677s, 595s, 468m.

Method B. To a stirred solution of salproH₃ (0.20 g, 0.67 mmol) in MeCN/MeOH (3/2 mL) was added triethylamine (0.08 mL, 0.55 mmol) followed by the addition of a solution of complex [Mn₁₂O₁₂(O₂CMe)₁₆(H₂O)₄] (0.32 g, 0.17 mmol) in MeCN (10 mL). This solution was left under magnetic stirring for one hour and then filtered through a medium frit. The homogeneous brown solution was left undisturbed for slow evaporation, giving X-ray quality crystals that grew slowly over the course of one week. These were collected by filtration, washed with acetonitrile, and dried *in vacuo*. Yield 16%. The product was identified as **2-1** by IR spectral comparison with material from method A.

Method C. To a stirred solution of salproH₃ (0.05 g, 0.17 mmol) in MeCN/MeOH (3/2 mL) was added triethylamine (0.08 mL, 0.55 mmol) followed by the addition of a solution of Mn(O₂CMe)₃·2H₂O (0.09 g, 0.34 mmol) in MeCN (10 mL). This solution was left under magnetic stirring for 30 minutes and then worked up as for Method B. Yield 28%. The product was identified as **2-1** by IR spectral comparison with material from method A.

[Mn₄O₂(O₂CEt)₅(salpro)] (2-2). To a stirred solution of salproH₃ (0.05 g, 0.17 mmol) in CH₂Cl₂/MeOH (3/2 mL) was added triethylamine (0.08 mL, 0.55 mmol) followed by the addition of a solution of complex [Mn₃O(O₂CEt)₆(py)₃]·py (0.31 g, 0.34 mmol) in CH₂Cl₂ (10 mL). This solution was left under magnetic stirring for 30 minutes and then filtered through a medium frit. X-ray quality crystals were obtained over the course of three days by vapour-diffusing diethyl ether into the filtrate. The resulting crystals were collected by filtration, washed with ether, and dried *in vacuo*. Yield 22%. Anal. Calcd (Found) for **2-2**·CH₂Cl₂

(C₃₃H₄₂Mn₄N₂O₁₅Cl₂): C, 39.74 (39.66); H, 4.24 (4.21); N, 2.80 (2.68). IR (KBr, cm⁻¹): 3441br, 2879m, 1626s, 1572s, 1446m, 1404m, 1299m, 1150w, 1080w, 1031w, 750w, 676m, 598s, 467m.

[Mn₄O₂(O₂CBu^t)₅(salpro)] (2-3). To a stirred solution of salproH₃ (0.05 g, 0.17 mmol) in CH₂Cl₂/MeOH (3/2 mL) was added triethylamine (0.08 mL, 0.55 mmol) followed by the addition of solution of complex [Mn₃O(O₂CBu^t)₆(py)₃] (0.29 g, 0.28 mmol) in CH₂Cl₂ (10 mL). This solution was left under magnetic stirring for 30 minutes and then filtered through a medium frit. X-ray quality crystals were obtained during the course of five days by layering the filtrate with heptane and allowing the solvents to slowly mix. The resulting crystals were collected by filtration, washed with heptane and dried *in vacuo*. Yield 25%. Anal. Calcd (Found) for **2-3**·½ CH₂Cl₂ (C_{42.5}H₆₁Mn₄N₂O₁₅Cl): C, 47.58 (47.44); H, 5.83 (5.86); N, 2.49 (2.74). IR (KBr, cm⁻¹): 3442br, 2959m, 1627m, 1560s, 1482m, 1447w, 1408m, 1358m, 1301m, 1221m, 1150w, 1029w, 895w, 757w, 678m, 599s, 439m.

NMe₄[Mn(O₂CPh)₂(salproH)] (2-4). To a stirred solution of salproH₃ (0.05 g, 0.17 mmol) in MeCN was added 25 wt % solution of NMe₄OH in MeOH (0.02 mL, 0.49 mmol) followed by the addition of a solution of complex [Mn₃O(O₂CPh)₆(py)₂(H₂O)] (0.08 g, 0.07 mmol) in CH₂Cl₂ (10 mL). This solution was left under magnetic stirring for one hour and then filtered through a medium frit. X-ray quality crystals were obtained during the course of five days by layering the filtrate with diethyl ether:hexane (1:1 v/v). Yield 25%. Anal. Calcd (Found) for **2-4**·½CH₂Cl₂ (C_{35.5}H₃₉MnN₃O₇Cl): C, 60.04 (60.34); H, 5.54 (5.90); N, 5.92 (6.02). IR (KBr, cm⁻¹): 1623s, 1599s, 1541m, 1530m, 1467m, 1446s, 1393w, 1399m, 1304m, 1193m, 1149m, 1089w, 1070w, 1008w, 905m, 861w, 758s, 614s, 599m, 577m, 459m.

2.2.2 X-ray Crystallography

Data were collected by Dr. Khalil A. Abboud using a Siemens SMART PLATFORM equipped with a CCD area detector and a graphite monochromator utilizing Mo-K α radiation (λ

= 0.71073 Å). Suitable crystals of **2-1**·MeCN, **2-3**·MeOH·2CH₂Cl₂·C₇H₁₆ and **2-4**·CH₂Cl₂ were attached to glass fibers using silicone grease and transferred to a goniostat where they were cooled to 173 K for data collection. Cell parameters were refined using up to 8192 reflections. A full sphere of data (1850 frames) was collected using the ω -scan method (0.3° frame width). The first 50 frames were remeasured at the end of data collection to monitor the instrument and crystal stability (maximum correction on *I* was < 1 %). Absorption corrections by integration were applied based on measured indexed crystal faces.

The structures were solved by direct methods in *SHELXTL6*,⁴⁶ and refined using full-matrix least squares. The non-H atoms were treated anisotropically, whereas the hydrogen atoms were placed in ideal, calculated positions and refined as riding on their respective carbon atoms. Refinement was done using F^2 . In **2-1**·MeCN, the asymmetric unit consists of the Mn₄ cluster and a disordered MeCN molecule. A total of 465 parameters were refined in the final cycle of refinement using 5581 reflections with $I > 2\sigma(I)$ to yield R_1 and wR_2 of 4.13 and 8.28%, respectively. In **2-3**·MeOH·2CH₂Cl₂·C₇H₁₆, the asymmetric unit consists of the cluster and one heptane, one methanol, and two dichloromethane molecules. The three methyl groups on C17 are disordered, and each dichloromethane molecule has one chlorine atom disordered. In each case, two disorder sites were included, and their site occupation factors independently refined. A total of 723 parameters were included in the final cycle of refinement using 9336 reflections with $I > 2\sigma(I)$ to yield R_1 and wR_2 of 4.73% and 12.20%, respectively. In **2-4**·CH₂Cl₂, A total of 920 parameters were refined in the final cycle of refinement using 7287 reflections with $I > 2\sigma(I)$ to yield R_1 and wR_2 of 4.58% and 8.44%, respectively.

The crystallographic data and structure refinement details for **2-1**·MeCN, **2-3** MeOH·2CH₂Cl₂·C₇H₁₆ and **2-4**·CH₂Cl₂ are listed in Table 2-1.

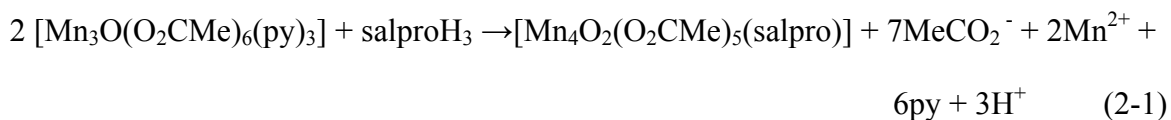
2.3 Results and Discussion

2.3.1 Syntheses

Trinuclear $[\text{Mn}_3\text{O}(\text{O}_2\text{CR})_6(\text{py})_3]^{0,+}$ clusters have proven to be very useful starting materials for the synthesis of higher nuclearity products, affording complexes of nuclearity 4 - 18. For example, reaction of $[\text{Mn}_3\text{O}(\text{O}_2\text{CMe})_6(\text{py})_3]^+$ with 2,2' bipyridine (bpy)³⁶ or picolinate (pic^-)³⁷ gave $[\text{Mn}_4\text{O}_2(\text{O}_2\text{CMe})_7(\text{bpy})_2]^+$ and $[\text{Mn}_4\text{O}_2(\text{O}_2\text{CMe})_7(\text{pic})_2]^-$ salts, respectively. In addition, the reaction of a mixture of $[\text{Mn}_3\text{O}(\text{O}_2\text{CMe})_6(\text{py})_3]^+$ and $[\text{Mn}_3\text{O}(\text{O}_2\text{CMe})_6(\text{py})_3]\cdot\text{py}$ with 2-(hydroxyethyl)pyridine (hepH) gave $[\text{Mn}_{18}\text{O}_{14}(\text{O}_2\text{CMe})_{18}(\text{hep})_4(\text{hepH})_2(\text{H}_2\text{O})_2]^{2+}$.³⁸ However, a chelating reagent is not always necessary: Treatment of $[\text{Mn}_3\text{O}(\text{O}_2\text{CPh})_6(\text{py})_2(\text{H}_2\text{O})]$ with phenol gives $[\text{Mn}_6\text{O}_2(\text{O}_2\text{CPh})_{10}(\text{py})_2(\text{MeCN})_2]$, the phenol merely acting as a reducing agent and triggering dimerization.⁴⁷ Thus, the choice of chelating or other co-reagent and the reaction conditions have significant effect not only on the nuclearity of the product but also on its metal topology.

Along the same lines, the reaction of $[\text{Mn}_3\text{O}(\text{O}_2\text{CMe})_6(\text{py})_3]\cdot\text{py}$ with salproH₃ and NEt₃ in a roughly 3:2:6 molar ratio in CH₂Cl₂:MeOH gave the novel tetranuclear complex $[\text{Mn}_4\text{O}_2(\text{O}_2\text{CMe})_5(\text{salpro})](\mathbf{2-1})$. Its formation can be summarized in eq. 2-1. The reaction is sensitive to the Mn₃:salproH₃ ratio, and complex **2-1** is obtained only when 0.5 - 0.7 equivalents of salproH₃ per Mn₃ is employed. We also found that the mixed CH₂Cl₂:MeOH solvent system is very important; no reaction was observed when the reaction was performed in CH₂Cl₂ alone, and only starting material was recovered. Presumably, the more polar MeOH facilitates the necessary proton transfer steps. However, the yield of the product decreases as the concentration of MeOH increases beyond that described in the Experimental Section, presumably due to the solubility of the product. Thus, a controlled amount of MeOH is essential for a high yield reaction. However, the same product was obtained using a CH₂Cl₂:EtOH solvent system. Further investigation

showed that the same complex **2-1** was also obtained from MeCN:MeOH. Also the same product is obtained in the absence of base but in lower yield.



Since complex **2-1** contains 4 Mn^{III} ions, we wondered if a higher oxidation state product might form if we employed a higher oxidation state reagent, and thus explored the reaction of salproH₃ with [Mn₁₂O₁₂(O₂CMe)₁₆(H₂O)₄], which contains 8Mn^{III}, 4Mn^{IV}. Thus, an MeCN:MeOH solution of [Mn₁₂O₁₂(O₂CMe)₁₆(H₂O)₄] was treated with 4 equivalents of salproH₃, but the same product, complex **2-1**, was again obtained, but only in poor yield (16%).

We also obtained complex **2-1** when the [Mn₃O(O₂CMe)₆(py)₃]:py starting material was replaced with “Mn(O₂CMe)₃·2H₂O”. This “Mn^{III} acetate” is really a polymer of Mn₃ trinuclear units similar to those in [Mn₃O(O₂CMe)₆(py)₃]:py, and so it was perhaps not surprising that its reaction with salproH₃ gave the same product.

Access to other carboxylate derivatives of **2-1** is possible using the described procedure of Method A. Thus, the reaction using the R = Et (propionate) or Bu^t (pivalate) derivatives of [Mn₃O(O₂CR)₆(py)₃] gave the corresponding [Mn₄O₂(O₂CR)₅(salpro)] complexes **2-2** and **2-3**, respectively. This provides access to more soluble versions of this new structural type of Mn₄ complex. However, all our attempts to prepare benzoate derivative of **2-1** resulted in the formation of the monomeric complex NMe₄[Mn(O₂CPh)₂(salproH)] (**2-4**).

2.3.2 Description of Structures

2.3.2.1 Structure of [Mn₄O₂(O₂CR)₅(salpro)] (R = Me (**2-1**), Bu^t (**2-3**))

The structures of **2-1** and **2-3** are shown in Figure 2-2. Selected interatomic distances and angles for **2-1** are listed in Table A-1. Complex **2-1** crystallizes in monoclinic space group *P*2₁/*n*. It contains a [Mn₄O₂]⁸⁺ core with peripheral ligation provided by five doubly-bridging acetate

groups and one pentadentate salpro³⁻ ligand (Figure 2-2). The core can be described as derived from two triangular, oxide-bridged [Mn₃O] units sharing an edge and thus giving a [Mn₄O₂] butterfly-like core as found in several other Mn₄ complexes (as well as with other transition metals), for example, [Mn₄O₂(O₂CMe)₇(bpy)₂]⁺ (Mn₄-bpy).³⁶ Atoms Mn1 and Mn3 occupy the ‘body’ positions of the butterfly and are five-coordinate (square pyramidal), and Mn2 and Mn4 occupy the ‘wingtip’ positions and are six-coordinate (octahedral). However, the [Mn₄O₂] in **2-1** is much more closed up, i.e. a more acute V-shape, than normally found in such butterfly units (Figure 2-3) This is reflected in the dihedral angle between the two Mn₃ planes, which is 79.2° in **2-1** compared with 134.3° in Mn₄-bpy,³⁶ which is typical of previous butterfly complexes. This can clearly be assigned to the fact that the wingtip Mn atoms of the butterfly topology, Mn2 and Mn4, are mono-atomically bridged by the salpro³⁻ oxygen atom O1 (Figure 2-2, top). In fact, this drastic closing up of the butterfly makes the core of **2-1** intermediate between a butterfly and a cubane (i.e. tetrahedral) Mn₄ topology. There is a carboxylate group bridging each body-wingtip Mn pair, and a fifth carboxylate bridges the body-body Mn pair. The pentadentate salpro³⁻ ligand completes the peripheral ligation, chelating each wingtip Mn atom and bridging them via O1.

All the Mn atoms are in the +3 oxidation state. This was established by qualitative consideration of the bond distances at each Mn, and confirmed quantitatively by bond valence sum (BVS) calculations (Table 2-2).^{48,49} This also agreed with charge considerations and the overall neutrality of the molecule, as well as the clear presence of a Jahn-Teller (JT) distortion at near-octahedral Mn2 and Mn4, the JT axes being along the O9, O7 and O15,O13 vectors, respectively.

Complex **2-3** crystallizes in monoclinic space group *P*2₁/*n*. Selected interatomic distances and angles are listed in Table A-2. Complex **2-3** is isostructural with complex **2-1** except for the

difference in the carboxylate R groups. In particular, the dihedral angle between the two Mn_3 planes is 79.8° , and the Mn^{III} JT axes have the same relative orientation. The bulky Bu' groups thus have only a minimal effect on the structure, as expected from the lack of any steric interactions.

As discussed above, the structures of **2-1** and **2-3** can be considered closed-up versions of the familiar butterfly structures observed on several previous occasions in Mn^{III} chemistry. It is thus of interest to structurally compare the two types, and this is done in Table 2-3. The metric parameters are fairly similar, as expected given that they are all Mn^{III} species, but some overall conclusions can nevertheless be drawn. The closing up of the core of **2-1** and **2-3**, which is effectively a pivoting of the wingtip Mn atoms (Mn_w) about the μ_3-O^{2-} ions, has the effect of greatly decreasing the Mn_w-O-Mn_b as expected (by $\sim 10-15^\circ$), but also slightly decreasing the Mn_b-O-Mn_b angles (by $\sim 1-2^\circ$) as the central $[Mn_2O_2]$ rhombus buckles into a non-planar conformation. These angle changes are also reflected in the $Mn\cdots Mn$ separations, which all decrease by $\sim 0.1-0.2 \text{ \AA}$, except for the $Mn_w\cdots Mn_w$ separation which is much shorter in **2-1** and **2-3**.

2.3.2.2 Structure of $NMe_4[Mn(O_2CPh)_2(\text{salproH})]$ (**2-4**)

Complex **2-4** crystallizes in monoclinic space group $P2_1/c$. Selected interatomic distances and angles are listed in Table A-3. The asymmetric unit contains two monomers, the structures of which are essentially superimposable, therefore structure of one of these will be discussed here. It contains a Mn^{III} ion in octahedral geometry as shown in Figure 2-4. The four equatorial sites are occupied by two N and two alkoxide oxygen atoms of salproH molecule and two η^1 benzoate groups disposed trans to each other along the axial direction forming the JT axis. The protonation level of the central alcohol arm (O7) of salproH was established by a BVS of 0.9.

O7 also forms an intramolecular hydrogen bond with the O3 of the benzoate anion; O7...O3 = 2.65 Å.

2.3.3 Magnetochemistry

Variable temperature dc magnetic susceptibility data were collected in the 5.0 - 300 K range in a 0.1 T magnetic field on powdered microcrystalline samples of **2-1**·CH₂Cl₂, **2-2**·CH₂Cl₂, **2-3**·½CH₂Cl₂ and **2-4**·½CH₂Cl₂ restrained in eicosane to prevent torquing. The $\chi_M T$ vs T for **2-1** to **2-3** are shown in Figure 2-5. For **2-1**·CH₂Cl₂, $\chi_M T$ smoothly decreases from 9.1 cm³Kmol⁻¹ at 300 K to 0.4 cm³Kmol⁻¹ at 5.0 K. The 300 K value is much less than the spin-only value of 12.0 cm³Kmol⁻¹ ($g = 2.0$) expected for four Mn^{III} ions with non-interacting metal centers, indicating the presence of appreciable intramolecular antiferromagnetic interactions between the Mn ions, with the low temperature data suggesting a spin $S = 0$ ground state. Similar data were obtained for **2-2**·CH₂Cl₂ and **2-3**·½CH₂Cl₂, consistent with their isostructural nature and a minimal influence of the different ligands in the three complexes (Figure 2-5).

The isotropic Heisenberg-Dirac-VanVleck (HDVV) spin Hamiltonian describing the exchange interactions within these Mn₄ complexes with virtual C_{2V} symmetry is given by eq. 2-2, where b = body, w = wingtip, \hat{S}_i ($i = 1 - 4$) is the spin operator for metal atom Mn_{*i*}, and J is the exchange parameter. The exchange and atom labeling are summarized in the Figure 2-6.

$$\mathcal{H} = -2J_{bb}\hat{S}_1\cdot\hat{S}_3 - 2J_{bw}(\hat{S}_1\cdot\hat{S}_2 + \hat{S}_1\cdot\hat{S}_4 + \hat{S}_2\cdot\hat{S}_3 + \hat{S}_3\cdot\hat{S}_4) - 2J_{ww}\hat{S}_2\cdot\hat{S}_4 \quad (2-2)$$

The eigenvalues of the spin Hamiltonian of eq. 2-2 can be determined analytically using the Kambe vector coupling method,⁵⁰ as described elsewhere for the more common butterfly complexes such as Mn₄-bpy, which also have C_{2V} symmetry.³⁶ Thus, use of the coupling scheme $\hat{S}_A = \hat{S}_1 + \hat{S}_3$, $\hat{S}_B = \hat{S}_2 + \hat{S}_4$, and $\hat{S}_T = \hat{S}_A + \hat{S}_B$ allows the spin Hamiltonian to be transformed into the equivalent form given by eq. 2-3, where S_T is the total spin of the molecule. The eigenvalues of eq. 2-3 can be determined using the relationship $\hat{S}_i^2\psi = S_i(S_i+1)\psi$, and are given in eq. 2-4,

where $E | S_T, S_A, S_B \rangle$ is the energy of state $| S_T, S_A, S_B \rangle$, and constant terms contributing equally to all states have been omitted. The overall multiplicity of the spin system is 625, made up of 85 individual spin states ranging from $S_T = 0 - 8$.

$$\mathcal{H} = -J_{bb}(\hat{S}_A^2 - \hat{S}_1^2 - \hat{S}_3^2) - J_{bw}(\hat{S}_T^2 - \hat{S}_A^2 - \hat{S}_B^2) - J_{ww}(\hat{S}_B^2 - \hat{S}_2^2 - \hat{S}_4^2) \quad (2-3)$$

$$E | S_T, S_A, S_B \rangle = -J_{bb}[S_A(S_A+1)] - J_{bw}[S_T(S_T+1) - S_A(S_A+1) - S_B(S_B+1)] - J_{ww}[S_B(S_B+1)] \quad (2-4)$$

An expression for the molar paramagnetic susceptibility, χ_M , was derived using the above and the Van Vleck equation,⁵¹ and assuming an isotropic g tensor (Appendix D-1). This equation was then used to fit the experimental $\chi_M T$ vs T data in Figure 2-5 as a function of the three exchange parameters J_{bb} , J_{bw} and J_{ww} and the g factor. A contribution from temperature independent paramagnetism (TIP) was held constant at $400 \times 10^{-6} \text{ cm}^3 \text{ mol}^{-1}$. The obtained fits are shown as the solid lines in Figure 2-5. The fitting parameters were: For **2-1**, $J_{bb} = -6.37 \text{ cm}^{-1}$, $J_{bw} = -5.72 \text{ cm}^{-1}$, $J_{ww} = -1.78 \text{ cm}^{-1}$ and $g = 2.00$; for **2-2**, $J_{bb} = -7.64 \text{ cm}^{-1}$, $J_{bw} = -6.73 \text{ cm}^{-1}$, $J_{ww} = -2.49 \text{ cm}^{-1}$ and $g = 2.00$; and for **2-3**, $J_{bb} = -7.37 \text{ cm}^{-1}$, $J_{bw} = -6.57 \text{ cm}^{-1}$, $J_{ww} = -1.79 \text{ cm}^{-1}$ and $g = 1.99$. The obtained values indicate that the ground state of the molecules is $| S_T, S_A, S_B \rangle = | 0, 4, 4 \rangle$, as anticipated from the low temperature data in Figure 2-5.

The exchange interactions within the Mn_4 cores of **2-1** to **2-3** are thus all antiferromagnetic and weak. The weakest is the J_{ww} between the wingtip Mn^{III} ions, but note that this is nevertheless a significant interaction relative to the others, unlike the more common types of butterfly species where this J_{ww} interaction is not a major contributor since the wingtip Mn atoms are not directly (monoatomically) bridged. Since the wingtip Mn atoms are bridged by an alkoxide O atom whereas the other Mn pairs are all bridged by either one or two oxide O atoms, it is qualitatively reasonable for J_{ww} to be the weakest interaction in the molecule, although the

precise values of all the J parameters are the net sum of contributions from ferro- and antiferromagnetic pathways and thus it is difficult to rationalize their differences precisely.

It is, however, of interest to compare the exchange parameters for **2-1** to **2-3** with those for the more common type of Mn^{III} butterfly complexes and see if any observed differences can be correlated with the structural differences mentioned earlier. In Table 2-4 are compared the exchange parameters for **2-1** to **2-3** with those for [Mn₄O₂(O₂CMe)₇(bpy)₂]⁺ (Mn₄-bpy),³⁶ [Mn₄O₂(O₂CMe)₇(pic)₂]⁻ (Mn₄-pic)³⁷ and [Mn₄O₂(O₂CET)₇(bpya)₂]⁺ (Mn₄-bpya).⁵² Although the J_{bw} interaction in **2-1** to **2-3** is within the range found for the previous complexes, the J_{bb} interaction in the former is distinctly weaker than in the latter. This is consistent with the significantly more acute angles at the μ₃-O²⁻ ions, since these will presumably weaken the antiferromagnetic contributions to the J_{bb} interaction by weakening the Mn(dπ)-O(pπ)-Mn(dπ) overlap that would be stronger when mediated by an essentially trigonal planar O atom as in Mn₄-bpy, Mn₄-pic and Mn₄-bpya. The buckling of the central [Mn₂O₂] no doubt also contributes to the change in J_{bb} by affecting the orbital overlap.

The fact that J_{bw} ≈ J_{bb} in **2-1** to **2-3** is expected to have a clear impact on the ground state because the butterfly [Mn₄O₂]⁸⁺ core in Mn₄-bpy, Mn₄-pic and Mn₄-bpya has been well established from previous work to experience spin frustration effects as a result of the presence of triangular Mn₃ within its structure.^{36,37,52} Since the interactions are all antiferromagnetic, they are competing and the precise ground state spin alignment is thus very sensitive to the J_{bw}:J_{bb} ratio, with J_{ww} not being a factor in Mn₄-bpy, Mn₄-pic and Mn₄-bpya because of its weakness. For example, the typical butterfly complexes Mn₄-bpy and Mn₄-pic have an S_T = 3 ground state spin, the |S_T, S_A, S_B> = |3, 1, 4> state, which results from the dominating J_{bb} interaction aligning the Mn_b spins almost perfectly antiparallel, but not quite (i.e. S_A = 1 not 0). The J_{bw}

interactions are individually weaker than J_{bb} , but there are four of them, and as a result prevent S_A being 0. An intermediate resultant spin is thus obtained in the ground state. In Mn_4 -bpya, $J_{bb} \gg J_{wb}$, and the Mn_b spins are now aligned antiparallel, i.e. $S_A = 0$, with the weak J_{ww} serving to couple the Mn_w spins antiparallel and giving an overall $S_T = 0$ ground state, the $|S_T, S_A, S_B\rangle = |0, 0, 0\rangle$ state. The ground state of **2-1** to **2-3** can now be satisfactorily rationalized within this description. In fact, it represents the situation at the other extreme compared to Mn_4 -bpya, i.e. the J_{bb} is now weakened relative to J_{bw} and the two interactions are comparable in magnitude. However, there are four of the latter, and thus J_{bw} now dominates the spin alignments, aligning the spins antiparallel to their neighbors along the outer edges of the $[Mn_4O_2]^{8+}$ butterfly. The J_{bb} interaction is antiferromagnetic but nevertheless completely frustrated, as is J_{ww} , with the two Mn_b spins and the two Mn_w spins both being aligned parallel by the J_{bw} interactions. Thus, the ground state is again $S_T = 0$, as in Mn_4 -bpya, but now it is the $|S_T, S_A, S_B\rangle = |0, 4, 4\rangle$ state as depicted in Figure 2-6. Table 2-5 calculates the spin states of **2-1**· CH_2Cl_2 in the $|S_T, S_A, S_B\rangle$ format arranged as a function of their energy calculated using the calculated exchange parameters, J_{bb} , J_{bw} and J_{ww} , and the Van Vleck equation

The $\chi_M T$ vs T for **2-4** is shown in Figure 2-7. For **2-4**· $\frac{1}{2}CH_2Cl_2$, the value of $\chi_M T$ decreases very smoothly from $3.19 \text{ cm}^3\text{Kmol}^{-1}$ at 300 K to $2.57 \text{ cm}^3\text{Kmol}^{-1}$ at 15.0 K and then drops sharply to $2.21 \text{ cm}^3\text{Kmol}^{-1}$ at 5.0 K. Complexes **2-4** exhibits behavior expected for high-spin Mn^{III} ($S = 2$) center exhibiting zero-field splitting (ZFS). To characterize the ZFS parameter D further, magnetization vs field data were collected in the 2.0 – 10.0 K range in fields of 0.1 – 7 T (Figure 2-7). Fitting of the data using the program *MAGNET*,⁵³ described elsewhere,^{36,54-56} that involves diagonalization of the spin Hamiltonian matrix, assuming that only the ground state spin is populated at these temperatures, includes axial ZFS and Zeeman interactions and carries out a

full powder average, gave $S = 2$, $g = 1.86$, and $D = -4.09 \text{ cm}^{-1}$. To ensure that the global minimum had been located, we calculated the root-mean-square error surface for the fit as a function of D and g (Figure 2-8). The plot clearly shows only the above mentioned minima.

2.4 Conclusions

SalproH₃ has proved an effective route to a novel type of tetranuclear Mn complex whose core can be described as a more closed up version of the butterfly-like core that is relatively common. Three isostructural complexes of this new family have been synthesized and characterized. These complexes also complement and extend the currently rich area of Mn^{III} schiff-base species. Complexes **2-1** to **2-3** extend the type of spin frustration effects observed within the Mn₄ butterfly core, giving an $S_T = 0$ ground state due to domination of the spin alignments by J_{bw} .

Table 2-1. Crystallographic Data for **2-1**·MeCN, **2-3**·MeOH·2CH₂Cl₂·C₇H₁₆ and **2-4**·CH₂Cl₂

	2-1	2-3	2-4
Formula ^a	C ₂₉ H ₃₃ Mn ₄ N ₃ O ₁₅	C ₅₂ H ₈₄ Cl ₄ Mn ₄ N ₂ O ₁₆	C ₃₆ H ₄₀ Cl ₂ MnN ₃ O ₇
Fw, g/mol ^a	883.34	1354.77	752.55
Space group	<i>P2</i> ₁ / <i>n</i>	<i>P2</i> ₁ / <i>n</i>	<i>P2</i> ₁ / <i>c</i>
<i>a</i> , Å	9.3368(6)	17.7518(13)	24.2193(12)
<i>b</i> , Å	22.5058(15)	17.3654(12)	17.4454(9)
<i>c</i> , Å	16.5079(11)	21.4029(15)	18.3088(9)
α , °	90	90	90
β , °	90.945(1)	100.856(1)	110.569(1)
γ , °	90	90	90
<i>V</i> , Å ³	3468.4(4)	6479.7(8)	7242.6(6)
<i>Z</i>	4	4	8
<i>T</i> , K	173(2)	173(2)	173(2)
λ , Å ^b	0.71073	0.71073	0.71073
ρ_{calc} , g/cm ³	1.692	1.389	1.380
μ , mm ⁻¹	1.097	0.988	0.563
<i>R</i> <i>I</i> ^{c,d}	0.0413	0.0473	0.0458
<i>wR</i> <i>2</i> ^e	0.0828	0.1220	0.0844

^a Including solvate molecules. ^b Graphite monochromator. ^c $I > 2\sigma(I)$. ^d $R1 = \Sigma(|F_o| - |F_c|) / \Sigma|F_o|$. ^e $wR2 = [\Sigma[w(F_o^2 - F_c^2)^2] / \Sigma[w(F_o^2)^2]]^{1/2}$, $w = 1/[\sigma^2(F_o^2) + [(ap)^2 + bp]$, where $p = [\max(F_o^2, O) + 2F_c^2]/3$.

Table 2-2. Bond-valence sums for the Mn atoms of complexes **2-1**, **2-3** and **2-4**^a

Atom	2-1 ·MeCN			2-3 ·MeOH·2CH ₂ Cl ₂ ·C ₇ H ₁₆			2-4 ·CH ₂ Cl ₂		
	Mn ^{II}	Mn ^{III}	Mn ^{IV}	Mn ^{II}	Mn ^{III}	Mn ^{IV}	Mn ^{II}	Mn ^{III}	Mn ^{IV}
Mn1	3.07	<u>2.81</u>	2.95	2.98	<u>2.73</u>	2.87	3.29	<u>2.84</u>	3.12
Mn2	3.28	<u>3.04</u>	3.13	3.30	<u>3.06</u>	3.14	3.30	<u>2.88</u>	3.14
Mn3	3.04	<u>2.78</u>	2.92	3.33	<u>3.26</u>	3.18			
Mn4	3.23	<u>3.16</u>	3.08	3.05	<u>2.79</u>	2.93			

^a The underlined value is the one closest to the charge for which it was calculated. The oxidation state of a particular atom can be taken as the nearest whole number to the underlined value

Table 2-3. Comparison of core parameters of selected [Mn₄O₂]⁸⁺ complexes (Å, °)

Complex	Mn _b ···Mn _b	Mn _b ···Mn _w	Mn _w ···Mn _w	Mn _b -O	Mn _w -O	Mn _b -O- Mn _b	Mn _b -O- Mn _w	Mn _w -O- Mn _w	Ref
2-1	2.770	3.171- 3.196	3.651	1.886- 1.906	1.909, 1.914 ^a 1.977, 1.991	94.30, 93.87	112.7- 114.5	133.88	43
2-3	2.794	3.136- 3.193	3.640	1.887- 1.910	1.907, 1.910 ^a 1.970, 1.984	94.97, 94.74	110.6- 114.6	134.1	43
Mn ₄ -bpy	2.848	3.299- 3.385	5.593	1.889- 1.930	1.804, 1.844	95.7, 96.8	123.3- 131.3	-	36
Mn ₄ -pic	2.842	3.308- 3.406	-	1.888- 1.910	1.840, 1.847	96.9	123.2- 129.7	-	37
Mn ₄ - bpya	2.871	3.307- 3.344	-	1.873- 1.957	1.833, 1.838	97.07, 97.25	125.3- 131.4	-	52

^a Top and bottom entries refer to distances to oxide and alkoxide O atoms, respectively.

Table 2-4. Comparison of exchange parameters in [Mn₄O₂]⁸⁺ complexes

Complex	J _{bb} ^a	J _{bw} ^a	J _{ww} ^a	g	Ref
2-1	-6.37	-5.72	-1.78	2.00	43
2-2	-7.64	-6.73	-2.49	2.00	43
2-3	-7.37	-6.57	-1.79	1.99	43
Mn ₄ -bpy	-23.5	-7.8		2.0	36
Mn ₄ -pic	-24.6	-5.3		1.96	37
Mn ₄ -bpya	-25.7	-3.3	-0.77	1.99	52

^a cm⁻¹

Table 2-5. Spin states of **2-1**·CH₂Cl₂ in the |S_T, S_A, S_B> format arranged as a function of their energy calculated using the calculated exchange parameters, J_{bb}, J_{bw} and J_{ww}, and the Van Vleck equation

S _T ,S _A ,S _B >	E (cm ⁻¹)	S _T ,S _A ,S _B >	E (cm ⁻¹)	S _T ,S _A ,S _B >	E (cm ⁻¹)
0,4,4>	0.00	1,1,0>	95.00	4,1,3>	159.20
1,4,4>	12.40	2,2,2>	95.30	4,4,2>	179.30
1,3,4>	14.00	2,1,2>	96.10	4,3,2>	180.90
0,3,3>	33.20	2,0,2>	96.50	4,2,2>	182.10
2,4,4>	37.20	3,4,3>	106.00	5,4,4>	186.00
2,3,4>	38.80	3,3,3>	107.60	5,3,4>	187.60
2,2,4>	40.00	3,2,3>	108.80	5,2,4>	188.80
1,4,3>	44.00	3,1,3>	109.60	5,1,4>	189.60
1,3,3>	45.60	2,3,1>	109.90	4,4,1>	195.10
1,2,3>	46.80	3,0,3>	110.00	4,3,1>	196.70
0,2,2>	58.10	2,2,1>	111.10	4,4,0>	203.00
2,4,3>	68.80	2,1,1>	111.90	5,4,3>	217.60
1,3,2>	69.30	2,2,0>	119.00	5,3,3>	219.20
2,3,3>	70.40	4,4,4>	124.00	5,2,3>	220.40
1,2,2>	70.50	4,3,4>	125.60	5,4,2>	241.30
1,2,2>	71.30	4,2,4>	126.80	5,3,2>	242.90
2,2,3>	71.60	4,1,4>	127.60	5,4,1>	257.10
2,1,3>	72.40	4,0,4>	128.00	6,4,4>	260.40
3,4,4>	74.40	3,4,2>	129.70	6,3,4>	262.00
0,1,1>	74.70	3,3,2>	131.30	6,2,4>	263.20
3,3,4>	76.00	3,2,2>	132.50	6,4,3>	292.00
3,2,4>	77.20	3,1,2>	133.30	6,3,3>	293.60
3,1,4>	78.00	3,4,1>	145.50	6,4,2>	315.70
0,0,0>	83.00	3,3,1>	147.10	7,4,4>	347.20
1,2,1>	86.30	3,2,1>	148.30	7,3,4>	348.80
1,1,1>	87.10	3,3,0>	155.00	7,4,3>	378.80
1,0,1>	87.50	4,4,3>	155.60	8,4,4>	446.40
2,4,2>	92.50	4,3,3>	157.20		
2,3,2>	94.10	4,2,3>	158.40		

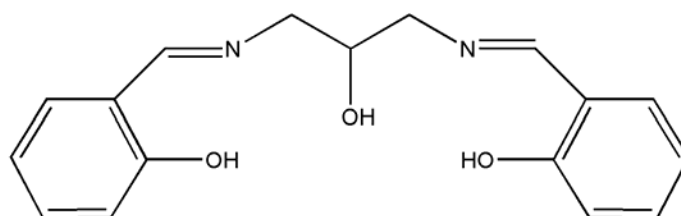


Figure 2-1. Structure of SalproH₃

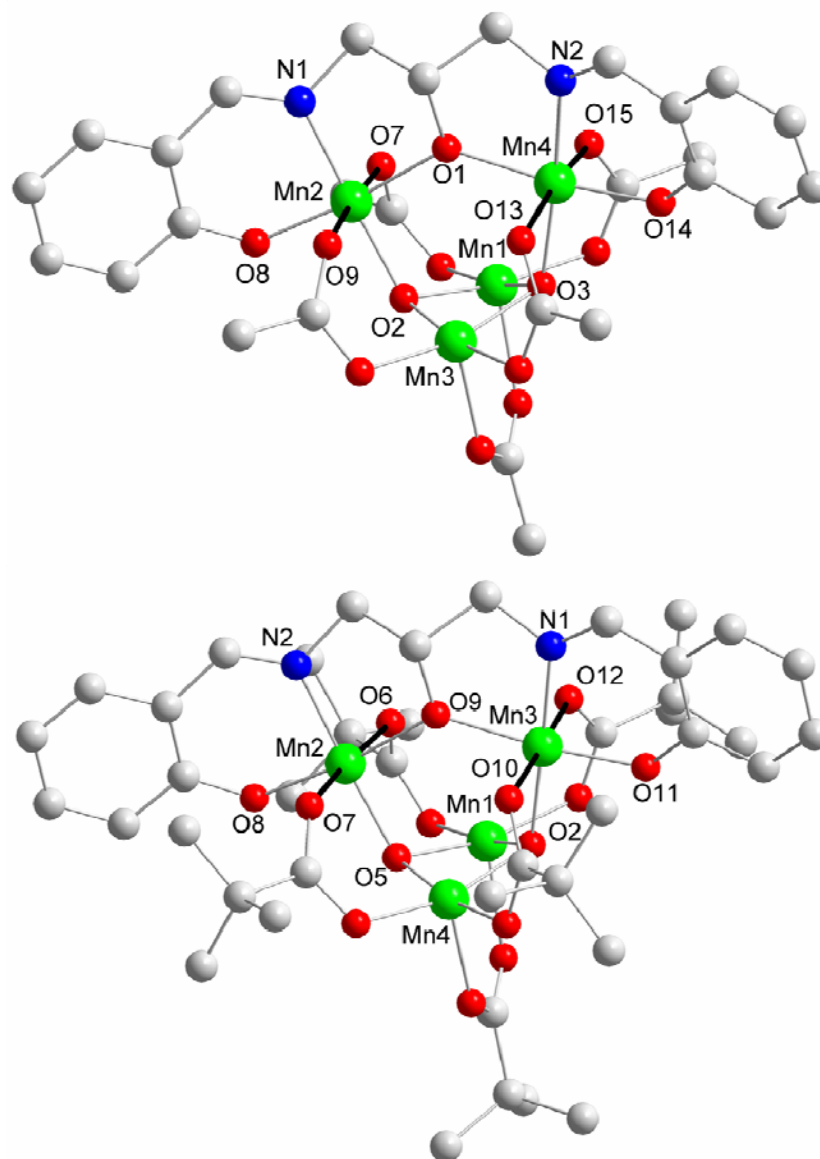


Figure 2-2. Labeled representation of the structure of **2-1** (top) and **2-3** (bottom). Hydrogen atoms have been omitted for clarity. JT axis on Mn^{III} are shown in black. Color code: Mn^{III}, green; O, red; N, blue; C, grey.



Figure 2-3. Comparison of the cores of **2-1** and **2-3** (left) with that of the normal butterfly complexes (right). Color code: Mn^{III}, green; O, red.

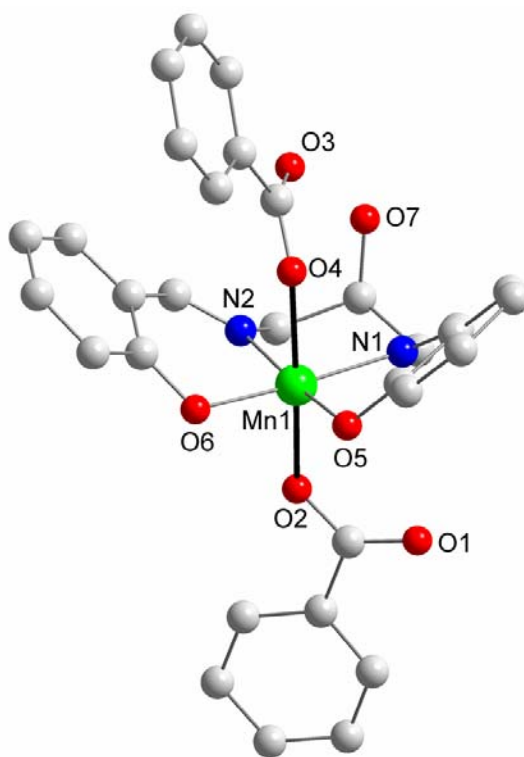


Figure 2-4. Labeled representation of the structure of **2-4**. Hydrogen atoms have been omitted for clarity. JT axis on Mn^{III} are shown in black. Color code: Mn^{III}, green; O, red; N, blue; C, grey.

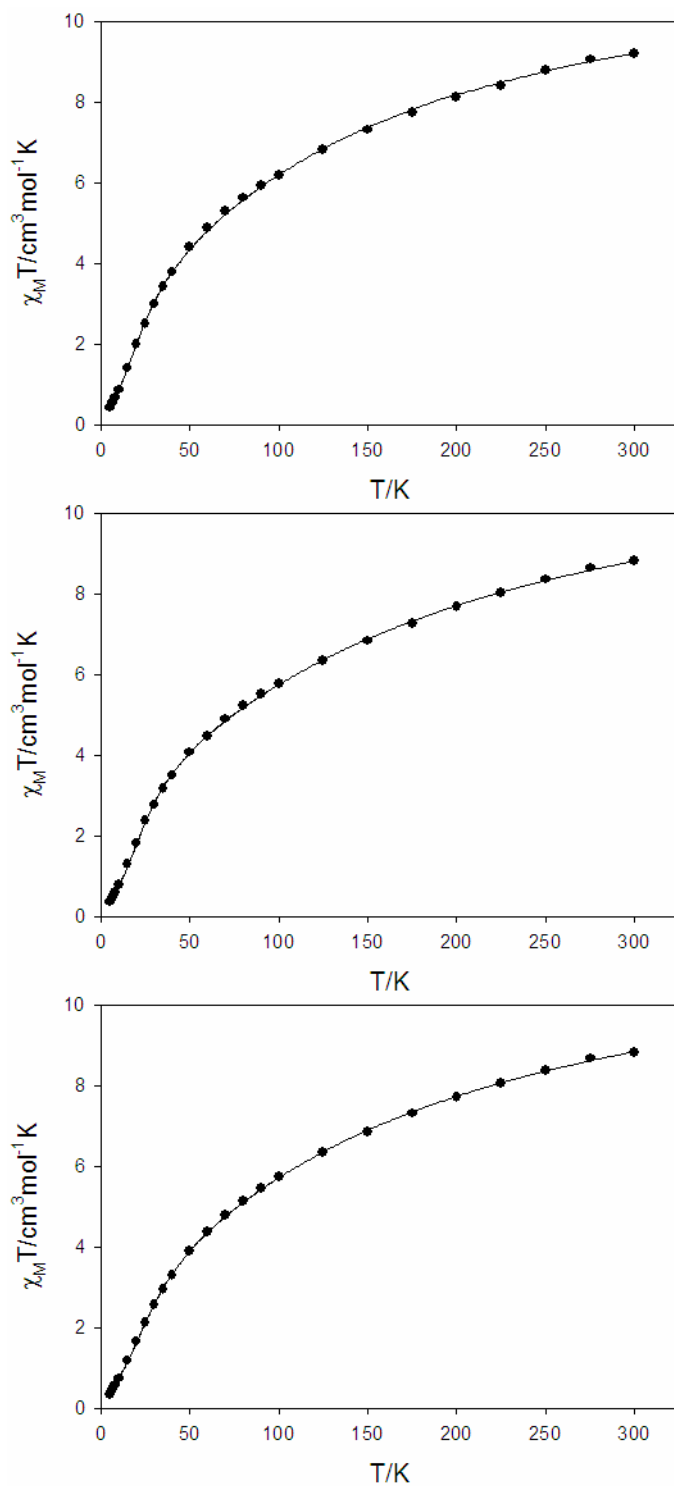


Figure 2-5. Plots of $\chi_M T$ vs T for complexes **2-1**·CH₂Cl₂ (top), **2-2**·CH₂Cl₂ (middle) and **2-3**·½CH₂Cl₂ (bottom). The solid line is the fit of the data; see the text for the fit parameters.



Figure 2-6. (left) The core of **2-1** defining the pairwise exchange interactions. (right) Rationalization of ground state spin of **2-1**.

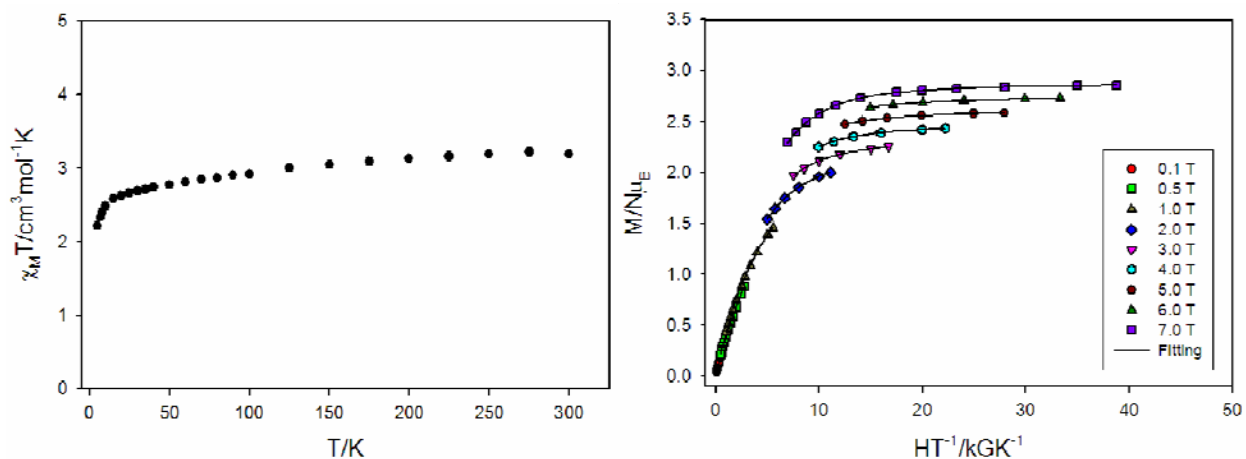


Figure 2-7. (left) Plots of $\chi_M T$ vs. T for complex **2-4**· $\frac{1}{2}$ CH₂Cl₂. (right) Plot of reduced magnetization ($M/N\mu_B$) vs H/T for complex **2-4**· $\frac{1}{2}$ CH₂Cl₂. The solid lines are the fit of the data; see the text for the fit parameters.

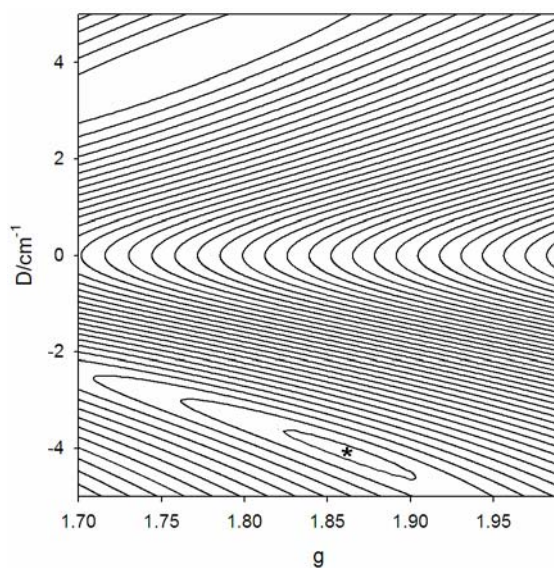


Figure 2-8. Two-dimensional contour plot of the fitting-error surface vs D and g for complex **2-4**· $\frac{1}{2}$ CH₂Cl₂.

CHAPTER 3
ROLE OF MIXED-LIGAND AND MIXED-SOLVENT SYSTEM: ROUTE TO Mn₄ AND Mn₂₅

3.1 Introduction

For a number of years, we have been engaged in developing manganese cluster chemistry with oxide bridges. The motivation for this is the relevance of manganese in bio-inorganic chemistry and molecular magnetism, not least their aesthetic qualities.^{27,35,57} In the field of molecular magnetism, single-molecule magnets (SMMs) hold great current interest. SMMs are molecular species that can function as nanoscale magnets as a result of their intrinsic properties rather than as a result of inter-unit interactions and long-range ordering as would be found in traditional magnetic materials (metals, metal oxides, etc).¹³ Thus each SMM is a single-domain magnetic particle, and this arises from the combination of a large ground state spin (S) and an Ising type (easy-axis) magnetoanisotropy (-ve zero field splitting parameter, D).¹³

As part of the search of new SMMs, it is important to build high spin and high anisotropy molecules. It is not possible to achieve a rational synthesis of a molecule with a high D , but there are certain approaches to high spin molecules.²² One of them being replacement of hydroxides by end-on azides and second is the use of ligands which generally promote ferromagnetic interactions.⁵⁸⁻⁶⁰ More recently, our group has demonstrated “spin tweaking”, the conversion of an already high-spin Mn₂₅ SMM with $S = 51/2$ into a structurally similar one with $S = 61/2$ by modification of the peripheral ligands and conversion of a low-spin Mn₃O triangular cluster to a high spin Mn₃ cluster by the use of appropriate chelate.^{34,61}

We and others have extensively investigated chelating agent 2-hydroxymethyl pyridine (hmpH) and 2,6-pyridinedimethanol (pdmH₂) in manganese cluster chemistry and these have proven to be very useful in affording high nuclearity and high spin complexes in Mn cluster chemistry.^{34,62,63} Examples of these include Mn₁₀ ($S = 22$)⁶³ and Mn₂₅ ($S = 51/2, 61/2$).^{34,62} We

have been continuing our investigation into the usefulness of the mixed-chelate system and therefore we decided to use mixture of hmpH and pdmH₂, which have already been proved to be very promising in high nuclearity Mn cluster chemistry, with [Mn₃O(O₂CMe)₆(py)₃]⁺ complexes. As mentioned in Chapter 2, Mn₃O trinuclear complexes have proven to be extremely useful in producing polynuclear clusters with high ground state spin and possible SMM behavior.⁶⁴⁻⁶⁷ Indeed, as will be described below, reaction of mixed chelate system (hmpH and pdmH₂) with [Mn₃O(O₂CMe)₆(py)₃]⁺ has led to a ferromagnetically coupled Mn₄ cluster and a Mn₂₅ cluster with a ground state spin of 65/2.

3.2 Experimental Section

3.2.1 Syntheses

All manipulations were performed under aerobic conditions and all chemicals were used as received unless otherwise noted. [Mn₃O(O₂CMe)₆(py)₃]ClO₄ was synthesized as reported elsewhere.⁴⁵

[Mn₄(hmp)₄(pdmH)₂(MeCN)₄](ClO₄)₄ (3-1). Method A. To a stirred solution of hmpH (0.05 mL, 0.50 mmol) and pdmH₂ (0.033 g, 0.25 mmol) in MeCN (15 mL) was added MeCO₂Na (0.08 g, 1.0 mmol) and Mn(ClO₄)₂ (0.40 g, 1.1 mmol) followed by the addition of NEt₃ (0.07 mL, 0.5 mmol). The resulting reddish-brown solution was stirred for two hours and then filtered to remove any undissolved solid and then left for slow evaporation. X-ray quality crystals of **3-1** grew over a period of two weeks in 20% yield. These were collected by filtration, washed with MeCN and dried *in vacuo*. Anal. Calcd (Found) for **3-1**(C₄₆H₅₂N₁₀Mn₄O₂₄Cl₄): C, 37.07 (36.85); H, 3.52 (3.46); N 9.40 (9.07)%. IR (ν, cm⁻¹): 1607m, 1578w, 1440m, 1369w, 1281w, 1145s, 1088s, 768w, 720w, 673w, 626m, 575w.

Method B. To a stirred solution of hmpH (0.02 mL, 0.21 mmol) and pdmH₂ (0.06 g, 0.45 mmol) in MeCN (15 mL) was added [Mn₃O(O₂CMe)₆(py)₃]ClO₄ (0.22 g, 0.25 mmol). The

resulting solution was stirred for 30 minutes and then filtered and left for slow evaporaton.

Reddish brown crystals of **3-1** were obtained after 15 days in 5% yield. The product was identifiield as **3-1** by IR spectral comparison with material from method A.

[Mn₂₅O₁₈(OH)₂(hmp)₆(pdm)₈(pdmH)₂(L)₂](ClO₄)₆ (3-2). To a stirred solution of [Mn₃O(O₂CMe)₆Py₃]ClO₄ (0.20 g, 0.23 mmol) in MeOH/MeCN (5/15 mL) was added hmpH (0.02 mL, 0.23 mmol) and pdmH₂ (0.06 g, 0.46 mmol). This was followed by the addition of NEt₃ (0.03 mL, 0.23 mmol). The resulting reddish brown solution was left under magnetic stirring for 30 minutes and then filtered through a medium frit. The resulting brown filtrate was left undisturbed to evaporate slowly at room temperature. The X-ray quality crystals of **3-2·8MeCN·4MeOH** were obtained over a period of two weeks in 10% yield. These were collected by filtration, washed with MeCN and MeOH and dried in *vacuo*. Anal. Calcd (Found) for **3-2·3H₂O** (C₁₂₀H₁₂₈N₁₈Mn₂₅O₇₉Cl₆): C, 30.85 (30.70); H, 2.76 (2.79); N 5.39 (5.05)%. IR (ν, cm⁻¹): 1600s, 1577s, 1440s, 1388m, 1276w, 1102s, 1074s, 774w, 676m, 635s, 559m, 503w, 438w.

3.2.2 X-ray Crystallography

Data were collected by Dr. Khalil A. Abboud on a Siemens SMART PLATFORM equipped with a CCD area detector and a graphite monochromator utilizing MoK α radiation ($\lambda = 0.71073$ Å). Suitable crystals of **3-1** and **3-2·8MeCN·4MeOH** were attached to glass fibres using silicone grease and transferred to a goniostat where they were cooled to 173 K for data collection. Cell parameters were refined using up to 8192 reflections. A full sphere of data (1850 frames) was collected using the ω -scan method (0.3° frame width). The first 50 frames were re-measured at the end of data collection to monitor instrument and crystal stability (maximum correction on I was < 1 %). Absorption corrections by integration were applied based on measured indexed crystal faces. The structure was solved by the Direct Methods in *SHELXTL6*,⁴⁶ and refined using

full-matrix least squares. The non-H atoms were treated anisotropically, whereas the hydrogen atoms were calculated in ideal positions and were riding on their respective carbon atoms.

Refinement was done using F^2 .

In **3-1**, the asymmetric unit consists of a half Mn_4 cluster and two perchlorate anions. A total of 403 parameters were refined in the final cycle of refinement using 10860 reflections with $I > 2\sigma(I)$ to yield R_1 and wR_2 of 4.97% and 11.82%, respectively.

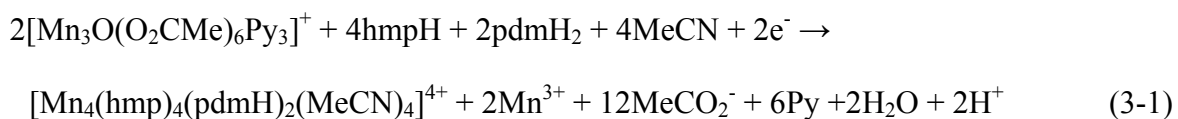
In **3-2**·8MeCN·4MeOH, the asymmetric unit consists of a half Mn_{25} cluster, three perchlorate anions, four acetonitrile molecules and two methanol molecules. All solvent molecules and the anions were disordered and could not be modeled properly, thus program SQUEEZE,⁶⁸ a part of the PLATON package of crystallographic software, was used to calculate the solvent disorder area and remove its contribution to the overall intensity data. In particular, the perchlorate anions were extensively disordered and each was refined in three parts before their contributions were removed from the intensity data by SQUEEZE. The cluster also has a couple of disorders. Two of the pdmH₂ ligands seem to have been oxidized during synthesis to produce, in each case, a carboxylate instead of one of the hydroxyl group. Both parts of each disorder were fixed at 50% occupancy after the refinement produced value close to 50%. A total of 979 parameters were refined in the final cycle of refinement using 55761 reflections with $I > 2\sigma(I)$ to yield R_1 and wR_2 of 6.70% and 15.77%, respectively. The crystallographic data and structure refinement details for **3-1** and **3-2**·8MeCN·4MeOH are listed in Table 3-1.

3.3 Results and Discussion

3.3.1 Syntheses

The reaction of preformed trinuclear complexes $[Mn_3O(O_2CMe)_6(py)_3]^{0,+}$ with chelating ligands has been used extensively in the past to trigger structural rearrangements leading to higher nuclearity products. The choice of chelate and the reaction conditions have significant

effect not only on the nuclearity of the product but also on its metal topology. Along the same lines, the reaction of $[\text{Mn}_3\text{O}(\text{O}_2\text{CMe})_6\text{Py}_3]\text{ClO}_4$ with hmpH and pdmH₂ in 1:1:1 molar ratio in MeCN gave $[\text{Mn}_4(\text{hmp})_4(\text{pdmH})_2(\text{MeCN})_4]^{4+}$ (**3-1**). Its formation is summarized in eq. 3-1. The yield of the reaction is extremely low and the attempts to increase the yield gave a mixture of products and were not further pursued. Instead, we sought its synthesis from a more convenient procedure that doesn't employ preformed triangular complex but only simple starting materials. This was successfully accomplished from the reaction of $\text{Mn}(\text{ClO}_4)_2$, hmpH and pdmH₂ in the presence of MeCO_2Na . Use of sodium acetate is found to be essential in this reaction, it does not appear in the final product but presumably acts as a base.



On the other hand, **3-2**·8MeCN·4MeOH is obtained upon the reaction of $[\text{Mn}_3\text{O}(\text{O}_2\text{CMe})_6\text{Py}_3]\text{ClO}_4$ with hmpH and pdmH₂ in MeCN/MeOH system. This reaction is very sensitive to the ratio of Mn_3 :hmpH:pdmH₂ and the clean product is obtained only when ratio mentioned in the experimental section is used. Using higher concentration of hmpH or pdmH₂ beyond that described in the experimental section gives a mixture of orange and red crystals. And the presence of MeOH is absolutely essential for the formation of product. Presumably, the more polar MeOH facilitates the necessary proton transfer steps. In addition, 3:1 v/v MeCN:MeOH is found to be the best for clean reaction. However, the yield of the product decreases as the concentration of MeOH increases, most likely due to the solubility of the product, while reducing the amount of MeOH gives white crystals along with the desired product. Also, the same product is obtained in the absence of base but in extremely low yield.

One remarkable feature of this reaction is the in situ formation of the oxidized pdmH₂ ligand. In **3-2**·8MeCN·4MeOH, oxidation of the chelate provides the reducing equivalents to lower the metal oxidation state of the product. The reduction of the Mn^{III} centers to Mn^{II} is associated with oxidation of some of the pdmH₂, possibly to the corresponding aldehyde, 6-(hydroxymethyl)-2-pyridine carboxaldehyde followed by the further oxidation to 6-(hydroxymethyl)-2-pyridine carboxylic acid (L, Figure 3-1). This has been seen before with hmpH⁶⁹ and pdmH₂⁷⁰ ligands in high-oxidation state Mn chemistry. The redox chemistry is also accompanied by the fragmentation and structural rearrangement of the Mn₃ cluster to yield Mn₂. Also filtrate after the isolation of the product is still dark colored, thus there is a possibility that disproportionation of Mn^{III} is occurring during the reaction and filtrate contains both Mn^{II} and Mn^{IV} ions.

For both compounds, the final yields are low, nevertheless the preparations are reproducible. As is usually the case for such reactions, several species in equilibrium are likely present in solution, and the low solubility of one of them is undoubtedly the reason a pure product can be obtained.

3.3.2 Description of Structures

3.3.2.1 Structure of [Mn₄(hmp)₄(pdmH)₂(MeCN)₄](ClO₄)₄ (**3-1**)

The labeled structure of complex **3-1** is shown in Figure 3-2 and selected interatomic distances and angles are listed in Table A-4. Complex **3-1** crystallizes in monoclinic space group *P*2₁/*c* with the cation lying on an inversion center. The centrosymmetric structure of **3-1** can be described as a planar mixed-valence Mn₄ rhombus consisting of 2Mn^{II} and 2Mn^{III} ions. Mn1 and Mn2 are assigned as Mn^{III} and Mn^{II} respectively on the basis of structural parameters and Bond Valence Sum (BVS)^{48,49} calculations that gave a value of 2.99 and 1.88 for Mn1 and Mn2 respectively and the presence at Mn1 of a Jahn Teller (JT) elongation axis (O4-Mn1-N1), as

expected for a high spin Mn^{III}. The rhombus is composed of two Mn₃ triangular faces each bridged by a μ_3 -oxygen, O4 from a bidentate chelating pdmH⁻ whose other arm O3 is protonated as evident from the BVS of 1.09. Hmp⁻ groups are also bidentate with O1 bridging Mn1 and Mn2 and O2 bridging Mn1 and Mn2'. Peripheral ligation is provided by four MeCN molecules at Mn2 and Mn2'; which are seven coordinated, whereas Mn1 is distorted octahedral. Structure of complex **3-1** is similar to the Mn₄ complexes seen with hmp⁻ and pdmH⁻ alone.

3.3.2.2 Structure of [Mn₂₅O₁₈(OH)₂(hmp)₆(pdm)₈(pdmH)₂(L)₂](ClO₄)₆ (**3-2**)

The structure of complex **3-2** is shown in Figure 3-3 and selected interatomic distances and angles are listed in Table A-5. Complex **3-2** crystallizes in triclinic space group *P* $\bar{1}$ with the cation lying on an inversion center. It can be described as having a barrel-like cage structure consisting of 6Mn^{II}, 18Mn^{III} and Mn^{IV} ions. The 12 μ_4 -O²⁻, 6 μ_3 -O²⁻ and 2 μ_3 -OH⁻ ions hold the core together, as well as chelating bridging hmp⁻ and pdmH⁻ and L groups, where L = 6-hydroxymethyl-2-pyridine carboxylic acid (Figure 3-1). The manganese oxidation states and protonation levels of OH⁻, hmp⁻, pdm²⁻, pdmH⁻ and L oxygen atoms were established by Mn and O BVS calculations (Table 3-2 and 3-3), inspection of metric parameters and detection of Mn^{III} JT elongation axes. The core can be dissected into five parallel layers of three types with an ABCBA arrangement (Figure 3-4). Layer A is a Mn^{II}₃ triangular unit (Mn1, Mn11 and Mn12) with a capping μ_3 -OH⁻ ions; layer B is a Mn^{III}₆ triangle (Mn2, Mn3, Mn5, Mn7, Mn10 and Mn13) comprising three corner-sharing Mn^{III}₃ triangles; and layer C is a Mn^{III}₆ hexagon (Mn4, Mn6, Mn8 and their symmetry equivalents) with a central Mn^{IV} ion (Mn9). Layer C has the Anderson type structure seen before in some Mn complexes. Each layer is held together and linked to its neighboring layers by a combination of oxide, alkoxide bridges. The outer coordination shell is occupied by hmp⁻, pdm²⁻, pdmH⁻ and L ligands. There are two types of

Mn^{III} ions; those in layer B are nearly octahedral while those in layer C are pentagonal bipyramidal.

There are two Mn₂₅ complexes reported in literature, [Mn₂₅O₁₈(OH)₂(N₃)₁₂(pdm)₆-(pdmH)₆](Cl)₂ (**Mn₂₅⁺²**) and [Mn₂₅O₁₈(OH)(OMe)(hmp)₆(pdm)₆(pdmH)₆](N₃)₂(ClO₄)₆ (**Mn₂₅⁺⁸**). All these Mn₂₅ complexes have the same layered arrangement of Mn ions, however the precise means by which layers are connected to each other are different. The main difference between **Mn₂₅⁺²** with $S = 51/2$ and **Mn₂₅⁺⁸** with $S = 61/2$ is that 12 bound azides in **Mn₂₅⁺²** are replaced by six $\eta^1:\eta^1:\mu_2$ hmp⁻ ligands in **Mn₂₅⁺⁸**. As a result, all intra- and inter layer bridges, as well as all M₂ pairwise exchange interactions are now through oxide anions. Complex **3-2** is very much similar to **Mn₂₅⁺⁸** except for the arrangement of layer A, where one alcohol arm of the pdmH⁻ group has been oxidized and the three Mn^{II} ions are bridged by an OH⁻ instead of OMe⁻ in **Mn₂₅⁺⁸**.

3.3.3 Magnetochemistry

3.3.3.1 Dc Studies

Variable-temperature dc magnetic susceptibility measurements were performed on dried microcrystalline sample of **3-1** and **3-2**·3H₂O at 0.1 T and 5.0-300 K range. The data for **3-1** is shown as $\chi_M T$ vs T plot in Figure 3-5. For **3-1**, the value of $\chi_M T$ increases from 16.44 cm³Kmol⁻¹ at 300 K to 35.3 cm³Kmol⁻¹ at 5 K. The $\chi_M T$ value at 300 K is higher than the spin only value of 14.75 cm³Kmol⁻¹ expected for two Mn^{III} and two Mn^{II} ions suggesting predominant ferromagnetic interactions within the molecule. The value of $\chi_M T$ at 5 K suggests $S = 9$ ground state spin. To determine the individual pair-wise exchange interactions J_{ij} between Mn_iMn_j pairs within the molecule, the $\chi_M T$ vs T data for complex **3-1** was fit to a simulation curve deduced from the Heisenberg-Dirac-VanVleck spin Hamiltonian given in eq. 3-2 where $\hat{S}_A = \hat{S}_1 + \hat{S}_3$, $\hat{S}_B = \hat{S}_2 + \hat{S}_4$, and $\hat{S}_T = \hat{S}_A + \hat{S}_B$. The exchange and the atom labeling scheme are summarized in Figure 3-6.

The energies of the resultant total spin states S_T , which are eigen functions of the Hamiltonian in this coupling scheme, are given by eq. 3-3. The overall multiplicity of the spin system is 900, made up of 110 individual spins states ranging from $S_T = 1$ to 9. An expression for the molar paramagnetic susceptibility was derived for this complex using the Van Vleck equation⁵¹ (see Appendix D-2, Refer Chapter 2 for details of vector coupling)

$$\mathcal{H} = -J_{wb}(\hat{S}_T^2 - \hat{S}_A^2 - \hat{S}_B^2) - J_{bb}(\hat{S}_A^2 - \hat{S}_1^2 - \hat{S}_3^2) \quad (3-2)$$

$$E|S_T, S_A, S_B\rangle = -J_{wb}[S_T(S_T+1) - S_A(S_A+1) - S_B(S_B+1)] - J_{bb}[S_A(S_A+1)] \quad (3-3)$$

Excellent fits were achieved when data below 10 K was omitted and TIP fixed to $6 \times 10^{-4} \text{ cm}^3 \text{ mol}^{-1}$. The obtained fit is shown as solid lines in Figure 3-5 and was obtained with $J_{bb} = 6.67 \text{ cm}^{-1}$, $J_{bw} = 0.36 \text{ cm}^{-1}$ and $g = 2.06$. These values identify the ground state as $|S_T, S_A, S_B\rangle = |9, 4, 5\rangle$. The values of J_{bb} , J_{bw} and g are similar to those reported in literature.^{54,65}

To confirm the above ground state spin estimates and to determine the magnitude of zero field splitting parameter (D), variable field (H) and temperature-magnetization (M) data were collected in the 1.8-10 K and 2-6 T ranges. The resulting data for **3-1** are plotted in Figure 3-7 as reduced magnetization ($M/N\mu_B$) vs H/T , where N is Avogadro's number and μ_B is the Bohr magneton. The data were fit, using the program *MAGNET*,⁵³ by diagonalization of the spin Hamiltonian matrix assuming that only the ground state is populated, incorporating axial anisotropy ($D\hat{S}_z^2$) and Zeeman terms, and employing a full powder average.^{36,54-56} The corresponding spin Hamiltonian is given by eq 3-4, where \hat{S}_z is the easy-axis spin operator, g is the Lande' g factor, μ_0 is the vacuum permeability, and H is the applied field. The last term in eq 3-3 is the Zeeman energy associated with an applied magnetic field. The best fit for **3-1** is shown as the solid lines in Figure 3-7 and was obtained with $S = 9$, $g = 2.00$ and $D = -0.27 \text{ cm}^{-1}$.

$$\mathcal{H} = D\hat{S}_z^2 + g\mu_B\mu_0\hat{S}\cdot H \quad (3-4)$$

To ensure that the true global minimum had been located and to ensure the hardness of the fit, root-mean-square error surface for the fit was generated using the program *GRID*,⁷¹ which calculates the relative difference between the experimental $M/N\mu_B$ data and those calculated for various combinations of D and g . This is shown as two-dimensional contour plot in Figure 3-7, the plot shows that fit minimum is a soft one, consistent with significant uncertainty in the precision of the obtained g and D fit values, which we estimate as ± 0.04 on g and $\pm 10\%$ on D .

For **3-2**·3H₂O, the value of $\chi_M T$ steadily increases from 117.5 cm³Kmol⁻¹ at 300 K to a maximum of 540.9 cm³Kmol⁻¹ at 15 K before dropping to 489.4 cm³Kmol⁻¹ at 5 K (Figure 3-9). The value of $\chi_M T$ at 15 K suggests a very large ground-state spin (S) value, with the sharp decrease at the lowest temperature, assigned to Zeeman effects, zero-field splitting, and/or weak intermolecular interactions. To determine the ground state, magnetization (M) data were collected in 0.1-0.8 T and 1.8-10.0 K ranges and are plotted as $(M/N\mu_B)$ vs H/T in Figure 3-9. We used only the low-field data (≤ 0.8 T) to avoid problems with the low-lying excited states. The best fit (solid-lines in figure 3-9) gave $S = 65/2$, $g = 1.99$ and $D = -0.0082$ cm⁻¹. The fits for 63/2, 67/2 were also good, with best fit parameters of $g = 2.08/D = -0.01$ and $g = 1.93/D = -0.0077$ cm⁻¹ respectively. We conclude that **3-2**·3H₂O has a ground state of $65/2 \pm 1$.

3.3.3.2 Ac Studies

Ac susceptibility measurements were performed on polycrystalline sample of **3-1** and **3-2**·3H₂O under 3.5 G oscillating ac field and zero dc field as a function of temperature and frequency. The obtained data for **3-1** is shown as $\chi_M' T$ vs T and χ_M'' vs T plots in Figure 3-8. Extrapolation of the $\chi_M' T$ plot to 0 K from temperatures above ~ 3.5 K gives value of ~ 43 cm³Kmol⁻¹, corresponding to $S = 9$ with $g = 1.95$ in very satisfying agreement with the conclusions from the fits of dc magnetization data. Complex **3-1** shows frequency-dependent in-

phase (χ_M') and out-of-phase (χ_M'') signals, which are a signature of slow relaxation of magnetization i.e. SMM behavior by analogy to related [Mn₄] compounds.

The in-phase ac susceptibility (χ_M') signal for **3-2**·3H₂O is shown as $\chi_M'T$ vs T in Figure 3-10, and extrapolation of the $\chi_M'T$ signal to 0 K from above about 8 K (to avoid the effect of intermolecular interactions at lower temperatures) gave 550 cm³Kmol⁻¹, consistent with the dc data. The value of 550 cm³Kmol⁻¹ is consistent with 1) $S = 65/2 / g = 2.01$, 2) $S = 63/2 / g = 2.07$ and 3) $S = 67/2 / g = 1.95$. The ac data thus confirms a ground state of $65/2 \pm 1$. No out-of-phase signal was observed down to 1.8 K. The very small D value seen for **3-2**·3H₂O is consistent with the nearly perpendicular disposition of the Mn^{III} anisotropy axes. We have not done with micro-SQUID hysteresis measurements on single crystals of **3-2** but on the basis of previously reported Mn₂₅ complexes (**Mn₂₅⁺²** and **Mn₂₅⁺⁸**), which show hysteresis loops and are SMMs, we believe that **3-2**·3H₂O is also an SMM, albeit at very low temperature.

3.4 Conclusions

The combination of mixed-chelate system (hmpH and pdmH₂) in Mn cluster chemistry has yielded a ferromagnetic coupled Mn₄ rhombus and an unusually high spin Mn₂₅ complex depending on the identity of the solvent employed. The latter point emphasizes the exquisite sensitivity of the reaction product on reaction conditions. Dc and ac studies have established that Mn₂₅ possesses an $S = 65/2 \pm 1$ ground state spin. Such a high spin value is extremely rare; in fact, it is the second highest in Mn chemistry. Achieving high spin ground state is one of the elusive goals in the search for obtaining superior SMMs. Once again manganese cluster chemistry continues to surprise and astound with the remarkable variety and aesthetic beauty of its molecular offspring.

Table 3-1. Crystallographic Data for **3-1** and **3-2**·8MeCN·4MeOH

	3-1	3-2
Formula ^a	C ₄₆ H ₅₂ Cl ₄ Mn ₄ N ₁₀ O ₂₄	C ₁₄₀ H ₁₆₂ Cl ₆ Mn ₂₅ N ₂₆ O ₈₀
Fw, g/mol ^a	1490.54	5075.16
Space group	<i>P2₁/n</i>	<i>C2/c</i>
<i>a</i> , Å	11.2401(9)	30.710(2)
<i>b</i> , Å	21.2408(15)	30.818(2)
<i>c</i> , Å	12.6654(2)	18.0521(13)
α , °	90	90
β , °	101.312(2)	91.415(2)
γ , °	90	90
<i>V</i> , Å ³	2965.1(4)	17080(2)
<i>Z</i>	2	4
<i>T</i> , K	173(2)	173(2)
λ , Å ^b	0.71073	0.71073
ρ_{calc} , g/cm ³	1.669	1.974
μ , mm ⁻¹	1.101	1.976
<i>R</i> <i>I</i> ^{c,d}	0.0497	0.0670
<i>wR2</i> ^e	0.1182	0.1577

^aIncluding solvate molecules. ^b Graphite monochromator. ^c $I > 2\sigma(I)$. ^d $R1 = \Sigma(|F_o| - |F_c|) / \Sigma|F_o|$. ^e $wR2 = [\Sigma[w(F_o^2 - F_c^2)^2] / \Sigma[w(F_o^2)^2]]^{1/2}$, $w = 1/[\sigma^2(F_o^2) + [(ap)^2 + bp]$, where $p = [\max(F_o^2, O) + 2F_c^2]/3$.

Table 3-2. Bond-valence sums for the Mn atoms of complex **3-2**^a

Atom	Mn ^{II}	Mn ^{III}	Mn ^{IV}	Atom	Mn ^{II}	Mn ^{III}	Mn ^{IV}
Mn1	<u>1.97</u>	1.82	1.88	Mn8	3.21	<u>2.97</u>	3.07
Mn2	3.23	<u>2.99</u>	3.08	Mn9	4.29	3.92	<u>4.12</u>
Mn3	3.25	<u>2.98</u>	3.12	Mn10	3.19	<u>2.96</u>	3.05
Mn4	3.17	<u>2.92</u>	3.03	Mn11	<u>1.92</u>	1.77	1.83
Mn5	3.26	<u>2.98</u>	3.13	Mn12	<u>1.96</u>	1.81	1.87
Mn6	3.22	<u>2.97</u>	3.07	Mn13	3.19	<u>2.95</u>	3.04
Mn7	3.24	<u>2.97</u>	3.11				

^aThe underlined value is the one closest to the charge for which it was calculated. The oxidation state of a particular atom can be taken as the nearest whole number to the underlined value

Table 3-3. Bond-valence sums for the O atoms of complex **3-2**^a

Atom	BVS	Assignment	Atom	BVS	Assignment
O2	1.94	O ²⁻	O13	1.85	O ²⁻
O3	2.06	O ²⁻	O15	1.16	OH ⁻
O4	1.85	O ²⁻	o17	1.85	O ²⁻
O11	1.81	O ²⁻	O26	1.05	OH ⁻

^aThe BVS values for O atoms of O²⁻, OH⁻ and H₂O groups are typically 1.8-2.0, 1.0-1.2 and 0.2-0.4, respectively, but can be affected somewhat by hydrogen-bonding.

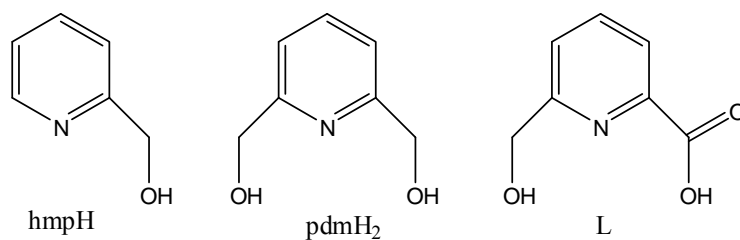


Figure 3-1. Structure of ligands: 2-hydroxymethyl pyridine (hmpH), 2,6-pyridine dimethanol (pdmH₂), 6-hydroxymethyl 2-pyridine carboxylic acid (L).

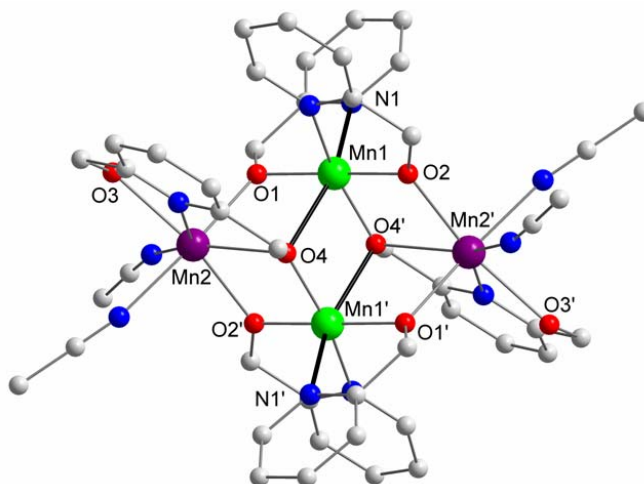


Figure 3-2. Labeled representation of the structure of **3-1**. JT axis on Mn^{III} are shown in black. Color code: Mn^{III}, green; Mn^{II}, purple; O, red; N, blue; C, grey.

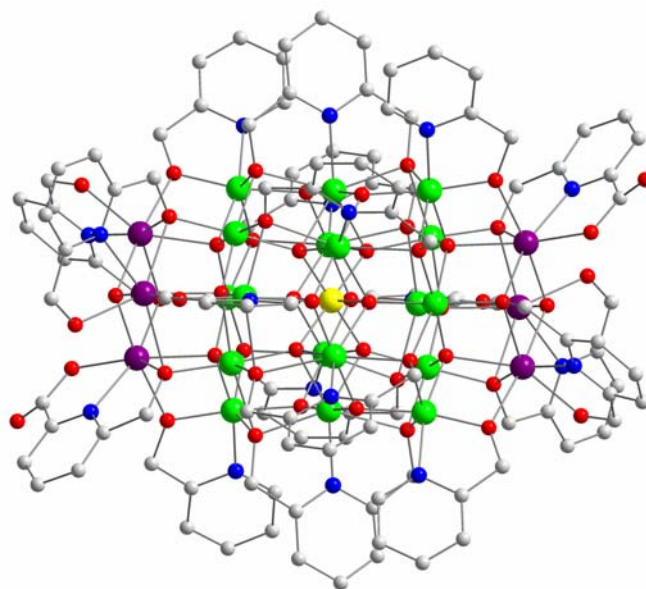


Figure 3-3. Structure of the cation of **3-2**. Color code: Mn^{IV}, yellow; Mn^{III}, green; Mn^{II}, purple; O, red; N, blue; C, grey.

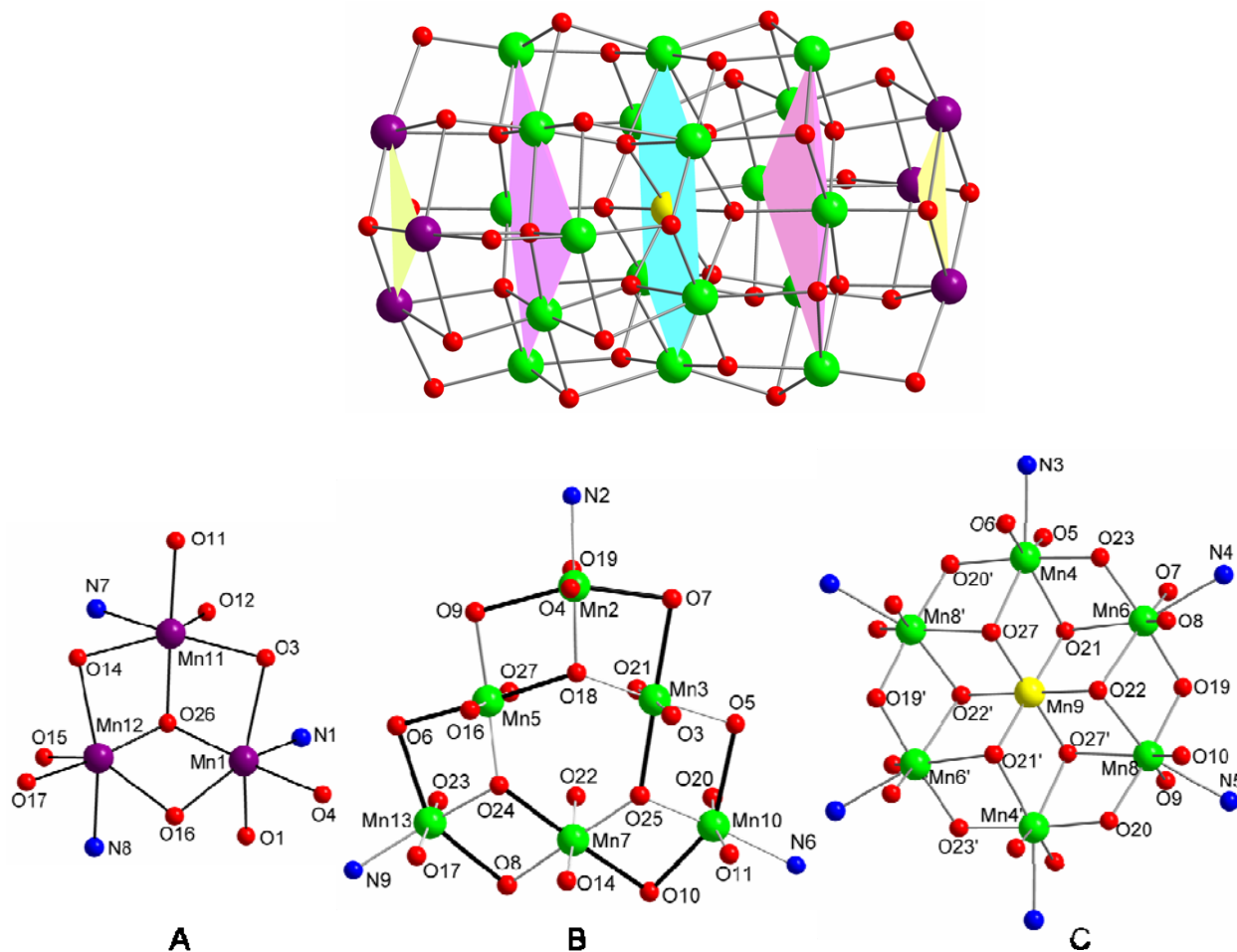


Figure 3-4. Centrosymmetric core of **3-2** (top) and its three types of constituent layers (bottom). JT axis on Mn^{III} are shown in bold. Color code: Mn^{IV}, yellow; Mn^{III}, green; Mn^{II}, purple; O, red; N, blue; C, grey.

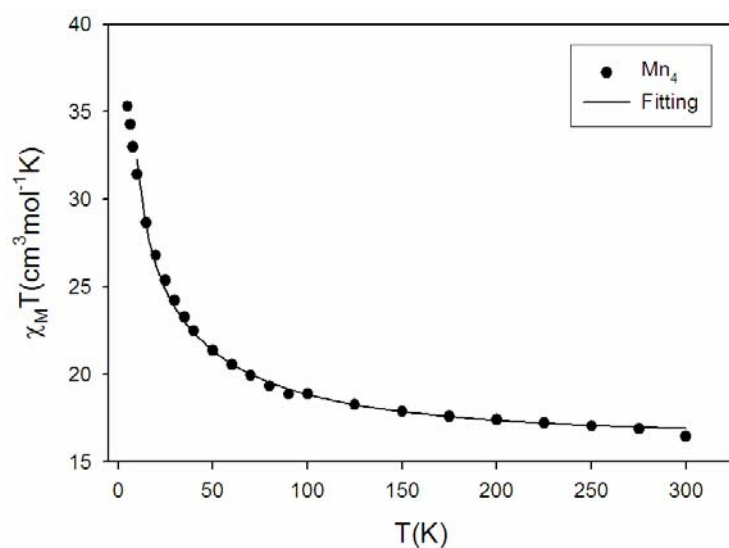


Figure 3-5. Plots of $\chi_M T$ vs T for complex **3-1**. The solid line is the fit of the data; see the text for the fit parameters.

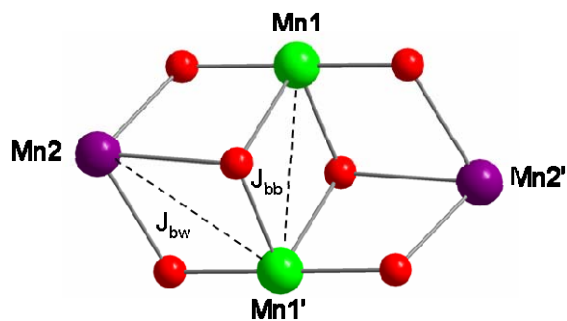


Figure 3-6. The core of **3-1** defining the pairwise exchange interactions.

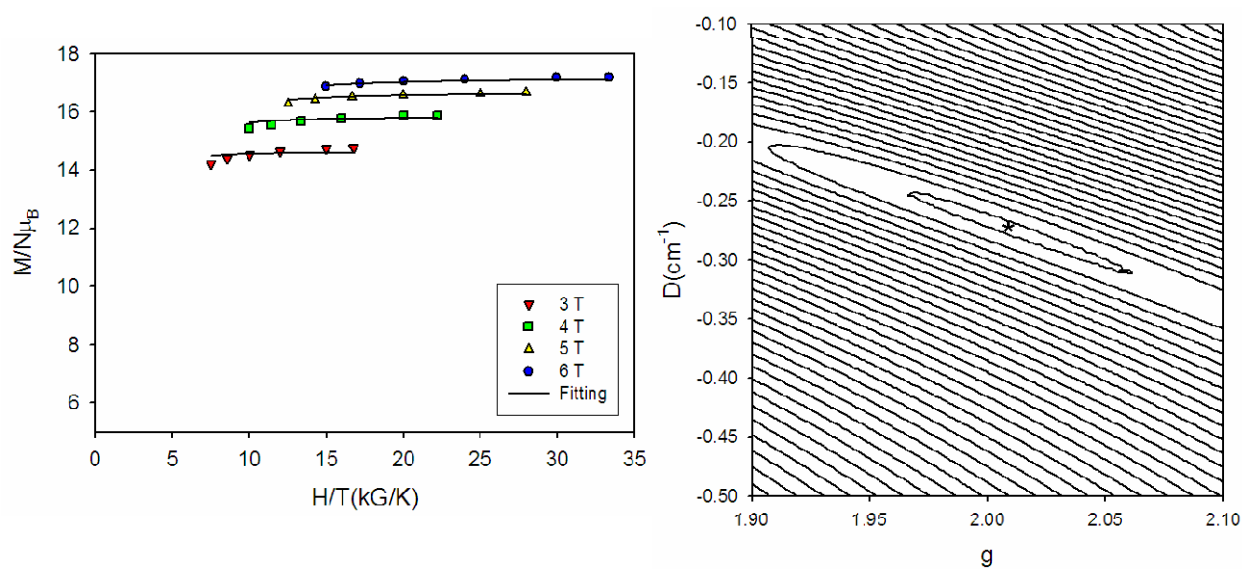


Figure 3-7. (left) Plot of reduced magnetization ($M/N\mu_B$) vs H/T for complex **3-1**. The solid lines are the fit of the data; see the text for the fit parameters. (right) Two-dimensional contour plot of the fitting error surface vs D and g for complex **3-1**.

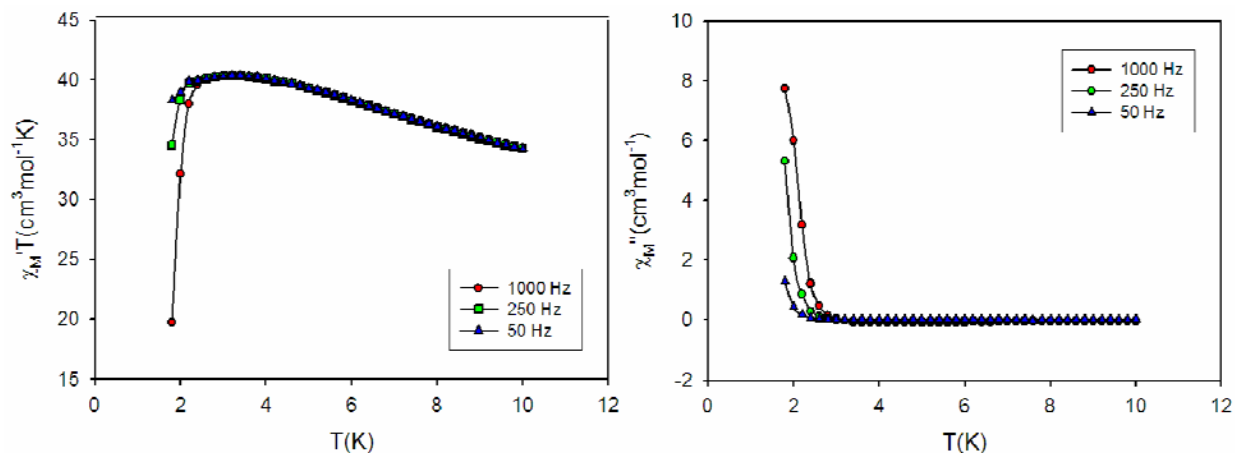


Figure 3-8. Plot of in-phase (χ_M') and out-of-phase (χ_M'') ac susceptibility data for complex **3-1**.

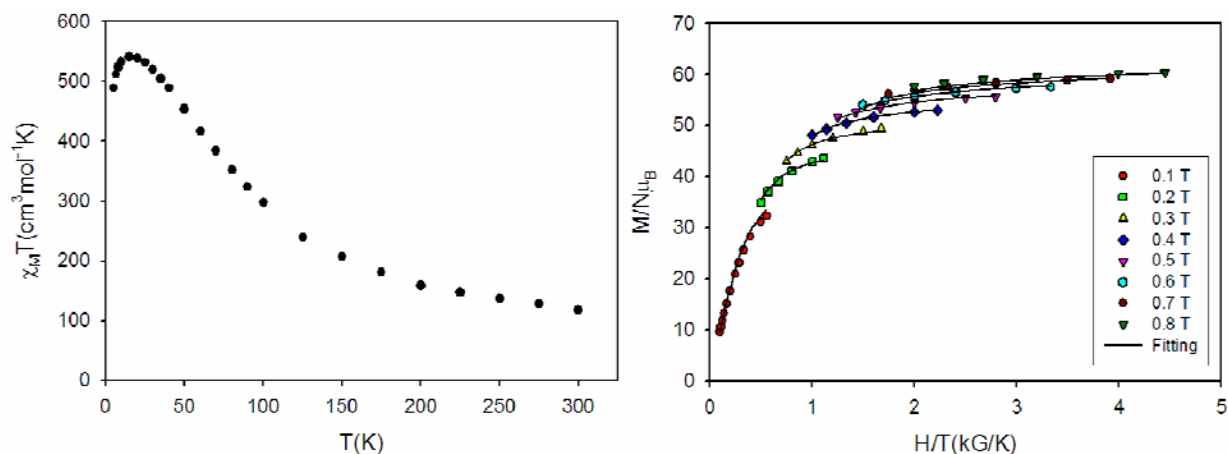


Figure 3-9. (left) Plot of $\chi_M T$ vs T for **3-2**· $3\text{H}_2\text{O}$ at 0.1 T. (right) Plot of reduced magnetization ($M/N\mu_B$) vs H/T for complex **3-2**· $3\text{H}_2\text{O}$. The solid lines are the fit of the data; see the text for the fit parameters.

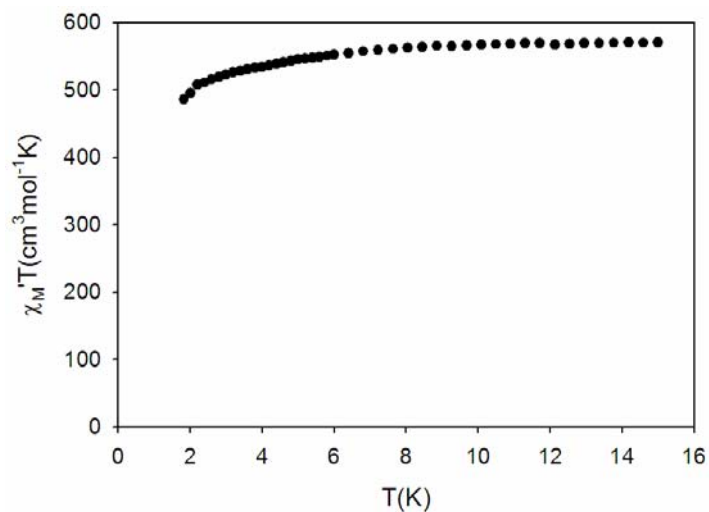


Figure 3-10. Plot of $\chi_M' T$ vs T (in-phase) ac susceptibility data for **3-2**· $3\text{H}_2\text{O}$.

CHAPTER 4
DIVERSITY OF STRUCTURAL TYPES IN POLYNUCLEAR IRON CHEMISTRY WITH A
(N, N, O)- TRIDENTATE LIGAND

4.1 Introduction

Polynuclear iron compounds with oxygen-based ligation are relevant to a variety of fields such as bioinorganic chemistry and magnetic materials. Iron-oxo centers are found in several non-heme metalloproteins and metalloenzymes; for example, in mammals iron is stored as ferritin, a protein that sequesters Fe^{III} as a polymeric oxo-hydroxo complex.²⁶ A number of polynuclear iron complexes have thus been synthesized and studied as possible models for ferritin in order to gain insights into the biomineralization process involved in the formation of its metal core.^{31,72,73} On the other hand, the paramagnetic nature of Fe in its common oxidation states can often lead to interesting magnetic properties for polynuclear Fe clusters, such as high ground state spin values and even single-molecule magnetism.¹³

Although the exchange interactions between Fe^{III} centers are almost always antiferromagnetic, certain Fe_x topologies can nevertheless possess large ground state spin values as a result of spin frustration. The latter is here defined in its more general sense of competing exchange interactions of comparable magnitude, preventing (frustrating) the preferred antiparallel alignment of all spins, and thus giving larger ground state spin values than might be predicted.⁷⁴⁻⁷⁸ In favorable cases, where these large ground state spins are coupled to a significant magnetic anisotropy, the compounds can behave as single-molecule magnets (SMMs).²⁰ This is the case for SMMs such as $[\text{Fe}_8\text{O}_2(\text{OH})_{12}(\text{tacn})_6]^{8+}$ and $[\text{Fe}_4(\text{OMe})_6(\text{dpm})_6]$ etc.⁷⁹⁻⁸²

The above considerations and others continue to stimulate groups around the world to develop new synthetic methods that can yield new polynuclear Fe/O clusters. A common approach has been to use chelates in order to encourage aggregation while ensuring discrete

products. Examples include 2,2'-bipyridine (bpy),⁷⁷ 1,4,7-triazacyclononane (tacn),⁸¹ and the anion of dibenzoylmethane (dbm⁻).⁸³ When the chelate also contains potentially bridging groups such as alkoxides, new high-nuclearity products can be obtained. Examples of this include the deprotonated, tridentate (N,O,O) form of N-methyldiethanolamine (mdaH₂) and (O,O,O) form of tris(hydroxymethyl)ethane (thmeH₃), and others.⁸⁴⁻⁸⁹ We decided to extend this approach to the potentially tridentate (N,N,O) chelate 2-[[2-(dimethylamino)ethyl]-methylamino] ethanol (dmemH, Figure 4-1). This has some similarity to mdaH₂, but it only has one alcohol group and it was thus anticipated to give new structural types of products. We were unable to locate previous examples in the literature of transition metal complexes with this chelate.

Our first investigations with dmemH have been in Fe chemistry using the triangular [Fe₃O(O₂CR)₆(H₂O)₃]⁺ complexes as reagents, a common strategy in both Fe^{III} and Mn^{III} chemistry.^{37,38,90-92} We have found from these reactions that dmemH is indeed a good route to a variety of interesting new cluster types. These results are described in this chapter, which reports the syntheses, structures, and magnetochemical characterization of four new Fe clusters containing dmem⁻.⁹³

4.2 Experimental Section

4.2.1 Syntheses

All preparations were performed under aerobic conditions using reagents and solvents as received. [Fe₃O(O₂CPh)₆(H₂O)₃](NO₃), [Fe₃O(O₂CBu^t)₆(H₂O)₃](NO₃), [Fe₃O(O₂CMe)₆(H₂O)₃](NO₃) and (NEt₄)₂(Fe₂OCl₆) were synthesized as reported elsewhere.⁹⁴⁻⁹⁷

[Fe₇O₄(O₂CPh)₁₁(dmem)₂] (4-1). Method A. An orange red solution of [Fe₃O(O₂CPh)₆(H₂O)₃](NO₃) (0.20 g, 0.19 mmol) in MeCN (20 mL) was treated with dmemH (0.06 mL, 0.38 mmol) and the solution stirred overnight at room temperature. It was then filtered to remove undissolved starting material, and the filtrate was allowed to stand undisturbed at

room temperature. X-ray quality orange crystals of **4-1**·4MeCN slowly formed over 5 days in 45% yield. These were collected by filtration, washed with MeCN, and dried under vacuum.

Anal. Calcd (Found) for **4-1**·½MeCN (C₉₂H_{90.5}N_{4.5}Fe₇O₂₈): C, 52.66 (52.55); H, 4.35 (4.38); N, 3.00 (3.05). Selected IR data (cm⁻¹): 1598(m), 1567(m), 1539(m), 1413(vs), 1175(w), 1069(w), 1025(w), 717(m), 675(w), 644(m), 461(m).

Method B. A solution of FeCl₃·6H₂O (0.20 g, 0.74 mmol) and NaO₂CPh (0.21 g, 1.48 mmol) in MeCN (15 mL) was treated with dmemH (0.06 mL, 0.37 mmol) and stirred for 3 hours. The resultant red brown solution was filtered to remove NaCl, and the filtrate was left undisturbed at room temperature for slow evaporation. Orange crystals slowly formed over 5 days in 30% yield; the product was identified by IR spectral comparison with material from Method A.

Method C. A solution of (NEt₄)₂(Fe₂OCl₆) (0.20 g, 0.33 mmol) and NaO₂CPh (0.14 g, 0.99 mmol) in MeCN (15 mL) was treated with dmemH (0.11 mL, 0.66 mmol) and stirred for few hours. The resultant red-brown solution was filtered and kept undisturbed at room temperature for slow evaporation. Orange crystals slowly formed over 3 days in 40% yield; the product was identified by IR spectral comparison with material from Method A.

[Fe₇O₄(O₂CMe)₁₁(dmem)₂] (4-2). Method A. A solution of FeCl₃·6H₂O (0.20 g, 0.74 mmol) and NaO₂CMe·3H₂O (0.25 g, 1.85 mmol) in MeCN (15 mL) was treated with dmemH (0.06 mL, 0.37 mmol) and stirred for 3 hours. The resultant red-brown solution was filtered to remove NaCl, and the filtrate was left undisturbed at room temperature for slow evaporation. X-ray quality, dark orange crystals appeared over 20 days in 15% yield. These were collected by filtration, washed with MeCN, and dried under vacuum. Anal. Calcd (Found) for **4-2**·2MeCN (C₄₀H₇₃N₆Fe₇O₂₈): C, 32.53 (32.66); H, 4.98 (5.26); N, 5.69 (5.46). Selected IR data (cm⁻¹):

3431(br), 2985(w), 2875(w), 1565(vs), 1426(vs), 1088(w), 1052(w), 1033(w), 886(w), 709(w), 668(m), 637(m), 615(m), 539(m), 487(m).

Method B. An orange-red solution of $[\text{Fe}_3\text{O}(\text{O}_2\text{CMe})_6(\text{H}_2\text{O})_3](\text{NO}_3)$ (0.20 g, 0.03 mmol) in MeCN (15 mL) was treated with dmemH (0.10 mL, 0.06 mmol) and the solution stirred overnight at room temperature. It was then filtered and the filtrate allowed to stand undisturbed at room temperature. Orange crystals of the product formed over 25 days in 10% yield; the product was identified by IR spectral comparison with material from Method A.

$[\text{Fe}_6\text{O}_2(\text{OH})_4(\text{O}_2\text{CCBu}^t)_8(\text{dmem})_2]$ (4-3). A solution of dmemH (0.03 ml, 0.19 mmol) in MeCN (5 mL) was treated with pyridine (15 μL , 0.19 mmol), followed by the addition of a solution of $[\text{Fe}_3\text{O}(\text{O}_2\text{CBu}^t)_6(\text{H}_2\text{O})_3](\text{NO}_3)$ (0.18 g, 0.19 mmol) in MeCN (12 mL). The resultant solution was filtered and the filtrate left undisturbed at room temperature. X-ray quality orange needles of **4-3**·2MeCN grew over 10 days in 20 % yield. These were collected by filtration, washed with MeCN, and dried under vacuum. Dried solid analyzed as solvent-free. Anal. calcd (Found) for **4-3** ($\text{C}_{54}\text{H}_{110}\text{N}_4\text{Fe}_6\text{O}_{24}$): C, 42.27 (42.53); H, 7.23 (7.40); N, 3.65 (3.68). Selected IR data (cm^{-1}): 2960(m), 2925(w), 2866(w), 1558(vs), 1484(s), 1427(vs), 1376(w), 1332(w), 1228(m), 1073(w), 903(w), 787(w), 662(m), 608(m), 530(m), 427(m).

$[\text{Fe}_3\text{O}(\text{O}_2\text{CBu}^t)_2(\text{N}_3)_3(\text{dmem})_2]$ (4-4). A solution of $[\text{Fe}_3\text{O}(\text{O}_2\text{CBu}^t)_6(\text{H}_2\text{O})_3](\text{NO}_3)$ (0.10 g, 0.11 mmol) in EtOH (15 mL) was treated with dmemH (34 μL , 0.20 mmol) and solid sodium azide (0.03 g, 0.46 mmol), and then stirred overnight at room temperature to give an orange precipitate. The solid was collected by filtration, washed with a little EtOH. It was recrystallized from a CH_2Cl_2 /hexanes layering to give X-ray quality orange crystals of **4-4**· $\frac{1}{2}\text{CH}_2\text{Cl}_2$ over 3 days in 25 % yield. Anal calcd (Found) for **4-4**· $\frac{1}{2}\text{CH}_2\text{Cl}_2$ ($\text{C}_{24.5}\text{H}_{53}\text{N}_{13}\text{Fe}_3\text{O}_7\text{Cl}$): C, 34.83 (34.77); H, 6.32 (6.30); N, 21.55 (21.16). Selected IR data (cm^{-1}): 3390(br), 2959(w), 2870(w), 2066(vs),

1543(m), 1480(w), 1418(m), 1342(w), 1225(w), 1087(m), 986(w), 720(m), 633(w), 606(w), 429(w).

4.2.2 X-ray Crystallography

Data were collected by Dr. Khalil A. Abboud on a Siemens SMART PLATFORM equipped with a CCD area detector and a graphite monochromator utilizing Mo-K α radiation ($\lambda = 0.71073 \text{ \AA}$). Suitable crystals of **4-1**·4MeCN, **4-2**·MeCN, **4-3**·2MeCN, and **4-4**·CH₂Cl₂ were attached to glass fibers using silicone grease and transferred to a goniostat where they were cooled to 173 K for data collection. Cell parameters were refined using up to 8192 reflections. A full sphere of data (1850 frames) was collected using the ω -scan method (0.3° frame width). The first 50 frames were remeasured at the end of data collection to monitor instrument and crystal stability (maximum correction on I was $< 1 \%$). Absorption corrections by integration were applied based on measured indexed crystal faces. The structure was solved by the Direct Methods in *SHELXTL6*,⁴⁶ and refined using full-matrix least squares. The non-H atoms were treated anisotropically, whereas the hydrogen atoms were calculated in ideal positions and were riding on their respective carbon atoms. Refinement was done using F^2 .

In **4-1**·4MeCN, the asymmetric unit consists of half the Fe₇ cluster and two MeCN molecules of crystallization. A total of 644 parameters were refined in the final cycle of refinement using 32986 reflections with $I > 2\sigma(I)$ to yield R_1 and wR_2 of 4.57 and 8.99 %, respectively. In **4-2**·MeCN, a total of 721 parameters were refined in the final cycle of refinement using 18637 reflections with $I > 2\sigma(I)$ to yield R_1 and wR_2 of 3.53 and 8.64 %, respectively. In **4-3**·2MeCN, a total of 924 parameters were refined in the final cycle of refinement using 17808 reflections with $I > 2\sigma(I)$ to yield R_1 and wR_2 of 4.15 and 10.0 %, respectively. In **4-4**·CH₂Cl₂, the azide ligand at N11 was disordered and it was refined in two positions with the site occupation factors dependently refined. A total of 472 parameters were

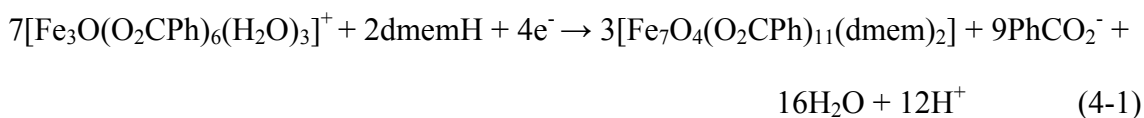
refined in the final cycle of refinement using 9205 reflections with $I > 2\sigma(I)$ to yield R_1 and wR_2 of 4.97 and 10.23 %, respectively. Unit cell data and details of the structure refinements for the four complexes are listed in Table 4-1.

4.3 Results and Discussion

4.3.1 Syntheses

Many synthetic procedures to polynuclear iron clusters rely on the reaction of $[\text{Fe}_3\text{O}(\text{O}_2\text{CR})_6(\text{H}_2\text{O})_3]^+$ species with a potentially chelating ligand, and this was one of the procedures chosen in the present work. In such reactions, the $[\text{Fe}_3\text{O}]^{7+}$ core of the trinuclear iron complex serves as a building block for higher nuclearity species, but the exact nuclearity and structure of the product depends on several factors; in the present work, we have found that the identity of the carboxylate group is one of these.

Reaction of $[\text{Fe}_3\text{O}(\text{O}_2\text{CPh})_6(\text{H}_2\text{O})_3](\text{NO}_3)$ with 1 - 3 equiv of dmemH in MeCN gave the heptanuclear complex $[\text{Fe}_7\text{O}_4(\text{O}_2\text{CPh})_{11}(\text{dmem})_2]$ (**4-1**) with a core topology not previously encountered (eq. 4-1). The same product was obtained from an EtOH reaction solvent, and also from the treatment of an MeCN solution of $\text{FeCl}_3 \cdot 6\text{H}_2\text{O}$ with sodium benzoate and dmemH in a 2:4:1 ratio. Increasing the amount of sodium benzoate or dmemH still gave complex **4-1**, but the reaction was not so clean. Reactions in which the MeCN was replaced by EtOH, and the $\text{FeCl}_3 \cdot 6\text{H}_2\text{O}$ by $\text{Fe}(\text{ClO}_4)_3 \cdot x\text{H}_2\text{O}$ or $(\text{NEt}_4)_2(\text{Fe}_2\text{OCl}_6)$, also gave the same product, for Fe:dmemH ratios of both 1:1 and 1:2. Clearly, complex **4-1** is a preferred product of these components and particular carboxylate group.

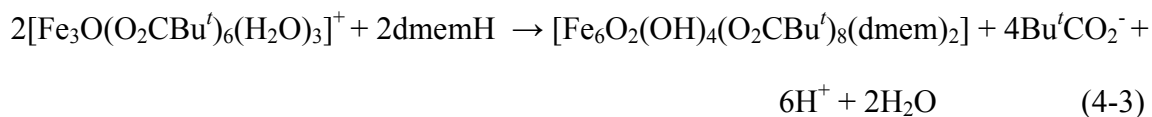


If the carboxylate employed was acetate instead of benzoate, then the product from the $\text{FeCl}_3/\text{MeCO}_2\text{Na}/\text{dmemH}$ (2:5:1) reaction system in MeCN (Method A of Experimental Section)

was another heptanuclear complex, $[\text{Fe}_7\text{O}_4(\text{O}_2\text{CMe})_{11}(\text{dmem})_2]$ (**4-2**) (eq. 4-2). Its formula is the same as that of **4-1**, except for the carboxylate identity, but structurally the two complexes are very different (vide infra). The same product **4-2** was obtained using $[\text{Fe}_3\text{O}(\text{O}_2\text{CMe})_6(\text{H}_2\text{O})_3]^+$ as the starting material in a reaction with two equiv. of dmemH in MeCN (Method B). The yields of **4-2** were much lower than **4-1**, although they could be improved somewhat by addition of some NEt_3 base to the reaction.



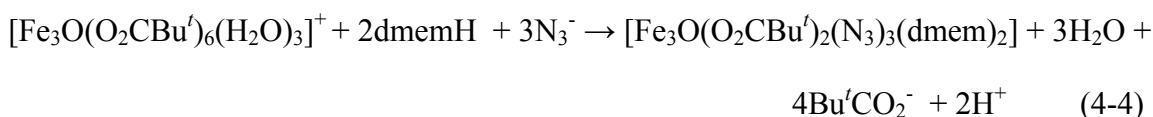
In contrast to the heptanuclear products from the use of benzoate and acetate reagents, the use of pivalate ones led to a hexanuclear product. Treatment of $[\text{Fe}_3\text{O}(\text{O}_2\text{CBu}^t)_6(\text{H}_2\text{O})_3](\text{NO}_3)$ with dmemH in MeCN led to subsequent isolation of $[\text{Fe}_6\text{O}_2(\text{OH})_4(\text{O}_2\text{CBu}^t)_8(\text{dmem})_2]$ (**4-3**) (eq. 4-3). The addition of one equivalent of NEt_3 or pyridine as base improves the yield from 10 to 20 %. The same product is obtained on increasing the amount of dmemH to three equivalents.



It is clear that the reactions that lead to **4-1** to **4-3** are very complicated, and the reaction solutions likely contain a complicated mixture of several species in equilibrium. In such cases, factors such as relative solubility, lattice energies, crystallization kinetics, and others determine the identity of the isolated products, and one (or more) of these factors is undoubtedly the reason that the reaction product is so dependent on the exact carboxylate employed.

Since complex **4-3** contains bridging hydroxide groups, a similar reaction was explored in the presence of sodium azide. Perlepes and coworkers have demonstrated that replacement of bridging hydroxide groups (which almost always mediate antiferromagnetic exchange interactions) with end-on bridging azide groups (which mediate ferromagnetic exchange) in

cobalt, nickel and iron clusters leads to products with much higher ground state spin values.⁵⁸⁻⁶⁰ Thus, we explored a variety of reaction conditions differing in the azide amount and/or solvent, and it was found that reaction of $[\text{Fe}_3\text{O}(\text{O}_2\text{CBu}')_6(\text{H}_2\text{O})_3](\text{NO}_3)$, dmemH and azide in a 1:2:4 ratio gave the new trinuclear complex $[\text{Fe}_3\text{O}(\text{O}_2\text{CBu}')_2(\text{N}_3)_3(\text{dmem})_2]$ (**4-4**) (eq. 4-4). The complex has its azide groups all in terminal sites, but it nevertheless has an interesting core structure. Complex **4-4** was also obtained in lower yield from the reaction of preformed complex **4-3** with four equivalents of sodium azide in EtOH.



4.3.2 Description of Structures

4.3.2.1 Structure of $[\text{Fe}_7\text{O}_4(\text{O}_2\text{CPh})_{11}(\text{dmem})_2]$ (**4-1**)

A labeled representation of complex **4-1** is shown in Figure 4-2(a). Selected interatomic distances and angles are summarized in Table A-6. Complex **4-1**·4MeCN crystallizes in the monoclinic space group $C2/c$ with the Fe_7 molecule lying on a crystallographic C_2 axis passing through the central Fe4 atom. The core can be described as two $[\text{Fe}_4(\mu_3\text{-O})_2]$ planar-butterfly units fused at body atom Fe4, one butterfly unit being atoms Fe1', Fe2, Fe3, Fe4, O9, O10'. Further, each butterfly unit can be considered as two edge-sharing Fe_3O triangular units, with the $\mu_3\text{-O}^{2-}$ bridging atoms O9 and O10 slightly above and below their Fe_3 planes. These O atoms bridge somewhat asymmetrically; the bonds to the wingtip Fe atoms ($\text{Fe1}\cdots\text{O10}$, 1.828 Å and $\text{Fe3}\cdots\text{O9}$, 1.844 Å) are shorter than the bonds to the body Fe atoms ($\text{Fe2}\cdots\text{O10}'$, 1.941 Å and $\text{Fe2}\cdots\text{O9}$, 1.923 Å). The two dmem⁻ groups bind as tridentate chelates to Fe1 and its symmetry partner Fe1', with their alkoxide O atoms bridging wingtip atom Fe1 in one Fe_4 unit with body atom Fe2 in the other. The remaining peripheral ligation about the $[\text{Fe}_7\text{O}_4]$ core is provided by

eleven benzoate groups, nine in their common $\eta^1: \eta^1: \mu$ - bridging mode and the other two in the rare η^2 chelating mode on Fe3 and Fe3'.

4.3.2.2 Structure of $[\text{Fe}_7\text{O}_4(\text{O}_2\text{CMe})_{11}(\text{dmem})_2]$ (**4-2**)

A labeled representation of complex **4-2** is provided in Figure 4-2(b). Selected interatomic distances and angles are given in Table A-7. Complex **4-2**·MeCN crystallizes in the triclinic space group *P* $\bar{1}$. The molecule contains a remarkable $[\text{Fe}_7(\mu_3\text{-O})_4]$ core. It can be described as consisting of a central $[\text{Fe}_3\text{O}_3]$ ring containing Fe2, Fe3 and Fe5, with each of the doubly-bridging O^{2-} ions of this hexagon becoming μ_3 by also bridging to a third, external Fe atom (Fe1, Fe4, Fe6). The fourth O^{2-} ion bridges ring atom Fe5, Fe6 and a seventh Fe atom (Fe7) on the periphery of the molecule. The two dmem^- groups bind one each to the external atoms Fe1 and Fe4 in a tridentate chelating manner with their alkoxide O atoms also bridging to ring atoms Fe2 and Fe3, respectively. Peripheral ligation is completed by eleven acetate groups, ten in $\eta^1: \eta^1: \mu$ -bridging modes and one η^2 chelating to Fe7.

The molecular structures of **4-1** and **4-2** can be said to represent two different ways of linking a number of Fe_3O triangular units, as is clear in Figure 4-3 where the cores of **4-1** to **4-3** are compared. The core topologies of complexes **4-1** and **4-2** are unprecedented within Fe^{III} chemistry. Indeed, there are only a few Fe_7 complexes in the literature, and they are all mixed-valent except for the one reported by Winpenny and coworkers containing phenylphosphonate ligand and Zheng and coworkers containing cyclohexenephosphonate ligand.^{98,99} In addition, very recently few disklike and domelike heptanuclear Fe^{III} clusters were also reported,¹⁰⁰⁻¹⁰² but they are significantly different from the ones obtained with dmemH . Complexes **4-1** and **4-2** are thus the novel heptanuclear Fe^{III} carboxylate complexes.

4.3.2.3 Structure of $[\text{Fe}_6\text{O}_2(\text{OH})_4(\text{O}_2\text{CBu}^t)_8(\text{dmem})_2]$ (**4-3**)

A labeled representation of complex **4-3** is shown in Figure 4-4(a). Selected interatomic distances and angles are given in Table A-8. Complex **4-3**·2MeCN crystallizes in the triclinic space group $P\bar{1}$ with the asymmetric unit containing two independent Fe_6 clusters, both lying on inversion centers; since the two molecules are essentially superimposable, we show and discuss the structure of only one of them here. The core consists of an $[\text{Fe}_4(\mu_3\text{-O})_2]$ unit (Fe1, Fe1', Fe2 and Fe2') on either side of which is attached a $[\text{Fe}(\mu\text{-OH})_2(\mu\text{-OR})]$ unit containing Fe3; the OH^- ions are O9 and O10 on one side, and their symmetry partners on the other. One OH^- bridge (O10) connects Fe3 to central Fe1 whereas the other (O9) connects to Fe2. The OH^- nature of O9 and O10 was confirmed by BVS calculations,¹⁰³ which gave values of 1.14 for O9 and 1.05 for O10. Peripheral ligation is provided by two dmem^- and eight pivalate groups. There are three types of pivalate binding modes: four are in the common $\eta^1:\eta^1:\mu$ bridging mode, two are in the rare η^2 chelating mode, and the remaining two are in an η^1 terminal mode.

A number of other Fe_6 complexes have been previously reported possessing a variety of metal topologies, such as planar, twisted boat, chair, parallel triangles, octahedral, ladder-like, cyclic, etc.¹⁰⁴ However, the only previous compounds structurally similar to **4-3** are $[\text{Fe}_6\text{O}_2(\text{OMe})_{12}(\text{tren})_2]^{2-}$ and $[\text{Fe}_6\text{O}_2(\text{OR})_8(\text{O}_2\text{CPh})_6]$.^{105,106} Both of the latter complexes contain a central $[\text{Fe}_4(\mu_3\text{-O})_2]^{8+}$ core with an additional Fe atom on each side, as in **4-3**, but the precise means of attachment are different.

4.3.2.4 Structure of $[\text{Fe}_3\text{O}(\text{O}_2\text{CBu}^t)_2(\text{N}_3)_3(\text{dmem})_2]$ (**4-4**)

A labeled representation of **4-4** is provided in Figure 4-4(b). Selected interatomic distances and angles are given in Table A-9. Complex **4-4**· CH_2Cl_2 crystallizes in the monoclinic space group $P2_1/n$. The structure consists of an Fe_3 isosceles triangle bridged by a $\mu_3\text{-O}^{2-}$ ion (O1) with a rare T-shaped geometry, rather than the common trigonal planar geometry usually seen in

triangular metal carboxylates.¹⁰⁷ The Fe1⋯Fe2 and Fe2⋯Fe3 edges are each additionally bridged by an alkoxide O atom of the dmem⁻ ligand and a η¹: η¹: μ pivalate group. As a result, Fe2⋯Fe1 (2.997(1) Å) and Fe2⋯Fe3 (2.980(1) Å) are much shorter than Fe1⋯Fe3 (3.694(2) Å). Similarly, Fe2-O1 (2.070(19) Å) is noticeably longer than Fe1-O1 (1.872(19) Å) and Fe3-O1 (1.865(19) Å). Fe1, Fe2, Fe3 and O1 are co-planar, and O2 and O3 are slightly above and below this plane. A chelating dmem⁻ and a terminal azide on each Fe atom complete the ligation at the metal atoms, which are all near-octahedral. The overall asymmetric Fe₃O is with little precedent in iron chemistry, the only previous discrete example being [Fe₃O(TIEO)₂(O₂CPh)₂Cl₃], where TIEO is 1,1,2-tris(1-methylimidazol-2-yl)ethoxide.^{73,108}

4.3.3 Magnetochemistry of Complexes 4-1 to 4-4

4.3.3.1 Dc Studies

Solid-state, variable-temperature dc magnetic susceptibility data in a 0.1 T field and in the 5.0-300 K range were collected on powdered crystalline samples of **4-1** to **4-4** restrained in eicosane. The obtained data are plotted as $\chi_M T$ vs T in Figure 4-5. For **4-1**·½MeCN, $\chi_M T$ steadily decreases from 6.95 cm³Kmol⁻¹ at 300 K to 4.07 cm³Kmol⁻¹ at 5.0 K. The 300 K value is much less than the spin-only ($g = 2.0$) value of 30.62 cm³Kmol⁻¹ for seven non-interacting Fe^{III} ions, indicating the presence of strong antiferromagnetic interactions. The 5.0 K value suggests an $S = 5/2$ ground state. For **4-2**·2MeCN, $\chi_M T$ steadily decreases from 8.19 cm³Kmol⁻¹ at 300 K to 4.14 cm³Kmol⁻¹ at 34 K, stays essentially constant until 10 K, and then decreases slightly to 3.85 cm³Kmol⁻¹ at 5.0 K. As for **4-1**·½MeCN, this behavior is indicative of antiferromagnetic interactions and an $S = 5/2$ ground state. For **4-3**, $\chi_M T$ increases from 9.73 cm³Kmol⁻¹ at 300 K to a maximum of 14.10 cm³Kmol⁻¹ at 20K and then drops to 12.92 at 5.0 K. The 300 K value is again much less than the spin-only value of 26.25 cm³Kmol⁻¹ expected for six non-interacting Fe^{III} ions, indicating predominantly antiferromagnetic interactions. The increase in $\chi_M T$ as the

temperature then decreases suggests the lowest lying states are of high spin values, and the maximum at 20 K of $14.10 \text{ cm}^3\text{Kmol}^{-1}$ is very close to the spin-only value of $15.00 \text{ cm}^3\text{Kmol}^{-1}$ for an $S = 5$ ground state. The decrease in $\chi_M T$ at the lowest temperatures is very likely due to zero-field splitting (ZFS) within the $S = 5$ ground state and perhaps some weak intermolecular interactions. For **4-4**· $\frac{1}{2}$ CH₂Cl₂, $\chi_M T$ steadily decreases from $5.74 \text{ cm}^3\text{Kmol}^{-1}$ at 300 K to $4.07 \text{ cm}^3\text{Kmol}^{-1}$ at 50 K, and then stays approximately constant until 15 K, below which it decreases slightly to $3.75 \text{ cm}^3\text{Kmol}^{-1}$ at 5.0 K. The latter value suggests an $S = 5/2$ ground state.

To confirm the above ground state spin estimates, variable-field (H) and -temperature magnetization (M) data were collected in the 0.1 to 7.0 T and 1.8-10 K ranges. The resulting data for **4-1**· $\frac{1}{2}$ MeCN are plotted in Figure 4-6 as reduced magnetization ($M/N\mu_B$) vs. H/T , where N is Avogadro's number and μ_B is the Bohr magneton. The saturation value at the highest fields and lowest temperatures is ~ 4.8 , as expected for an $S = 5/2$ and g slightly less than 2; the saturation value should be gS . The data were fit, using the program *MAGNET*⁵³ described elsewhere.⁵⁴⁻⁵⁶ The best-fit for **4-1**· $\frac{1}{2}$ MeCN is shown as the solid lines in Figure 4-6, and was obtained with $S = 5/2$ and either of two sets of parameters, $g = 1.94$ and $D = -0.56 \text{ cm}^{-1}$, or $g = 1.95$ and $D = 0.77 \text{ cm}^{-1}$. Alternative fits with $S = 3/2$ or $7/2$ were rejected because they gave unreasonable values of g and D . It should be noted that it is common to obtain two acceptable fits of magnetization data for a given S value, one with $D > 0$ and the other with $D < 0$. This was indeed the case for the magnetization fits for all of the complexes **4-1** to **4-4** in this work. In order to assess which is the superior fit in these cases, and also to ensure that the true global minimum had been located for each compound, we calculated the root-mean-square error surface for the fits as a function of D and g , and have plotted them as two-dimensional contour plots in Figure 4-7. For **4-1**· $\frac{1}{2}$ MeCN,

the plot clearly shows only the above-mentioned minima with positive and negative D values, with both fits being of comparable quality as shown in Figure 4-7.

For **4-2**·2MeCN, the reduced magnetization plot saturates at ~ 4.5 , again suggesting an $S = 5/2$ ground state. The fit, shown as the solid lines in Figure 4-8(a), gave $S = 5/2$ with either $g = 1.91$ and $D = -0.76 \text{ cm}^{-1}$, or $g = 1.91$ and $D = 0.98 \text{ cm}^{-1}$. The error surface contour plot is shown in Figure 4-8(b) and shows the above minima, with the one with negative D clearly the superior fit since it has a lower (deeper) minimum. Figure 4-8(b) also clearly shows that the fit minimum is a soft one, consistent with a significant uncertainty in the precision of the obtained g and D fit values, which we estimate as ± 0.01 on g and $\pm 5 - 10 \%$ on D .

For **4-3**, the reduced magnetization plot saturates at ~ 9.5 , suggesting an $S = 5$ state with $g < 2$ (Figure 4-9(a)). A satisfactory fit could only be obtained if data collected at fields above 5 T were excluded, suggesting that some low-lying excited states with $S > 5$ are being stabilized by the applied field to the point that they are significantly populated at these temperatures. To avoid this, the data at 6 and 7 T were excluded, and now a good fit was obtained (solid lines in Figure 4-9(a)) with $S = 5$ and either $g = 1.95$ and $D = -0.28 \text{ cm}^{-1}$, or $g = 1.92$ and $D = 0.33 \text{ cm}^{-1}$. The error surface for the fit shows again that the fit with negative D is far superior (Figure 4-9(b)), suggesting this is the true sign of D .

4.3.3.2 Rationalization of the Ground State Spin of **4-1** and **4-3**

It is of interest to try to rationalize the observed ground state spin values of **4-1** to **4-3**. It is assumed that all Fe_2 pairwise exchange interactions are antiferromagnetic, as is essentially always the case for high-spin Fe^{III} , and there will thus be competing antiferromagnetic exchange interactions and spin frustration effects within the many Fe_3 triangular units in these complexes. The ground state of **4-1** is the easiest to rationalize: the discrete Fe_4 butterfly (planar or bent rhombus) topology is known to usually give an $S = 0$ ground state as a result of the

antiferromagnetic interactions along the four outer edges overcoming, and thus frustrating, the diagonal interaction.^{77,109-111} In **4-1**, two such Fe₄ units are fused at body (central) Fe₄ of the two butterfly units, and assuming the same spin alignments as in the discrete Fe₄ molecules, then the ground state spin alignments are predicted to be those shown in Figure 4-10(a), giving an $S = 5/2$ ground state, as observed experimentally. It is worth mentioning here that disklike and domelike heptanuclear amino alkoxo clusters reported in literature have also been shown to possess $S = 5/2$ ground state spin.^{101,102}

The ground state for **4-2** is not so easy to rationalize convincingly because of its high content of triangular units. For **4-3**, the recognizable Fe₄ unit as in **4-1** suggests that the spin of this sub-unit is zero, and then the two Fe atoms Fe₃ and Fe_{3'} above and below would have their spins parallel to each other by both being antiparallel to the spins of Fe₁ and Fe_{1'} as shown in Figure 4-10(b). This would thus rationalize an overall $S = 5$ ground state for **4-3**.

For **4-4**·½CH₂Cl₂, the reduced magnetization saturates at ~4.7, suggesting an $S = 5/2$ ground state and $g < 2$ (Figure 4-11(a)). The fit of the data (solid lines in Figure 4-11(a)) gave $S = 5/2$ with either $g = 1.92$ and $D = -0.69 \text{ cm}^{-1}$, or $g = 1.92$ and $D = 0.82 \text{ cm}^{-1}$. The D vs. g error surface (Figure 4-11(b)) shows that the fit with negative D is again superior suggesting this may be the true sign of D . Since complex **4-4** is only trinuclear, we determined its pairwise Fe₂ exchange interactions by fitting the variable temperature susceptibility data to the appropriate theoretical expression.

4.3.3.3 Determination of the Exchange Interactions in 4-4

The Heisenberg spin Hamiltonian describing the isotropic exchange interactions within an isosceles Fe₃ triangle of C_{2v} symmetry (Figure 4-12(a)) is given by eq. 4-5, where J_a refers to the interactions between Fe₂···Fe₃ and Fe₁···Fe₂, and J_b refers to the Fe₃···Fe₁ interaction; S_i refers

to the spin of atom Fe_i. The energies of the resultant total spin states S_T , which are eigenfunctions of the Hamiltonian in this coupling scheme, are given by eq. 4-6, where $\hat{S}_A = \hat{S}_I + \hat{S}_3$. The overall multiplicity of the spin system is 216 made up of 27 individual spin states ranging from $S_T = 1/2$ to 15/2.

$$\mathcal{H} = -2J_a(\hat{S}_2 \cdot \hat{S}_3 + \hat{S}_2 \cdot \hat{S}_I) - 2J_b(\hat{S}_3 \cdot \hat{S}_I) \quad (4-5)$$

$$E|S_T, S_A\rangle = -J_a[S_T(S_T+1) - S_A(S_A+1)] - J_b[S_A(S_A+1)] \quad (4-6)$$

An expression for the molar paramagnetic susceptibility was derived for this complex using the Van Vleck equation.⁵¹ This was then used to fit the experimental $\chi_M T$ vs T data, with fit parameters J_a, J_b and an isotropic g value (see Appendix D-3). The fit is shown as the solid line in Figure 4-5, which gave $J_a = -3.6 \text{ cm}^{-1}$, $J_b = -45.9 \text{ cm}^{-1}$ and $g = 1.93$. These values identify the ground state as the $|S_T, S_A\rangle = |5/2, 0\rangle$ state shown in Figure 4-12(b), which is in agreement with the reduced magnetization fit.

The marked inequality in the exchange constants, $|J_b| \gg |J_a|$, is as expected on the basis of the iron-oxo bond lengths, where $\text{Fe3-O1} = \text{Fe1-O1} < \text{Fe2-O1}$. A similar situation was also observed in the previous Fe₃ complex with a similar core, $[\text{Fe}_3\text{O}(\text{TIEO})_2(\text{O}_2\text{CPh})_2\text{Cl}_3]$, for which $J_a = -8(4) \text{ cm}^{-1}$ and $J_b = -55(6) \text{ cm}^{-1}$. It has been established that the magnitude of the exchange coupling constant J for an oxo-bridged Fe^{III}₂ unit can be approximately correlated with a single structural parameter P by the equation in eq. 4-7, if the Fe-O-Fe does not alter too much. In this relationship, $A = 8.763 \times 10^{11}$, $B = -12.663$ and P is the shortest superexchange pathway.¹¹² Applying this relationship to complex **4-4** gives $J_a = -12.9 \text{ cm}^{-1}$ and $J_b = -46.4 \text{ cm}^{-1}$, which are in reasonable overall agreement with the experimental values obtained from fitting the susceptibility data, and given that an angular dependence is of lesser importance than the radial one, and is ignored by eq. 4-7. In particular, the acute values of angles of Fe2-O2-Fe3 and Fe2-

O3-Fe1 (96.07(8) and 96.77(8) Å, respectively), which lead to the weak J_a coupling, are significantly smaller than those found in dinuclear Fe^{III}_2 complexes on which the relationship of eq. 4-7 was based and probably reflect a greater angular dependence. The value of J_b is stronger than the magnitude of the antiferromagnetic coupling constant found for the triangular Fe^{III} carboxylate complexes with an approximately equilateral $[\text{Fe}_3\text{O}]^{7+}$ core ($\sim 30\text{cm}^{-1}$),¹¹³ but weaker than the 80-130 cm^{-1} values observed for the $[\text{Fe}_2\text{O}]^{4+}$ and $[\text{Fe}_2\text{O}(\text{O}_2\text{CR})_2]^{2+}$ dinuclear cores.¹¹⁴⁻

116

$$-J = A e^{\text{BP}} \quad (4-7)$$

None of the compounds **4-1** to **4-4** exhibited an out-of-phase AC magnetic susceptibility signal down to 1.8 K in an AC field of 3.5 Oe oscillating with frequencies up to 997 Hz. This indicates that they do not exhibit a large enough barrier (*vs kT*) to exhibit the characteristic signature of slow magnetization relaxation characteristic of single-molecule magnets (SMMs), at least down to 1.8 K.

As discussed above, fits of variable-temperature and variable-field magnetization data are not the most reliable way to obtain the most precise and accurate values of D , or its sign. The magnetization fits suggested D to be negative for **4-2** and **4-3**, but they could not suggest the sign of D for **4-1**. Since the sign and magnitude of D are crucial to the potential ability of a complex to function as a SMM, we desired to better characterize D for these new and relatively rare examples of Fe_x clusters with significant ground state spin values. The perfect technique for this is high-frequency electron paramagnetic resonance spectroscopy.

4.3.4 High-Frequency EPR Spectroscopy

A detailed single-crystal study of representative complexes **4-1**·4MeCN and **4-3**·2MeCN has been carried out by HFEPN spectroscopy. The main overall objective was to measure the ZFS parameters in the spin Hamiltonian of eq. 4-8, which is the same as that in eq. 3-4 except

that it also now includes the rhombic ZFS term, $E(\hat{S}_x^2 - \hat{S}_y^2)$, where E is the rhombic ZFS parameter, and \hat{S}_x and \hat{S}_y are the x and y components of the total spin operator \hat{S} . EPR is a high resolution spectroscopic technique that can be used to investigate the more complete spin Hamiltonian of eq. 4-8, whereas fits of bulk magnetization data are essentially insensitive to inclusion of the rhombic E term.

$$\mathcal{H} = D\hat{S}_z^2 + E(\hat{S}_x^2 - \hat{S}_y^2) + g\mu_B\mu_0\hat{S}\cdot H \quad (4-8)$$

Single-axis angle dependence studies were first performed to roughly determine the orientation of each crystal in the magnetic field. Both complexes **4-1**·4MeCN and **4-3**·2MeCN possess low symmetry structures. Thus, determining the precise symmetry directions represents a highly complex task requiring detailed two-axis rotation studies. However, one can readily obtain basic information from single-axis studies; in particular, the sign of D , which is the crucial factor in whether a particular complex is a SMM.^{100,117}

Figure 4-13(a) displays the angle-dependence of the field positions of the strongest EPR transitions determined from field-swept spectra recorded at 116 GHz and 1.4 K for complex **4-3**·2MeCN; given the low temperature, these data points must correspond to transitions from the lowest-lying m_S levels. Two series of resonances are observed (black and red data points) which shift significantly upon rotating the field, thus providing the clearest evidence for a significant magnetoanisotropy. Both series exhibit 180° periodicity, with virtually identical amplitudes. The source of the two series has a natural explanation for complex **4-3**·2MeCN for which there are two differently oriented molecules in the unit cell. Thus, one naturally expects two distinct EPR signatures, one from each species. The solid curves represent phenomenological fits to the two sets of data, and are intended to capture the qualitative nature of the angle dependence. The phase shift between the two data sets is $75\pm 2^\circ$.

In order to determine the sign of D , frequency- and temperature-dependent data were collected on complex **4-3**·2MeCN with the field oriented along one of the minima in Figure 4-13(a) (191°). Figure 4-13(b) displays the frequency dependence of the angle-dependent peak from Figure 4-13(a), and the inset displays representative spectra taken at higher temperatures. A remarkable feature of the frequency-dependent data is that all peaks lie on a straight line which extrapolates to a finite frequency on the vertical axis, i.e. there is no evidence for curvature in the data. Assuming $|DS| \approx 1.5 \text{ cm}^{-1}$ (from reduced magnetization measurements), one realizes that at least a 3 T magnetic field would be required to overcome the axial term in eq. 4-8. This suggests that the Zeeman interaction commutes with the dominant axial term in eq. 4-8 across the entire range of fields for which data were collected (0.6 to 2 T). In other words, the minima in Figure 4-13(a) and the data in Figure 4-13(b) correspond to field orientations parallel to, or very close to the z axes of the two species. This is quite coincidental, as the sample orientation was not previously known.

Figure 4-14(a) displays a simulation of the Zeeman diagram for a SMM with $S = 5$, i.e. with $D < 0$. As can clearly be seen, the transition from the lowest-lying m_S level occurs at the lowest field; the excited state transitions all occur at higher field. This agrees qualitatively with the data in Figure 4-13(b). Therefore, we can conclude that D is negative, and that **4-3** is a SMM. The intercept on the frequency axis in Figure 4-13(b) (66.4 GHz) then corresponds to the ZFS between the ground and first excited state. If one assumes that $S = 5$, then $D = -0.25(1) \text{ cm}^{-1}$, which is in reasonable agreement with the value from the magnetization fits ($D = -0.28(3) \text{ cm}^{-1}$). Because of the uncertainty in the precise orientation of the field relative to the easy-axis, we cannot quote a precise value for g ; the main purpose of the HFEPR measurements was to unambiguously determine the sign of D , which was successfully achieved.

Single-axis rotation experiments for complex **4-1**·4MeCN were not able to locate the axial direction (presumably the rotation plane was inclined significantly with respect to the magnetic z -axis of the molecule). Nevertheless, we were able to locate the plane perpendicular to the axial direction (xy plane) from measurements similar to those shown in Figure 4-13(a). Thus, all of the temperature- and frequency- dependent studies were carried out with the field aligned within the magnetic xy plane of the Fe_7 molecule. Only a single molecular species was anticipated for complex **4-1**·4MeCN, making interpretation of the data more straightforward. Furthermore, this complex exhibits sharper EPR peaks, as evident from Figure 4-15(a), which shows the high-field xy -plane spectra obtained at different temperatures and a frequency of 197 GHz. Comparison of the data in Figure 4-14(a) with the simulated Zeeman diagram in Figure 4-13(b) reveals that complex **4-1** *cannot be* a SMM because its D value is positive. As can be seen from Figure 4-14(b), upon reducing the temperature, the stronger EPR peaks should be observed at the lowest fields for an easy-plane magnet ($D > 0$) when the field is applied parallel to the easy (xy) plane; this is exactly what is seen in the data. If **4-1**·4MeCN were a SMM, the intensities of the five transitions (labeled a to e in the Figure 4-15(a)) would be reversed.

Figure 4-15(b) displays the results of a multi-frequency study for complex **4-1**·4MeCN, with the field applied within the easy plane; the temperature was 20 K. Fits (solid curves) to the positions of the EPR peaks were performed via exact diagonalization of eq. 4-8. It is very clear from Figure 4-15(b) that the data lie on a series of lines that are *not* evenly spaced, and exhibit significant curvature at low frequencies and fields. These trends are a characteristic of xy -plane spectra obtained for a system with a significant uniaxial anisotropy (both positive and negative D), due to the competition between the orthogonal Zeeman and ZFS (DS_z^2) interactions. In other words, the data displayed in Figure 4-15(b) provide further confirmation that the field is in the

xy-plane and, when combined with the temperature dependence in Figure 4-15(a), also confirm the positive sign of D . The fit assumes an $S = 5/2$ ground state, and yields $g = 2.0$ and $D = +0.62 \text{ cm}^{-1}$. This value again agrees reasonably well with that from the reduced magnetization studies ($D = +0.77(7) \text{ cm}^{-1}$). The low value of g obtained from the reduced magnetization fits can be explained as the limitation of the fitting program Magnet which assumes axial anisotropy; therefore HFEPR data is more reliable. The best fit to the data required the inclusion of a rhombic ZFS anisotropy, $|E| \geq 0.067 \text{ cm}^{-1}$. This is not unexpected, given the low symmetry of the molecule. Our estimate of E represents a lower bound, as the orientation of the field within the easy plane was not known. Low-temperature EPR measurements on domelike Fe_7 cluster yield a D value of 0.28 cm^{-1} ,¹⁰¹ which is considerably lower than calculated for **4-1**·4MeCN. This can be attributed to their different structural arrangements leading to the differences in single-ion anisotropy and spin-spin anisotropy.

4.4 Conclusions

The tridentate N, N, O ligand dmem^- has proven to be a very fruitful new route to a variety of new Fe^{III} clusters comprising two Fe_7 and one Fe_6 species, depending on the identity of the carboxylate employed. The latter point emphasizes the exquisite sensitivity of the reaction product on a variety of reaction conditions and reagents employed. For example, even though complexes **4-1** and **4-2** have the same formula except for the identity of the carboxylate, the structures of the two complexes are very different. It was interesting that the azide ligands in **4-4** were only terminal rather than bridging, but yet nevertheless fostered formation of a product very different from that of the non-azide product **4-3**.

Fitting of the reduced magnetization vs H/T data established that **4-1**, **4-2** and **4-4** each possess an $S = 5/2$ ground state spin, whereas **4-3** has an $S = 5$ ground state. The complexes all serve to clearly emphasize again how ground state spin values of significant magnitude can result

from spin frustration effects even though all the pairwise exchange interaction constants are antiferromagnetic. The magnetization fits of **4-1** to **4-4** serve to emphasize, however, the difficulty of determining the sign of D for Fe^{III} clusters from such measurements, making it thus difficult to predict whether a given cluster might be a new example of a SMM. Representative complexes **4-1** and **4-3** were therefore studied by HFEPR spectroscopy, a tremendously powerful and sensitive technique, not least for obtaining accurate and precise values for spin Hamiltonian parameters such as D , including an unequivocal determination of its sign. From these measurements, we concluded that complex **4-3** has $D < 0$ and thus is a potential SMM, whereas complex **4-1** has $D > 0$ and is not. In fact, none of the compounds **4-1** to **4-4** exhibited an out-of-phase ac magnetic susceptibility signal down to 1.8 K in ac frequencies up to 997 Hz. Even for **4-3**, which was confirmed by HFEPR spectroscopy to have a negative D value, its $S = 5$ and $D = -0.25 \text{ cm}^{-1}$ gives a barrier (U) to magnetization relaxation with an upper value of $U = S^2|D| = 6.3 \text{ cm}^{-1}$ (= 9.0 K). Remembering that the true or effective barrier (U_{eff}) is less than U due to quantum tunneling of the magnetization (QTM) through the barrier, it is not surprising that no sign of slow relaxation is seen at temperatures above 1.8 K. Studies significantly below 1 K will be required in order to better investigate the potential SMM behavior. Nevertheless, the present work does establish interesting new examples of Fe_x clusters with significant ground state S values and negative D values.

Finally, the preparation of complexes **4-1** to **4-4** again serves to emphasize the utility of alkoxide-containing chelates in polynuclear metal cluster chemistry.

Table 4-1. Crystallographic data for **4-1**·4MeCN, **4-2**·MeCN, **4-3**·2MeCN and **4-4**·CH₂Cl₂

	4-1	4-2	4-3	4-4
Formula ^a	C ₉₉ H ₁₀₁ Fe ₇ N ₈ O ₂₈	C ₃₈ H ₇₀ Fe ₇ N ₅ O ₂₈	C ₅₈ H ₁₁₆ Fe ₆ N ₆ O ₂₄	C ₂₅ H ₅₄ Cl ₂ Fe ₃ N ₁₃ O ₇
Fw, g/mol ^a	2241.83	1435.94	1616.67	887.26
Space group	<i>C2/c</i>	<i>P</i> $\bar{1}$	<i>P</i> $\bar{1}$	<i>P2</i> ₁ / <i>n</i>
<i>a</i> , Å	18.6028(14)	12.4586(8)	12.9769(10)	12.3260(8)
<i>b</i> , Å	26.8523(14)	13.5495(9)	14.4142(11)	25.3961(17)
<i>c</i> , Å	20.8083(13)	18.690(12)	23.9082(18)	13.1400(9)
α , °	90	70.636(2)	87.6240(10)	90
β , °	103.879(2)	79.731(2)	88.5620(10)	99.1490(10)
γ , °	90	73.099(2)	66.0920(10)	90
<i>V</i> , Å ³	10090.9(11)	2836.2(3)	4084.7(5)	4060.9(5)
<i>Z</i>	4	2	2	4
<i>T</i> , K	173(2)	173(2)	173(2)	173(2)
Radiation, Å ^b	0.71073	0.71073	0.71073	0.71073
ρ_{calc} , g/cm ³	1.476	1.681	1.311	1.451
μ , mm ⁻¹	1.058	1.828	1.105	1.244
<i>R</i> 1 ^{c,d}	0.0457	0.0463	0.0415	0.0497
<i>wR</i> 2 ^e	0.0899	0.0927	0.1009	0.1023

^a Including solvate molecules. ^b Graphite monochromator. ^c $I > 2\sigma(I)$. ^d $R1 = \Sigma(|F_o| - |F_c|) / \Sigma|F_o|$. ^e $wR2 = [\Sigma[w(F_o^2 - F_c^2)^2] / \Sigma[w(F_o^2)^2]]^{1/2}$, $w = 1/[\sigma^2(F_o^2) + [(ap)^2 + bp]$, where $p = [\max(F_o^2, O) + 2F_c^2]/3$.

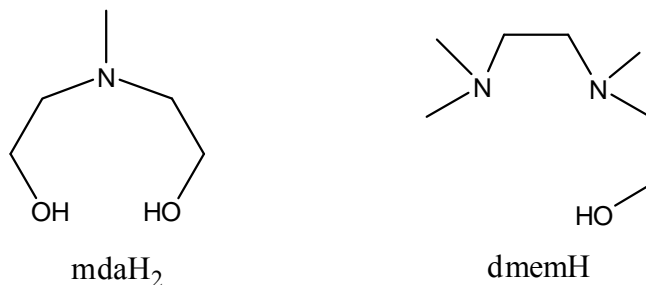


Figure 4-1. Structure of ligands: mdaH₂ and dmemH.

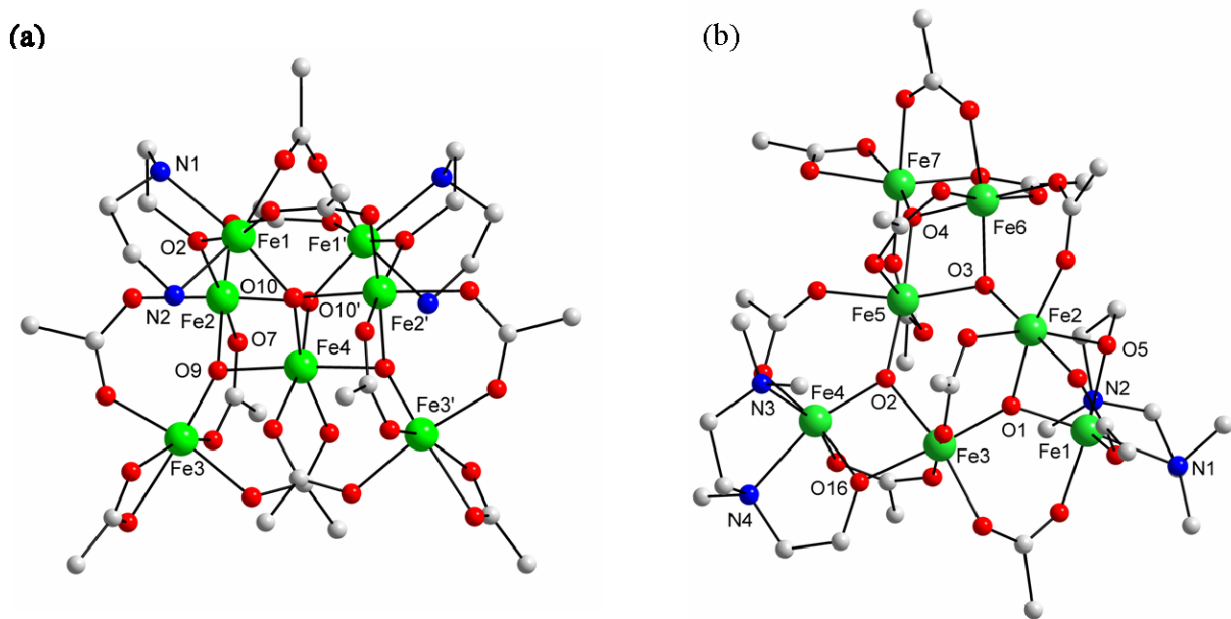


Figure 4-2. (a) Labeled representation of the structure of **4-1**. Hydrogen atoms and phenyl rings (except for the *ipso* carbon atoms) have been omitted for clarity. The C_2 symmetry axis is approximately vertical. Color code: Fe^{III} , green; O, red; N, blue; C, grey. (b) Labeled representation of the structure of **4-2**. Hydrogen atoms have been omitted for clarity. Color code: Fe^{III} , green; O, red; C, grey; N, blue

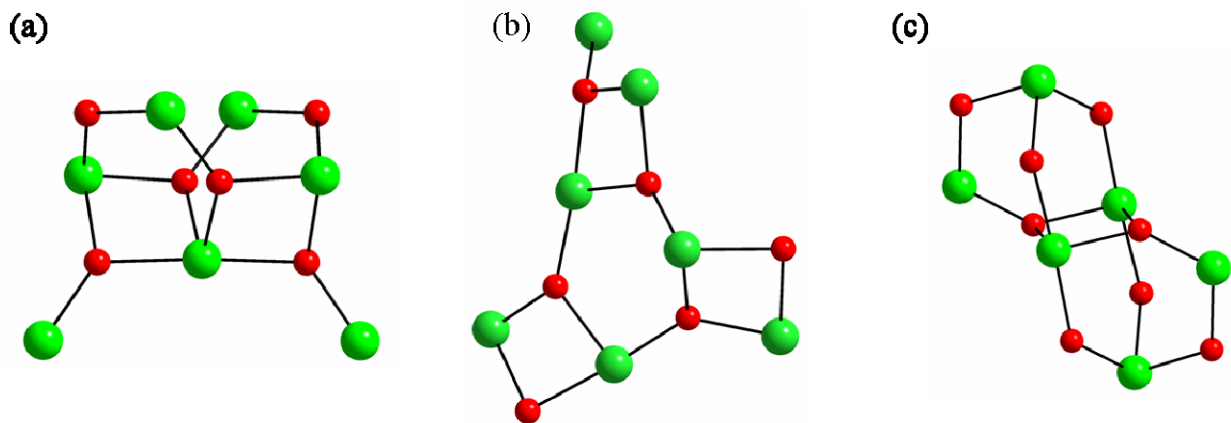


Figure 4-3. Comparison of cores of **4-1** (a), **4-2** (b), and **4-3** (c). Color code: Fe^{III} , green; O, red

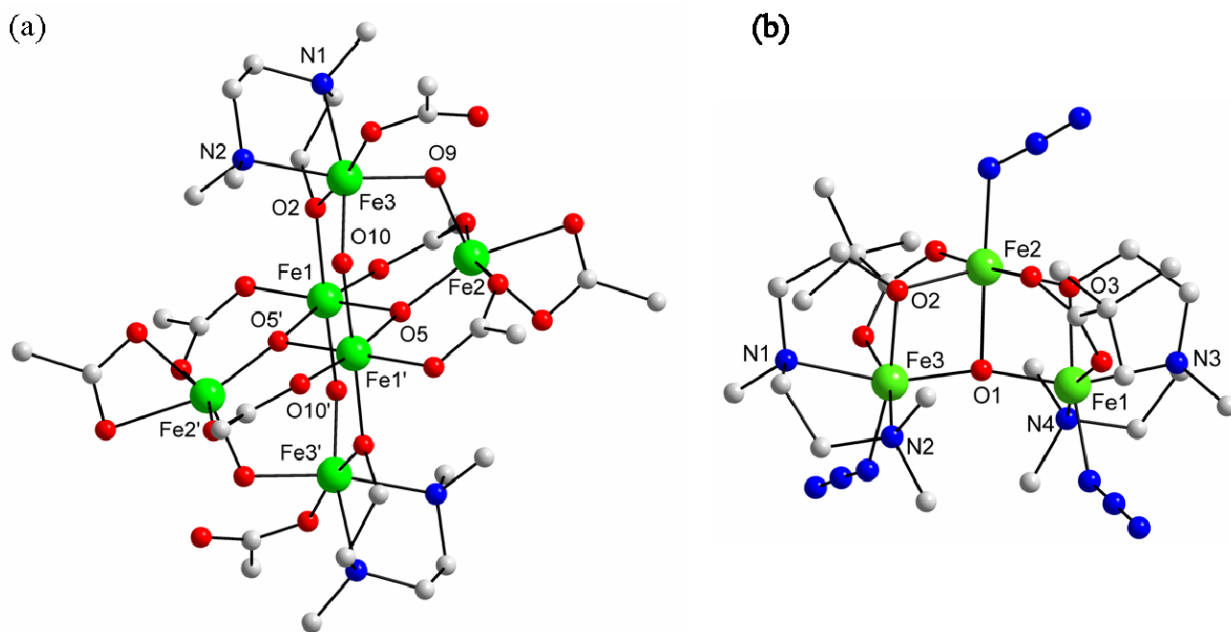


Figure 4-4. (a) Labeled representation of the centrosymmetric structure of **4-3**. Hydrogen atoms and methyl groups on pivalate groups have been omitted for clarity. Color code: Fe^{III}, green; O, red; C, grey; N, blue. (b) Labeled representation of the structure of **4-4**. Hydrogen atoms have been omitted for clarity. Color code: Fe^{III}, green; O, red; C, grey; N, blue.

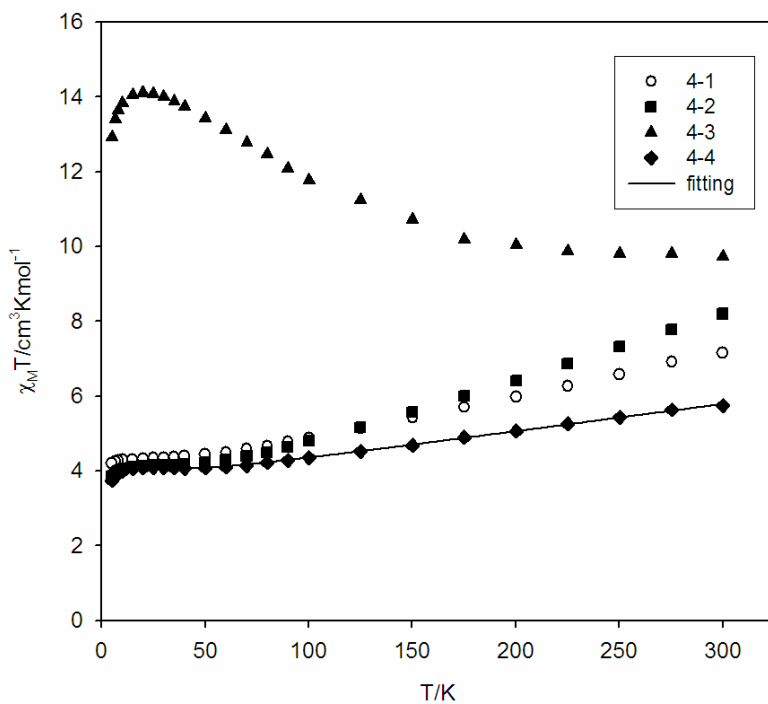


Figure 4-5. Plots of $\chi_M T$ vs T for complexes **4-1** (○), **4-2** (■), **4-3** (▲) and **4-4** (◆). The solid line is the fit of the data for **4-4**; see the text for the fit parameters.

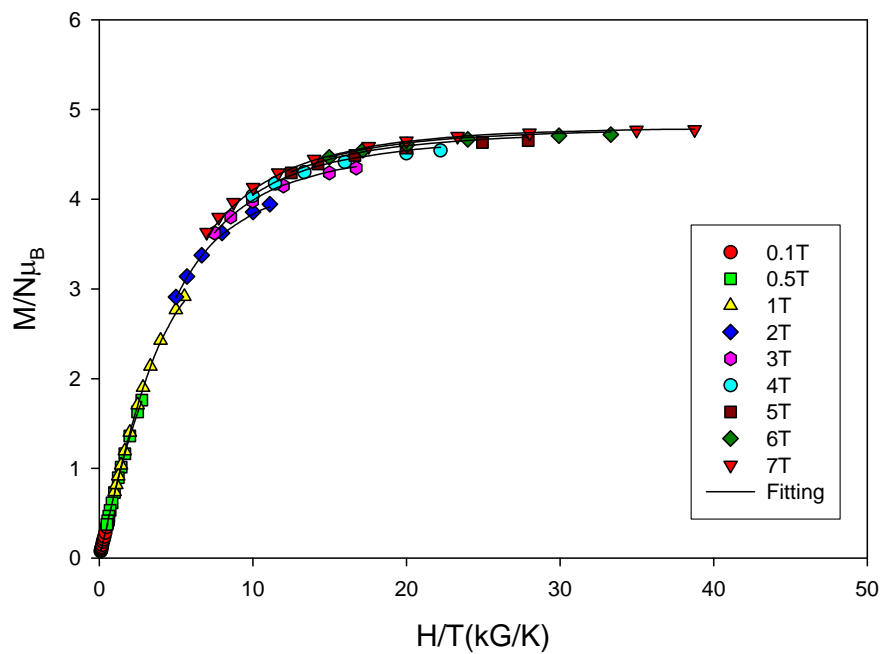


Figure 4-6. Plot of reduced magnetization ($M/N\mu_B$) vs H/T for complex **4-1**· $\frac{1}{2}$ MeCN. The solid lines are the fit of the data; see the text for the fit parameters.

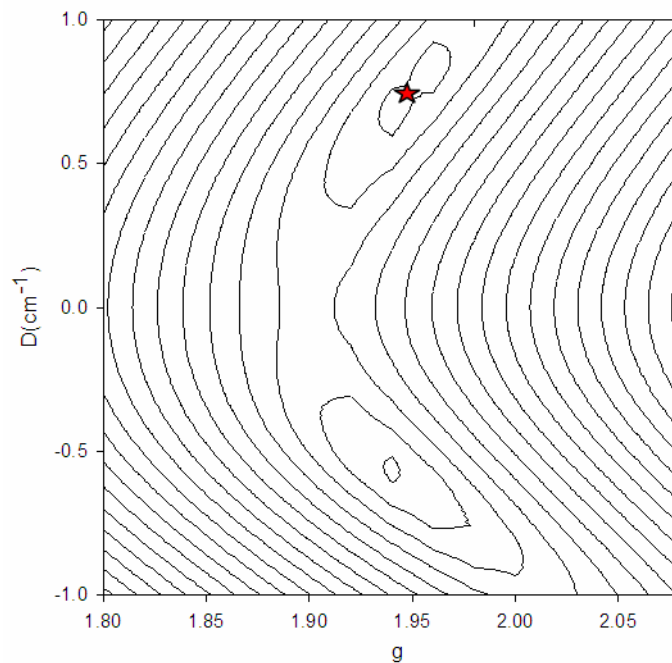


Figure 4-7. Two-dimensional contour plot of the fitting error surface vs D and g for **4-1**· $\frac{1}{2}$ MeCN.

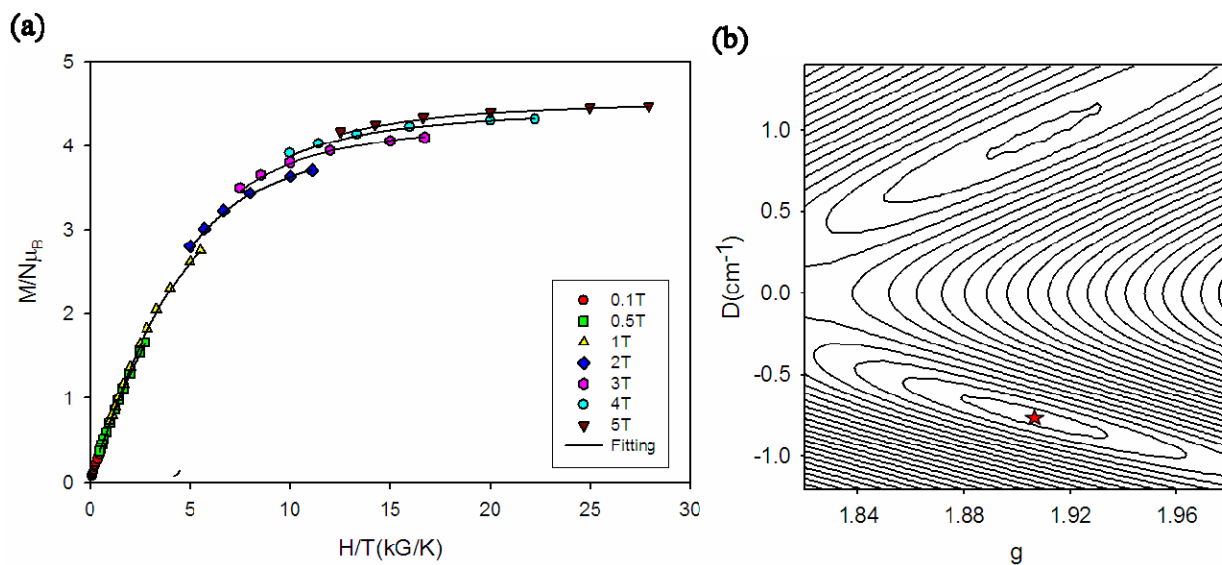


Figure 4-8. (a) Plot of reduced magnetization ($M/N\mu_B$) vs H/T for complex **4-2·2MeCN**. The solid lines are the fit of the data; see the text for the fit parameters. (b) Two-dimensional contour plot of the fitting error surface vs D and g for **4-2·2MeCN**.

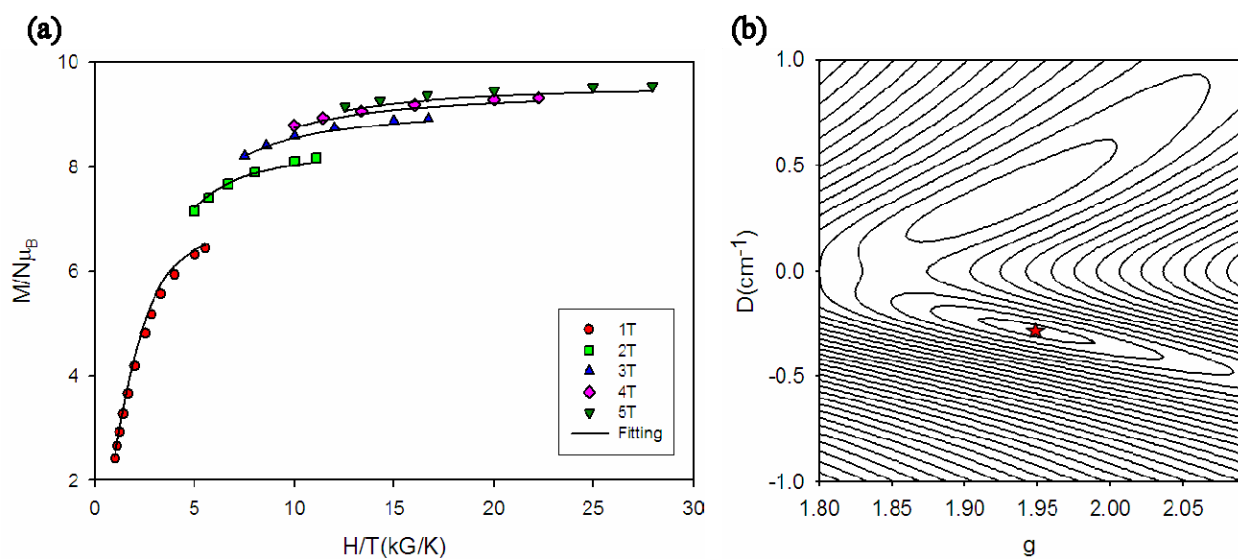


Figure 4-9. (a) Plot of reduced magnetization ($M/N\mu_B$) vs H/T for complex **4-3**. The solid lines are the fit of the data; see the text for the fit parameters. (b) Two-dimensional contour plot of the fitting error surface vs D and g for **4-3**.

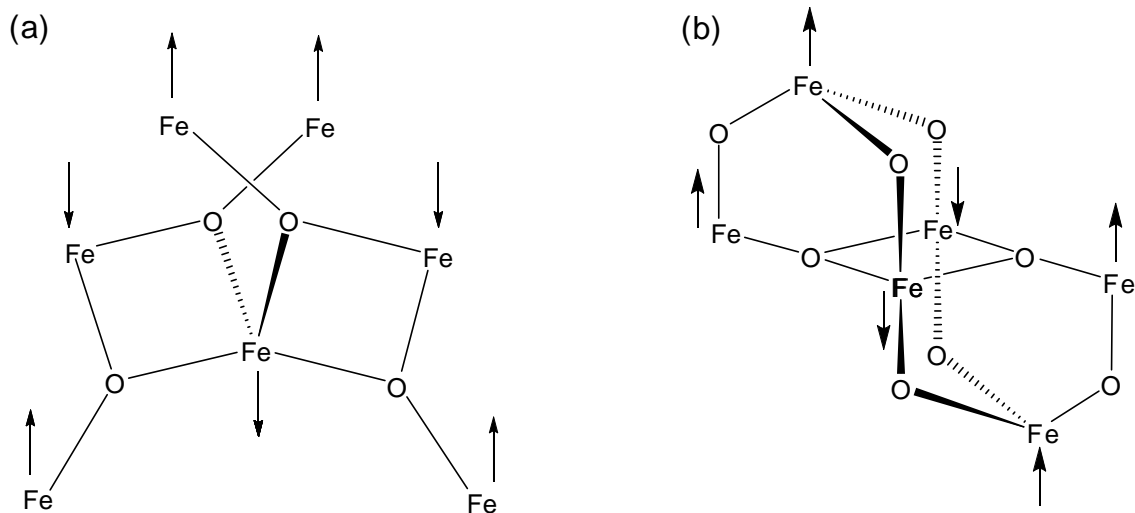


Figure 4-10. Rationalization of the ground state spin of (a) **4-1** and (b) **4-3**.

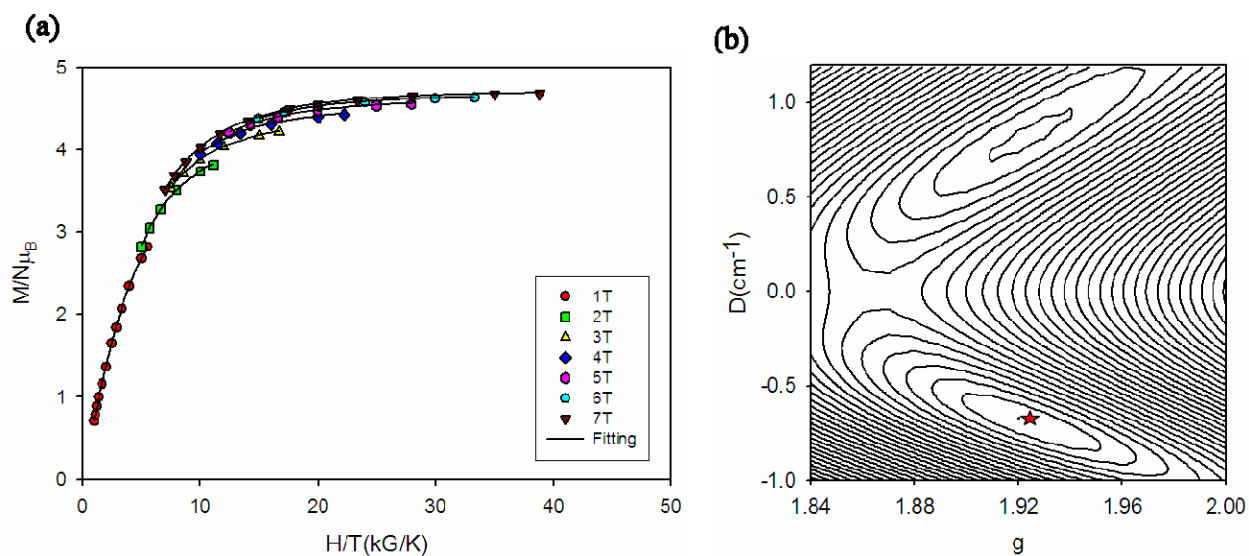


Figure 4-11. (a) Plot of reduced magnetization ($M/N\mu_B$) vs H/T for **4-4**· $\frac{1}{2}$ CH₂Cl₂. The solid lines are the fit of the data; see the text for the fit parameters (b) Two-dimensional contour plot of the fitting error surface vs D and g for **4-4**· $\frac{1}{2}$ CH₂Cl₂.

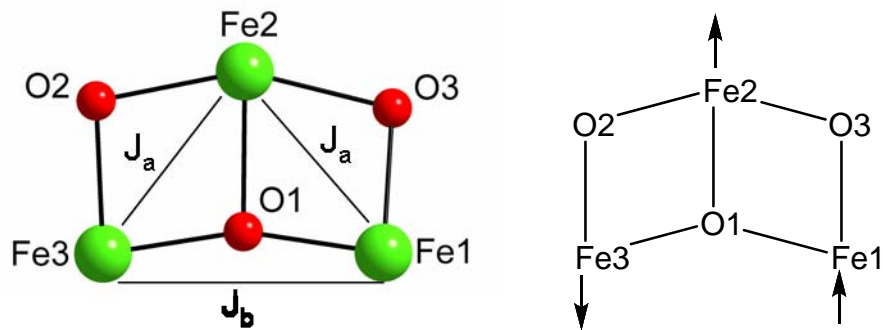


Figure 4-12. (left) The core of **4-4** defining the pairwise exchange interactions. (right) Rationalization of the ground state spin of **4-4**.

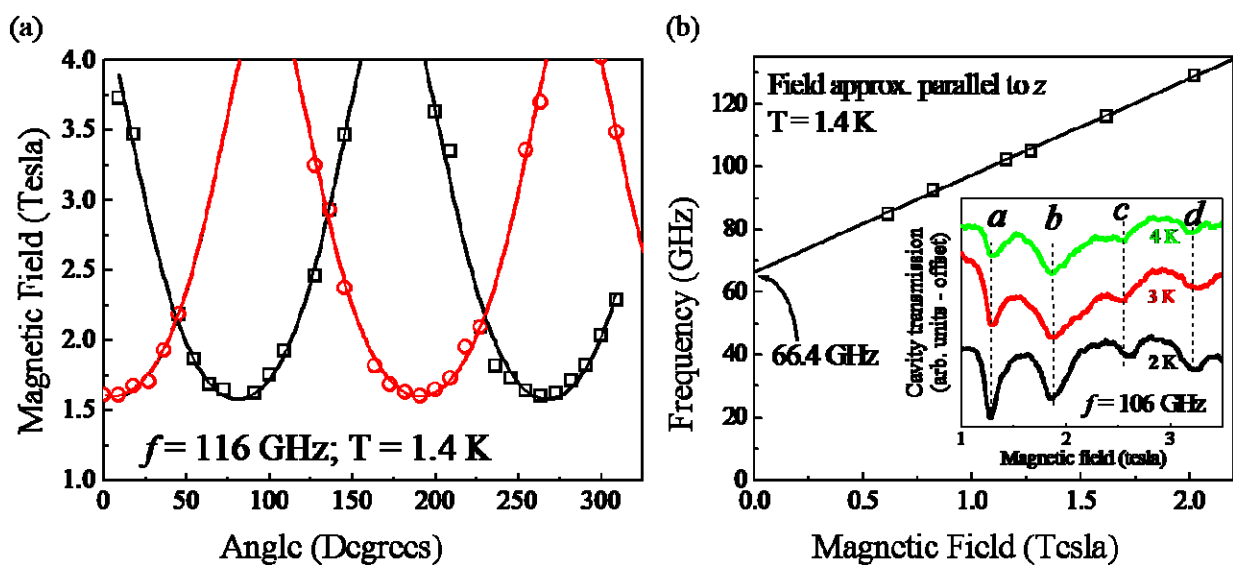


Figure 4-13. (a) Plot of the HFEP R peak positions for **4-3-2MeCN** obtained from angle-dependent studies at 116 GHz and 1.4 K. (b) Frequency dependence for **4-3-2MeCN** with the field oriented along one of the minima in Figure 4-13(a) (191°); the inset displays temperature-dependent spectra obtained at 106 GHz.

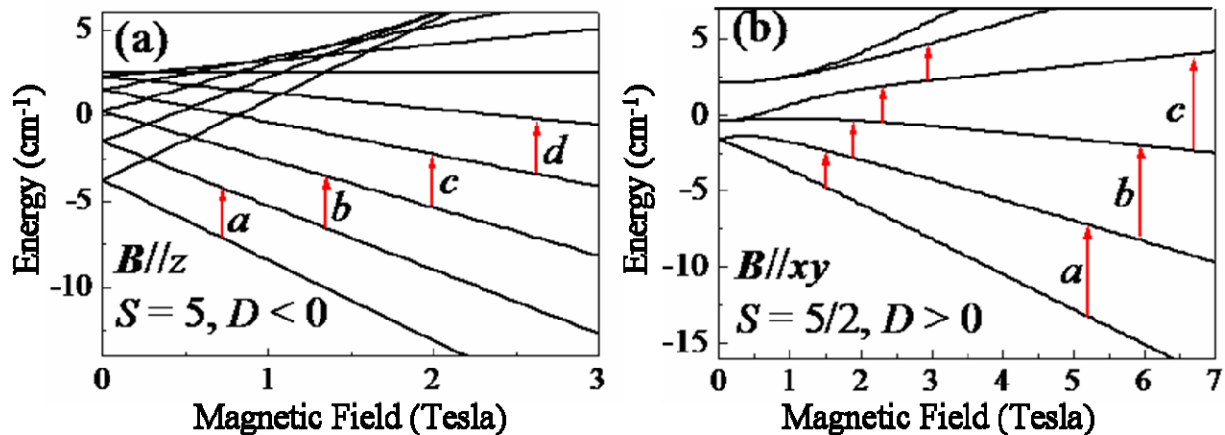


Figure 4-14. (a) Simulated Zeeman diagram for a spin $S = 5$ system with $D < 0$ with the magnetic field parallel to the z axis. The red lines (labeled *a* to *d*) correspond to the transitions shown in the inset of Figure 4-13(b). (b) Simulated Zeeman diagram for a spin $S = 5/2$ system with $D > 0$ with the magnetic field parallel to the xy plane. The red lines (labeled *a* to *c*) correspond to the transitions shown in Figure 4-15(a).

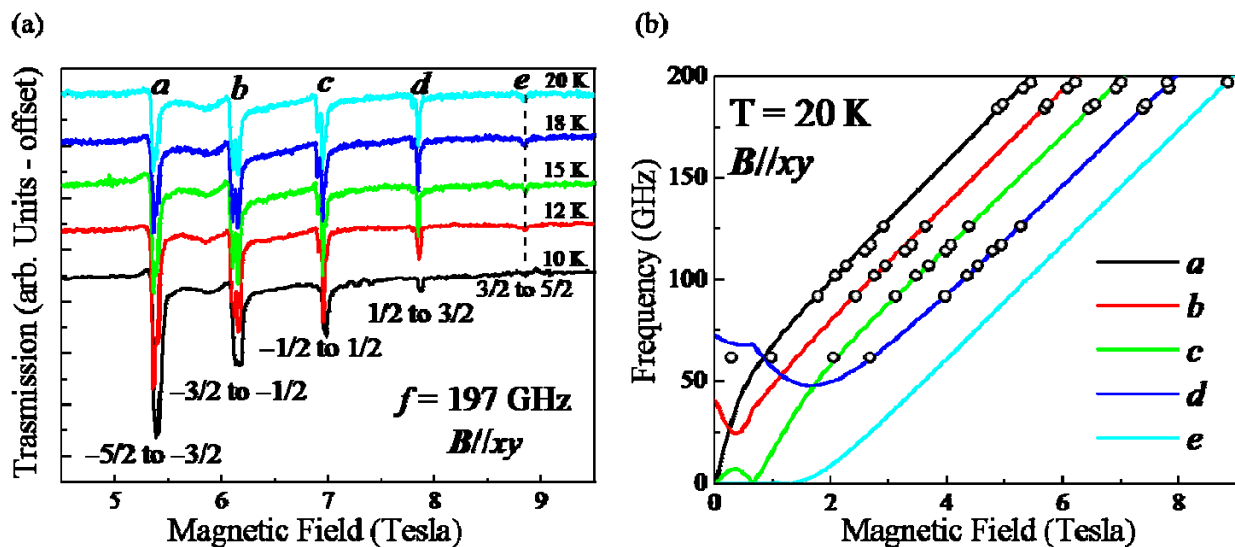


Figure 4-15. (a) Temperature dependent spectra for 4-1·4MeCN at 197 GHz with the DC magnetic field applied within the easy (xy) plane. (b) Easy-plane peak positions for 4-1·4MeCN plotted versus frequency at 20 K. The solid lines are simulations using the ZFS parameters given in the main text

CHAPTER 5
A NEW N, N, O CHELATE FOR TRANSITION METAL CLUSTER CHEMISTRY: Fe₅ AND
Fe₆ CLUSTERS FROM THE USE OF 6-HYDROXYMETHYL-2, 2' BIPYRIDINE

5.1 Introduction

There continues to be a great interest by many groups around the world in the synthesis and study of 3d transition metal cluster compounds, not least for the structural aesthetics possessed by such species. Other reasons for this interest are varied. For Fe^{III} chemistry, for example, there are bioinorganic areas of relevance such as the great desire to understand and model the assembly of the polynuclear iron core of the iron storage protein ferritin.^{26,30,31} There is also a materials interest in that high nuclearity iron compounds can sometimes exhibit unusual and occasionally novel magnetic properties, with some of them even being examples of single-molecule magnets (SMMs);^{13,20,82} the latter are molecules with a combination of a relatively large ground state spin and a significant magnetoanisotropy of the easy-axis (Ising) type.^{20,118} That Fe^{III} is one area where high nuclearity species are often encountered is as expected from the high charge-to-size ratio of this oxidation state and the resulting propensity to favor oxide-bridged multinuclear products. Indeed, the formation of the Fe/O/OH core of ferritin that was mentioned as a bioinorganic area of interest is merely an extreme example of such polynuclear chemistry. As a result, many large Fe^{III} clusters have been reported to date with nuclearities up to 22.^{72,75,87,119}

Although the exchange interactions between Fe^{III} centers are almost always antiferromagnetic, certain Fe_x topologies can nevertheless possess large ground state spin values as a result of spin frustration. The latter is here defined in its more general sense of competing exchange interactions of comparable magnitude, preventing (frustrating) the preferred antiparallel alignment of all spins, and thus giving larger ground state spin values than might be expected.⁷⁴⁻⁷⁸ In some cases, as mentioned above, the compounds can behave as SMMs. This is

the case for clusters such as $[\text{Fe}_8\text{O}_2(\text{OH})_{12}(\text{tacn})_6]^{8+}$,^{81,82,120} and $[\text{Fe}_4(\text{OMe})_6(\text{dpm})_6]^{79}$ for example.

For the above reasons and more, there is a continuing search for new synthetic methods that can yield new polynuclear Fe/O clusters. One approach that has proven successful in this regard is the use of alcohol-containing chelate groups that, on deprotonation, can provide alkoxide groups that are excellent bridging units and thus foster formation of high nuclearity products.^{74,86,88} In chapter 4, we reported the use of deprotonated 2- $\{[2-(\text{dimethylamino})\text{ethyl}]\text{-methylamino}\}$ ethanol (dmemH; Figure 5-1) as a new and flexible N,N,O – chelate for the synthesis of Fe_3 , Fe_6 and two Fe_7 complexes, some of which possess novel Fe_x topologies. As part of these continuing efforts to synthesize new Fe_x clusters, we have now turned to another potential chelating group that has also never before been employed, to our knowledge, in transition metal chemistry. This is 6-hydroxymethyl-2,2'-bipyridine (hmbpH; Figure 5-1), whose deprotonated form, like dmem^- , would be a potential N,N,O-chelate, but a more rigid one than dmem^- . In fact, hmbpH was selected as a ‘fusion’ of two chelates that have each proven a rich source of M_x , and particularly Fe_x , species in the past, 2,2'-bipyridine and the anion of 2-(hydroxymethyl)pyridine (hmpH).^{77,109,121-126} We thus considered it a potentially viable route to new clusters, and probably of a different type than previously encountered with bpy or hmp^- separately. Our first investigations with hmbpH have been in Fe^{III} chemistry and we have indeed found it to lead to new structural types of products. We herein report the syntheses, crystal structures and magnetochemical characterization of new Fe_5 and Fe_6 molecular species.¹²⁷

5.2 Experimental Section

5.2.1 Syntheses

All preparations were performed under aerobic conditions using reagents and solvents as received. $[\text{Fe}_3\text{O}(\text{O}_2\text{CPh})_6(\text{H}_2\text{O})_3](\text{NO}_3)$, $[\text{Fe}_3\text{O}(\text{O}_2\text{CBu}^\dagger)_6(\text{H}_2\text{O})_3](\text{NO}_3)$ and

$[\text{Fe}_3\text{O}(\text{O}_2\text{CMe})_6(\text{H}_2\text{O})_3](\text{NO}_3)$ were synthesized as reported elsewhere.⁹⁶ The known organic molecule hmbpH was synthesized, according to Figure 5-2, using previously reported procedures.¹²⁸⁻¹³⁰

$[\text{Fe}_5\text{O}_2(\text{OH})(\text{O}_2\text{CMe})_5(\text{hmbp})_3](\text{ClO}_4)_2$ (5-1). To a stirred solution of $\text{Fe}(\text{ClO}_4)_3 \cdot x\text{H}_2\text{O}$ (0.19 g, 0.54 mmol) and sodium acetate (0.18 g, 2.0 mmol) in EtOH (15 mL) was added hmbpH (0.10 g, 0.54 mmol). The resulting orange solution was stirred for 3 hours at room temperature, during which time precipitated an orange solid. The precipitate was collected by filtration, washed with EtOH, and dried. It was then dissolved in MeCN (15 mL), filtered, and the filtrate layered with Et_2O . X-ray quality crystals of **5-1**·5MeCN slowly grew over five days in 18% yield. These were collected by filtration, washed with MeCN and dried *in vacuo*; dried solid analyzed as solvent-free. Anal. Calcd (Found) for **5-1** ($\text{C}_{43}\text{H}_{43}\text{N}_6\text{Cl}_2\text{Fe}_5\text{O}_{24}$): C, 37.48 (37.05); H, 3.14 (3.12); N, 6.09 (5.89). Selected IR data (cm^{-1}): 1599(s), 15429(s), 1490(m), 1402(s), 1175(m), 1068(m), 1025(m), 937(w), 820(w), 777(m), 719(s), 663(s), 600(w), 547(w), 463(m).

$[\text{Fe}_6\text{O}_2(\text{OH})_2(\text{O}_2\text{CPh})_6(\text{hmbp})_4](\text{NO}_3)_2$ (5-2). An orange-red solution of $[\text{Fe}_3\text{O}(\text{O}_2\text{CPh})_6(\text{H}_2\text{O})_3](\text{NO}_3)$ (0.14 g, 0.14 mmol) in MeCN (20 mL) was treated with hmbpH (0.05 g, 0.27 mmol). The solution was stirred for 2 hours, filtered, and the orange-red filtrate left undisturbed to concentrate slowly by evaporation. X-ray quality, orange-red crystals of **5-2**·3MeCN·H₂O formed over five days in 25% yield. These were collected by filtration, washed with MeCN and dried *in vacuo*. Anal. Calcd (Found) for **5-2**·H₂O ($\text{C}_{86}\text{H}_{70}\text{N}_{10}\text{Fe}_6\text{O}_{27}$): C, 51.37 (51.34); H, 3.51 (3.37); N, 6.97 (6.82). Selected IR data (cm^{-1}): 3426(br), 1602(m), 1539(s), 1490(m), 1433(s), 1350(m), 1299(w), 1254(w), 1226(w), 1088(s), 1044(s), 779(m), 690(m), 662(m), 623(m), 556(m), 429(w).

[Fe₆O₂(OH)₂(O₂CMe)₆(hmbp)₄](NO₃)₂ (5-3). An orange-red solution of [Fe₃O(O₂CMe)₆(H₂O)₃](NO₃) (0.11 g, 0.17 mmol) in MeCN (20 mL) was treated with hmbpH (0.065 g, 0.35 mmol). The solution was stirred for 2 hours, filtered, and the orange-red filtrate left undisturbed to concentrate slowly by evaporation. Orange-red crystals formed over five days in 15% yield. These were collected by filtration, washed with MeCN and dried *in vacuo*. Anal. Calcd (Found) for **5-3**·H₂O (C₅₆H₅₈N₁₀Fe₆O₂₇): C, 41.06 (41.13); H, 3.57 (3.61); N, 8.55 (8.33). Selected IR data (cm⁻¹): 3399(br), 1601(m), 1546(s), 1491(m), 1438(s), 1384(s), 1256(w), 1225(w), 1166(w), 1090(w), 1037(s), 905(w), 833(w), 781(m), 664(s), 645(m), 556(m), 434(w), 413(w).

[Fe₆O₂(OH)₂(O₂CBu^t)₆(hmbp)₄](NO₃)₂ (5-4). An orange-red solution of [Fe₃O(O₂CBu^t)₆(H₂O)₃](NO₃) (0.13 g, 0.14 mmol) in MeCN (20 ml) was treated with hmbpH (0.05 g, 0.27 mmol). The solution was stirred for 2 hours, filtered, and the orange-red filtrate layered with Et₂O. Orange crystals slowly grew over four days in 20% yield. Anal. Calcd (Found) for **5-4**·H₂O (C₇₄H₉₄N₁₀Fe₆O₂₇): C, 47.01 (46.64); H, 5.01 (4.76); N, 7.41 (7.50). Selected IR data (cm⁻¹): 3408(br), 3077(w), 2962(m), 1601(w), 1539(s), 1484(m), 1459(m), 1425(s), 1383(s), 1361(s), 1300(w), 1227(m), 1163(w), 1091(w), 1036(m), 900(w), 832(w), 785(m), 663(s), 600(m), 553(m), 434(m).

5.2.2 X-ray Crystallography

Data were collected by Dr. Khalil A. Abboud on a Siemens SMART PLATFORM equipped with a CCD area detector and a graphite monochromator utilizing Mo-K α radiation (λ = 0.71073 Å). Suitable crystals of **5-1**·5MeCN and **5-2**·3MeCN·H₂O were attached to glass fibers using silicone grease and transferred to a goniostat where they were cooled to 173 K for data collection. Cell parameters were refined using up to 8192 reflections. A full sphere of data (1850 frames) was collected using the ω -scan method (0.3° frame width). The first 50 frames were re-

measured at the end of the data collection to monitor instrument and crystal stability (maximum correction on I was $<1\%$). Absorption corrections by integration were applied based on measured indexed crystal faces. The structure was solved by the direct methods in *SHELXTL6*,⁴⁶ and refined on F^2 using full-matrix least-squares. The non-H atoms were treated anisotropically, whereas the hydrogen atoms were calculated in ideal positions and refined as riding on their respective carbon atoms.

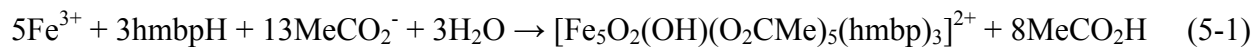
In **5-1**·5MeCN, the asymmetric unit consists of the Fe_5 cluster, two ClO_4^- anions, and five MeCN solvent molecules. The latter molecules were disordered and could not be modeled properly, thus program SQUEEZE,⁶⁸ a part of the PLATON package of crystallographic software, was used to calculate the solvent disorder area and remove its contribution to the overall intensity data. One of the ClO_4^- anions was disordered and was refined in two positions with their site occupation factors refined dependently. Both disorder components are H-bonded to the hydroxyl proton on O4. A total of 720 parameters were refined in the final cycle of refinement using 42942 reflections with $I > 2\sigma(I)$ to yield R_1 and wR_2 of 6.11 and 17.05%, respectively.

In **5-2**·3MeCN·H₂O, the asymmetric unit consists of a half Fe_6 cluster, one and a half MeCN molecules, one NO_3^- anion disordered over three positions, and a half water molecule which exists counter to one of the half NO_3^- anions. One nitrate exists with 50% occupancy, while the other has all but one O atom disordered. The latter was refined in two parts with occupation factors fixed at 20 and 30%. A total of 633 parameters were refined in the final cycle of refinement using 15661 reflections with $I > 2\sigma(I)$ to yield R_1 and wR_2 of 4.85 and 12.76%, respectively. Unit cell data and structure refinement details for the two compounds are listed in Table 5-1.

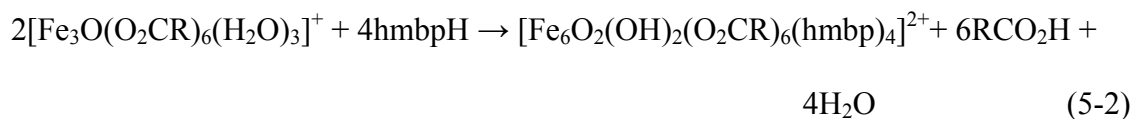
5.3 Results and Discussion

5.3.1 Syntheses

The reaction of $\text{Fe}(\text{ClO}_4)_3$ with hmbpH and sodium acetate in a 1:1:4 ratio in EtOH gave an orange precipitate that after recrystallization from MeCN/Et₂O gave crystals of the novel pentanuclear cluster $[\text{Fe}_5\text{O}_2(\text{OH})(\text{O}_2\text{CMe})_5(\text{hmbp})_3](\text{ClO}_4)_2$ (**5-1**). The acetate acts as the proton acceptor in this reaction, as well as providing ligand groups. The same product was also obtained using MeCN as the reaction solvent, but the precipitate was found to be contaminated with some other solid products. The formation of **5-1** is summarized in eq. 5-1. Decreasing the amount of acetate from 4 to 2 equiv reduces the reaction yield, as expected from eq. 5-1. Other reactions with small variations in the $\text{Fe}^{3+}:\text{hmbpH}:\text{MeCO}_2^-$ ratio also gave compound **5-1**.



Many synthetic procedures to polynuclear iron clusters rely on the reaction of $[\text{Fe}_3\text{O}(\text{O}_2\text{CR})_6(\text{H}_2\text{O})_3]^+$ species with a potentially chelating ligand,^{84,91,92,98,119,125,126} and we thus also explored this starting material for reactions with hmbpH. In such reactions, the $[\text{Fe}_3\text{O}]^{7+}$ core of the trinuclear iron complex serves as a useful building block for higher nuclearity species, but we have occasionally found that the exact nuclearity and structure of the product is sensitive to the identity of the carboxylate employed. An example of this is the reaction of $[\text{Fe}_3\text{O}(\text{O}_2\text{CR})_6-(\text{H}_2\text{O})_3]^+$ species with dmemH.⁹³ Thus, we have also studied the product of reactions with hmbpH as a function of the carboxylate, but in this case have found that we obtain the same structural type in each case. Thus, the reaction of $[\text{Fe}_3\text{O}(\text{O}_2\text{CR})_6(\text{H}_2\text{O})_3]^+$ (R = Ph, Me, Bu^t) with 1 - 3 equiv of hmbpH in MeCN led to the isolation of the corresponding hexanuclear cluster $[\text{Fe}_6\text{O}_2(\text{OH})_2(\text{O}_2\text{CR})_6(\text{hmbp})_4]^{2+}$ (R = Ph (**5-2**), Me (**5-3**), Bu^t (**5-4**)). The formation of this family is summarized in eq. 5-2.



5.3.2 Description of Structures

5.3.2.1 Structure of $[\text{Fe}_5\text{O}_2(\text{OH})(\text{O}_2\text{CMe})_5(\text{hmbp})_3](\text{ClO}_4)_2$ (**5-1**)

A labeled representation of complex **5-1** is shown in Figure 5-3. Selected interatomic distances and angles are listed in Table A-10. Complex **5-1** crystallizes in monoclinic space group $P2_1/c$. The core can be described as consisting of a $[\text{Fe}_4(\mu_3\text{-O})_2]^{8+}$ butterfly-like subunit (Fe1, Fe3, Fe4 and Fe5), on the top of which is attached a $[\text{Fe}(\mu\text{-OH})(\mu\text{-OR})_3]$ unit containing Fe2. There is an O atom monoatomically bridging Fe2 to each of the four Fe atoms of the butterfly. Three of these O atoms (O3, O5, O6) are the alkoxide arms of the three hmbp⁻ groups, and the fourth is the OH⁻ ion (O4). The protonated OH⁻ nature of O4 was confirmed by bond valence sum (BVS) calculations,^{103,131} which gave a value of 1.09. The bipyridyl portions of two hmbp⁻ groups chelate one each to the two wingtip Fe atoms, Fe1 and Fe3, while the third chelates Fe2. Peripheral ligation about the core is then completed by five acetate groups in the common $\eta^1 : \eta^1 : \mu$ - bridging mode. It is interesting to note that bpy itself will react with Fe^{III} in the presence of carboxylate groups to give the Fe₄ butterfly complexes of formula $[\text{Fe}_4\text{O}_2(\text{O}_2\text{CR})_7(\text{bpy})_2]^+$ with the two bpy groups attached at the wingtip Fe atoms.⁷⁷ Thus, the bpy ‘fragments’ of the hmbp⁻ chelates are giving the analogous Fe₄ butterfly unit, but the alkoxide arms also then foster attachment of the fifth Fe atom. The core of complex **5-1** is unprecedented in pentanuclear Fe^{III} chemistry. Indeed, there are relatively few pentanuclear Fe^{III} complexes in the literature, and these have Fe₅ topologies such as a square pyramid, a centered tetrahedron, and a partial cubane extended at one face by a partial adamantane unit.¹³²⁻¹⁴¹

5.3.2.2 Structure of $[\text{Fe}_6\text{O}_2(\text{OH})_2(\text{O}_2\text{CPh})_6(\text{hmbp})_4](\text{NO}_3)_2$ (**5-2**)

A labeled representation of complex **5-2** is shown in Figure 5-4, and selected interatomic distances and angles are listed in Table A-11. Complex **5-2** crystallizes in triclinic space group $P\bar{1}$. The core can be described as a modification of the structure of **5-1**, and consists of a central $[\text{Fe}_4(\mu_3\text{-O})_2]^{8+}$ flattened-butterfly unit (Fe2, Fe2', Fe3 and Fe3') on either side of which is attached a $[\text{Fe}(\mu\text{-OH})(\mu\text{-OR})_2]$ unit containing Fe1 and Fe1'. There are now four hmbp⁻ groups, two again on the wingtip positions of the butterfly unit, and one each on Fe1 and Fe1'. Unlike **28**, there are now only three monoatomically-bridging O atoms linking Fe1 to the butterfly unit, two hmbp⁻ alkoxide arms (O3', O9) and the OH⁻ group (O7). The OH⁻ nature of O7 was again confirmed by BVS calculations, which gave a value of 1.16. The peripheral ligation about the $[\text{Fe}_6\text{O}_2(\text{OH})_2(\text{hmbp})_4]^{8+}$ core is completed by six benzoate groups, four in the $\eta^1 : \eta^1 : \mu$ -bridging mode and two in an η^1 -terminal mode. The main overall difference between the core structures of **5-1** and **5-2** is that one of the wingtip hmbp⁻ groups of **5-1** has rotated by 180°, bringing its alkoxide arm to the opposite side of the molecule from the fifth Fe atom and thus allowing attachment of a sixth Fe atom.

A number of other Fe₆ complexes have been reported in the literature, and these possess a variety of metal topologies such as planar, twisted boat, chair, parallel triangles, octahedral, ladder-like, cyclic, etc.¹⁰⁴ However, the only previous compounds somewhat structurally similar to **5-2** are $[\text{Fe}_6\text{O}_2(\text{OMe})_{12}(\text{tren})_2]^{2-}$,¹⁰⁵ $[\text{Fe}_6\text{O}_2(\text{OR})_8(\text{O}_2\text{CPh})_6]^{106}$ and $[\text{Fe}_6\text{O}_2(\text{OH})_2(\text{O}_2\text{CBu}^t)_8(\text{dmem})_2]$.⁹³ In these compounds there is again a central $[\text{Fe}_4(\mu_3\text{-O})_2]^{8+}$ core with an additional Fe atom on each side (as in **5-2**), but the precise means by which the latter are connected to the Fe₄ unit are different from the situation in **5-2**.

5.3.3 Magnetochemistry of Complexes 5-1 to 5-4

5.3.3.1 Dc Studies

Solid-state, variable-temperature dc magnetic susceptibility data in a 0.1 T field and in the 5.0-300 K range were collected on powdered crystalline samples of **5-1** to **5-4** restrained in eicosane. The obtained data are plotted as $\chi_M T$ vs T in Figure 5-5. For **5-1**, $\chi_M T$ steadily decreases from 6.69 cm³mol⁻¹K at 300 K to 4.01 cm³mol⁻¹K at 5.0 K. The 300 K value is much less than the spin-only ($g = 2$) value of 21.87 cm³mol⁻¹K for five non-interacting Fe^{III} ions, indicating the presence of strong antiferromagnetic interactions, as expected for oxo-bridged Fe^{III} systems. The 5.0 K value of 4.01 cm³mol⁻¹K suggests a spin $S = 5/2$ ground state.

The $\chi_M T$ vs T plots for the three complexes **5-2** to **5-4** in Figure 5-5 are very similar, indicating a minimal influence of the different carboxylate groups and supporting the conclusion that not just their formulations are identical but also their structures. $\chi_M T$ for **5-2**·H₂O, **5-3**·H₂O and **5-4**·H₂O increases from 11.88, 11.11 and 11.51 cm³mol⁻¹K at 300 K to a maximum of 14.95, 14.52 and 15.07 cm³mol⁻¹K at 30 K, and then decreases very slightly to 14.65, 14.35 and 14.91 cm³mol⁻¹K respectively at 5.0 K. The $\chi_M T$ at 300 K is again much less than the spin-only value of 26.25 cm³mol⁻¹K expected for six non interacting Fe^{III} ions indicating the presence of strong antiferromagnetic interactions. However, the increase in $\chi_M T$ with decreasing temperature suggests that the lowest lying spin states are of high spin values, and the near-plateau value of 14.6 - 14.9 cm³mol⁻¹K at low temperatures is very close to the spin- only value of 15.0 cm³mol⁻¹K for an $S = 5$ ground state. The small decrease in $\chi_M T$ at the lowest temperatures is very likely due to the zero-field splitting (ZFS) within the $S = 5$ ground state and perhaps some weak intermolecular interactions. The differences in $\chi_M T$ vs T for the three complexes are almost certainly just reflecting small differences in g values, intramolecular exchange coupling constants (J), zero-field splitting parameters (D), and intermolecular antiferromagnetic

interactions, but the overall almost identical $\chi_M T$ vs T plots indicates these factors are nevertheless almost identical for **5-2** to **5-4**.

To confirm the above ground state spin estimates, variable-field (H) and -temperature magnetization (M) data were collected in the 0.1 to 7.0 T and 1.8 to 10 K ranges. The resulting data for **5-1** are plotted in Figure 5-6(a) as reduced magnetization ($M/N\mu_B$) vs. H/T , where N is Avogadro's number and μ_B is the Bohr magneton. The saturation value at the highest fields and lowest temperatures is ~ 4.86 , as expected for an $S = 5/2$ ground state and g slightly less than 2; the saturation value should be gS in the absence of complications from low-lying excited states. The data were fit, using the program *MAGNET*,⁵³ by diagonalization of the spin Hamiltonian matrix assuming only the ground state is populated, incorporating axial anisotropy ($D\hat{S}_z^2$) and Zeeman terms, and employing a full powder average. The corresponding spin Hamiltonian is given by eq. 5-3, where \hat{S}_z is the easy-axis spin operator, g is the electronic g factor, μ_0 is the vacuum permeability, and H is the applied field. The last term in eq. 5-3 is the Zeeman energy associated with an applied magnetic field.

$$\mathcal{H} = D\hat{S}_z^2 + g\mu_B\mu_0\hat{S}\cdot H \quad (5-3)$$

The best-fit for **5-1** is shown as the solid lines in Figure 5-6(a), and was obtained with $S = 5/2$ and either of the two sets of parameters: $g = 1.96$ and $D = 0.75 \text{ cm}^{-1}$, or $g = 1.95$ and $D = -0.59 \text{ cm}^{-1}$. Alternative fits with $S = 3/2$ or $7/2$ were rejected because they gave unreasonable values of g and D . It is common to obtain two acceptable fits of magnetization data for a given S value, one with $D > 0$ and the other with $D < 0$, since magnetization fits are not very sensitive to the sign of D . This was indeed the case for the magnetization fits for all complexes **5-1** to **5-4**. In order to assess which is the superior fit in all these cases, and also to ensure that the true global minimum had been located for each compound, we calculated the root-mean-square error surface

for the fits as a function of D and g . For **5-1**, the error surface (Figure 5-6(b)) clearly shows only two minima with positive and negative D values, with both fits being of comparable quality.

The reduced magnetization plots saturate at 9.78 for **5-2**·H₂O, 9.64 for **5-3**·H₂O and 9.88 for **5-4**·H₂O, suggesting an $S = 5$ ground state and $g < 2$. The best fit for **5-2**·H₂O is shown as the solid lines in Figure 5-7(a, top), and was obtained with $S = 5$ and either $g = 2.00$ and $D = 0.36$ cm⁻¹, or $g = 1.97$ and $D = -0.20$ cm⁻¹. In this case, the fit error surface (Figure 5-7b, top) clearly shows that the fit with positive D is far superior, suggesting that this is the true sign of D . The best fit for **5-3**·H₂O was obtained with $S = 5$ and either $g = 1.98$ and $D = 0.46$ cm⁻¹, or $g = 1.94$ and $D = -0.21$ cm⁻¹. For **5-4**·H₂O, the best fit was with $S = 5$ and either $g = 2.02$ and $D = 0.36$ cm⁻¹, or $g = 1.99$ and $D = -0.19$ cm⁻¹. The corresponding figures and the two-dimensional D vs g error plots for **5-3**·H₂O and **5-4**·H₂O are provided in Figure 5-7 (middle and bottom respectively).

5.3.3.2 Rationalization of the Ground State Spin

It is interesting to try to rationalize the observed ground state spin values of **5-1** and **5-2**. It is assumed that all Fe₂ pairwise exchange interactions are antiferromagnetic, as is essentially always the case for high-spin Fe^{III}, and there will thus be competing antiferromagnetic exchange interactions and spin frustration effects within the many Fe₃ triangular units in these complexes. The ground state of **5-1** is the easiest to rationalize: the discrete Fe₄ butterfly (rhombus) topology is known to usually give an $S = 0$ ground state as a result of the antiferromagnetic interactions along the four outer (wingtip-body) edges overcoming, and thus frustrating, the diagonal (body-body) interaction.^{77,109-111,142,143} The structure of **5-2** comprises such an Fe₄ unit with an additional Fe above it, and assuming the same spin alignments as in the discrete Fe₄ molecules, then the ground state spin alignments are predicted to be those shown in Figure 5-8(a), giving the $S = 5/2$ ground state observed experimentally. Note that whether the spin of the fifth Fe atom is

aligned parallel to the wingtip spins (as shown) or parallel to the body spins, an $S = 5/2$ ground state will still result as long as the interactions within the butterfly are stronger than those between it and the fifth Fe atom. This seems reasonable given that the interactions within the butterfly involve monoatomically bridging oxide ions. For **5-2**, we can again rationalize the ground state, using a simple extension of the argument for **5-1**, on the basis of a central $S = 0$ planar-butterfly unit coupling with the fifth and sixth Fe atoms as shown in Figure 5-8(b). This will give an overall $S = 5$ ground state for **5-2** as observed experimentally. It should be noted that we have sought to rationalize the ground states of **5-1** and **5-2** on the basis of previous observations for the Fe_4 butterfly units, and with as straightforward a description as possible. Thus, we have not invoked intermediate spin alignments of individual spins. In reality, the spin alignments leading to the observed $S = 5/2$ and 5 ground states could be more complicated than shown in Figure 5-8.

None of the compounds exhibited an out-of-phase ac magnetic susceptibility signal down to 1.8 K in an ac field of 3.5 Oe oscillating with frequencies up to 997 Hz, indicating that they do not exhibit a barrier large enough *vs* kT , down to 1.8 K at least, to exhibit slow relaxation of their magnetization vectors, i.e. they are not single-molecule magnets. This is not surprising that the D values for **5-2** to **5-4** were concluded to be positive, whereas negative D values are required to yield the easy-axis (Ising) anisotropy necessary for SMMs. For **5-1**, we could not conclude the sign of D : assuming it is negative, the combination of $S = 5/2$ and $D = -0.59 \text{ cm}^{-1}$ would yield an upper limit to the magnetization relaxation barrier (U) of $U = (S^2 - 1/4)|D| = 3.5 \text{ cm}^{-1} = 5.1 \text{ K}$. Remembering that the actual or effective barrier (U_{eff}) is significantly less than U , it is not surprising that even with a negative D complex **5-1** does not display slow relaxation down to 1.8

K. Studies at much lower temperatures would be required to search for what would at best be a tiny barrier.

5.4 Conclusions

We have reported the initial use of a new N,N,O - based tridentate chelate in coordination chemistry, one that amalgamates the chelating property of 2,2'-bipyridine (bpy) with the chelating/bridging properties of the anion of 2-(hydroxymethyl)pyridine (hmpH). The resulting hmbp⁻ has been employed in Fe^{III} chemistry, and it has provided clean access to four new polynuclear Fe^{III} clusters **5-1** to **5-4**. The structures of **5-2** to **5-4** are concluded to be the same, given their identical formulation and almost superimposable magnetic properties. Note that identical formulation by itself does not mean identical structure: we reported two compounds in chapter 4, [Fe₇O₄(O₂CPh)₁₁(dmem)₂] (**4-1**) and [Fe₇O₄(O₂CMe)₁₁(dmem)₂] (**4-2**) that have the same formula (except for the carboxylate) but very different structures.

The structures of **5-1** and **5-2** show the manifestation of the 'hybrid' bpy/hmp⁻ nature of hmbp⁻ in that the bpy portion gives an Fe₄ butterfly subunit, as does bpy itself, while the alkoxide arm acts as an additional bridging group and raises the nuclearity to five or six. As a result, the complexes have significant ground state spin values of $S = 5/2$ and 5, respectively.

Table 5-1. Crystallographic Data for **5-1**·5MeCN and **5-2**·3MeCN·H₂O.

	5-1	5-2
Formula ^a	C ₅₃ H ₅₈ Cl ₂ Fe ₅ N ₁₁ O ₂₄	C ₉₂ H ₇₉ Fe ₆ N ₁₃ O ₂₇
Fw, g/mol ^a	1583.25	2133.77
Space group	<i>P2</i> ₁ / <i>c</i>	<i>P</i> $\bar{1}$
<i>a</i> , Å	21.6352(2)	13.8233(6)
<i>b</i> , Å	13.4154(6)	14.0671(6)
<i>c</i> , Å	23.1971(11)	14.2856(6)
α , °	90	65.175(2)
β , °	102.456(2)	70.147(2)
γ , °	90	89.561(2)
<i>V</i> , Å ³	6574.4(5)	2341.55(17)
<i>Z</i>	4	1
<i>T</i> , K	173(2)	173(2)
λ , Å ^b	0.71073	0.71073
ρ_{calc} , g/cm ³	1.600	1.512
μ , mm ⁻¹	1.244	0.990
<i>R</i> 1 ^{c,d}	0.0611	0.0487
<i>wR</i> 2 ^e	0.1705	0.1276

^a Including solvate molecules. ^b Graphite monochromator. ^c $I > 2\sigma(I)$. ^d $R1 = \Sigma(|F_o| - |F_c|) / \Sigma|F_o|$. ^e $wR2 = [\Sigma[w(F_o^2 - F_c^2)^2] / \Sigma[w(F_o^2)^2]]^{1/2}$, $w = 1/[\sigma^2(F_o^2) + (ap)^2 + bp]$, where $p = [\max(F_o^2, O) + 2F_c^2]/3$.

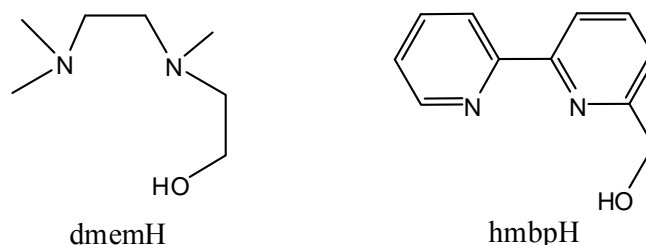


Figure 5-1. Structure of ligands.

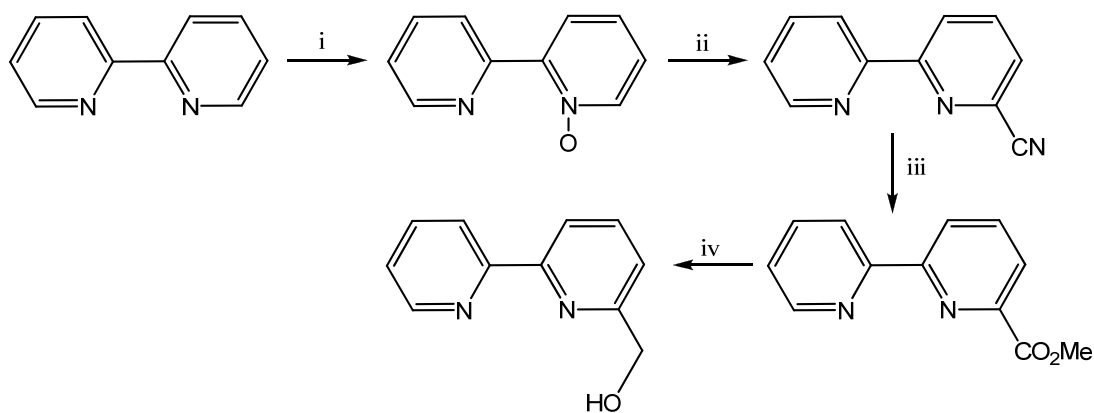


Figure 5-2. Synthetic scheme for hmbpH (i) H₂O₂, CF₃CO₂H (Ref. 117) (ii) Me₃SiCN, PhCOCl, CH₂Cl₂ (Ref. 118) (iii) NaOMe, MeOH (Ref. 118) (iv) (a) NaBH₄, EtOH (b) H₂SO₄, H₂O (Ref. 119)

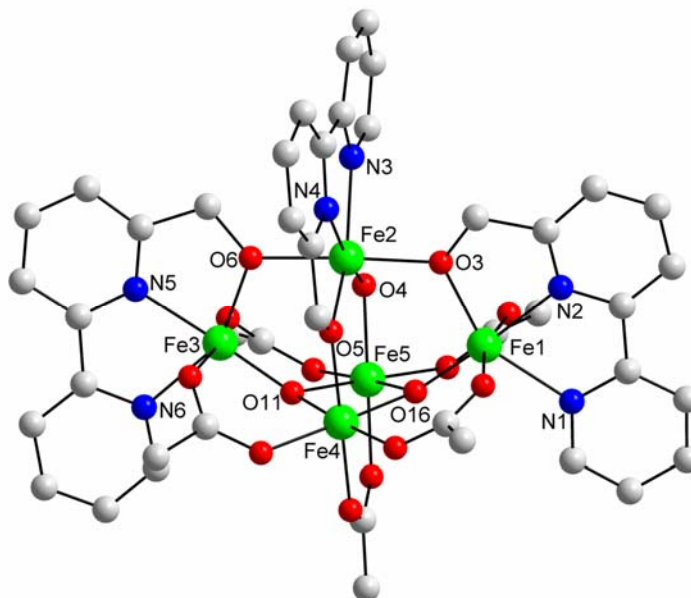


Figure 5-3. Labeled representation of the structure of **5-1**. Hydrogen atoms have been omitted for clarity. Color code: Fe^{III}, green; O, red; N, blue; C, grey.

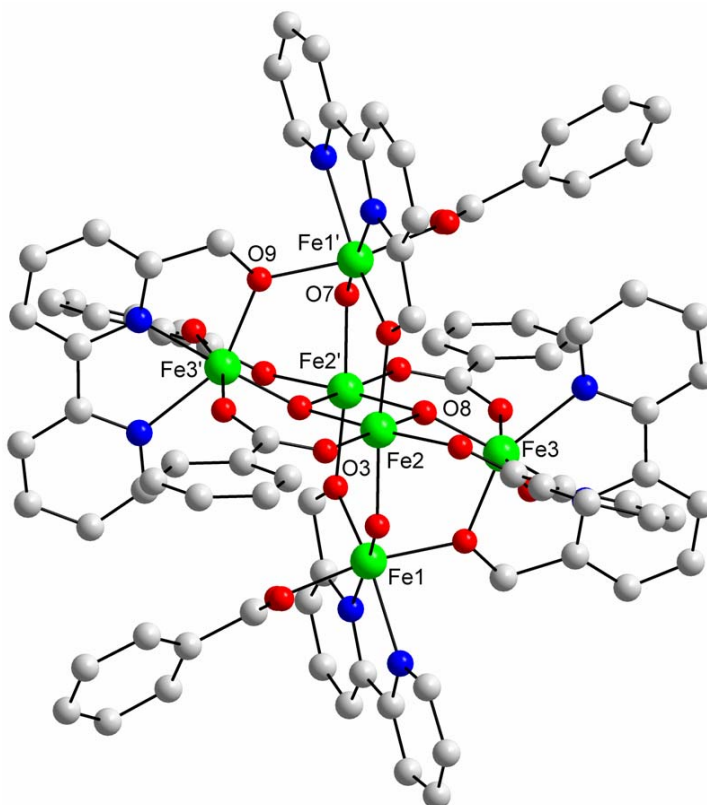


Figure 5-4. Labeled representation of the structure of **5-2**. Hydrogen atoms have been omitted for clarity. Color code: Fe^{III}, green; O, red; C, grey; N, blue.

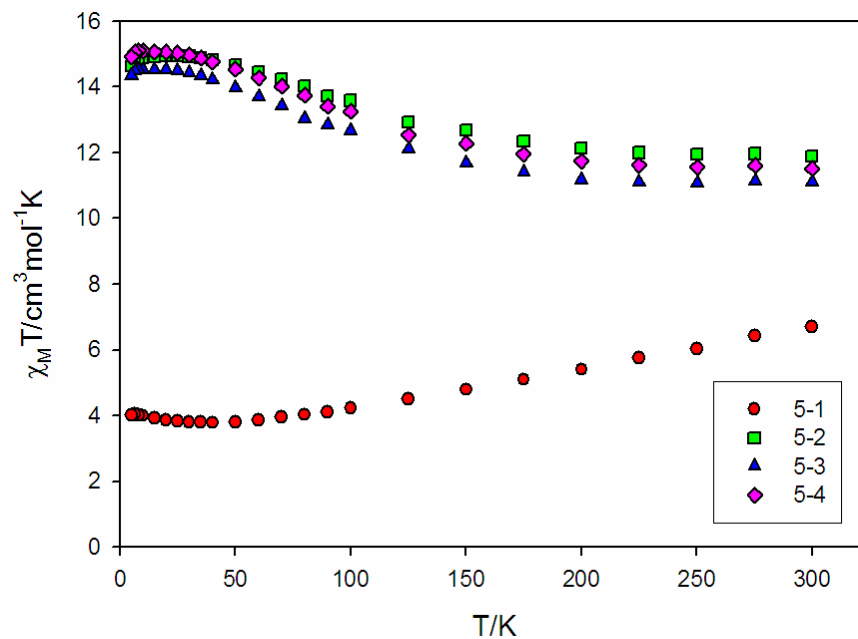


Figure 5-5. Plots of $\chi_M T$ vs T for complexes **5-1** (●), **5-2**·H₂O (■), **5-3**·H₂O (▲) and **5-4**·H₂O (◆).

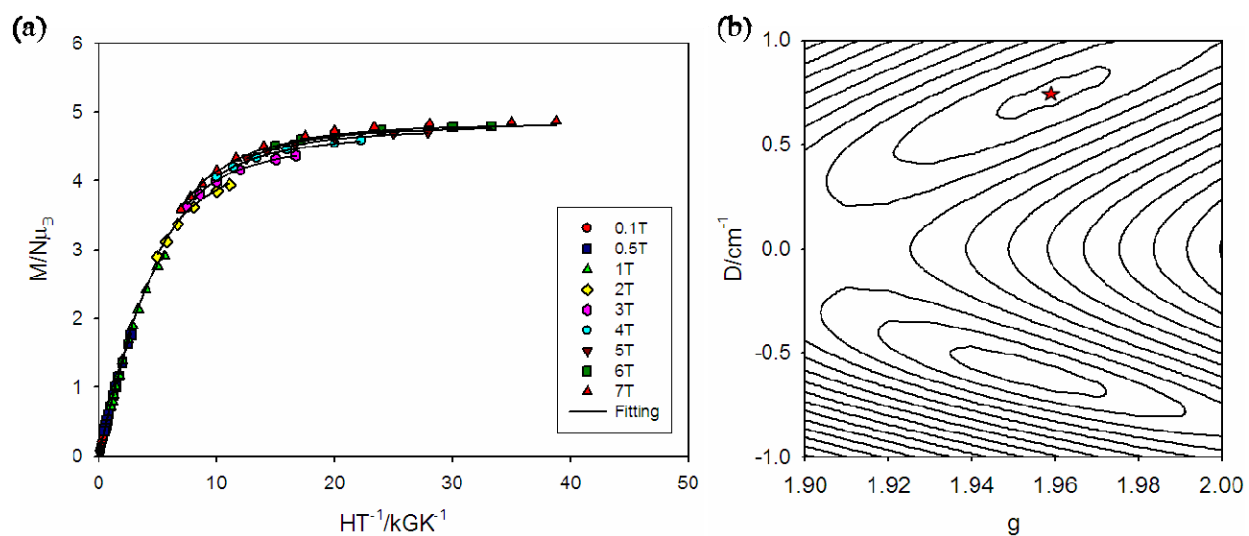


Figure 5-6 (a) Plot of reduced magnetization ($M/N\mu_B$) vs H/T for complex **5-1**. The solid lines are the fit of the data; see the text for the fit parameters. (b) Two-dimensional contour plot of the fitting error surface vs D and g for **5-1**.

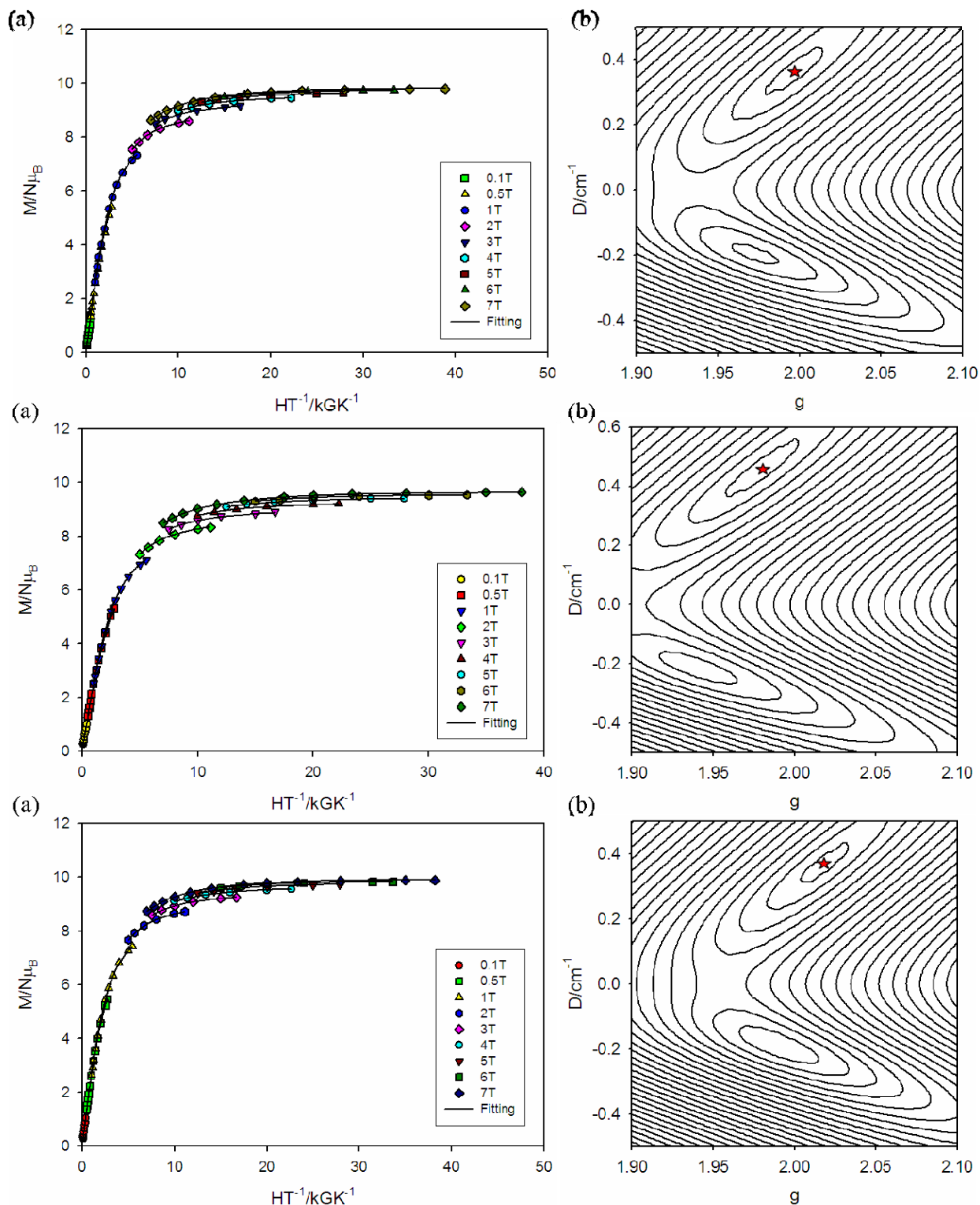


Figure 5-7 (a) Plot of reduced magnetization ($M/N\mu_B$) vs H/T for complexes $5\text{-}2\cdot\text{H}_2\text{O}$ (top), $5\text{-}3\cdot\text{H}_2\text{O}$ (middle), $5\text{-}4\cdot\text{H}_2\text{O}$ (bottom). The solid lines are the fit of the data (b) Two-dimensional contour plot of the fitting error surface vs D and g for complexes $5\text{-}2\cdot\text{H}_2\text{O}$ (top), $5\text{-}3\cdot\text{H}_2\text{O}$ (middle), $5\text{-}4\cdot\text{H}_2\text{O}$ (bottom).

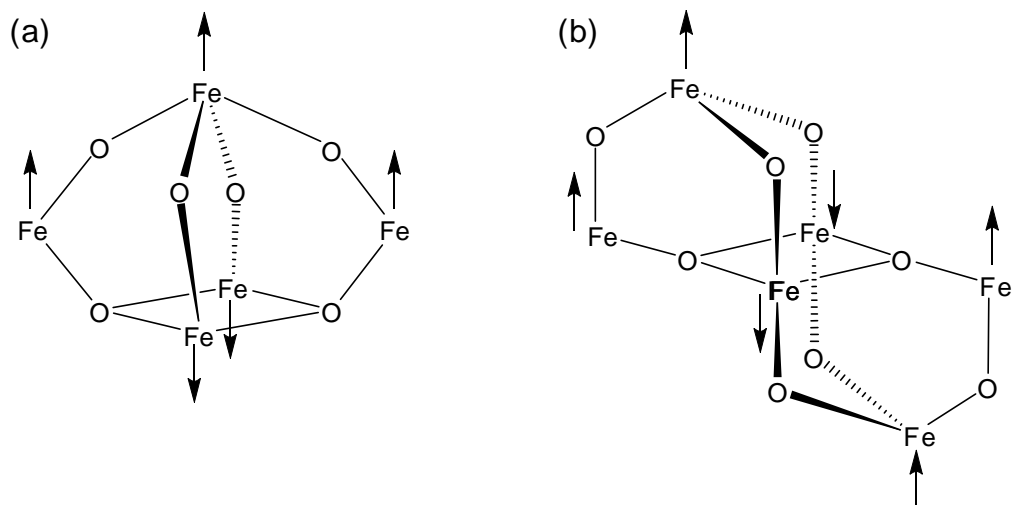


Figure 5-8. Rationalization of spin ground state of complex (a) **5-1** and (b) **5-2**.

CHAPTER 6
NEW STRUCTURAL TYPES IN POLYNUCLEAR IRON CLUSTERS INCORPORATING
O,N,N,O LIGAND: A SNAKE LIKE CHAIN AND A SUPRAMOLECULAR DIMER OF
SMMs

6.1 Introduction

Molecular clusters of magnetic transition metal ions have been generating great interest since the discovery that these molecules can behave as nanoscale magnets and show magnetic bistability of pure molecular origin which can be used for information storage.¹³ The first molecule to show this behaviour was $[\text{Mn}_{12}\text{O}_{12}(\text{O}_2\text{CMe})_{16}(\text{H}_2\text{O})_4]$,¹⁵ which led to the field of single molecule magnetism. Since then much effort has been put into finding new systems with interesting magnetic properties. Although a variety of Mn containing SMMs have been reported in recent years but to date, SMMs based on Fe^{III} are still rare.²²

In addition, oxo-bridged Fe^{III} clusters of various nuclearities have been studied as models of Fe sites in proteins and enzymes, as well as models of intermediate stages of the growth of the giant Fe/O core of the Fe storage protein ferritin.¹⁴⁴ In fact, the biological and magnetic areas essentially involve the same Fe/O chemistry as emphasized by the fact that Fe/O core of ferritin can be considered a nanoscale magnetic particle and has been investigated for quantum tunneling effects of magnetization.³¹

SMMs derive their properties from the combination of a large ground-state spin quantum number (S) and a magnetoanisotropy of the easy-axis (Ising)-type (negative zero-field splitting parameter, D), rather than from intermolecular interactions and long-range ordering as in traditional magnets.¹³ This combination leads to a significant barrier (U) to relaxation (reorientation) of the magnetization vector, whose maximum value is given by $S^2|D|$ or $(S^2 - 1/4)|D|$ for integer and half-integer spin, respectively. The use of high spin Fe^{III} can theoretically lead to large spin values even for quite small number of paramagnetic centers.²⁰ Although the

interactions between Fe^{III} are generally antiferromagnetic, some topological arrangements can result in large ground state spin due to the phenomenon of spin frustration. In general, molecules with high spin ground state have many spin states which are thermally populated at room temperature; therefore the SMM properties manifest itself at low temperature when excited states are depopulated.

Fe^{III} clusters do not provide SMMs by design because the conditions for large Ising type anisotropy depend very unpredictably on minor features of the coordination environment of the metal ion.²⁰ The above considerations and others continue to stimulate groups around the world to develop new synthetic methods that can yield new polynuclear Fe/O clusters. However there is no obvious and guaranteed route to such species. Different approaches to the synthesis of iron-oxo clusters are controlled hydrolysis or alcoholysis reactions of simple iron salts or more complicated starting materials.^{30,122} Also, trinuclear iron oxo clusters have also proved to be very useful building blocks for the preparation of higher nuclearity clusters in the presence of appropriately chosen chelate.¹⁴⁵ One successful strategy in producing polynuclear clusters is the use of alkoxide-based ligands,³² since this functionality is an excellent bridging group that fosters higher nuclearity product formation. In chapter 4, we reported our results in polynuclear iron clusters with N,N,O based chelate 2- {[2-(dimethylamino)ethyl] methylamino}- ethanol (dmemH).⁹³ In the present work, we have been investigating the use of a new O,N,N,O-based chelate *N,N'*-bis(2-hydroxyethyl)ethylenediamine (heenH₂; Figure 6-1) for transition metal cluster chemistry. It has been used before in the literature to make mononuclear Pt and Cu molecules in its fully protonated form but there are no previous use of it in polynuclear metal (i.e. cluster) chemistry, protonated or otherwise. Our first investigations with heenH₂ have been in Fe^{III} chemistry, and we have indeed found it to lead to new structural types of products. We

herein report the syntheses, crystal structures and magentochemical characterization of four new iron complexes Fe₆, Fe₇, Fe₉ and Fe₁₈.^{145,146}

6.2 Experimental Section

6.2.1 Syntheses

All preparations were performed under aerobic conditions using reagents and solvents as received. [Fe₃O(O₂CBu^t)₆(H₂O)₃]NO₃ and [Fe₃O(O₂CPh)₆(H₂O)₃]NO₃, were synthesized as reported elsewhere.⁹⁶

[Fe₁₈O₈(OH)₂(O₂CBu^t)₂₈(heen)₄] (6-1). To a stirred dichloromethane solution (20 mL) of [Fe₃O(O₂CBu^t)₆(H₂O)₃]NO₃ (0.20 g, 0.21 mmol) was added heenH₂ (0.05 g, 0.31 mmol) and the reaction mixture was stirred for 3 hours and then filtered to remove undissolved solid and layered with pentane. Orange crystals of **6-1**·4C₅H₁₂·4CH₂Cl₂ suitable for X-ray crystallography formed over a week in 30% yield. Anal. calcd (Found) for **6-1** (C₁₆₄H₃₀₈N₈Fe₁₈O₇₄): C, 42.98 (43.25); H, 6.82 (6.99); N, 2.44 (2.43). Selected IR data (cm⁻¹): 2961(s), 2928(m), 2871(w), 1580(s), 1551(s), 1484(vs), 1421(vs), 1376(m), 1228(m), 1090(w), 906(w), 787(w), 663(w), 602(m), 508(w), 438(m).

[Fe₉O₄(OH)₄(O₂CPh)₁₃(heenH)₂] (6-2). Ligand heenH₂ (0.11 g, 0.74 mmol) was added to a stirred MeCN solution (15 mL) of FeCl₃·6H₂O (0.20 g, 0.74 mmol) and NaO₂CPh (0.21 g, 0.15 mmol). The reaction mixture was stirred for 2 hours and then filtered. Slow evaporation of the filtrate gave X-ray quality crystals of **6-2**·9MeCN in three weeks days in 15% yield. Anal. calcd (Found) for **6-2** (C₁₀₃H₉₉N₄Fe₉O₃₈): C, 49.41 (48.99); H, 3.98 (3.90); N, 2.24 (2.57). Selected IR data (cm⁻¹): 3421(br), 1599(m), 1558(s), 1597(s), 1176(w), 1025(w), 827(w), 715(m), 676(m), 592(w), 469(m).

[Fe₇O₃(OMe)₃(MeOH)₁(heen)₃Cl_{4.5}(H₂O)_{1.5}]Cl_{1.25}[FeCl₄]_¼ (6-3). To a stirred solution of FeCl₂·4H₂O (0.20 g, 1.0 mmol) in methanol (10 mL) was added heenH₂ (0.15 g, 1.9 mmol) and

the resulting solution was refluxed for 2 hours. It was filtered hot and kept for slow evaporation. Orange needle like crystals of **6-3**·2MeOH·½H₂O appeared in seven days in 10 % yield. Anal. Calcd (Found) for **6-3** (C₂₂H₅₈N₆Fe_{7.25}O_{14.5}Cl_{6.75}): C, 20.60 (21.09); H, 4.56 (4.93); N, 6.56 (6.08). Selected IR data (cm⁻¹): 3224(s,br), 2952(m), 2868(m), 1634(m), 1455(m), 1344(w), 1236(w), 1090(s), 1066(s), 963(s), 886(w), 810(w), 670(s), 633(m), 558(m), 505(m), 407(m).

[Fe₆O₂(O₂CPh)₅(heen)₃(heenH)](ClO₄)₂ (6-4**) Method A.** A solution of Fe(ClO₄)₃ (0.20 g, 0.56 mmol) and NaO₂CPh (0.16 g, 0.11 mmol) in EtOH (15 mL) was treated with heenH₂ (0.08 g, 0.57 mmol) and stirred for 3 hours. The resultant red brown solution was filtered to remove NaCl and the filtrate was left undisturbed for slow evaporation. X-ray quality crystals of **6-4**·2EtOH·1.5H₂O appeared in 5 days in 25% yield. Anal. calcd. (Found) for **6-4**·H₂O (C₅₉H₈₄N₈Fe₆O₂₉Cl₂): C, 39.92 (39.84); H, 4.77 (4.62); N, 6.31 (6.19). Selected IR data (cm⁻¹): 2968(m), 1596(m), 1557(m), 1400(s), 1341(w), 1302(w), 1176(w), 1190(s), 1024(m), 981(m), 829(w), 724(s), 624(m), 533(w), 468(m).

Method B. An orange red solution of [Fe₃O(O₂CPh)₆(H₂O)₃]NO₃ (0.20 g, 0.19 mmol) in EtOH (15 mL) was treated with heenH₂ (0.06 g, 0.39 mmol) and NaClO₄ (0.05 g, 0.41 mmol) and the resulting solution stirred for 2 hours at room temperature. Next, it was filtered to remove undissolved starting material and the filtrate was allowed to stand undisturbed at room temperature. Orange crystals of the product formed over 5 days in 15 % yield.

6.2.2. X-ray Crystallography

Data were collected by Dr. Khalil A. Abboud on a Siemens SMART PLATFORM equipped with a CCD area detector and a graphite monochromator utilizing Mo-K_α radiation (λ = 0.71073 Å). Suitable crystals of **6-1**·4C₅H₁₂·4CH₂Cl₂, **6-2**·9MeCN, **6-3**·2MeOH·½H₂O and **6-4**·2EtOH·1.5H₂O were attached to glass fibers using silicone grease and transferred to a goniostat

where they were cooled to 173 K for data collection. Cell parameters were refined using up to 8192 reflections. A full sphere of data (1850 frames) was collected using the ω -scan method (0.3° frame width). The first 50 frames were remeasured at the end of data collection to monitor instrument and crystal stability (maximum correction on I was < 1 %). Absorption corrections by integration were applied based on measured indexed crystal faces. The structure was solved by the Direct Methods in *SHELXTL6*,⁴⁶ and refined using full-matrix least squares. The non-H atoms were treated anisotropically, whereas the hydrogen atoms were calculated in ideal positions and were riding on their respective carbon atoms. Refinement was done using F^2 .

In **6-1**, the asymmetric unit consists of a half Fe_{18} cluster, two pentane molecules and two dichloromethane molecules. The latter molecules were disordered and could not be modeled properly, thus program SQUEEZE⁶⁸ was used to calculate the solvent disorder area and remove its contribution to the overall intensity data. A total of 1183 parameters were included in the final cycle of refinement 42915 reflections with $I > 2\sigma(I)$ to yield R_1 and wR_2 of 4.67 % and 12.52 %, respectively.

In **6-2**, the asymmetric unit consists of the cluster and 9 acetonitrile molecules. The latter were disordered and could not be modeled properly, thus program SQUEEZE⁶⁸ was used to calculate the solvent disorder area and remove its contribution to the overall intensity data. There are three phenyl groups that are disordered (at C81, C91 and C121) and each was refined as a rigid group and in two parts with their site occupation factors dependently refined. The last two of them cause a disorder in an uncoordinated EtOH arm of the N4 diamine. Both hydroxy group protons of the uncoordinated diamines were calculated in idealized positions and refined riding on their O atoms. A total of 1375 parameters were included in the final cycle of refinement using 42636 reflections with $I > 2\sigma(I)$ to yield R_1 and wR_2 of 7.41 % and 18.03 %, respectively.

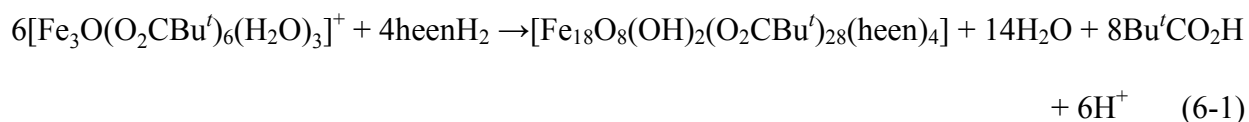
In **6-3**, the asymmetric unit consists of one Fe₇ cluster and FeCl₄ located on a 222 symmetry site (thus 1/4 is in the asymmetric unit). The structure has several disorders one of which is in the N1 ligand where two CH₂ units are disordered and were refined in two parts with their site occupation factors dependently refined. The O4 position is a disorder between a coordinated water molecule and a methanol solvent (O18) in one parts against a coordinated methanol ligand and a water solvent (O19) molecule. Another disorder has a coordinated methanol and a solvent methanol in one part (O11 and O15) against coordinated water and a solvent methanol molecule (O11 and O16). The coordinated Cl4 ligand is disordered with a water (O4'') ligand while a lattice Cl7 anion is disordered against a lattice water (O7'') molecule. The last two disorders lead to balanced charges in the asymmetric unit. A total of 566 parameters were refined in the final cycle of refinement using 11605 reflections with $I > 2\sigma(I)$ to yield R₁ and wR₂ of 4.64 % and 10.44 %, respectively.

In **6-4**, the asymmetric unit consists of a 1/2 cluster, a perchlorate anion, disordered ethanol molecules and three partial water molecules. The cluster has one arm of the diamine ligand disordered against a benzoate anion. Due to symmetry, the two parts of the disorder were 0.5 occupation factors. The perchlorate anion is disordered and was refined in two parts with Cl and Cl'. Further, the Cl' part was also disordered along a three fold rotation axis. The ethanol solvent molecule was also disordered and refined in two parts with their site occupation factors dependently refined. A total of 586 parameters were included in the final cycle of refinement using 8642 reflections with $I > 2\sigma(I)$ to yield R₁ and wR₂ of 6.22 % and 15.51 %, respectively. Unit cell data and details of the structure refinements for **6-1** to **6-4** are listed in Table 6-1.

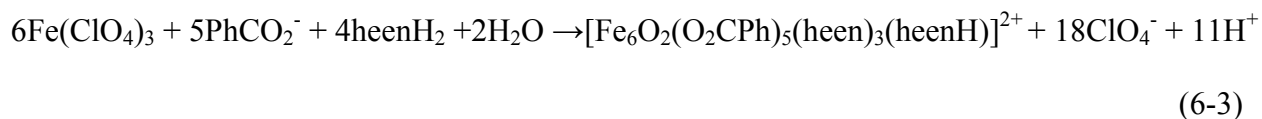
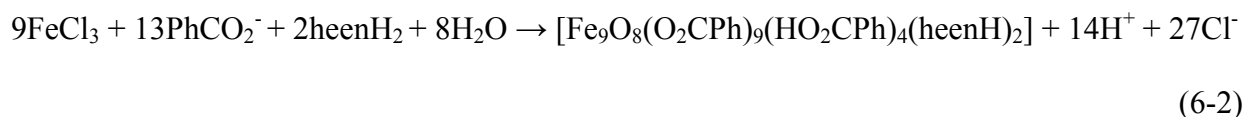
6.3 Results and Discussion

6.3.1 Syntheses

Reaction of $[\text{Fe}_3\text{O}(\text{O}_2\text{CBu}')_6(\text{H}_2\text{O})_3]^+$ and heenH_2 in a 2 : 3 molar ratio in CH_2Cl_2 , followed by layering with pentanes, gave orange crystals of an octadecanuclear product $[\text{Fe}_{18}\text{O}_8(\text{OH})_2(\text{O}_2\text{CBu}')_{28}(\text{heen})_4]$ (**6-1**) with the core topology not previously encountered. Its formation is summarized in eq. 6-1. Use of methylene chloride as the reaction medium was found to be very essential for obtaining a clean product. Using acetonitrile as the reaction medium gives a mixture of white and orange crystals, which were difficult to separate, and hence could not be characterized. Further we decided to use polar alcoholic solvents seeking formation of higher nuclearity products via methanolysis or ethanolysis, but always insoluble yellow precipitates were obtained.



A similar reaction involving FeCl_3 , NaO_2CPh and heenH_2 in 1:2:1 molar ratio in MeCN, gave $[\text{Fe}_9\text{O}_4(\text{OH})_4(\text{O}_2\text{CPh})_{13}(\text{heenH})_2]$ (**6-2**) (eq. 6-2). On the other hand, reaction of $\text{Fe}(\text{ClO}_4)_3$, O_2CPh^- and heenH_2 in 1:2:1 ratio in ethanol gave $[\text{Fe}_6\text{O}_2(\text{O}_2\text{CPh})_5(\text{heen})_3(\text{heenH})](\text{ClO}_4)_2$ (**6-4**) (eq. 6-3). The reaction procedure employed contains an excess of ligand over that required by stoichiometric reaction and this might be beneficial in providing H^+ acceptors.



In both these reactions (eq. 6-2 and 6-3) choice of solvent and ratio of starting materials is very crucial as other ratios do not give clean reaction. In the former reaction, using lower

concentration of sodium benzoate and heenH₂ gives the crystals of trinuclear iron cluster and using higher concentration of sodium benzoate and ligand gives messy reactions. Additionally, nothing crashes out of reaction mixture if ethanol is used as the reaction medium. In the latter reaction also, 1:2:1 ratio is very important in getting single crystals. In other ratios, different products are obtained, whose IR is different from **6-4** but these could not be characterized as single crystals could not be obtained. Further, the reaction mixture gives oily droplets if acetonitrile is used as the solvent, making ethanol absolutely essential for the formation of **6-4**.

Refluxing FeCl₂ and heenH₂ in 1:1 ratio in MeOH gave **6-3**, while nothing comes out of reaction mixture if EtOH is used instead of MeOH. Using lower or higher concentration of ligand also gives the same product but very bad quality crystals are obtained.

It is clear that the reactions that lead to **6-1** to **6-4** are very complicated, and the reaction solutions likely contain a complicated mixture of several species in equilibrium. In such cases, factors such as relative solubility, lattice energies, crystallization kinetics, and others determine the identity of the isolated products, and one (or more) of these factors is undoubtedly the reason that the reaction product changes from an octadecanuclear complex to a nonanuclear complex on changing the carboxylate employed from pivalate to benzoate.

6.3.2 Description of Structures

6.3.2.1 Structure of [Fe₁₈O₈(OH)₂(O₂CBu')₂₈(heen)₄] (**6-1**)

A labeled representation of **6-1** is shown in Figure 6-2. Selected interatomic distances and angles are given in Table A-12. Complex **6-1** crystallizes in triclinic *P* $\bar{1}$ space group. The structure of centrosymmetric **6-1** comprises a remarkable Fe₁₈ cluster that can be described as seven [Fe₂O₂] rhombs linked into a chain, and attached to four end Fe atoms (Fe8, Fe8', Fe9, Fe9'). Alternatively, it can be better described as the linkage by heen²⁻ alkoxide arms O5 and O5' of two central [Fe₄(μ_3 -O)₂]⁸⁺ butterfly units (Fe1, Fe2, Fe3 and Fe4, and its symmetry partner),

and then connected to additional $[\text{Fe}_4(\mu_3\text{-O})_2]^{8+}$ butterfly units at each end via intermediate Fe atoms Fe5 and Fe5', the bridges being heen²⁻ alkoxide arms O16 and O17 on one side of Fe5, and heen²⁻ alkoxide arm O18 and a hydroxide ion O19 on the other side. Peripheral ligation is provided by a total of four chelating heen²⁻ and twenty-eight pivalate groups, twenty-two of the latter in their common $\eta^1:\eta^1:\mu$ -mode, four in a η^2 chelating mode on Fe8, Fe8', Fe9 and Fe9', and two in a η^1 terminal mode on Fe4 and Fe4'. Two of the four heen²⁻ groups are in a $\eta^2:\eta^1:\eta^1:\eta^2:\mu_3$ -mode (N3 and N4 are bound to Fe5 while O17 is bridging Fe4 and Fe5, and O18 is bridging Fe5 and Fe6) and the other two are in $\eta^2:\eta^1:\eta^1:\eta^2:\mu_3$ - mode (N1, N2 are chelating Fe3 and O5 is bridging Fe1 and Fe1', and O16 is bridging Fe4 and Fe5).

The overall topology of **6-1** is chain-like and resembles a double-headed serpent or alligator with both sets of jaws wide open. Such a molecule is not only unprecedented in Fe chemistry, it represents the highest-nuclearity, chain-like metal-containing molecule to be yet discovered, and can reasonably be called a 'molecular chain'. The next longest such molecular chain is a Cr₁₂Ni species.¹⁴⁷ There are only two previous Fe₁₈ clusters known, and they are both wheel complexes, i.e. closed molecular chains.^{89,148}

6.3.2.2 Structure of $[\text{Fe}_9\text{O}_4(\text{OH})_4(\text{O}_2\text{CPh})_{13}(\text{heenH})_2]$ (**6-2**)

A labeled representation of **6-2** is shown in Figure 6-3 with selected geometric parameters listed in Table A-13. Complex **6-2** crystallizes in the triclinic *P* $\bar{1}$ space group. The structure consists of pairs of Fe₉ clusters arranged as head-to-head dimers. Each Fe₉ contains two $[\text{Fe}_4(\mu_3\text{-O})(\mu_3\text{-OH})]^{8+}$ butterfly-like sub-units (Fe1, Fe5, Fe6, Fe7, O5, O27 and Fe4, Fe7, Fe8, Fe9, O21, O31) fused at body atom Fe7 (Figure 6-3), and attached to two additional Fe atoms Fe2 and Fe3 by two $\mu_3\text{-OH}^-$ (O6 and O11) and two $\mu_3\text{-O}^{2-}$ ions (O7 and O14). There are thirteen PhCO₂⁻ groups, nine $\eta^1:\eta^1:\mu$ -bridging and four η^1 terminal on Fe1, Fe4, Fe6 and Fe8, with their noncoordinated O atom intramolecularly H-bonded to OH⁻ ions (O6, O11, O5 and O21,

respectively). Each heenH⁻ group is a tridentate chelate to an Fe atom (Fe5 and Fe9) and bridges through its deprotonated arm to a neighboring Fe atom. Each remaining heenH⁻ protonated arm (O30 and O38) is unbound and involved in hydrogen-bonding. The one on Fe9 forms a H-bond to benzoate O atom O32 (O38...O32 = 2.788 Å) with no disorder. The one on Fe5, however, is disordered, forming intramolecular H-bonds to benzoate O atom O28 (O30...O28 = 2.882 Å) or to the same heenH⁻ arm of the corresponding chelate on the neighboring Fe9 molecule (O30...O39 = 2.753 Å) (Figure 6-4). Refinement of the disorder components gave an essentially statistical 36:64% mixture of the intramolecular and intermolecular H-bonding situations, since there are two equivalent forms of the latter, as shown in Figure 6-4. Thus, 2/3 of the molecules in the crystal are linked within H-bonded [Fe₉]₂ dimers, whereas the other third of the molecules are within non-H-bonded [Fe₉]₂ dimers.

The core of **6-2** is unprecedented in nonanuclear Fe(III) chemistry. Indeed, there are relatively few Fe₉ clusters known in literature and they are described as ferric “Triple-Decker”, nonanuclear ring, rhomb-like array, two distorted Fe₄ tetrahedra linked to another Fe atom via oxide and alkoxides, central Fe atom surrounded by four dinuclear Fe₂ units etc.^{58,80,149-152}

6.3.2.3 Structure of [Fe₇O₃(OMe)₃(MeOH)₁(heen)₃Cl_{4.5}(H₂O)_{1.5}]Cl_{1.25}[FeCl₄]_¼ (**6-3**)

A labeled representation of **6-3** is shown in Figure 6-5. Selected interatomic distances and angles are given in Table A-14. Complex **6-3** crystallizes in the high symmetry orthorhombic *I*₂₂₂ space group and it consists of a planar arrangement of six Fe^{III} ions with a seventh central Fe^{III} ion 1.437 Å below the Fe₆ plane. The central Fe atom, Fe1, is tetracoordinated. It establishes bonds with three μ₃-O²⁻ ions and with a terminal Cl ligand. Every peripheral iron is connected to one of its adjacent Fe atoms through one μ-OMe⁻ and one alkoxide group from heen²⁻ and to the neighboring iron atom through the second alkoxide arm of heen²⁻ and a μ₃-O²⁻ bridge, which in turn are bridging the alternate peripheral iron atoms to the central tetrahedral iron atom. N atoms

of the heen²⁻ group complete the octahedral coordination of alternating iron atoms, Fe3, Fe5 and Fe7 while terminal Cl ligand and H₂O/MeOH molecules complete the octahedral coordination of alternating iron atoms Fe2, Fe4 and Fe6.

There is one molecule of FeCl₄⁻ anion per four formula units of Fe₇ for charge balance. Additionally there are lattice Cl⁻ ions for charge balance and molecules of water and methanol as solvents of crystallization. There are several features which makes this structure especially remarkable. First, it is one of very few polynuclear iron-oxo complexes with an odd number of metal ions. Second striking feature of this compound is rather unusual coordination of central iron atom. Fe1 has an almost regular tetrahedral geometry with O-Fe-O angles ranging between 108.1-111.4°.

The core topology of **6-3** is new within Fe^{III} chemistry. There are only a few Fe₇ complexes in the literature and they are described as cagelike, disklike and domelike.^{98,101,102} Also, we reported two new heptanuclear clusters in chapter 4, [Fe₇O₄(O₂CPh)₁₁(dmem)₂] and [Fe₇O₄(O₂CMe)₁₁(dmem)₂]. These complexes had the same formula except for the identity of the carboxylate but the structures were very different. The former had two [Fe₄(μ₃-O)₂]⁸⁺ butterfly units sharing a common body iron atom while in the other a number of Fe₃O triangular units were linked in an unusual way.⁹³

6.3.2.4 Structure of [Fe₆O₂(O₂CPh)₅(heen)₃(heenH)](ClO₄)₂ (**6-4**)

A labeled representation of **6-4** is shown in Figure 6-6. Selected interatomic distances and angles are given in Table A-15. Complex **6-4** crystallizes in triclinic *P* $\bar{1}$ space group. The asymmetric unit consists of half of the cluster, a perchlorate ion and an ethanol molecule and one and a half water molecule as the solvents of crystallization. The structure of the centrosymmetric cation of **6-4** can be described as a central [Fe₄(μ₃-O)₂]⁸⁺ butterfly-like unit (Fe1, Fe1', Fe2 and Fe2') connected through both its body (Fe1, Fe1') and wingtip atoms (Fe2, Fe2') to two

additional Fe atoms Fe3 and Fe3' by heen^{2-} (O8, O9, O10) alkoxide arms. At one end of the molecule (Fe3), the remaining heen^{2-} alkoxide arm (O11) binds terminally; at the other end (Fe3'), this arm (O20) is protonated and unbound (i.e. a heenH^- group) and there is instead a PhCO_2^- bound terminally (Figure 6-6; only benzoate ipso C atoms shown). These two situations at the two ends are, of course, disordered by the centre of symmetry which makes Fe3 and Fe3' equivalent; only one of the disorder components is shown in Figure 6-6. Ligation is completed by four benzoate groups in the common $\eta^1:\eta^1:\mu$ -mode bridging the body and wingtip iron atoms of the central butterfly unit, only the *ipso* C atoms of benzoate rings have been shown for clarity in Figure 6-6. A number of Fe_6 complexes have been previously reported possessing a variety of metal topologies such as planar, twisted boat, chair, parallel triangles, linked triangles, fused butterflies, octahedral, ladder-like, cyclic etc.¹⁰⁴

6.3.3 Magnetochemistry of complexes 6-1 to 6-4

6.3.3.1 Dc Studies

Solid-state, variable temperature dc magnetic susceptibility data in a 0.1 T and 5.0-300 K range were collected on powdered crystalline samples of **6-1** to **6-4** restrained in eicosane. The obtained data are plotted as $\chi_M T$ vs T in Figure 6-7. For **6-1**, $\chi_M T$ steadily decreases from 22.83 $\text{cm}^3\text{Kmol}^{-1}$ at 300 K to 1.16 $\text{cm}^3\text{Kmol}^{-1}$ at 5.0 K indicating predominant antiferromagnetic interactions between Fe^{III} magnetic centers. Value of $\chi_M T$ at 300 K is much less than spin-only ($g = 2.0$) value of 78.75 $\text{cm}^3\text{Kmol}^{-1}$ for eighteen non-interacting Fe^{III} ions, the behavior with decreasing temperature and the low value of $\chi_M T$ at 5 K are indicative of $S = 0$ ground state spin. This is not unexpected given that this is the most common ground state for Fe^{III}_x clusters where x is even. There are common exceptions to this rule, however, when the topology is such so as to introduce competing antiferromagnetic exchange interactions and spin frustration effects that result in often significant ground state S values. For complex **6-1**, the $S = 0$ ground state can be

rationalized as shown in Figure 6-8: the central butterfly units are known to exhibit spin frustration effects within their triangular subunits and to possess an $S = 0$ ground state as a result of the four ‘wingtip-body’ interactions of the four edges overcome (frustrating) the ‘body-body’ interaction.⁷⁷ The antiferromagnetic interactions between separate butterfly units and between them and Fe5/Fe5' then lead to an expected $S = 0$ ground state, as found experimentally. Of course, since **6-1** has an $S = 0$ ground state, the depicted spin alignments in Figure 6-8 represent only one of the component wave functions of the ground state eigenstate of the molecule.

For **6-2**, the value of the χ_{MT} gradually decreases from $13.35 \text{ cm}^3\text{Kmol}^{-1}$ at 300 K to $11.65 \text{ cm}^3\text{Kmol}^{-1}$ at 150 K, stays essentially constant until 60 K and then decreases to $8.73 \text{ cm}^3\text{Kmol}^{-1}$ at 5.0 K. The 300 K value is again less than the spin-only value of $39.37 \text{ cm}^3\text{Kmol}^{-1}$ expected for nine non-interacting Fe^{III} ions, indicating predominantly antiferromagnetic interactions. The 5.0 K value suggests $S = 7/2$ ground state. For **6-3**, the value of χ_{MT} gradually increases from $29.92 \text{ cm}^3\text{Kmol}^{-1}$ at 300 K to $48.16 \text{ cm}^3\text{Kmol}^{-1}$ at 50 K before dropping slowly to $32.83 \text{ cm}^3\text{Kmol}^{-1}$ at 5.0 K. The decrease of χ_{MT} at low temperature may be a consequence of zeeman effects from the DC field and/or the presence of antiferromagnetic interactions between clusters. Subtracting out the χ_{MT} contribution for the $[\text{FeCl}_4]^-$ anion indicates an $S = 15/2$ ground state. For **6-4**· H_2O , the value of χ_{MT} steadily decreases from a value of $10.05 \text{ cm}^3\text{Kmol}^{-1}$ at 300 K to $8.13 \text{ cm}^3\text{Kmol}^{-1}$ at 70 K and then rises to a value of $10.32 \text{ cm}^3\text{Kmol}^{-1}$ at 5.0 K. The 300 K value is again much less than the spin-only value of $26.25 \text{ cm}^3\text{Kmol}^{-1}$ expected for six non-interacting Fe^{III} ions, indicating predominant antiferromagnetic interactions. The increase in χ_{MT} as the temperature then decreases suggests the lowest lying states are of high spin values, and the value at 5.0 K suggests $S = 4$ ground state.

To confirm the above ground state spin estimates, variable field (H) and temperature magnetization (M) data were collected in the 0.1 T to 7 T and 1.8 K-10 K ranges. The resulting data for **6-2** to **6-4** are plotted as reduced magnetization ($M/N\mu_B$) vs H/T in Figures 6-9 and 6-10. These data were fit using the program *MAGNET*,⁵³ described elsewhere.⁵⁶ The best-fit for **6-2** is shown as the solid lines in Figure 6-9. A satisfactory fit could only be obtained if data collected at fields above 4 T were excluded, suggesting that some low-lying excited states with $S > 7/2$ are being stabilized by the applied field to the point that they are significantly populated at these temperatures. The best fit was obtained using only the low-field data (≤ 4 T) (solid lines in Figure 6-9) gave $S = 7/2$, $D = -0.85 \pm 0.01 \text{ cm}^{-1}$ and $g = 2.06 \pm 0.01$. Alternative fits with $S = 5/2$ or $9/2$ were rejected because they gave unreasonable values of g and D . In order to ensure that the true global minimum had been located for each compound, we calculated the root-mean-square error surface for the fits as a function of D and g , and have plotted them as two-dimensional contour plots. For **6-2**, the plot clearly shows only the above-mentioned minima with negative D value (Figure 6-9).

For **6-3**, the best fit (obtained using low-field data; ≤ 2 T) is shown as solid lines in Figure 6-10 (magnetization data was corrected for the paramagnetic anion) and was obtained with $S = 15/2$ and either of the two sets of parameters, $g = 2.12/D = -0.13 \text{ cm}^{-1}$ or $g = 2.07/D = 0.16 \text{ cm}^{-1}$. The error surface contour plot is shown in Figure 6-11 and shows the above two minima, with the one with negative D clearly the superior fit since it has a lower (deeper) minimum.

For **6-4**·H₂O, a good fit was obtained using 0.1-4 T data (solid lines in Figure 6-10) with $S = 4$ and either of the two sets of parameters, $g = 2.06/D = -0.29 \text{ cm}^{-1}$ or $g = 2.05/D = 0.35 \text{ cm}^{-1}$. A rms error analysis shows that the one with $D < 0$ is superior, suggesting this to be the true sign of D (Figure 6-11).

6.3.3.2 Ac Studies

Ac magnetic susceptibility studies were performed on vacuum-dried microcrystalline samples of **6-2** to **6-4** in the temperature range 1.8-10 K with a zero dc field and a 3.5 G ac field oscillating at frequencies in the 5 – 1000 Hz range. The in-phase (χ_M') component of the ac susceptibility for **6-2**, plotted as $\chi_M'T$ vs T, is shown in Figure 6-12. The in-phase $\chi_M'T$ decreases with decreasing T before exhibiting a frequency dependent drop below ~ 3 K. Extrapolation from above 3 to 0 K gives a value of $\sim 7.9 \text{ cm}^3\text{Kmol}^{-1}$, confirming an $S = 7/2$ ground state. The drop below ~ 3 K and the concomitant frequency dependent out-of-phase (χ_M'') signal suggest **6-2** possibly be a SMM. The $\chi_M'T$ vs T plot for **6-3** and **6-4**·H₂O is shown in Figure 6-13. Extrapolation from above ~ 4 to 0 K gives a value of ~ 30 and $\sim 10 \text{ cm}^3\text{Kmol}^{-1}$ for **6-3** and **6-4**·H₂O, confirming an $S = 15/2$ and 4 ground state respectively. No out-of-phase signals were seen for both complexes.

6.3.3.3 Single-Crystal Hysteresis Studies

To probe the possible SMM behavior further, single-crystal hysteresis loop and relaxation measurements were performed using a micro-SQUID¹⁵³ setup. It was found that complex **6-2** indeed behaves as an SMM as shown by the presence of magnetic hysteresis loops whose coercivity is strongly temperature and sweep rate dependent, increasing with decreasing temperature and increasing sweep rate as expected for the superparamagnetic like behavior of a SMM, as shown in Figure 6-14. QTM steps were observed, the first appearing before zero-field as expected for an exchange-bias effect from the neighbor within the [Fe₉]₂ dimer, and as seen for [Mn₄]₂.¹⁵⁴ However, a QTM step at zero field was also seen, and this is not expected for an exchange biased dimer. However, this and the $\sim 2:1$ ratio of the steps at 0.11 and 0.0 T can be explained with reference to Figure 6-4 as due to an antiferromagnetic exchange interaction between the two Fe₉ units mediated by the intermolecular H-bond. Thus, 64% of the [Fe₉]₂

dimers show an exchange-bias (ON), whereas the remaining 36% do not (OFF). The spin Hamiltonian (\mathcal{H}) for each Fe₉ SMM with Ising-like anisotropy is given by $\mathcal{H} = \mathcal{H}_1 + \mathcal{H}_2 - 2J\hat{S}_1\cdot\hat{S}_2$. From the $H_{\text{ex}} = 0.11$ T (H_{ex} = exchange-bias field) and the relationship $J' = -g\mu_{\text{B}}H_{\text{ex}}/(2S)$ ($\mathcal{H} = -2J\hat{S}_i\cdot\hat{S}_j$ convention)¹⁵⁵ can be calculated that the intermolecular interaction is $J' = -0.04$ K, that is, very weakly antiferromagnetic.

Thus, 64% of the dimers in the crystal are in an ON state and 36% are OFF (Figure 6-4). Since the intermolecular interaction J' will serve to quantum mechanically entangle the two molecules and generate superposition states,^{154,156,157} the ON and OFF states with respect to the interaction thus correspond to potential ON and OFF states of a coupled two-qubit system for quantum computation. Being able to have the interaction ON or OFF in some simple way is important, and the present work shows that a super exchange pathway via a single H-bond will suffice. Note that the [Fe₉]₂ head-to-head dimer structure does not depend on the intermolecular H-bond, unlike [Mn₄]₂ where a total of six equivalent C-H...Cl intermolecular H-bonds clearly control the crystallization of the dimer.

6.4 Conclusions

The use of dialcohol based ligand heenH₂ in Fe(III) chemistry has led to fascinating new polynuclear clusters, Fe₆, Fe₇, Fe₉ and Fe₁₈. Complex Fe₁₈ is a new structural type with a serpentine topology. The diamagnetic ground state of Fe₁₈ is not unexpected given that this is the most common ground state for Fe^{III}_x clusters where x is even. Some important exceptions however include [Fe₈O₂(OH)₁₂(tacn)₆]⁸⁺ ($S = 10$) and Fe₆ presented in this paper, where the nonzero ground state is caused by spin frustration effects induced by the architecture of these complexes. A new Fe₉ single-molecule magnet has been synthesized and found to crystallize as head-to-head dimers. Two-thirds of these are exchange-coupled through a hydrogen-bond

whereas the other third of the dimers are non-interacting, as monitored by magnetization hysteresis measurements. The crystal thus contains a mixture of ON and OFF dimers with respect to the quantum mechanical coupling through the hydrogen-bond.

Identification of these new clusters suggests that introduction of alcohol based ligands can lead to new Fe_x topologies/high spin molecules/SMMs not seen or accessible with oxide and carboxylate ligands alone using a simple bottom up approach. These results continue to emphasize the utility of small nuclearity preformed clusters as stepping-stones to higher nuclearity products, in this case through the use of alcohol based chelate. Overall we feel that this system is fascinating both in terms of the aesthetic appeal of the structural concepts and its potential to provide nanoscale magnets.

Table 6-1. Crystallographic data for **6-1**·4C₅H₁₂·4CH₂Cl₂, **6-2**·9MeCN, **6-3**·2MeOH·½H₂O and **6-4**·2EtOH·2H₂O

	6-1	6-2	6-3	6-4
Formula ^a	C ₁₈₈ H ₃₆₄ Cl ₈ Fe ₁₈ N ₈ O ₇₄	C ₁₀₃ H ₉₉ Fe ₉ N ₄ O ₃₈	C ₂₄ H ₆₇ N ₆ Fe _{7.25} O ₁₇ Cl _{6.75}	C ₆₃ H ₉₇ Cl ₂ Fe ₆ N ₈ O _{31.5}
fw, g/mol ^a	5209.77	2503.546	1356.04	1876.49
Space group	<i>P</i> $\bar{1}$	<i>P</i> $\bar{1}$	<i>I</i> ₂₂₂	<i>P</i> 2 ₁ / <i>n</i>
<i>a</i> , Å	15.7923(12)	17.0412(15)	20.8859(14)	11.7319(8)
<i>b</i> , Å	17.9984(13)	19.8622(16)	21.5851(15)	13.5034(9)
<i>c</i> , Å	24.8805(19)	19.9519(17)	22.6380(16)	13.8033(10)
α , °	106.938(2)	89.227(2)	90	113.332(1)
β , °	104.711(2)	77.146(2)	90	92.028(1)
γ , °	90.867(2)	77.433(2)	90	99.130(1)
<i>V</i> , Å ³	6513.0(8)	6421.9(9)	10205.8(12)	1970.8(2)
<i>Z</i>	1	2	8	1
<i>T</i> , K	173(2)	173(2)	173(2)	173(2)
Radiation, Å ^b	0.71073	0.71073	0.71073	0.71073
ρ_{calc} , g/cm ³	1.328	1.474	1.765	1.581
μ , mm ⁻¹	1.124	1.277	2.420	1.231
<i>R</i> 1 ^{c,d}	0.0467	0.0741	0.0464	0.0622
<i>wR</i> 2 ^e	0.1252	0.1803	0.1044	0.1551

^a Including solvate molecules. ^b Graphite monochromator. ^c $I > 2\sigma(I)$. ^d $R1 = \Sigma(|F_o| - |F_c|) / \Sigma|F_o|$.
^e $wR2 = [\Sigma[w(F_o^2 - F_c^2)^2] / \Sigma[w(F_o^2)^2]]^{1/2}$, $w = 1/[\sigma^2(F_o^2) + [(ap)^2 + bp]$, where $p = [\max(F_o^2, O) + 2F_c^2]/3$.

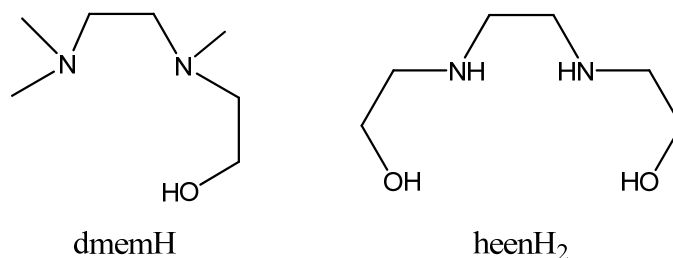


Figure 6-1. Structure of chelates: dmemH, heenH₂

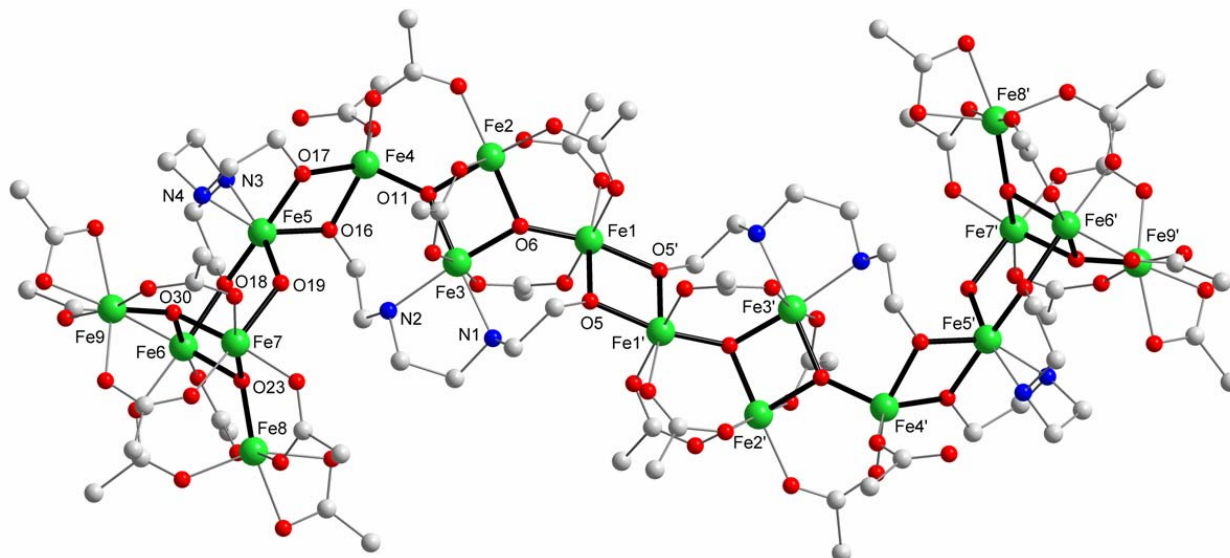


Figure 6-2. Labeled representation of the structure of **6-1**, with core Fe-O bonds shown as thicker black lines and pivalate Me groups omitted. Color code: Fe, green; O, red; N, blue; C, grey.

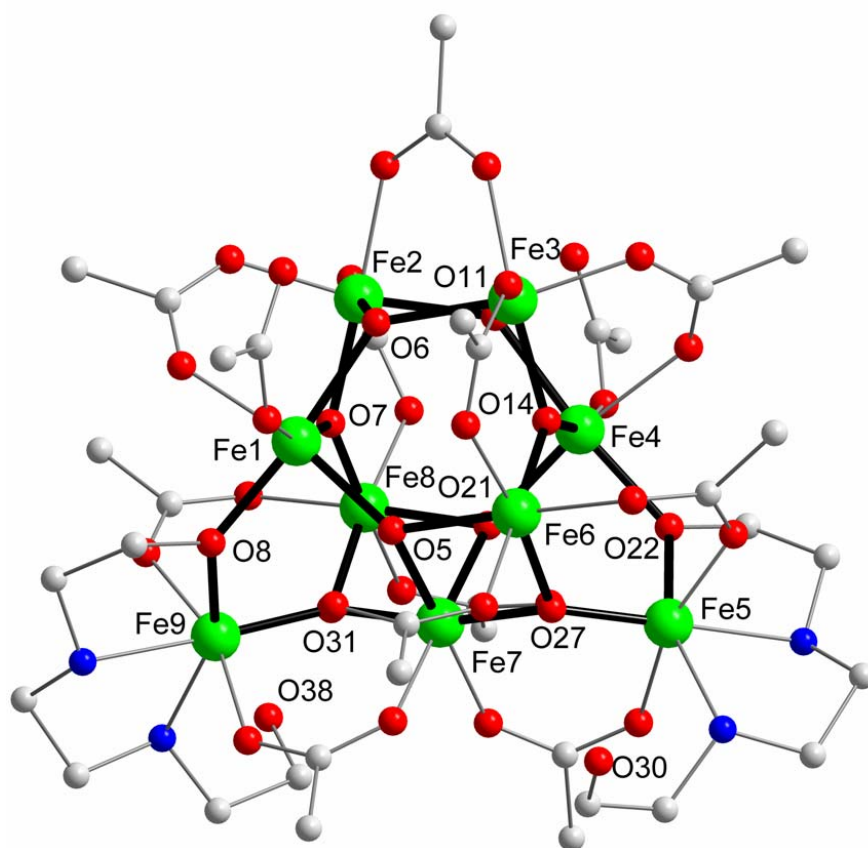


Figure 6-3. Labeled representation of the structure of **6-2** with only the *ipso* C atoms of benzoate rings shown for clarity. The core is outlined in bold. Color code: Fe, green; O, red; N, blue; C, grey.

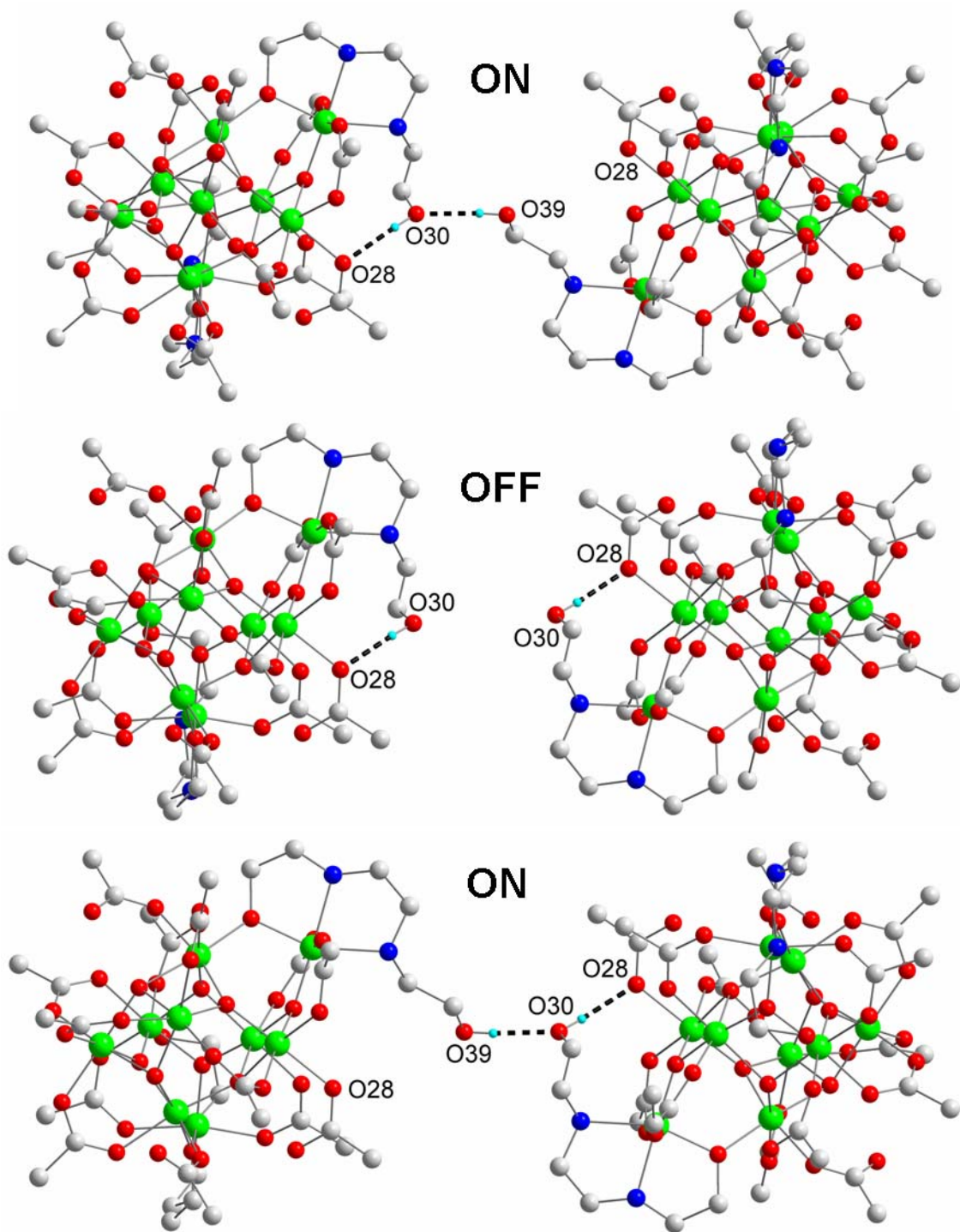


Figure 6-4. The [Fe₉]₂ dimer showing intermolecular (top, bottom) or only intramolecular (middle) O-H...O hydrogen-bonding, and the resultant ON or OFF state with respect to the coupling of the two molecules. Color code: Fe, green; O, red; N, blue; C, grey; H, sky blue.

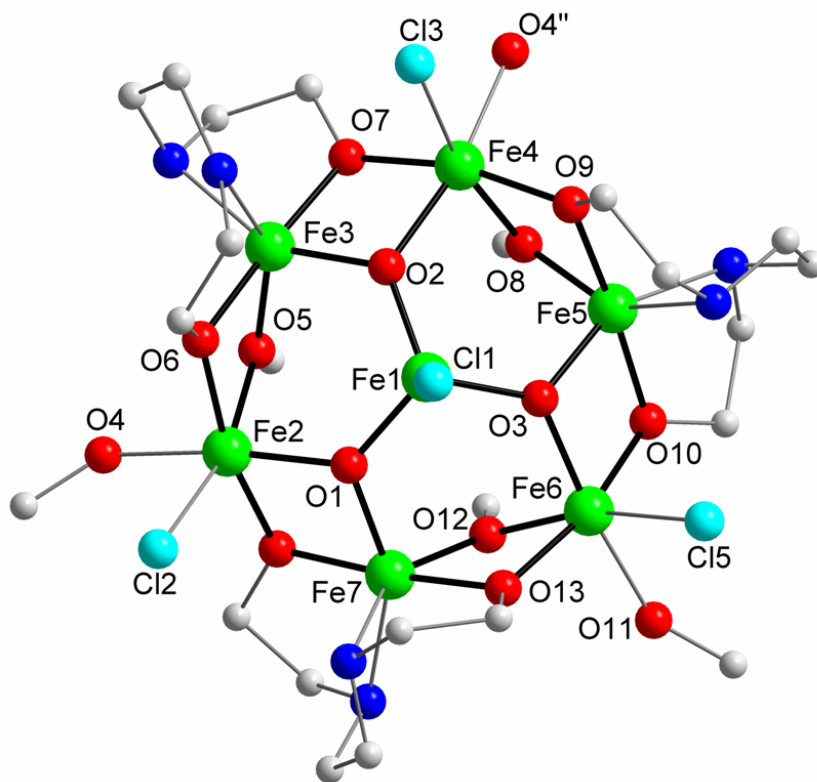


Figure 6-5. Labeled representation of the structure of **6-3**, with core Fe-O bonds shown as thicker black lines. Color code: Fe, green; Cl, cyan; O, red; N, blue; C, grey.

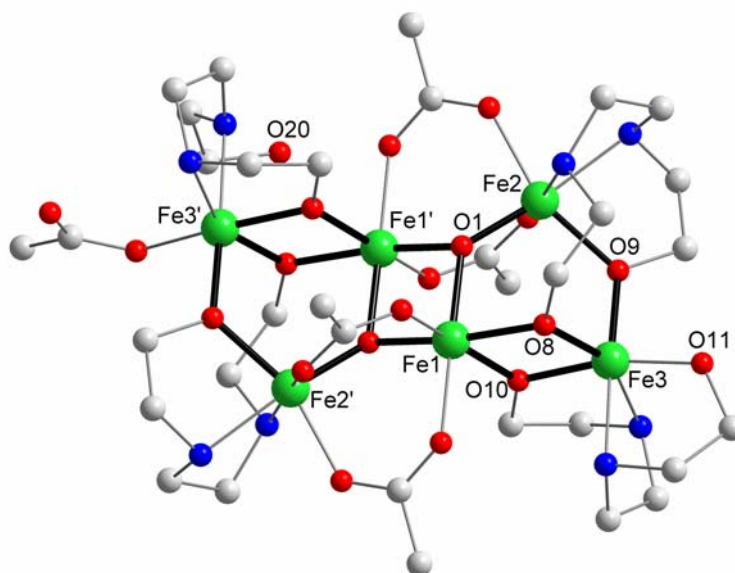


Figure 6-6. Labeled representation of the cation of **6-4** with only the *ipso* C atoms of benzoate rings shown for clarity. Core Fe-O bonds are shown as thicker lines. Colour code: Fe, green; O, red; N, blue; C, grey.

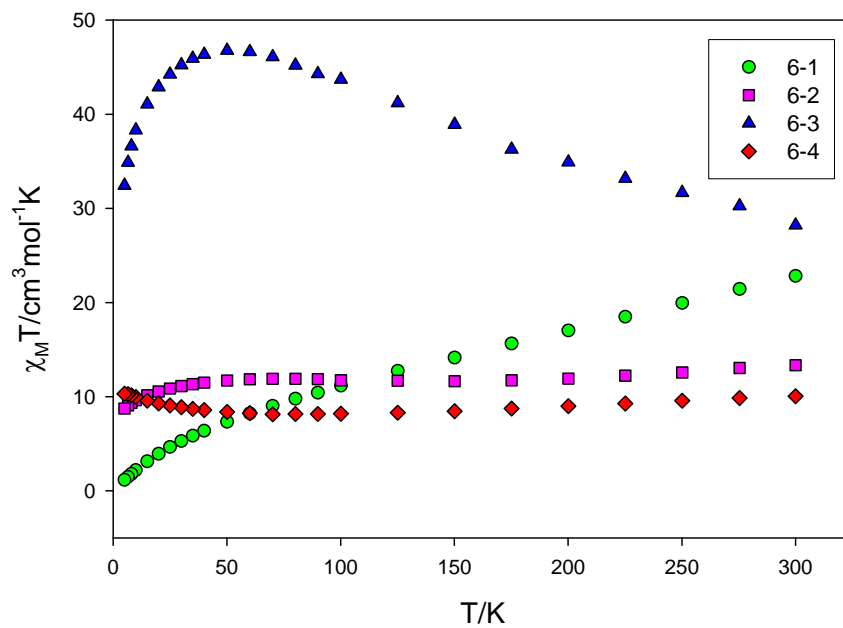


Figure 6-7. Plot of $\chi_M T$ vs T for complexes **6-1** to **6-4**.

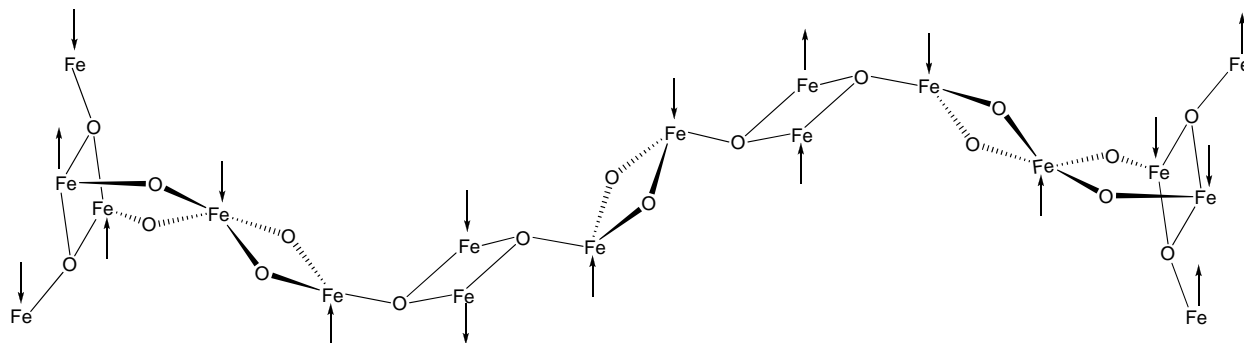


Figure 6-8. Spin alignments at the eighteen $S = 5/2$ Fe(III) atoms of **6-1** rationalizing its $S = 0$ ground state, based on the arguments given in the text

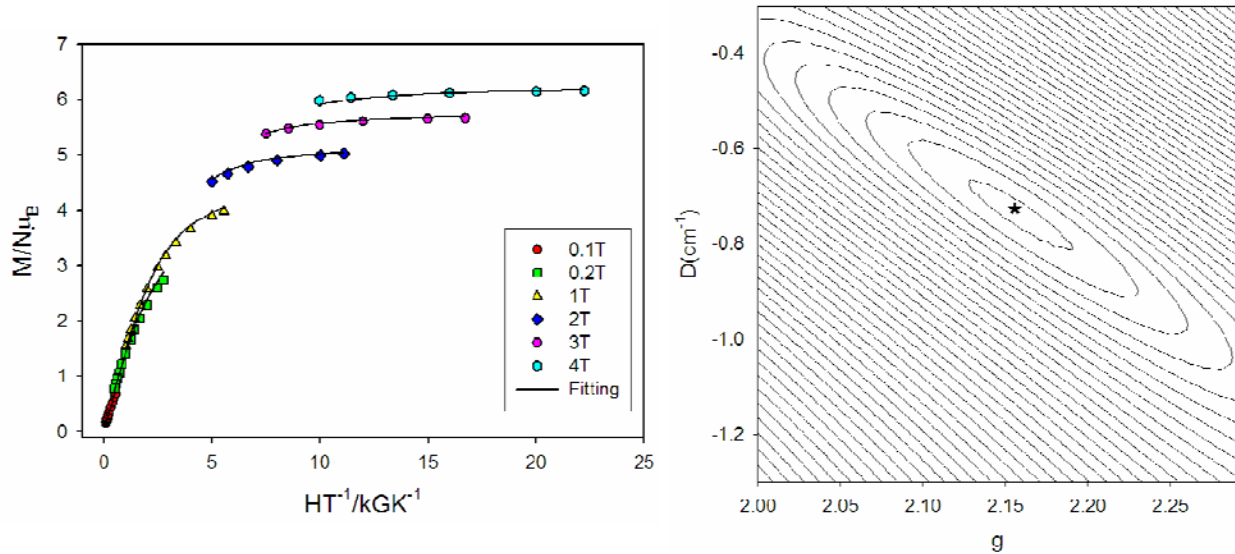


Figure 6-9. (left) Plot of reduced magnetization ($M/N\mu_B$) vs H/T for **6-2**. (right) Two-dimensional contour plot of the r.m.s. error vs D and g for the fit for **6-2**. The asterisk marks the best-fit position (error minimum).

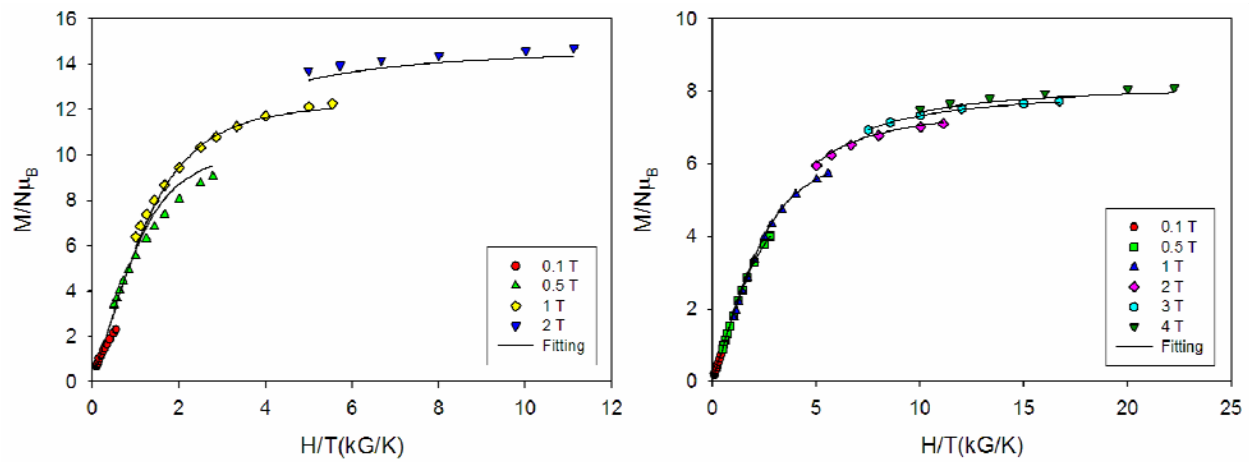


Figure 6-10. Plot of reduced magnetization ($M/N\mu_B$) vs H/T for **6-3** (left) and **6-4** (right).

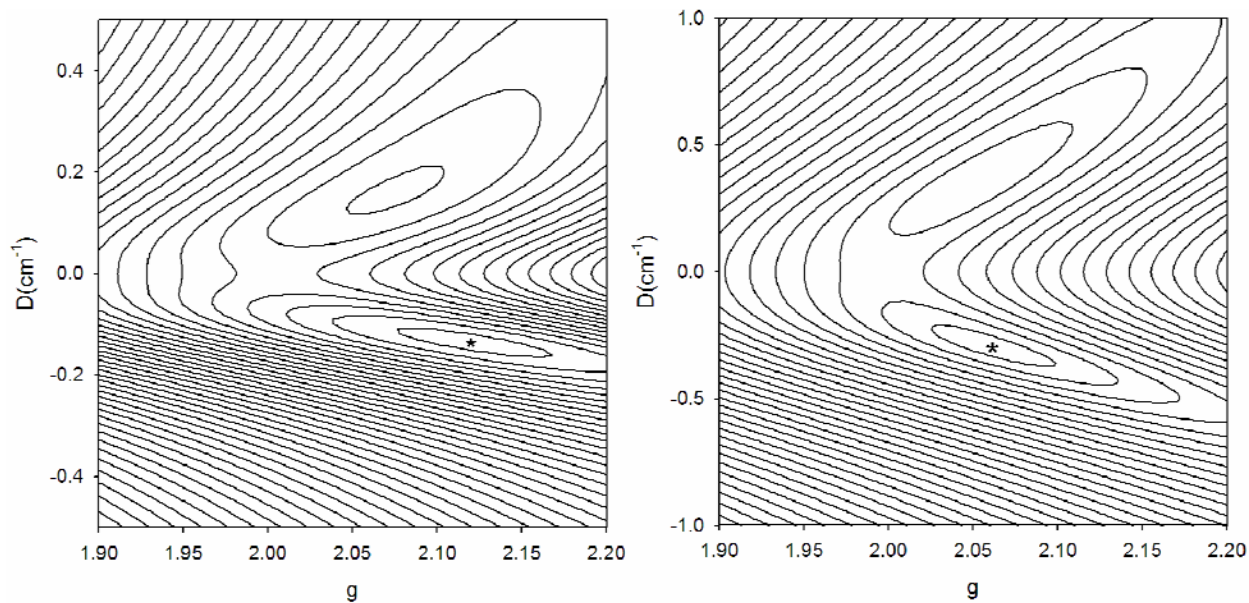


Figure 6-11. Two-dimensional contour plot of the r.m.s. error vs D and g for the fit for **6-3** (left) and **6-4** (right). The asterisk marks the best-fit position (error minimum).

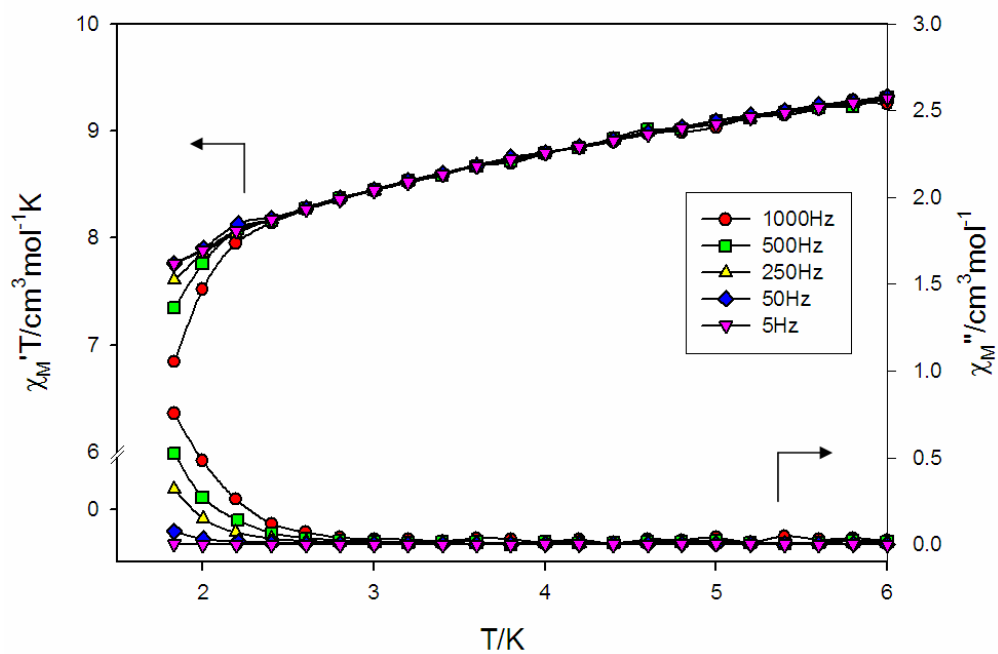


Figure 6-12. Plot of the in-phase (χ_M') and out-of-phase (χ_M'') ac susceptibility data for **6-2**.

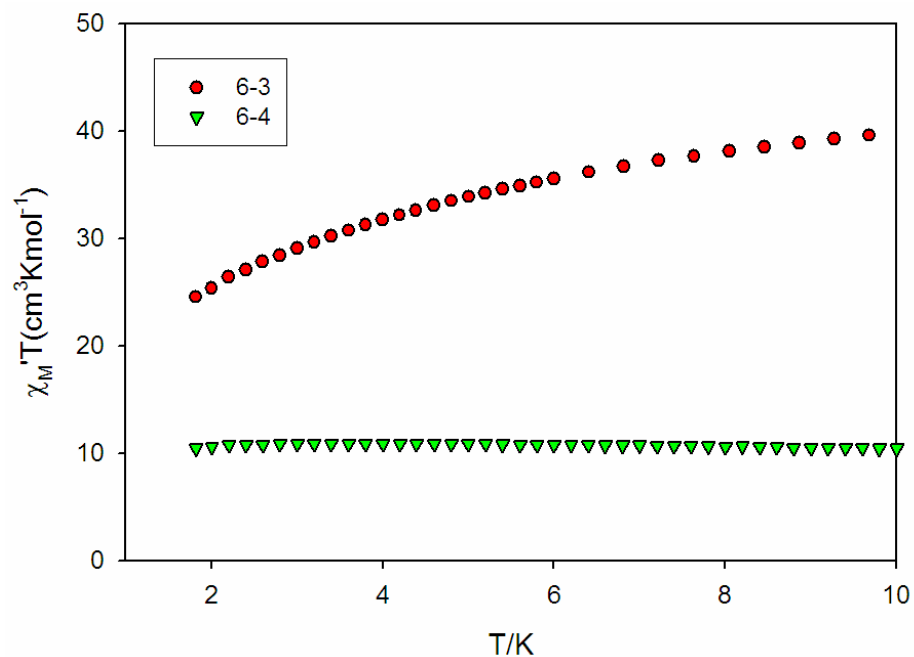


Figure 6-13. Plot of in-phase ac susceptibility data for **6-3** and **6-4**.

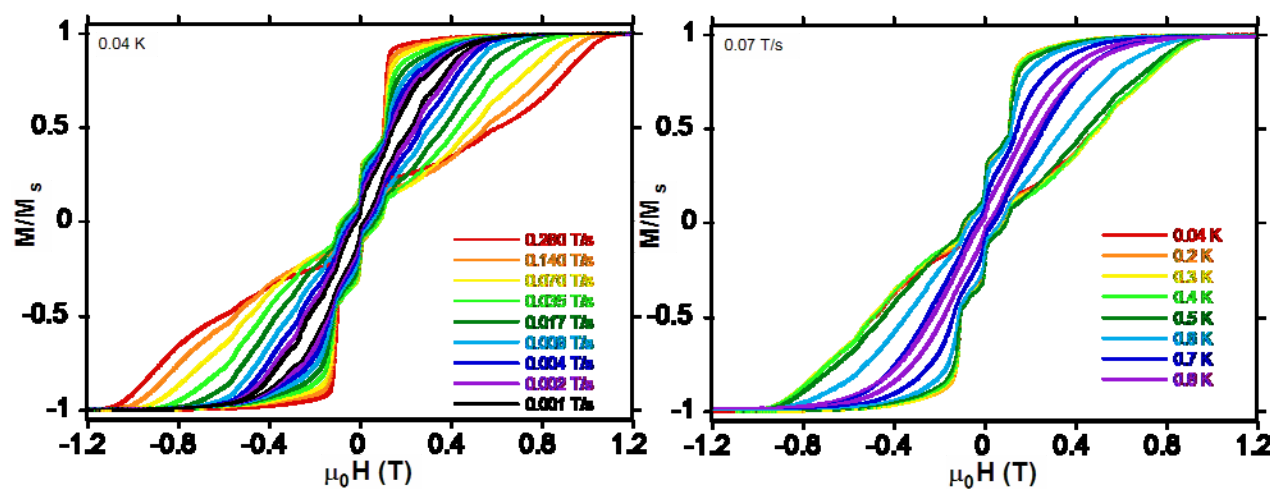


Figure 6-14. Single-crystal magnetization (M) vs dc field (H) hysteresis loops for **6-2** at different scan rates (left) and at various temperatures (right).

CHAPTER 7
UNUSUAL STRUCTURAL TYPES IN Mn AND Fe CHEMISTRY FROM THE USE OF
N,N,N',N' TETRAKIS (2-HYDROXYETHYL)ETHYLENEDIAMINE

7.1 Introduction

Interest in the preparation of polynuclear Mn and Fe complexes has developed worldwide for both fundamental scientific and technological reasons since the discovery that some of these molecules can behave as zero-dimensional nanoscale magnets now called single-molecule magnets (SMMs).^{13,22} Since then, many polynuclear clusters containing 3d transition metals have been reported to be SMMs,^{20,158-160} the vast majority of which are Mn complexes.^{21,161-164} In addition, polynuclear Mn and Fe compounds with O and N based ligation are of interest because of their relevance in bioinorganic chemistry.²⁶

For the above reasons and more, we continue to seek new synthetic methods to new Mn_x and Fe_x complexes. In the design of a potentially new synthetic route to a polynuclear cluster, the choice of the ligands and bridging groups is vital. As part of our continuing search for such new methods, we have begun exploring the use of chelating/bridging groups based on the ethylenediamine backbone. In chapter 4 and 6, we reported the use of *dmemH* and *heenH₂* (Figure 7-1) as new and flexible *N,N,O* and *O,N,N,O* chelates, respectively, for the synthesis of Fe_3 , Fe_6 , Fe_7 , Fe_9 and Fe_{18} complexes, some of which possess novel Fe_x topologies.^{93,145,146} The hydroxyethyl arms, on deprotonation, usually act as bridging groups and thus foster formation of a high nuclearity product. In the present work, we have extended this study by exploring the use in Mn and Fe cluster chemistry of the related, potentially hexadentate ligand *N,N,N',N'*-tetrakis(2-hydroxyethyl)ethylenediamine (*edteH₄*; Figure 7-1). The *edteH₄* molecule now provides four hydroxyethyl arms on an ethylenediamine backbone, and was considered an attractive potential new route to high nuclearity products. Previous use of *edteH₄* in the literature with other metals has been limited to the preparation only of mononuclear Ca and dinuclear Ba,

Cu and V complexes.¹⁶⁵⁻¹⁶⁷ We herein report that the use of edteH₄ in a variety of reactions with Mn reagents has yielded novel Mn₈, Mn₁₂ and Mn₂₀ complexes with core structures that are distinctly different from any seen previously.¹⁶⁸ The use of edteH₄ in Fe chemistry also leads to interesting new structural types of products, Fe₅, Fe₆ and Fe₁₂ complexes. The syntheses, structures and magnetochemical properties of these complexes will be described.¹⁶⁹

7.2 Experimental Section

7.2.1 Syntheses

All preparations were performed under aerobic conditions using reagents and solvents as received. [Mn₃O(O₂CPh)₆(py)₂H₂O],⁴⁵ [Fe₃O(O₂CPh)₆(H₂O)₃]NO₃ and [Fe₃O(O₂CBu^t)₆(H₂O)₃]OH was synthesized as reported elsewhere.^{94,95,170}

[Mn₈O₃(OH)(OMe)(O₂CPh)₇(edte)(edteH₂)](O₂CPh) (7-1). Method A. To a stirred solution of edteH₄ (0.05 g, 0.21 mmol) in CH₂Cl₂/MeOH (16/4 mL) was added [Mn₃O(O₂CPh)₆(py)₂H₂O] (0.23 g, 0.21 mmol). The mixture was stirred for 30 minutes, filtered, and the filtrate layered with Et₂O. X-ray quality dark orange-brown crystals of **7-1**·2CH₂Cl₂·MeOH slowly formed over a week. They were collected by filtration, washed with Et₂O and dried *in vacuo*. The yield was 40%. Dried solid appeared to be hygroscopic, analyzing as the dihydrate. Anal. Calcd (Found) for **7-1**·2H₂O (C₇₇H₉₀N₄Mn₈O₃₁): C, 46.08 (45.97); H, 4.52 (4.36); N, 2.79 (2.81). Selected IR data (cm⁻¹): 2868(w), 1649(w), 1595(m), 1547(m), 1447(w), 1383(s), 1315(m), 1174(w), 1122(w), 1066(m), 911(w), 719(m), 676(w), 603(m), 536(m).

Method B. To a stirred solution of edteH₄ (0.10 g, 0.42 mmol) in MeCN/MeOH (10/5 mL) was added NEt₃ (0.18 mL, 1.28 mmol) followed by Mn(O₂CPh)₂ (0.42 g, 1.26 mmol). The resulting mixture was stirred for one hour, filtered, and the filtrate layered with Et₂O. Dark orange-brown crystals of **7-1** slowly formed over 5 days and were then isolated as in Method A. The yield was 20%. The product was identified by IR spectral comparison with material from

Method A and elemental analysis. Anal. Calcd (Found) for **7-1**·2H₂O (C₇₇H₉₀N₄Mn₈O₃₁): C, 46.08 (45.79); H, 4.52 (4.37); N, 2.79 (2.76).

[Mn₁₂O₄(OH)₂(edte)₄Cl₆(H₂O)₂] (7-2). To a stirred solution of edteH₄ (0.15 g, 0.64 mmol) in MeCN/MeOH (10/1 mL) was added NEt₃ (0.09 mL, 0.64 mmol) followed by MnCl₂·4H₂O (0.25 g, 1.26 mmol). The solution was stirred for 2 hours and then filtered, and the brown filtrate was left undisturbed to evaporate slowly, giving X-ray quality crystals of **7-2**·6MeCN·½H₂O over five days. These were collected by filtration, washed with MeCN, and dried *in vacuo*. The yield was 25%. Dried solid analyzed as solvent-free. Anal. Calcd (Found) for **7-2** (C₄₀H₈₆N₈Mn₁₂O₂₄Cl₆): C, 24.83 (24.57); H, 4.48 (4.50); N, 5.79 (6.20); Cl, 10.99 (11.89). Selected IR data (cm⁻¹): 2854(m), 1631(w), 1465(w), 1359(w), 1270(w), 1160(w), 1088(s), 1059(s), 926(m), 899(m), 741(w), 669(m), 619(m), 557(m).

[Mn₂₀O₈(OH)₄(O₂CMe)₆(edte)₆](ClO₄)₂ (7-3). To a stirred solution of edteH₄ (0.10 g, 0.42 mmol) in MeOH (12 mL) was added NEt₃ (0.12 mL, 0.85 mmol) followed by Mn(O₂CMe)₂·4H₂O (0.21 g, 0.86 mmol) and then NaClO₄ (0.05 g, 0.41 mmol). The mixture was stirred for one hour, filtered, and the filtrate layered with Et₂O. X-ray quality dark orange-brown crystals of **7-3**·10MeOH slowly formed over a week. They were collected by filtration, washed with a little Et₂O, and dried *in vacuo*. The yield was 20%. Dried solid appeared to be hygroscopic, analyzing as the pentahydrate. Anal. Calcd (Found) for **7-3**·5H₂O (C₇₂H₁₅₂N₁₂Mn₂₀O₆₁Cl₂): C, 25.96 (25.92); H, 4.60 (4.69); N, 5.04 (4.54). Selected IR data (cm⁻¹): 2929(w), 1560(s), 1418(s), 1145(m), 1112(m), 1088(s), 910(m), 627(s), 563(m).

[Fe₅O₂(O₂CPh)₇(edte)(H₂O)] (7-4). To a stirred solution of edteH₄ (0.05 g, 0.21 mmol) in CH₂Cl₂ (15 mL) was added [Fe₃O(O₂CPh)₆(H₂O)₃](NO₃) (0.38 g, 0.37 mmol). The mixture was stirred for 30 minutes, filtered to remove undissolved solid, and the filtrate layered with a 1:1

(v/v) mixture of Et₂O and hexanes. X-ray quality orange crystals of **7-4**·CH₂Cl₂ slowly formed over a period of five days. These were collected by filtration, washed with Et₂O, and dried *in vacuo*. The yield was 20%. Anal. Calcd (Found) for **7-4** (C₅₉H₅₇N₂Fe₅O₂₁): C, 50.28 (50.63); H, 4.07 (4.27); N, 1.99 (1.85). Selected IR data (cm⁻¹): 2862(w), 1597(m), 1552(s), 1534(s), 1400(s), 1175(w), 1087(m), 1067(m), 1024(w), 928(w), 892(w), 863(w), 720(s), 653(m), 602(w), 529(w), 465(m).

[Fe₆O₂(O₂CBu')₈(edteH)₂] (7-5). To a stirred solution of edteH₄ (0.10 g, 0.42 mmol) in CHCl₃ (15 mL) was added [Fe₃O(O₂CBu')₆(H₂O)₃](OH) (0.18 g, 0.21 mmol). The mixture was stirred for 30 minutes, filtered to remove undissolved solid, and the filtrate layered with pentanes. X-ray quality orange crystals of **7-5**·2CHCl₃ slowly formed over a week. These were collected by filtration, washed with pentanes, and dried *in vacuo*. The yield was 10 %. Dried solid appeared to be very hygroscopic, analyzing as the tetrahydrate. Anal. Calcd (Found) for **7-5**·2CHCl₃·4H₂O (C₆₂H₁₂₄N₄Fe₆Cl₆O₃₀): C, 38.12 (37.98); H, 6.40 (6.33); N, 2.87 (3.24). Selected IR data (cm⁻¹): 2960(m), 2869(m), 1562(s), 1483(s), 1421(s), 1375(m), 1360(m), 1227(m), 1098(m), 1042(w), 909(w), 788(w), 694(m), 603(m), 554(m), 480(w), 429(m).

[Fe₁₂O₄(OH)₂(O₂CMe)₆(edte)₄(H₂O)₂](ClO₄)₄ (7-6). To a stirred solution of edteH₄ (0.10 g, 0.42 mmol) in MeCN (15 mL) was added NaO₂CMe·3H₂O (0.23 g, 1.69 mmol) followed by Fe(ClO₄)₃·6H₂O (0.39 g, 0.85 mmol). The mixture was stirred for 30 minutes, filtered to remove undissolved solid, and the filtrate left to slowly concentrate by evaporation. X-ray quality orange crystals of **7-6**·4MeCN slowly formed over a week. These were collected by filtration, washed with MeCN, and dried *in vacuo*. The yield was 40%. Anal. Calcd (Found) for **7-6** (C₅₂H₁₀₄N₈Fe₁₂Cl₄O₅₂): C, 25.13 (24.82); H, 4.22 (4.21); N, 4.51 (4.47). Selected IR data (cm⁻¹):

2884(m), 1559(s), 1455(s), 1336(w), 1271(w), 1086(s), 933(m), 904(m), 744(w), 624(s), 532(m), 466(w), 437(w).

[Fe₁₂O₄(OH)₈(edte)₄(H₂O)₂](ClO₄)₄ (7-7). To a stirred solution of edteH₄ (0.05 g, 0.21 mmol) in EtOH (15 mL) was added Fe(ClO₄)₃·6H₂O (0.39 g, 0.85 mmol). The mixture was stirred for 30 minutes, filtered to remove undissolved solid, and the filtrate left to slowly concentrate by evaporation. X-ray quality orange crystals of **7-7** slowly formed over a week. These were collected by filtration, washed with EtOH, and dried *in vacuo*. The yield was 20%. Anal. Calcd (Found) for **7-7** (C₄₀H₉₂N₈Fe₁₂Cl₄O₄₆): C, 21.66 (21.51); H, 3.74 (4.15); N, 5.31 (5.02). Selected IR data (cm⁻¹): 2867(m), 1628(w), 1469(w), 1363(w), 1270(w), 1088(s), 935(m), 910(m), 740(w), 661(m), 627(s), 583(w), 490(m).

[Fe₁₂O₄(OH)₈(edte)₄(H₂O)₂](NO₃)₄ (7-8). To a stirred solution of edteH₄ (0.10 g, 0.42 mmol) in MeOH (15 mL) was added NEt₃ (0.12 mL, 0.85 mmol) followed by Fe(NO₃)₃·9H₂O (0.34 g, 0.85 mmol). The mixture was stirred for 30 minutes, and filtered to remove undissolved solid. Vapor diffusion of THF into the filtrate gave needle-like orange crystals of **7-8**. These were collected by filtration, washed with THF, and dried *in vacuo*. The yield was 10%. Anal. Calcd (Found) for **7-8** (C₄₀H₉₂N₁₂Fe₁₂O₄₂): C, 23.29 (23.06); H, 4.61 (4.45); N, 8.12 (8.07). Selected IR data (cm⁻¹): 2938(w), 2677 (m), 1650(w), 1385(s), 1171(w), 1057(m), 934(m), 909(m), 825(m), 636(m), 613(w), 525(w), 492(m).

7.2.2 X-ray Crystallography

Data were collected by Dr. Khalil A. Abboud on a Siemens SMART PLATFORM equipped with a CCD area detector and a graphite monochromator utilizing Mo-K_α radiation ($\lambda = 0.71073 \text{ \AA}$). Suitable crystals of **7-1**·2CH₂Cl₂·MeOH, **7-2**·6MeCN·½H₂O, **7-3**·10MeOH, **7-4**·CH₂Cl₂, **7-5**·2CHCl₃, **7-6**·4MeCN and **7-7** were attached to glass fibers using silicone grease and

transferred to a goniostat where they were cooled to 173 K for data collection. Cell parameters were refined using up to 8192 reflections. A full sphere of data (1850 frames) was collected using the ω -scan method (0.3° frame width). The first 50 frames were remeasured at the end of data collection to monitor instrument and crystal stability (maximum correction on I was < 1 %). Absorption corrections by integration were applied based on measured indexed crystal faces. The structure was solved by direct methods in *SHELXTL6*,⁴⁶ and refined on F^2 using full-matrix least squares. The non-H atoms were treated anisotropically, whereas the hydrogen atoms were placed in ideal, calculated positions and were refined as riding on their respective C atoms.

For **7-1**·2CH₂Cl₂·MeOH, the asymmetric unit consists of the Mn₈ cation, a benzoate anion, and one MeOH and two CH₂Cl₂ molecules. The solvent molecules were disordered and could not be modeled properly, thus program SQUEEZE,⁶⁸ a part of the PLATON package of crystallographic software, was used to calculate the solvent disorder area and remove its contribution to the overall intensity data. A total of 1068 parameters were refined in the final cycle of refinement using 10920 reflections with $I > 2\sigma(I)$ to yield R₁ and wR₂ of 3.34 and 8.12%, respectively.

For **7-2**·6MeCN·½H₂O, the asymmetric unit contains ¼ of the Mn₁₂ cluster, two ¼ MeCN molecules, one MeCN in a general position, and a 1/8 water molecule. All solvent molecules were disordered and could not be modeled properly, thus program SQUEEZE⁶⁸ was used to calculate the solvent disorder area and remove its contribution to the overall intensity data. A total of 204 parameters were refined in the final cycle of refinement using 2799 reflections with $I > 2\sigma(I)$ to yield R₁ and wR₂ of 4.64 and 10.46%, respectively.

For **7-3**·10MeOH, the asymmetric unit consists of half the Mn₂₀ cluster, one ClO₄⁻ anion, and five MeOH molecules. The latter were disordered and could not be modeled properly, thus

program SQUEEZE⁶⁸ was again used to calculate the solvent disorder area and remove its contribution to the overall intensity data. The cluster exhibits two disorders: A large part of the N4 ligand is disordered and was refined in two parts; attempts to resolve the two parts of C17'-C18' were not successful, and thus this part remained common to both. C28 is also disordered and was also refined in two parts. The two parts of each disorder were dependently refined. Three O atoms of the ClO₄⁻ anion containing Cl2 were also disordered and were refined in two parts related by rotation along the Cl2-O32 axis. A total of 687 parameters were refined in the final cycle of refinement using 6689 reflections with $I > 2\sigma(I)$ to yield R₁ and wR₂ of 8.12 and 21.74%, respectively.

For **7-5**·2CHCl₃, the asymmetric unit consists of half an Fe₆ cluster and a CHCl₃ molecule. Two Bu^t groups are disordered and were refined in two parts each. A total of 481 parameters were refined in the final cycle of refinement using 6037 reflections with $I > 2\sigma(I)$ to yield R₁ and wR₂ of 5.75 and 13.64%, respectively.

For **7-6**·4MeCN, the asymmetric unit consists of the Fe₁₂ cluster, three whole and two half perchlorate anions, which are all disordered, and four MeCN molecules, three of which are very disordered. Program SQUEEZE,⁶⁸ a part of the PLATON package of crystallographic software, was used to calculate the solvent disorder area and remove its contribution to the overall intensity data. The N9 MeCN molecule was not removed by SQUEEZE⁶⁸ because it is hydrogen-bonded to the O17-H17 hydroxyl group and not disordered. The Cl1 perchlorate is hydrogen-bonded to the opposite hydroxyl group (O17-H17) through O38. While each disordered perchlorate anion was refined in two parts, the second part of the Cl3 (Cl3') was not complete, only one O atom being located. The charges are balanced by the fact that the groups occupying the O5 and O27 positions represent a disorder between a water molecule and a carboxyl group.

The others could not be found due to the heavy disorder. Finally, the hydroxyl protons and the coordinated water protons were obtained from a difference Fourier map and included as riding on their parent O atoms. A total of 1165 parameters were refined in the final cycle of refinement using 10158 reflections with $I > 2\sigma(I)$ to yield R_1 and wR_2 of 7.88 and 22.19%, respectively.

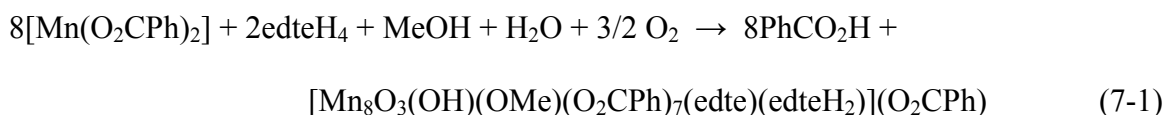
Severe disorder problems were encountered for **7-4**·CH₂Cl₂ and **7-7**. For **7-4**·CH₂Cl₂, the asymmetric unit consists of an Fe₅ cluster and a dichloromethane molecule; the structure exhibited much disorder in the benzoate phenyl rings and edte⁴⁻ groups, preventing satisfactory refinement of the structure. However, the core was well observed and showed no disorder. For **7-7**, the asymmetric unit consists of half a Fe₁₂ cluster and two perchlorate anions; again, the structure exhibited bad disorder among the peripheral ligands. Despite examination of many crystals of both compounds, we could not find ones that diffracted well enough to allow data of sufficient quantity and quality to be obtained for satisfactory structure refinement. Thus, the structures were refined as far as possible so that we could at least identify the overall structure and nuclearity of the complexes for comparison with **7-5** and **7-6**, which we were able to successfully do. Knowing the number and arrangement of the Fe atoms in the core was also essential for the interpretation of the magnetic data of **7-4** and **7-7**. We include and briefly describe the structures of these two complexes in this chapter only for the mentioned purposes; the metric parameters are unreliable and are not discussed. Unit cell data and details of the structure refinements for complexes **7-1** to **7-3** are listed in Table 7-1 and **7-4** to **7-7** are listed in Table 7-2.

7.3 Results and Discussion

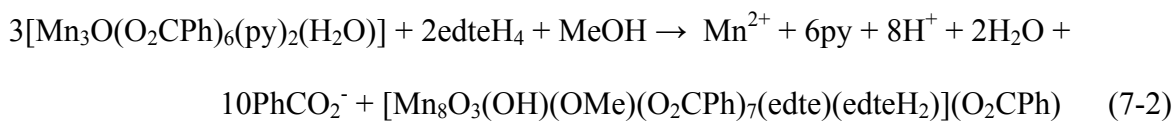
7.3.1 Syntheses

In order to make clusters containing Mn^{III} ions, it is generally necessary to either oxidize simple Mn^{II} salts, or use preformed higher oxidation state Mn_x clusters. Both of these strategies

have previously proved to be useful routes to a variety of higher nuclearity complexes with chelating ligands ranging from bidentate to pentadentate.^{34,35,43,63,171,172} Therefore, we decided to employ them both with the potentially hexadentate ligand edteH₄. Thus, a variety of reaction ratios, reagents, and other conditions were investigated. The reaction of edteH₄ with Mn(O₂CPh)₂ and NEt₃ in a 1:3:3 molar ratio in MeOH afforded a reddish-brown solution from which was subsequently obtained the octanuclear complex [Mn₈O₃(OH)(OMe)(O₂CPh)₇(edte)(edteH₂)](O₂CPh) (**7-1**) in ~20% yield. Its formation is summarized in eq. 7-1, where atmospheric oxygen gas is assumed to provide the oxidizing equivalents required to form the mixed-valence 6Mn^{III}, 2Mn^{II} product.



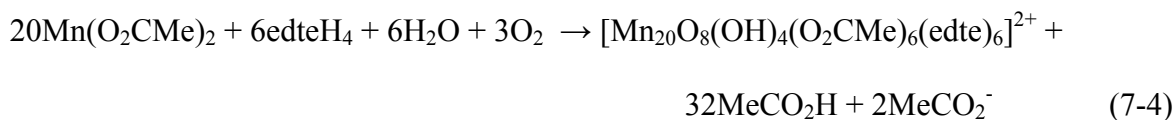
Complex **7-1** was also obtained, and in a higher yield of ~40%, from the reaction of edteH₄ with [Mn₃O(O₂CPh)₆(py)₂H₂O] in a 1:1 molar ratio in CH₂Cl₂/MeOH. Such trinuclear [Mn₃O] clusters have often proved to be very useful starting materials for the synthesis of higher nuclearity products, some of which have also been new SMMs.^{38,173} The formation of **7-1** via this route is summarized in eq. 7-2. The mixed solvent system was needed to ensure adequate solubility of all reagents, and it also led to methoxide incorporation; no isolable products were obtained when only CH₂Cl₂ was used. Small variations in the Mn:edteH₄:PhCO₂⁻ ratio also gave complex **7-1**, which clearly is a preferred product of these components, and with benzoate. When [Mn₃O(O₂CR)₆(py)₃]^{0,+} clusters with other R groups were employed, we were unable to isolate pure, crystalline materials for satisfactory characterization.



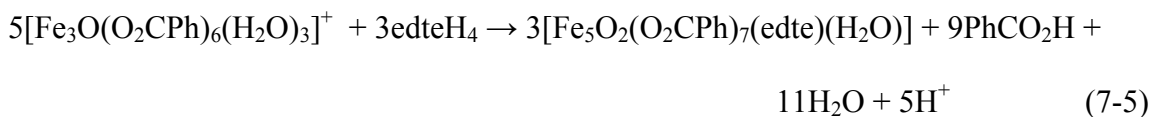
The reaction of edteH₄ with MnCl₂·4H₂O, and NEt₃ in 1:2:1 molar ratio in MeCN/MeOH gave a brown solution from which was isolated [Mn₁₂O₄(OH)₂(edte)₄Cl₆(H₂O)₂] (**7-2**) in 25% yield. As found for **7-1**, complex **7-2** is mixed-valent, containing 8Mn^{III} and 4Mn^{II} ions, and its formation is summarized in eq. 7-3, again assuming the participation of atmospheric O₂. Increasing or decreasing the amount of edteH₄ or NEt₃ also gave complex **7-2**, but the product was not as pure. We were also unable to isolate any clean products when we employed an MeCN/EtOH solvent system.



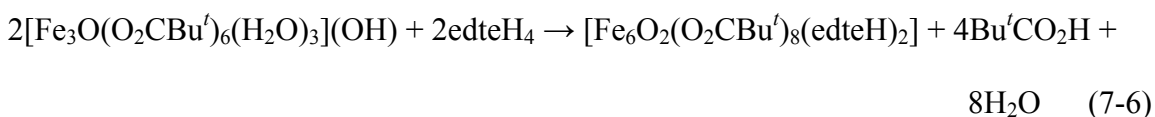
Finally, the reaction of edteH₄ with Mn(O₂CMe)₂ and NEt₃ in a 1:2:2 ratio in MeOH, followed by addition of NaClO₄, gave a dark orange-brown solution from which was subsequently isolated [Mn₂₀O₈(OH)₄(O₂CMe)₆(edte)₆](ClO₄)₂ (**7-3**) in 20% yield. This product is once again mixed-valence, containing 12Mn^{III}, 8Mn^{II} ions, and its formation is summarized in eq. 7-4, with O₂ again included as the oxidizing agent.



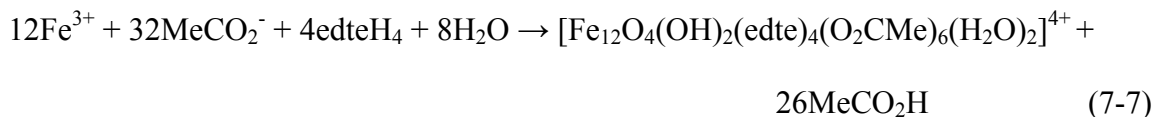
A variety of reactions of edteH₄ were explored with a number of different Fe(III) starting materials and under different reagent ratios, solvents and other conditions before the following successful procedures were identified. The reaction of [Fe₃O(O₂CPh)₆(H₂O)₃](NO₃) with edteH₄ in a ~3:2 molar ratio in CH₂Cl₂ followed by layering with Et₂O - hexanes (1:1 v/v) gave orange needle-like crystals of [Fe₅O₂(O₂CPh)₇(edte)(H₂O)] (**7-4**). Its formation is summarized in eq. 7-5. The benzoate groups clearly function as proton acceptors facilitating the deprotonation of edteH₄ in the absence of added base.



With other chelates such as dmemH,⁹³ we have found that the identity of the Fe_x product depends on the carboxylate employed,⁹³ and thus we also explored reactions of edteH₄ with other [Fe₃O(O₂CR)₆(H₂O)₃]⁺ reagents. With pivalate (R = Bu^t), a related reaction to that which gave **7-4**, but with a [Fe₃O(O₂CBu^t)₆(H₂O)₃]⁺ to edteH₄ molar ratio of 1:2 in CHCl₃, gave a brown solution and subsequent isolation of [Fe₆O₂(O₂CBu^t)₈(edteH)₂] (**7-5**) on layering with pentanes. The proton acceptors in this reaction are the carboxylate groups and the OH⁻ anions; the formation of **7-5** is summarized in eq. 7-6.



The same product was also obtained using CH₂Cl₂ as the solvent, but in poor crystallinity and decreased yield. We also explored the use of simple Fe(III) salts as reagents, in the presence of added carboxylate groups as proton acceptors. The reaction of Fe(ClO₄)₃·6H₂O with edteH₄ and NaO₂CMe·3H₂O in a 2:1:4 ratio in MeCN gave a brown solution from which was obtained [Fe₁₂O₄(OH)₂(edte)₄(O₂CMe)₆(H₂O)₂](ClO₄)₄ (**7-6**). Its preparation is summarized in eq. 7-7.



Decreasing the the amount of acetate from 4 to 2 equiv drastically reduced the reaction yield, as expected from eq. 7-7. Complex **7-6** was also obtained from a MeCN:MeOH solvent system. However, when the reaction of Fe(ClO₄)₃·6H₂O with edteH₄ in a 4:1 ratio was carried out in neat EtOH in the absence of NaO₂CMe, the product was [Fe₁₂O₄(OH)₈(edte)₄(H₂O)₂](ClO₄)₄ (**7-7**), obtained as orange needles on layering the solution with CHCl₃. Complex **7-7** is

structurally very similar to **7-6**, except that the acetate groups have been replaced by hydroxide ions (vide infra). In a related fashion, the reaction of $\text{Fe}(\text{NO}_3)_3$ with edteH_4 and NEt_3 in a 2:1:2 ratio in MeOH gave $[\text{Fe}_{12}\text{O}_4(\text{OH})_8(\text{edte})_4(\text{H}_2\text{O})_2](\text{NO}_3)_4$ (**7-8**) on vapor diffusion with tetrahydrofuran. The product was identified by elemental analysis, and IR and magnetic comparisons with complexes **7-6** and **7-7** (vide infra).

It is clear that the described reactions to complexes **7-1 to 7-8** are very complicated and involve acid/base and redox chemistry, as well as structural fragmentations and rearrangements. As a result, the reaction solutions likely contain a complicated mixture of several species in equilibrium. For this reason, we were happy to settle for the relatively low yields of **7-1 to 7-8**, given that the products were reproducibly obtained in a pure, crystalline form from the described procedures.

7.3.2 Description of Structures

7.3.2.1 Structure of $[\text{Mn}_8\text{O}_3(\text{OH})(\text{OMe})(\text{O}_2\text{CPh})_7(\text{edte})(\text{edteH}_2)](\text{O}_2\text{CPh})$ (**7-1**)

A labeled representation of the cation of **7-1** is shown in Figure 7-2, and selected interatomic distances and angles are summarized in Table A-16. Complex **7-1** crystallizes in the monoclinic space group $P2_1/n$. The core is mixed valence (6Mn^{III} , 2Mn^{II}), with Mn3 and Mn6 being the Mn^{II} ions, and contains a $[\text{Mn}_7\text{O}_7]$ subunit consisting of two distorted $[\text{Mn}^{\text{III}}_3\text{Mn}^{\text{II}}(\mu_5\text{-O})(\mu_3\text{-O})(\mu_3\text{-OR})_2]^{5+}$ cubanes sharing the Mn6-O1 edge. This double-cubane unit is additionally bridged by a $\mu\text{-OMe}^-$ (O21) between Mn7/Mn8 and a $\mu_3\text{-OH}^-$ (O6) between Mn2/Mn4. The latter $\mu_3\text{-OH}^-$ additionally connects the double-cubane to the eighth Mn atom, Mn3. The edteH_2^{2-} group is hexadentate-chelating on Mn^{II} atom Mn3, with the two deprotonated alkoxide O atoms, O7 and O10, bridging to Mn2 and Mn4, respectively, and thus the edteH_2^{2-} group is overall μ_3 -bridging; oxygen atoms O8 and O9 are protonated. The edte^{4-} group is also hexadentate chelating to a Mn^{II} atom, Mn6, with the four deprotonated alkoxide O atoms all adopting μ_3 bridging

modes within the double-cubane, and thus the edte⁴⁻ group is overall μ_7 -bridging. The chelating/bridging modes of the μ_7 -edte⁴⁻ and μ_3 -edteH₂²⁻ groups are shown in Figures 7-3(a) and (b), respectively. The remaining ligation is provided by seven benzoate groups, five of which are $\eta^1:\eta^1:\mu$ -bridging and the remaining two are η^1 terminal on Mn1 and Mn5.

The oxidation states of the Mn atoms and the protonation levels of O²⁻, OH⁻, OMe⁻ and OR⁻ groups were determined from a combination of charge balance considerations, inspection of bond lengths, and bond valence sum (BVS) calculations.^{48,49,103} BVS values for Mn and O atoms are listed in Table 7-3 and 7-4, respectively. All the Mn^{III} atoms are six-coordinate and display a Jahn-Teller (JT) elongation, as expected for high spin Mn^{III} in octahedral geometry, with the JT axes (shown as thicker black bonds in Figure 7-2) not co-parallel. The Mn^{II} atoms, Mn3 and Mn6, are seven coordinate. The anion of complex **1** is a PhCO₂⁻ group (not shown in Figure 7-2), which forms an intimate ion-pair with the Mn₈ cation by hydrogen-bonding with O6 of the μ_3 -OH⁻ ion (O6...O29 = 2.580 Å) and O8 of an edteH₂²⁻ protonated alcohol arm (O8...O28 = 2.584 Å). This also has the effect of raising the BVS of μ_3 -OH⁻ ion O6 to 1.43, higher than normally expected for a OH⁻ group (1.0-1.2). The BVS for O8 (1.21) is much less affected by the hydrogen-bonding (compare with 1.17 for O9), no doubt due to the only monodentate binding of O8, which thus retains greater basicity and a stronger O-H bond than the μ_3 -OH⁻ ion.

A number of other Mn₈ complexes have previously been reported. These possess a variety of metal topologies such as rod-like, serpentine, rectangular, linked Mn₄ butterfly units, linked tetrahedral, etc,^{67,174-188} but none have possessed the core of complex **7-1**, which is unprecedented. In addition to this novel core structure, another unusual feature of **7-1** is the presence of its μ_5 -O²⁻ ion, O1. There are only two previous structural types with a μ_5 -O²⁻ ion in molecular Mn chemistry, certain Mn₁₂^{189,190} and Mn₁₃¹⁹¹⁻¹⁹³ complexes.

7.3.2.2 Structure of $[\text{Mn}_{12}\text{O}_4(\text{OH})_2(\text{edte})_4\text{Cl}_6(\text{H}_2\text{O})_2]$ (7-2)

The labeled structure of **7-2** is shown in Figure 7-4, and selected interatomic distances and angles are listed in Table A-17. Complex **7-2** crystallizes in the tetragonal space group $P4/ncc$ with the Mn_{12} molecule lying on an S_4 symmetry axis and thus only $1/4$ of it in the asymmetric unit. The structure consists of a $[\text{Mn}^{\text{III}}_8\text{Mn}^{\text{II}}_4(\mu_4\text{-O})_4(\mu\text{-OH})_2(\mu\text{-Cl})_4(\mu_3\text{-OR})_4(\mu\text{-OR})_{12}]^{2+}$ core consisting of two near-planar Mn_6 layers sandwiched between three near-planar layers of O atoms (Figure 7-4, bottom). For the sake of brevity, reference to specific atoms in the following discussion includes their symmetry-related partners. BVS calculations for the Mn atoms (Table 7-5) identified Mn1, Mn2 and Mn3 as Mn^{II} , Mn^{III} and Mn^{III} atoms, respectively. Mn1 and Mn2 are six coordinate while Mn3 is seven coordinate. The four $\mu_4\text{-O}^{2-}$ ions (O1) together serve to connect all twelve Mn atoms. Each edte^{4-} group is hexadentate-chelating on a Mn^{III} atom, Mn3, with each of its deprotonated alkoxide arms bridging to either one (O3, O5, O6) or two (O2) additional Mn atoms. Thus, the edte^{4-} groups are overall μ_5 -bridging, as shown in Figure 7-3(c).

Charge balance considerations require that, with eight Mn^{III} , four Mn^{II} , four O^{2-} and four edte^{4-} groups, there must be eight additional negatively charged ligands to give neutral complex **7-2**. The simplest conclusion is that with eight apparent Cl^- ions in the complex, the two $\mu\text{-O}$ atoms O4 and O4' bridging Mn2 atoms belong to H_2O groups. However, we were unhappy with this conclusion, being unaware of any precedent in the literature for H_2O groups bridging two Mn^{III} atoms; the high Lewis acidity of two Mn^{III} would be expected to make the water molecule in a $[\text{Mn}^{\text{III}}_2(\mu\text{-OH}_2)]$ unit very (Bronsted) acidic (very low pK_a) and unlikely to be stable. In contrast, a water molecule bridging two Mn^{II} atoms is known.¹⁹⁴⁻¹⁹⁷ We thus decided to determine the protonation levels of all O atoms in **7-2** by BVS calculations, and the results are listed in Table 7-5. The oxide and edte^{4-} O atoms have BVS values of >1.89 , confirming them as completely deprotonated, as concluded above from their bridging modes. In contrast, O4 has a

BVS of only 0.99, as expected for an OH⁻ group. In addition, the Mn2-O4 bond length of 2.0098(15) Å is typical of Mn^{III}-OH⁻ bond lengths in the literature.¹⁹⁸⁻²⁰⁰ This is a more realistic bridging group between two Mn^{III} atoms. Thus, we conclude that O4 and O4' are OH⁻ groups. This now requires six additional anionic ligands for a neutral molecule, and we suspected that the *S*₄ symmetry was masking a disorder between the Cl⁻ and a neutral ligand such as H₂O at the terminal positions (Cl1). Crystallographic refinement of these terminal Cl atoms was inconclusive as to whether there was a Cl/H₂O disorder, and so we investigated the Cl content of the molecule more directly with a chlorine elemental analysis. This did indeed give a value less than expected for eight Cl atoms, whose formula of [Mn₁₂O₄(H₂O)₂(edte)₄Cl₈] would have a calculated 14.40% Cl content, much higher than the experimental 11.89%. The latter is, however, consistent with the expected six Cl⁻ ions that are required for the observed neutrality of complex **7-2** if O4 is a OH⁻ ion. Thus, we conclude that the correct formula of **7-2** is [Mn₁₂O₄(OH)₂(edte)₄Cl₆(H₂O)₂]. Note that for the reasons already mentioned, we disfavor the H₂O groups being disordered with Cl at the μ-Cl⁻ positions (Cl2) bridging Mn^{III}Mn^{II} pairs, but this is not as unlikely as water bridging two Mn^{III} atoms, and thus cannot be completely ruled out. Indeed, maybe the two water molecules are disordered amongst the eight bridging and terminal positions, and this is why the crystallographic refinement is fine with eight Cl atoms. Recently, a complex apparently identical to complex **7-2** was reported by Zhou et al., but who instead formulated it as [Mn₁₂O₄(H₂O)₂(edte)₄Cl₈].²⁰¹

There are many other structural types of Mn₁₂ complexes already in the literature, the most well-studied being the [Mn₁₂O₁₂(O₂CR)₁₆(H₂O)₄] (Mn₁₂) family, which has been extended over the years to include one, two and three-electron reduced [Mn₁₂]^{Z-} (Z = 0 - 3) versions.^{12,202-207} Another Mn₁₂ family of complexes was more recently obtained by reductive aggregation of

MnO₄⁻ in MeOH-containing media; this family differs from the previous one in having a central Mn^{IV}₄ rhombus rather than a Mn^{IV}₄ tetrahedron.^{208,209} The remaining Mn₁₂ complexes cover a variety of other structural types, including loops and more complicated face-sharing cuboidal units, amongst others.^{189,210-215}

7.3.2.3 Structure of [Mn₂₀O₈(OH)₄(O₂CMe)₆(edte)₆](ClO₄)₂ (**7-3**)

The structure of the cation of **7-3** is shown in Figures 7-5 and 7-6, the latter providing the atom labeling. Selected interatomic distances and angles are listed in Table A-18. Complex **7-3** crystallizes in the monoclinic space group *P2*₁/*c* with the Mn₂₀ cation lying on a crystallographic inversion center; again, reference to a specific atom will include its symmetry-related partner. The cation can be described as consisting of two sets of three edge-sharing [Mn₄O₄] cubanes (Figure 7-5, middle), with the upper and lower sets connected by face-sharing to give a 3 x 2 arrangement of six cubanes. This central [Mn₁₄O₁₆] unit is then attached to three additional Mn ions at each end by additional O atoms (Figure 7-5, bottom). This gives an overall tube-like arrangement of twenty Mn atoms inside of which are four O²⁻ ions. Note that the Mn₇ edge-sharing double-cubane structure of complex **7-1** is a recognizable sub-fragment of the central [Mn₁₄O₁₆] unit of **7-3**, and thus **7-3** can be considered a more extended version of **7-1**. The overall core is thus [Mn^{III}₁₂Mn^{II}₈(μ₆-O)₂(μ₄-O)₂(μ₃-O)₄(μ-OH)₄(μ₃-OR)₁₀(μ-OR)₁₄]²⁺ with the two μ₆-O (O24), two μ₄-O (O19) and four μ₃-O (O20, O22) atoms being O²⁻ ions. The four μ-OH groups, O21 and O23, (The BVS values of O21 and O23 are 1.19 and 1.20 respectively) bridge Mn8/Mn9' and Mn5/Mn9, respectively, and thus provide additional linkages between the cubanes. The ten μ₃-OR and fourteen μ-OR oxygen atoms are provided by the alkoxide arms of six edte⁴⁻ groups. As seen in **7-1** and **7-2**, each edte⁴⁻ group binds as a hexadentate chelate to one Mn and then bridges through its deprotonated alkoxide arms to a number of additional Mn atoms; four edte⁴⁻ groups are overall μ₅-bridging, and the remaining two are μ₇-bridging, and

these modes are shown in Figures 7-3(c) and (d), respectively. The remaining ligation in the molecule is provided by six acetate groups, two of which are $\eta^1:\eta^1:\mu$ -bridging, two are η^2 chelating on Mn1, and two are η^1 terminal on Mn7.

Inspection of metric parameters and BVS calculations (Table 7-3) indicate that there are twelve Mn^{III} and eight Mn^{II} atoms in the molecule. The BVS values for Mn5 and Mn8 are a little higher than normally expected for Mn^{II}, and those for Mn4 and Mn9 are a little lower than normally expected for Mn^{III}, so it is possible there is some Mn^{II}/Mn^{III} static disorder within the core. All the Mn ions are six-coordinate except Mn5, which is seven coordinate. The JT elongation axes on six-coordinate Mn^{III} atoms are shown as thicker black bonds in Figure 7-6. There is only one other Mn₂₀ cluster in the literature, a complex with benzylphosphonate ligands reported by Winpenny and coworkers,¹⁷³ which contains twelve Mn atoms in one plane. Complex **7-3** is thus structurally very different from this previous example. In addition to the novel overall structure, there is again, as for **7-1**, another unusual feature, namely the presence of $\mu_6 - O^{2-}$ ions (O24). There are only two previous examples of such a $\mu_6 - O^{2-}$ in Mn chemistry, [Mn₁₀O₂Cl₈(thme)₆]²⁻ and [Mn₁₈O₁₄(OMe)₁₄(O₂CBu')₈(MeOH)₆].²¹⁶⁻²¹⁸

7.3.2.4 Structure of [Fe₅O₂(O₂CPh)₇(edte)(H₂O)] (**7-4**)

A labeled representation of **7-4** is shown in Figure 7-7. Complex **7-4** crystallizes in monoclinic space group *P2₁/c*. The core can be described as consisting of a [Fe₄(μ_3 -O)₂]⁸⁺ butterfly like subunit (Fe2, Fe3, Fe4 and Fe5) on the top of which is attached a [Fe(μ -OR)₄] unit containing Fe1. There is an O atom monoatomically bridging Fe1 to each of the four Fe atoms of the butterfly. These four O atoms (O4, O6, O10 and O11) are the alkoxide arms of edte⁴⁻ group. The edte⁴⁻ group is hexadentate with the four deprotonated alkoxide O atoms all adopting μ -bridging modes and thus edte⁴⁻ group is overall μ_5 -bridging as shown in Figure 7-8(a). Peripheral ligation about the core is provided by one water molecule on Fe5 and seven benzoates, out of

which five are in $\eta^1:\eta^1:\mu$ - bridging mode and one is η^1 terminal on Fe5 and one is η^2 chelating on Fe2. There are relatively few Fe5 clusters reported in literature, and these have Fe5 topologies such as square pyramid, a centered tetrahedron, and a partial cubane extended at one face by a partial adamantane unit.¹³²⁻¹⁴¹ However, the only previous compound structurally similar to **7-4** is $[\text{Fe}_5\text{O}_2(\text{OH})(\text{O}_2\text{CMe})_5(\text{hmbp})_3]^{2+}$ (**5-1**), where hmbpH = 6-hydroxy methyl-2,2' bipyridine.¹²⁷ In **5-1** also, there is a $[\text{Fe}_4(\mu_3\text{-O})_2]^{8+}$ core with an additional iron atom on top (as in **7-4**) but the precise means by which latter is connected to the Fe_4 unit is different from the situation in **7-4**. Specifically, one of the bridging alkoxide in **7-4** is replaced by a hydroxide.

7.3.2.5 Structure of $[\text{Fe}_6\text{O}_2(\text{O}_2\text{CBu}^t)_8(\text{edteH})_2]$ (**7-5**)

A labeled representation of **7-5** is shown in Figure 7-9. Selected interatomic distances and angles are summarized in Table A-19. Complex **7-5** crystallized in monoclinic space group $C2/c$. The structure comprises roughly planar arrangement of six Fe atoms and the core can be described as consisting of two triangular $[\text{Fe}_3(\mu_3\text{-O})]^{7+}$ units joined together via six alkoxide edte O atoms. Specifically Fe2 one triangular unit is bridged to Fe3' of next triangular unit by O4. In addition, Fe3 and Fe3' are bridged via O13 and O13'. Each triangular unit is essentially isosceles, ($\text{Fe1}\cdots\text{Fe2} = 2.986 \text{ \AA}$, $\text{Fe2}\cdots\text{Fe3} = 3.313 \text{ \AA}$ and $\text{Fe1}\cdots\text{Fe3} = 3.344 \text{ \AA}$) and essentially planar (the oxide, O12, is only 0.359 \AA from the Fe_3 plane). The two Fe_3 triangular units are trans to each other. The peripheral ligation is provided by 8 pivalates out of which 6 are $\eta^1:\eta^1:\mu$ - bridging and two are η^1 terminal on Fe1 and Fe1'. All the Fe atoms are six-coordinate. Additionally, Fe1 and Fe2 of each triangular unit are bridged by alkoxide arm of edteH^{3-} (O3), while fourth arm (O5) is protonated. The BVS for the O atoms of edteH^{3-} is provided in Table 7-6. The protonated oxygen atom, O5, is involved in intermolecular H-bonding to O1 (pivalate) of next molecule forming one dimensional chains that run in two directions in lattice. The edteH^{3-} group is overall μ_4 -bridging as shown in Figure 7-8(b). The core of complex **7-5** is unprecedented in hexanuclear

Fe(III) chemistry. A number of Fe₆ clusters have been reported in the literature and a recent listing of these, together with their structural types, is available elsewhere.¹⁰⁴ Among these are a family of Fe₆ clusters whose cores comprise linked [Fe₃(μ₃-O)]⁷⁺ triangular subunits as in **7-5**, but the two units are bridged by multiple hydroxo or alkoxo groups and overall all these prior complexes possess core structures different from that of the present complex **7-5**.

7.3.2.6 Structure of [Fe₁₂O₄(OH)₂(O₂CMe)₆(edte)₄(H₂O)₂](ClO₄)₄ (**7-6**)

The labeled structure of cation of **7-6** is shown in Figure 7-10, and selected interatomic distances and angles are listed in Table A-20. Complex **7-6** crystallizes in the monoclinic space group *C2/c*. The structure consists of a [Fe^{III}₁₂(μ₄-O)₄(μ-OH)₂(μ-O₂CMe)₄(μ₃-OR)₄(μ-OR)₁₂]²⁺ core consisting of two near-planar Fe₆ layers sandwiched between three near-planar layers of O atoms (Figure 7-10, bottom). All the iron atoms are six coordinate except Fe1, Fe3, Fe9 and Fe12 which are seven coordinate. The four μ₄-O²⁻ ions (O7, O13, O29 and O37) together serve to connect all twelve Fe atoms. Each edte⁴⁻ group is hexadentate-chelating on a Fe^{III} atom, Fe1, Fe3, Fe9 and Fe12, with each of its deprotonated alkoxide arms bridging to either one or two additional Fe atoms. Thus, the edte⁴⁻ groups are overall μ₅-bridging, as shown in Figure 7-8(c). The protonation levels of O²⁻, OH⁻, and OR⁻ groups were determined from a combination of charge balance considerations, inspection of bond lengths, and BVS calculations (Table 7-6). The edte⁴⁻ O atoms have BVS values of >1.87, confirming them as completely deprotonated, as concluded above from their bridging modes. In contrast, O17 and O18 have a BVS of 1.24 and 1.20 as expected for an OH⁻ group. Peripheral ligation is provided by two terminal water molecules and six acetate groups, out of which 4 are η¹:η¹:μ- bridging and two are η¹ terminal on Fe8 and Fe10.

Complex **7-6** is only one of a very few dodecanuclear Fe(III) clusters known in the literature, of which the majority have a wheel or loop structure.²¹⁹⁻²²¹ Among the remainder, one

is composed of face-sharing defect cuboidal units in the central fragment of the core, and the other consists of four edge sharing $[\text{Fe}_3(\mu_3\text{-O})]^{7+}$ units.^{91,222} The structure of complex **7-6** is thus unprecedented in Fe chemistry, but is similar to Mn cluster **7-2** with the formula $[\text{Mn}_{12}\text{O}_4(\text{OH})_2(\text{edte})_4\text{Cl}_6(\text{H}_2\text{O})_2]$ and a mixed-valence $\text{Mn}^{\text{III}}_8\text{Mn}^{\text{II}}_4$ description.¹⁶⁸

The labeled structure of the cation of $[\text{Fe}_{12}\text{O}_4(\text{OH})_8(\text{edte})_4(\text{H}_2\text{O})_2](\text{ClO}_4)_4$ (**7-7**) is shown in Figure 7-11. The core is essentially the same as that of **7-6** except that acetate groups have been replaced by hydroxide ones. Complex **7-8** gave an elemental analysis consistent with it being the NO_3^- salt of the same cation as **7-7**, and is thus formulated as $[\text{Fe}_{12}\text{O}_4(\text{OH})_8(\text{edte})_4(\text{H}_2\text{O})_2](\text{NO}_3)_4$. This conclusion is also supported by the very similar magnetic properties of **7-7** and **7-8** (vide infra), and indeed the very similar magnetic properties of all three complexes **7-6** to **7-8**, which is consistent with the conclusion that they all possess the same or very similar Fe_{12} core structure.

7.3.3 Magnetochemistry

7.3.3.1 Dc Studies on 7-1 to 7-3

Solid-state, variable-temperature dc magnetic susceptibility data in a 0.1 T field and in the 5.0-300 K range were collected on powdered microcrystalline samples of **7-1**·2H₂O, **7-2** and **7-3**·5H₂O restrained in eicosane. The obtained data are plotted as $\chi_M T$ vs T in Figure 7-12. The $\chi_M T$ at 300 K is 26.8, 37.5 and 50.4 $\text{cm}^3\text{Kmol}^{-1}$ for **7-1** to **7-3**, respectively. The 300 K value is equal to or less than the spin-only ($g = 2$) value of 26.75, 41.5, and 71.0 $\text{cm}^3\text{Kmol}^{-1}$ expected for non-interacting $\text{Mn}^{\text{III}}_6\text{Mn}^{\text{II}}_2$, $\text{Mn}^{\text{III}}_8\text{Mn}^{\text{II}}_4$, and $\text{Mn}^{\text{III}}_{12}\text{Mn}^{\text{II}}_8$ mixed-valence situations of **7-1** to **7-3**, respectively. For **7-1**·2H₂O, $\chi_M T$ stays essentially constant with decreasing temperature until 25 K and then increases to 32.1 $\text{cm}^3\text{Kmol}^{-1}$ at 8.0 K before dropping slightly to 31.4 $\text{cm}^3\text{Kmol}^{-1}$ at 5.0 K. The $\chi_M T$ at the lowest temperatures suggests $S = 8$ ground state spin with $g < 2$, as expected for Mn. For **7-2**, $\chi_M T$ again stays essentially constant with decreasing temperature until 70 K and then decreases smoothly to 26.2 $\text{cm}^3\text{Kmol}^{-1}$ at 5.0 K, which is suggestive of an $S = 7$

ground state. For **7-3**·5H₂O, χ_{MT} decreases smoothly with decreasing temperature to a minimum of 28.2 cm³mol⁻¹K at 35 K and then increases to 36.0 cm³Kmol⁻¹ at 5.0 K, which again suggests an $S = 8$ ground state.

To confirm the above initial estimates of the ground state spin of the three compounds, variable-field (H) and -temperature magnetization (M) data were collected in the 0.1-7 T and 1.8-10 K ranges. The resulting data for **7-1**·2H₂O are plotted in Figure 7-13 (left) as reduced magnetization ($M/N\mu_B$) vs. H/T , where N is Avogadro's number and μ_B is the Bohr magneton. The data were fit, using the program *MAGNET*,⁵³ described elsewhere.⁵⁶ The best-fit for **7-1**·2H₂O is shown as the solid lines in Figure 7-13 and was obtained with $S = 8$, $g = 2.00$ and $D = -0.30$ cm⁻¹. Alternative fits with $S = 7$ and $S = 9$ gave unreasonable values of g of 2.28 and 1.78, respectively. In order to ensure that the true global minimum had been located and to assess the hardness of the fit, a root-mean-square D vs g error surface for the fit was generated using the program *GRID*,⁷¹ which calculates the relative difference between the experimental $M/N\mu_B$ data and those calculated for various combinations of D and g . This is shown as a 2-D contour plot in Figure 7-14 (left) covering the $D = -0.10$ to -0.50 cm⁻¹ and $g = 1.90$ to 2.10 ranges. Only one minimum was observed, and this was a relatively soft minimum; we thus estimate the fit uncertainties as $D = -0.30 \pm 0.01$ cm⁻¹ and $g = 2.00 \pm 0.02$.

For **7-2**, we could not obtain a satisfactory fit if data collected at all field values were employed. In our experience, the usual reason for this is the presence of low-lying excited states because (i) the excited states are close enough to the ground state and they have a non-zero Boltzmann population even at the low temperatures used in the magnetization data collection, and/or (ii) even excited states that are more separated from the ground state but have an S value greater than that of the ground-state become populated as their larger M_S levels rapidly decrease

in energy in the applied dc magnetic field and approach (or even cross) those of the ground state. Either (or both) of these two effects will lead to poor fits because the fitting program assumes population of only the ground state. A large density of low-lying excited states is expected for higher nuclearity complexes and/or those with a significant content of Mn^{II} atoms, which give weak exchange couplings. Thus, it is reasonable that such problems are more likely for **7-2** than for **7-1**, given both the higher nuclearity and the higher relative Mn^{II} content of **7-2** vs **7-1**. As described elsewhere,^{69,70,223,224} one way around effect (ii) is to use only data collected at low fields. Indeed, a satisfactory fit (solid lines in Figure 7-13, right) was now obtained using data in fields up to 0.8 T, with fit parameters $S = 7$, $D = -0.16 \text{ cm}^{-1}$ and $g = 1.90$. Alternative fits with $S = 6$ and $S = 8$ gave $g = 2.20$ and 1.67 , respectively. The corresponding error surface vs D and g (Figure 7-14, right) gives a harder minimum than that for **7-1**, with estimated fit uncertainties of $D = -0.16 \pm 0.01 \text{ cm}^{-1}$ and $g = 1.90 \pm 0.01$.

For **7-3**·5H₂O, the even higher metal nuclearity and Mn^{II} content again necessitated using data collected at lower fields in the fit, and in this case a satisfactory fit (solid lines in Figure 7-15) was obtained for data up to 1 T with fit parameters $S = 8$, $g = 1.90$ and $D = -0.16 \text{ cm}^{-1}$. Alternative fits with $S = 7$ and $S = 9$ gave $g = 2.16$ and 1.70 , respectively. The corresponding error surface vs D and g (Figure 7-15) is similar to that for **7-2** and gives estimated fit uncertainties of $D = -0.16 \pm 0.01 \text{ cm}^{-1}$ and $g = 1.90 \pm 0.01$. The magnetization fits confirmed the preliminary estimates of the ground state spin S of **7-1** to **7-3**.

7.3.3.2 Dc Studies on 7-4 to 7-8

Solid-state, variable-temperature dc magnetic susceptibility data were collected in a 0.1 T field and in the 5.0-300 K range on powdered crystalline samples of **7-4** to **7-8** restrained in eicosane. The obtained data are plotted as $\chi_M T$ vs T in Figure 7-16. For **7-4**, $\chi_M T$ steadily decreases from $6.73 \text{ cm}^3 \text{Kmol}^{-1}$ at 300 K to $3.88 \text{ cm}^3 \text{Kmol}^{-1}$ at 40.0 K, then stays approximately

constant until 25.0 K, and increases slightly to 4.02 cm³Kmol⁻¹ at 5.0 K. The 300 K value is much less than the spin-only ($g = 2$) value of 21.87 cm³Kmol⁻¹ for five non-interacting Fe(III) atoms, indicating the presence of strong antiferromagnetic interactions, as expected for oxo-bridged Fe(III) systems. The 5.0 K value of 4.02 cm³Kmol⁻¹ suggests an $S = 5/2$ ground state spin. $\chi_M T$ for **7-5**·2CHCl₃·4H₂O is 11.03 cm³Kmol⁻¹ at 300 K, and stays approximately constant with decreasing temperature to 100 K and then increases to 13.83 cm³Kmol⁻¹ at 5 K. $\chi_M T$ at 300 K is again much less than the spin-only value of 26.25 cm³Kmol⁻¹ expected for six non-interacting Fe(III) ions indicating strong antiferromagnetic interactions. The 5.0 K value of 13.83 cm³Kmol⁻¹ suggests an $S = 5$ ground state spin.

The $\chi_M T$ vs T plots for the three complexes **7-6** to **7-8** in Figure 7-16 are very similar, indicating a minimal influence of the peripheral groups and supporting the conclusions above that they possess similar core structures. For **7-6** to **7-8**, $\chi_M T$ steadily decreases from 22.04, 23.37, 20.53 cm³Kmol⁻¹ at 300 K to 0.25, 0.51, 0.50 cm³Kmol⁻¹ at 5.0 K, respectively. The change in $\chi_M T$ with decreasing temperature and the low value at 5 K are indicative of an $S = 0$ ground state. The differences in $\chi_M T$ vs T for the three complexes are almost certainly just reflecting small differences in intramolecular exchange coupling constants (J), and perhaps in ZFS parameters (D) and any intermolecular interactions.

To confirm the initial ground state spin estimates above for **7-4** and **7-5**, variable-field (H) and -temperature magnetization (M) data were collected in the 0.1-7.0 T and 1.8-10 K ranges. The resulting data for **7-4** are plotted in Figure 7-17 as reduced magnetization ($M/N\mu_B$) vs H/T , where N is Avogadro's number and μ_B is the Bohr magneton. The saturation value at the highest fields and lowest temperatures is ~4.90, as expected for an $S = 5/2$ ground state and g slightly less than 2; the saturation value should be gS in the absence of complications from low-lying

excited states. The data were fit, using the program *MAGNET*,⁵³ described elsewhere.⁵⁶ The best fit for **7-4** is shown as the solid lines in Figure 7-17 (left) and was obtained with $S = 5/2$ and either of the two sets of parameters: $g = 1.96$ and $D = 0.58 \text{ cm}^{-1}$, and $g = 1.96$ and $D = -0.50 \text{ cm}^{-1}$. Alternative fits with $S = 3/2$ or $7/2$ were rejected because they gave unreasonable values of g and D . It is common to obtain two acceptable fits of magnetization data for a given S value, one with $D > 0$ and the other with $D < 0$, since magnetization fits are not very sensitive to the sign of D . This was indeed the case for the magnetization fits for both the complexes **7-4** and **7-5**. In order to assess which is the superior fit for these complexes and also to ensure that the true global minimum had been located in each case, we calculated the root-mean-square error surface for the fits as a function of D and g using the program *GRID*.⁷¹ For **7-4**, the error surface (Figure 7-18, left) clearly shows the two minima with positive and negative D values, with the fit with negative D being clearly superior and suggesting that this is the true sign of D . However, it would require a more sensitive technique such as EPR spectroscopy to confirm this.

The obtained magnetization data for **7-5** are plotted in Figure 7-17 (right) as $M/N\mu_B$ vs H/T , and it can be seen to saturate at ~ 9.29 , suggesting an $S = 5$ ground state and $g < 2$. The resulting best fit of the data is shown as the solid lines in Figure 7-17 (right), and was obtained with $S = 5$ and either $g = 1.90$, $D = 0.45 \text{ cm}^{-1}$ or $g = 1.89$, $D = -0.28 \text{ cm}^{-1}$. In this case also, the fit error surface (Figure 7-18, right) clearly shows that the fit with negative D is far superior, suggesting this to be the true sign of D .

7.3.3.3 Ac Studies on 7-1 to 7-5

To independently confirm the ground state S values, ac susceptibility data was collected on microcrystalline samples of **7-1** to **7-5** in a 3.5 G ac field. The in-phase (χ_M') ac susceptibility signal is invaluable for assessing S without any complications from a dc field,^{62,69,224} and these signals for complexes **7-1** to **7-3** at 997 Hz are plotted as $\chi_M'T$ vs T in Figure 7-19. Extrapolation

of the plots to 0 K, from temperatures above ~5 K to avoid the effect of weak intermolecular interactions (dipolar and superexchange), gives values of ~ 33, ~27 and ~37 cm³Kmol⁻¹ for **7-1** to **7-3**, respectively, corresponding to $S = 8, 7$ and 8 , respectively, with $g \sim 1.91, 1.96$ and 2.02 , in very satisfying agreement with the conclusions from the fits of the dc magnetization data.

None of the complexes displayed out-of-phase (χ_M'') ac susceptibility peaks above 1.8 K. There were some very weak signs of the beginning of signals whose peaks would lie well below 1.8 K, and these may correspond to the very small dips in the $\chi_M'T$ plots of Figure 7-19 (left) at $T < 2$ K. However, it is clear that if any of the complexes **7-1** to **7-3** were single-molecule magnets (SMMs), they would at best have very small barriers to magnetization relaxation. In fact, complex **7-1**, with its combination of $S = 8$ and $D = -0.30$ cm⁻¹, would be predicted to have the largest barrier of the three complexes, with an upper limit (U) of $U = S^2|D| = 19.2$ cm⁻¹. However, the true or effective barrier (U_{eff}) is expected to be significantly less than U , especially given the low symmetry of the molecule, and it is perhaps not surprising that even if **7-1** were a SMM, it would be one only at very low temperatures < 1 K and thus not a significant new addition to the family of SMMs.

In-phase ac susceptibility signals for complexes **7-4** and **7-5** at 997 Hz are plotted as $\chi_M'T$ vs T in Figure 7-19 (right). The $\chi_M'T$ is essentially temperature independent below 15 K until ~ 4 - 5 K where there is a small decrease that can be assigned to low temperature effects such as ZFS of the ground state and/or very weak intermolecular interactions. The essentially constant values at > 5 K of ~4 and ~14 cm³Kmol⁻¹ for **7-4** and **7-5**, respectively, confirm $S = 5/2$ and 5 ground states with $g < 2$, whose spin-only ($g = 2.0$) values are 4.38 and 15.0 cm³Kmol⁻¹, respectively. Neither complex displayed out-of-phase (χ_M'') ac susceptibility peaks above 1.8 K.

7.3.3.4 Rationalization of the Ground State Spin of 7-4 and 7-5

It is of interest to attempt to rationalize the observed ground state spin values of **7-4** and **7-5**. It is assumed that all Fe₂ pairwise exchange interactions are antiferromagnetic, as is essentially always the case for high-spin Fe(III), and there will thus be competing antiferromagnetic exchange interactions and spin frustration effects within the many Fe₃ triangular units in these complexes. In fact, for complex **7-4**, its $S = 5/2$ ground state can be rationalized in an identical fashion based on spin frustration as we previously described for complex **5-1** in chapter 5, which has a similar [Fe₅O₆] core topology as **7-4**, as stated earlier, and an identical $S = 5/2$ ground state.¹²⁷

For complex **7-5**, the spin alignments giving rise to the $S = 5$ ground state are again not obvious owing to spin frustration within the triangular units of the Fe₆ core. There are five inequivalent types of exchange interactions, J_{12} , J_{13} , J_{23} , $J_{23'}$ and $J_{33'}$, the subscripts referring to the atom labels of Figure 7-9. In Table 7-7, we list the average Fe-O distances and the Fe-O-Fe angles for bridged Fe₂ pairs within the molecule. It is well known that short Fe-O bond distances and large Fe-O-Fe angles lead to the larger J values.^{76,112,225,226} In complex **7-5**, the Fe1/Fe3 and Fe2/Fe3 pairs, with only a single monoatomic bridge, have both the shortest Fe-O superexchange pathways and the largest Fe-O-Fe angles in the molecule and are thus expected on the basis of magnetostructural correlations⁷⁶ to have the strongest J values, in the order of ~ 38 cm⁻¹. The Fe2/Fe3' pair, also with a single monoatomic bridge, has a slightly longer Fe-O pathway but still a large Fe-O-Fe angle; thus, it would also be expected to have a relatively strong J value, in the ~ 15 cm⁻¹ region. In contrast, the Fe1/Fe2 and Fe3/Fe3' pairs, which are now bis-monoatomically bridged, have Fe-O distances similar to that for Fe2/Fe3' but by far the smallest Fe-O-Fe angles in the molecule, and would thus be expected to have the weakest J values, in the ~ 7 cm⁻¹ region. The estimates given for all the pairs are based on the J values of Fe₂ pairs with similar metric

parameters in other Fe(III) clusters. Thus, we conclude that the Fe1/Fe2 and Fe3/Fe3' exchange will be frustrated by the other, stronger interactions, and as a result, the ground state spin alignments in the molecule will be as shown in Figure 7-20 (top). The spins within Fe₂ pairs monoatomically bridged by a single O atom are aligned antiparallel, whereas those within the three bis-monoatomically bridged Fe₂ pairs are spin frustrated by the other stronger interactions and forced to align parallel even though their exchange interactions are intrinsically antiferromagnetic. This situation predicts an $S = 5$ ground state for **7-5**, as experimentally obtained. Note that it is not easy to formulate reasonable alternative ways of getting an $S = 5$ ground state, and thus we feel confident on the above proposal. For example, if the Fe2/Fe3' interaction were considered weak enough to be frustrated by the Fe3/Fe3' interaction, then this situation would give the spin alignments of Figure 7-20 (bottom) and an $S = 0$ ground state.

It is difficult to rationalize the $S = 0$ ground state spin for **7-6** due to the high content of triangular units and large number of non-zero exchange interactions.

7.4 Conclusions

The initial use of edteH₄ has proven to be a useful new route to a variety of novel Mn_x and Fe_x clusters. It is a hexadentate chelate whose four alcohol groups offer, on deprotonation, the possibility of each bridging to one or more additional Mn and Fe atoms and thus fostering formation of high nuclearity products. In the present work, we have described the synthesis and characterization of new Mn₈, Mn₁₂ and Mn₂₀ products, all with unprecedented structural features and all with significant ground state spin values of $S = 7$ or 8. Although the core of complex **7-4** is overall similar to that of a previous Fe₅ complex with hmbp⁻, those of Fe₆ complex **7-5** and particularly that of Fe₁₂ complex **7-6** are unprecedented in Fe(III) chemistry. The structures of the cations **7-7** and **7-8** are concluded to be the same given their identical formulations and almost superimposable magnetic properties. We have also successfully rationalized the $S = 5$

ground state of **7-6**. The combined results emphasize the usefulness of the poly-alcohol-based chelate edteH₄ as a route to new high-nuclearity products.

Table 7-1. Crystallographic Data for **7-1**·2CH₂Cl₂·MeOH, **7-2**·6MeCN·½H₂O and **7-3**·10MeOH

	7-1	7-2	7-3
Formula ^a	C ₈₀ H ₉₄ Cl ₄ Mn ₈ N ₄ O ₃₀	C ₅₂ H ₉₉ Cl ₈ Mn ₁₂ N ₁₄ O _{22.5}	C ₈₂ H ₁₈₂ Cl ₂ Mn ₂₀ N ₁₂ O ₆₆
Fw, g/mol ^a	2172.91	2223.33	3562.05
Space group	<i>P2₁/n</i>	<i>P4/ncc</i>	<i>P2₁/c</i>
<i>a</i> , Å	16.0450(16)	19.7797(12)	17.0570(16)
<i>b</i> , Å	17.6428(17)	19.7797(12)	25.409(2)
<i>c</i> , Å	31.896(3)	20.851(2)	15.9322(15)
α°	90	90	90
β°	95.425(2)	90	100.463(2)
γ°	90	90	90
<i>V</i> , Å ³	8988.6(15)	8157.7(12)	6790.3(11)
<i>Z</i>	4	4	2
<i>T</i> , K	173(2)	173(2)	173(2)
λ , Å ^b	0.71073	0.71073	0.71073
ρ_{calc} , g/cm ³	1.577	1.810	1.573
μ , mm ⁻¹	1.340	2.125	1.886
<i>R</i> <i>I</i> ^{c,d}	0.0334	0.0464	0.0812
<i>wR</i> 2 ^e	0.0812	0.1046	0.2174

^a Including solvate molecules. ^b Graphite monochromator. ^c $I > 2\sigma(I)$. ^d $R1 = \Sigma(|F_o| - |F_c|) / \Sigma|F_o|$. ^e $wR2 = [\Sigma[w(F_o^2 - F_c^2)^2] / \Sigma[w(F_o^2)^2]]^{1/2}$, $w = 1/[\sigma^2(F_o^2) + [(ap)^2 + bp]$, where $p = [\max(F_o^2, 0) + 2F_c^2]/3$.

Table 7-2. Crystallographic Data for **7-4**·CH₂Cl₂, **7-5**·2CHCl₃, **7-6**·MeCN and **7-7**

	7-4	7-5	7-6	7-7
Formula ^a	C ₆₀ H ₅₉ Cl ₂ Fe ₅ N ₂ - O ₂₁	C ₆₂ H ₁₁₆ Cl ₆ Fe ₆ N ₄ - O ₂₆	C ₆₀ H ₁₁₆ Cl ₄ Fe ₁₂ - N ₁₂ O ₅₂	C ₄₀ H ₉₂ Cl ₄ Fe ₁₂ - N ₈ O ₄₆
Fw, g/mol ^a	1494.27	1881.39	2649.61	2233.17
Space group	<i>P</i> 2 ₁ / <i>c</i>	<i>C</i> 2/ <i>c</i>	<i>C</i> 2/ <i>c</i>	<i>C</i> 2/ <i>c</i>
<i>a</i> , Å	21.3735(10)	14.211(2)	29.590(4)	30.502(3)
<i>b</i> , Å	18.6612(9)	24.297(2)	29.641(4)	11.9702(11)
<i>c</i> , Å	17.7842(8)	25.676(3)	23.174(3)	30.517(3)
α°	90	90	90	90
β°	113.280(1)	94.783(3)	104.088(2)	111.404(1)
γ°	90	90	90	90
<i>V</i> , Å ³	6515.81	8988.6(15)	19714(5)	10373.7
<i>Z</i>	4	4	8	4
<i>T</i> , K	173(2)	173(2)	173(2)	173(2)
λ , Å ^b	0.71073	0.71073	0.71073	0.71073
ρ_{calc} , g/cm ³	-	1.414	1.764	-
μ , mm ⁻¹	-	1.210	1.916	-
<i>R</i> ^{c,d}	-	0.0575	0.0788	-
<i>wR</i> ^e	-	0.1364	0.2219	-

^a Including solvate molecules. ^b Graphite monochromator. ^c $I > 2\sigma(I)$. ^d $R1 = \Sigma(|F_o| - |F_c|) / \Sigma|F_o|$. ^e $wR2 = [\Sigma[w(F_o^2 - F_c^2)^2] / \Sigma[w(F_o^2)^2]]^{1/2}$, $w = 1/[\sigma^2(F_o^2) + [(ap)^2 + bp]$, where $p = [\max(F_o^2, O) + 2F_c^2]/3$.

Table 7-3. Bond-valence sums for the Mn atoms of complex **7-1** and **7-3**^a

Atom	7-1			7-3		
	Mn ^{II}	Mn ^{III}	Mn ^{IV}	Mn ^{II}	Mn ^{III}	Mn ^{IV}
Mn1	3.21	<u>2.93</u>	3.08	<u>1.85</u>	1.70	1.78
Mn2	3.18	<u>2.91</u>	3.05	3.12	<u>2.90</u>	2.98
Mn3	<u>2.01</u>	1.87	1.92	3.21	<u>2.93</u>	3.08
Mn4	3.13	<u>2.87</u>	3.01	2.99	<u>2.77</u>	2.85
Mn5	3.14	<u>2.87</u>	3.01	<u>2.48</u>	2.26	2.38
Mn6	<u>1.96</u>	1.83	1.86	3.17	<u>2.90</u>	3.04
Mn7	3.17	<u>2.90</u>	3.04	3.22	<u>2.94</u>	3.09
Mn8	3.18	<u>2.91</u>	3.05	<u>2.45</u>	2.24	2.35
Mn9	-	-	-	3.05	<u>2.79</u>	2.93
Mn10	-	-	-	<u>1.88</u>	1.75	1.79

^a The underlined value is the one closest to the charge for which it was calculated. The oxidation state of a particular atom can be taken as the nearest whole number to the underlined value.

Table 7-4. Bond-valence sums for the O atoms of complex **7-1**^a

Atom	BVS	Assignment	group
O21	1.99	OR ⁻	OMe ⁻
O6	1.43	OH ⁻	OH ⁻
O15	1.95	OR ⁻	edte ⁴⁻
O16	1.93	OR ⁻	edte ⁴⁻
O17	1.94	OR ⁻	edte ⁴⁻
O18	1.96	OR ⁻	edte ⁴⁻
O7	2.02	OR ⁻	edte ⁴⁻
O8	1.21	ROH	edteH ₂ ²⁻
O9	1.17	ROH	edteH ₂ ²⁻
O10	1.98	OR ⁻	edte ⁴⁻

^aThe BVS values for O atoms of O²⁻, OH⁻ and H₂O groups are typically 1.8-2.0, 1.0-1.2 and 0.2-0.4, respectively, but can be affected somewhat by hydrogen-bonding.

Table 7-5. Bond-valence sums^a for the Mn and O atoms of complex **7-2**.

Atom	Manganese BVS		
	Mn ^{II}	Mn ^{III}	Mn ^{IV}
Mn1	<u>2.23</u>	2.12	2.17
Mn2	3.34	<u>3.09</u>	3.22
Mn3	3.05	<u>2.82</u>	2.91

Atom	Oxygen BVS		
	BVS	assignment	group
O1	1.98	O ²⁻	O ²⁻
O4	0.99	OH ⁻	OH ⁻
O2	1.89	OR ⁻	edte ⁴⁻
O3	1.97	OR ⁻	edte ⁴⁻
O5	1.97	OR ⁻	edte ⁴⁻
O6	2.03	OR ⁻	edte ⁴⁻

^a The underlined value is the one closest to the charge for which it was calculated. The oxidation state of a particular atom can be taken as the nearest whole number to the underlined value. ^aThe BVS values for O atoms of O²⁻, OH⁻ and H₂O groups are typically 1.8-2.0, 1.0-1.2 and 0.2-0.4, respectively.

Table 7-6. Bond-valence sums for the O atoms of complex **7-5** and **7-6**^a

Atom	7-5		
	BVS	assignment	group
O3	1.82	OR ⁻	edte ⁴⁻
O4	1.94	OR ⁻	edte ⁴⁻
O5	0.90	ROH	edteH
O13	1.88	OR ⁻	edte ⁴⁻
Atom	7-6		
	BVS	assignment	group
O1	1.95	OR ⁻	edte ⁴⁻
O2	1.87	OR ⁻	edte ⁴⁻
O3	1.97	OR ⁻	edte ⁴⁻
O4	1.98	OR ⁻	edte ⁴⁻
O5	0.50	H ₂ O	H ₂ O
O16	0.41	H ₂ O	H ₂ O
O17	1.24	OH ⁻	OH ⁻
O18	1.20	OH ⁻	OH ⁻

^aThe BVS values for O atoms of O²⁻, OH⁻ and H₂O groups are typically 1.8-2.0, 1.0-1.2 and 0.2-0.4, respectively.

Table 7-7. Selected Fe-O distances and Fe-O-Fe angles for **7-5**

Fe ₂ pair	Avg. Fe-O (Å)	Angle (deg)
Fe1/Fe3	1.895	123.8
Fe2/Fe3	1.883	123.2
Fe2/Fe3'	2.000	118.7
Fe3/Fe3'	2.026	102.3
Fe1/Fe2	1.980	98.1 (avg.)

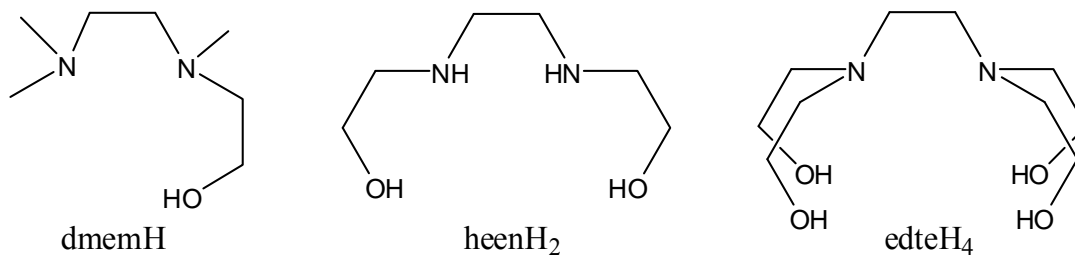


Figure 7-1. Structure of ligands.

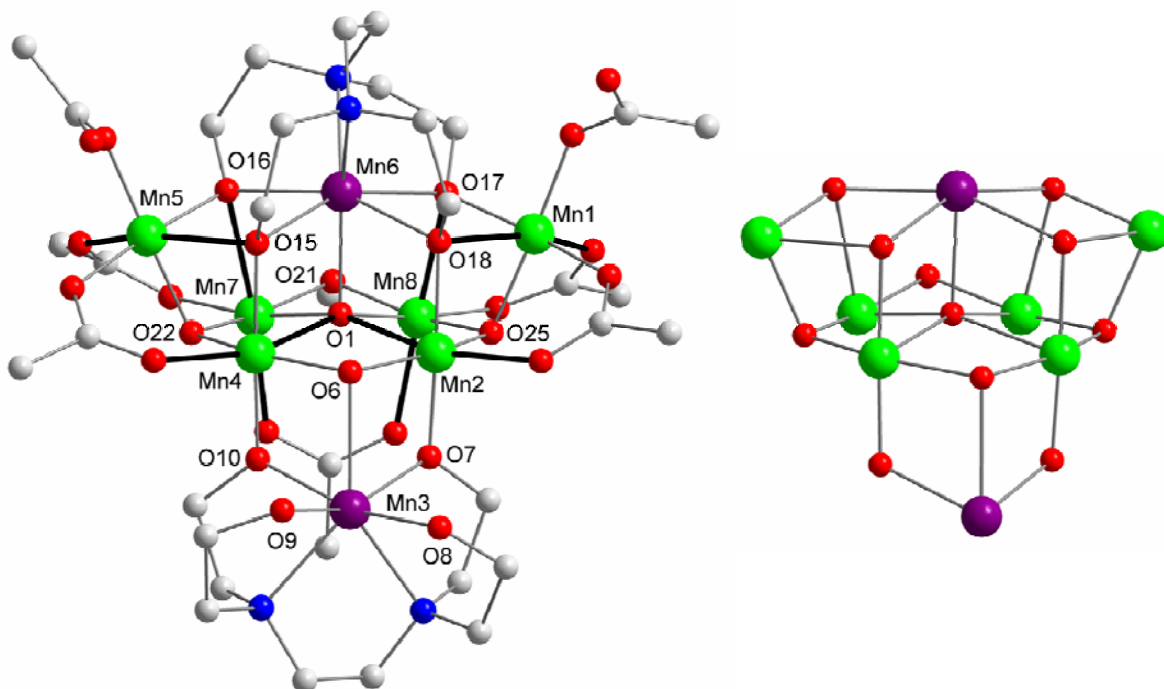


Figure 7-2. (left) Labeled representation of the cation of **7-1**. Hydrogen atoms and phenyl rings (except for the *ipso* carbon atoms) have been omitted for clarity. JT axes are shown as thicker black bonds. (right) The core of **7-1**. Color code: Mn^{III}, green; Mn^{II}, purple; O, red; N, blue; C, grey.

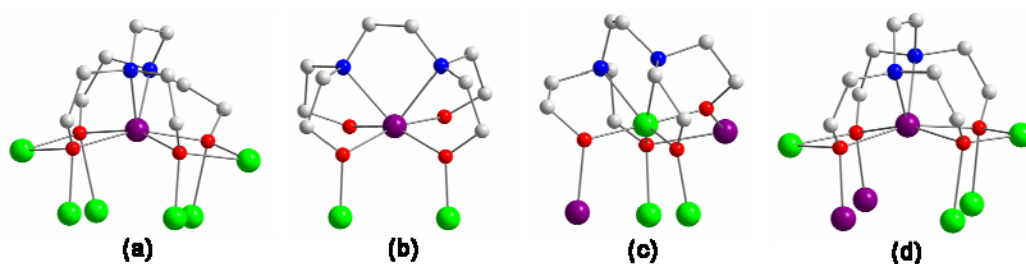


Figure 7-3. Crystallographically established coordination modes of edte^{4-} and edteH_2^{2-} found in complexes **7-1** to **7-3**. Color code: Mn^{III}, green; Mn^{II}, purple; O, red; N, blue; C, grey.

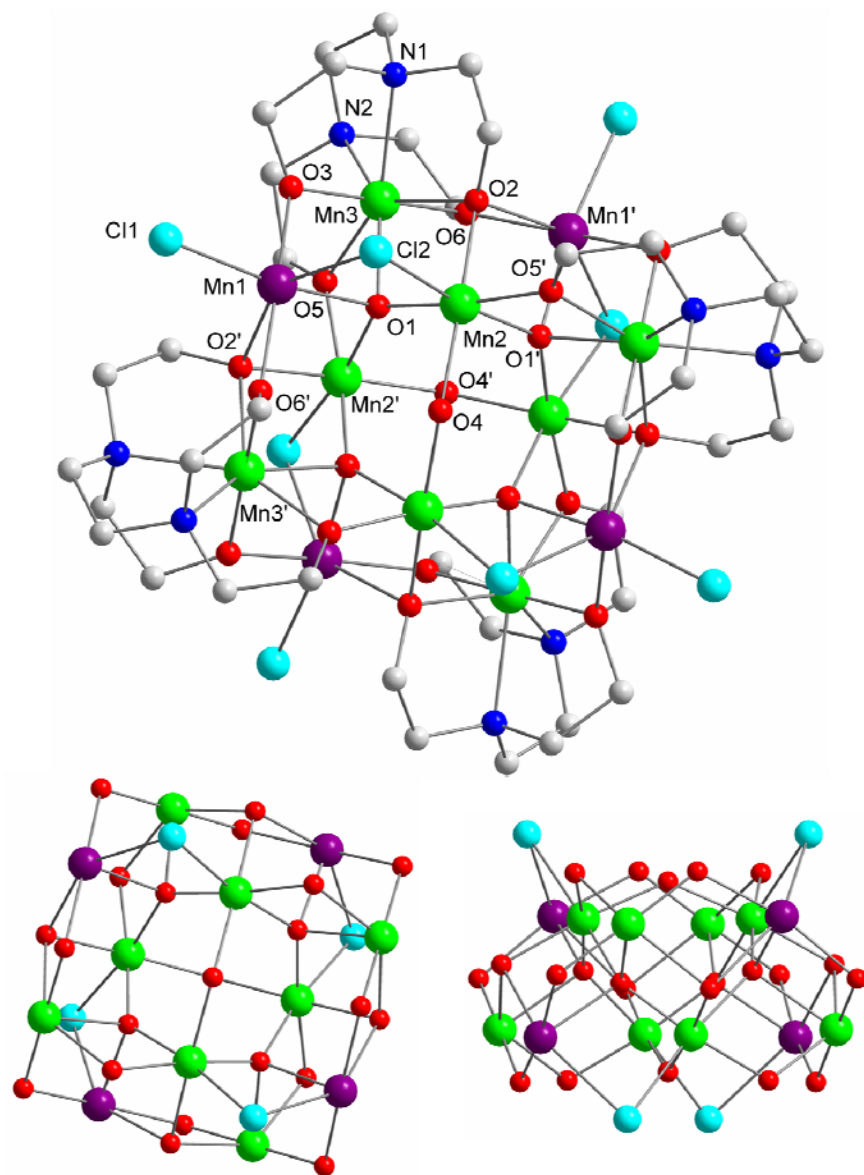


Figure 7-4. (top) Labeled representation of the structure of **7-2**. (bottom) The core of **7-2** viewed along (left) the *c* axis, and (right) the *b* axis. Color code: Mn^{III}, green; Mn^{II}, purple; Cl, cyan; O, red; N, blue; C, grey.

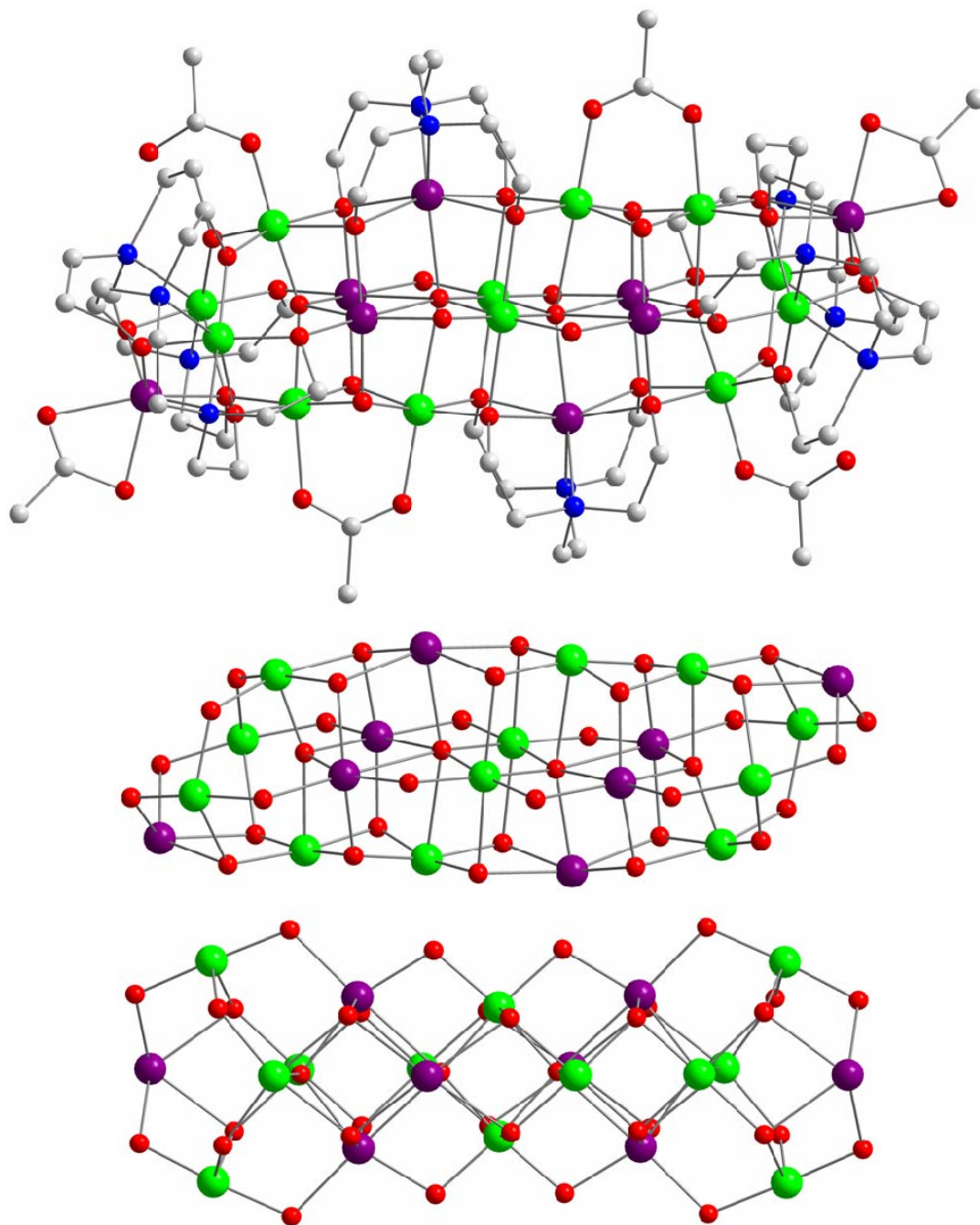


Figure 7-5. (top) The structure of the cation of **7-3**. (middle and bottom) The core of **7-3** from different viewpoints emphasizing the 3 x 2 cubane arrangement. Color code: Mn^{III}, green; Mn^{II}, purple; O, red; N, blue; C, grey.

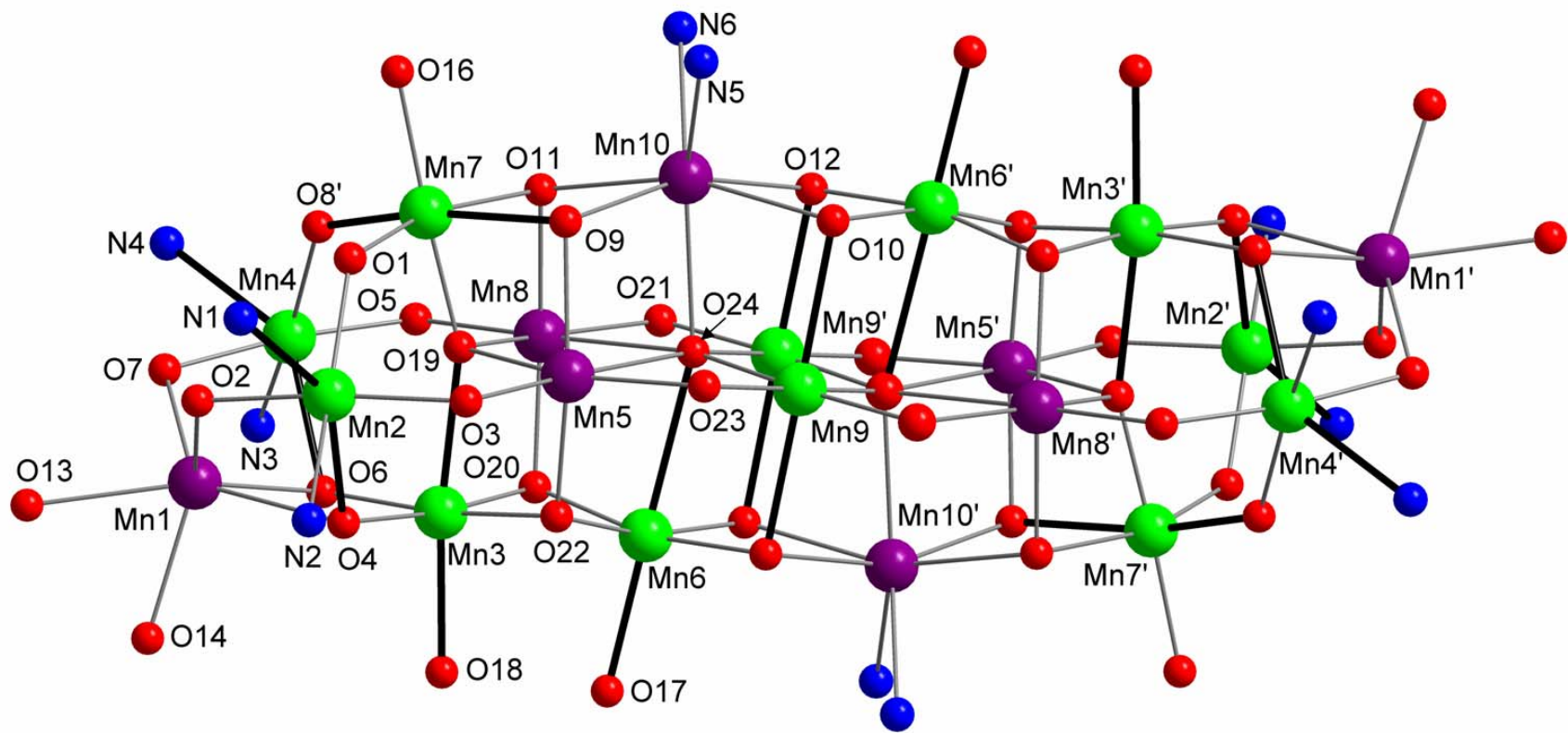


Figure 7-6. Labeled representation of the core of **7-3**. JT axes are shown as thicker black bonds. Color code: Mn^{III}, green; Mn^{II}, purple; O, red; N, blue; C, grey.

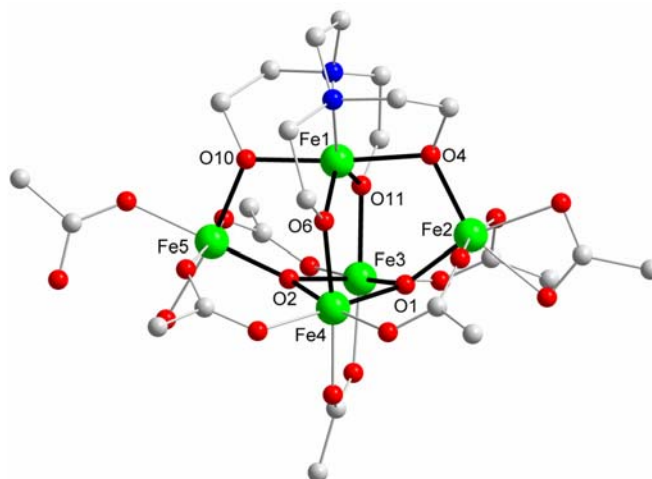


Figure 7-7. Labeled representation of the structure of **7-4** with core Fe-O bonds as thick black lines; only the *ipso* benzoate carbon atoms are shown. Color code: Fe, green; O, red; N, blue; C, grey.

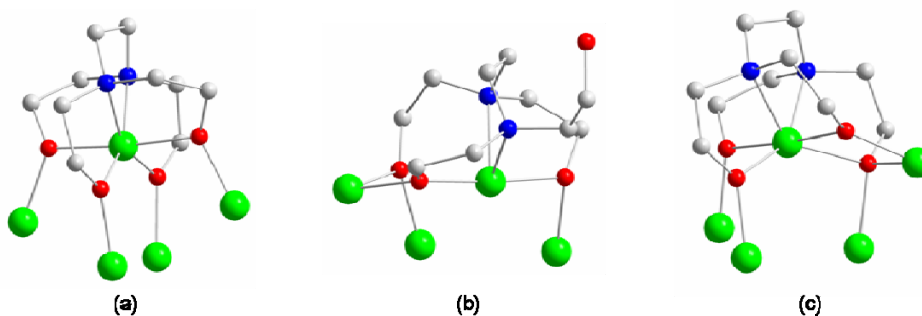


Figure 7-8. Crystallographically established coordination modes of edte^{4-} and edteH^{3-} found in complexes **7-4** to **7-6**. Color code: Fe, green; O, red; N, blue; C, grey.

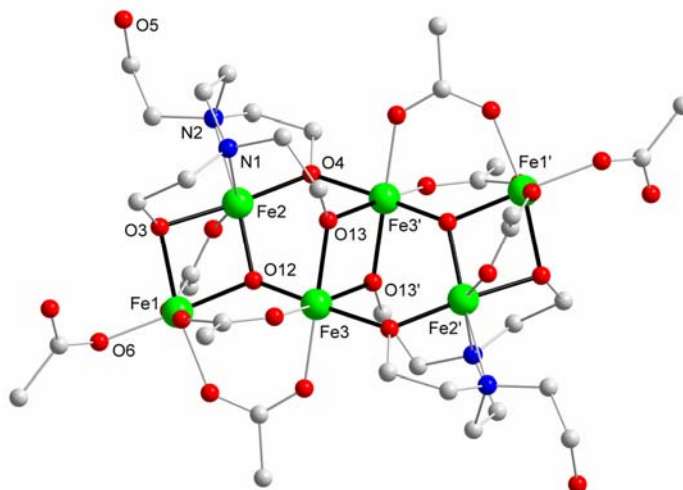


Figure 7-9. Labeled representation of the structure of **7-5** with core Fe-O bonds as thick black lines; methyl groups on pivalate groups have been omitted for clarity. Color code: Fe, green; O, red; N, blue; C, grey.

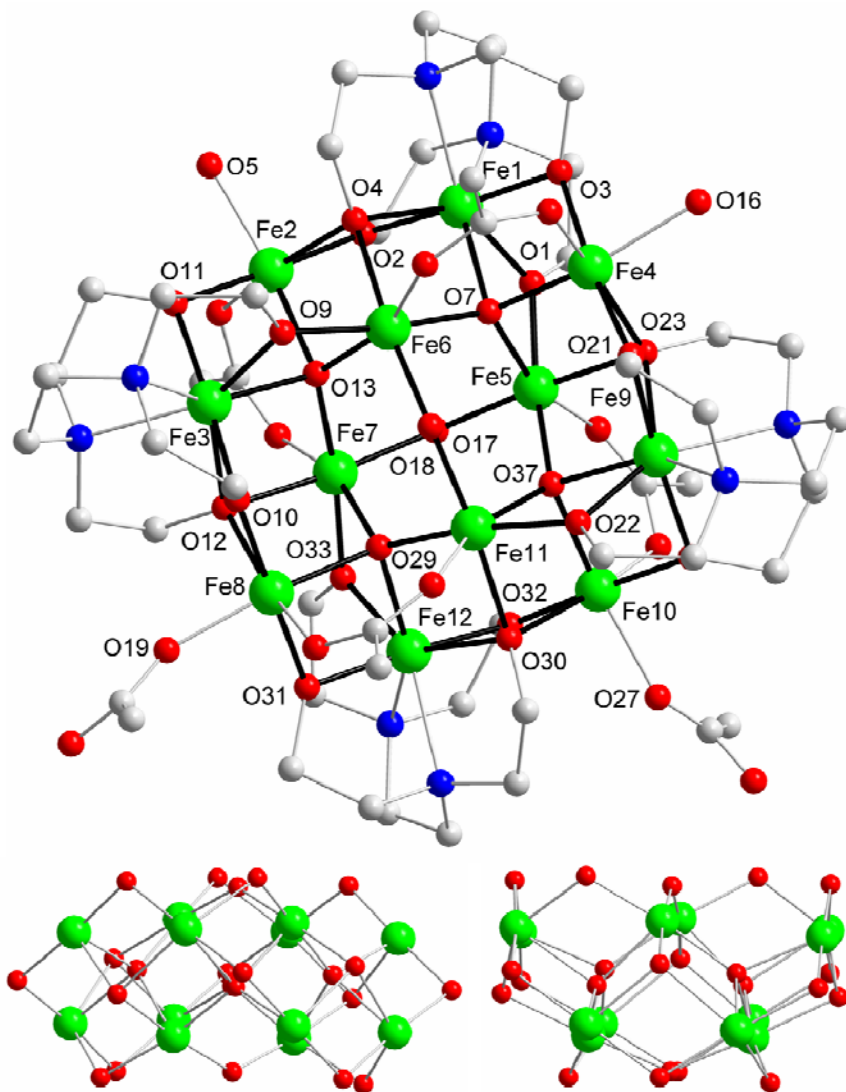


Figure 7-10. (top) Labeled representation of the cation of **7-6** with core Fe-O bonds as thick black lines. (bottom) Core of **7-6**. Color code: Fe, green; O, red; N, blue; C, grey.

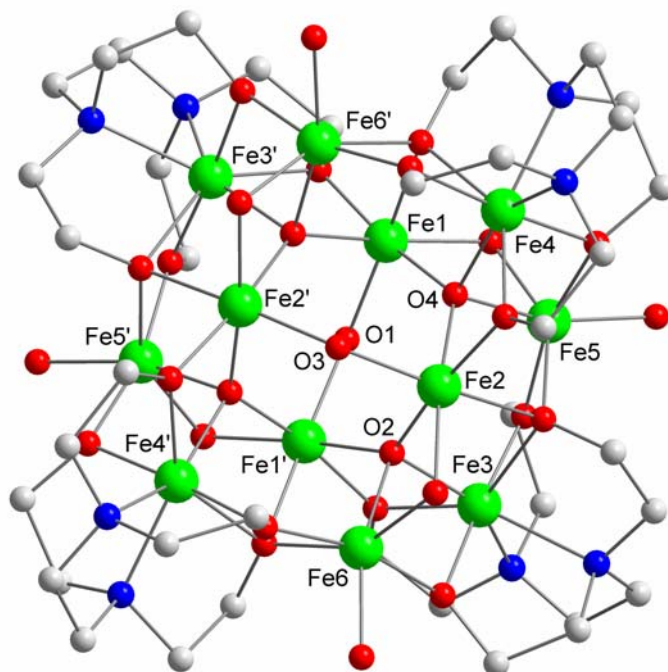


Figure 7-11. Labeled representation of the cation of **7-7**. Color code: Fe, green; O, red; N, blue; C, grey.

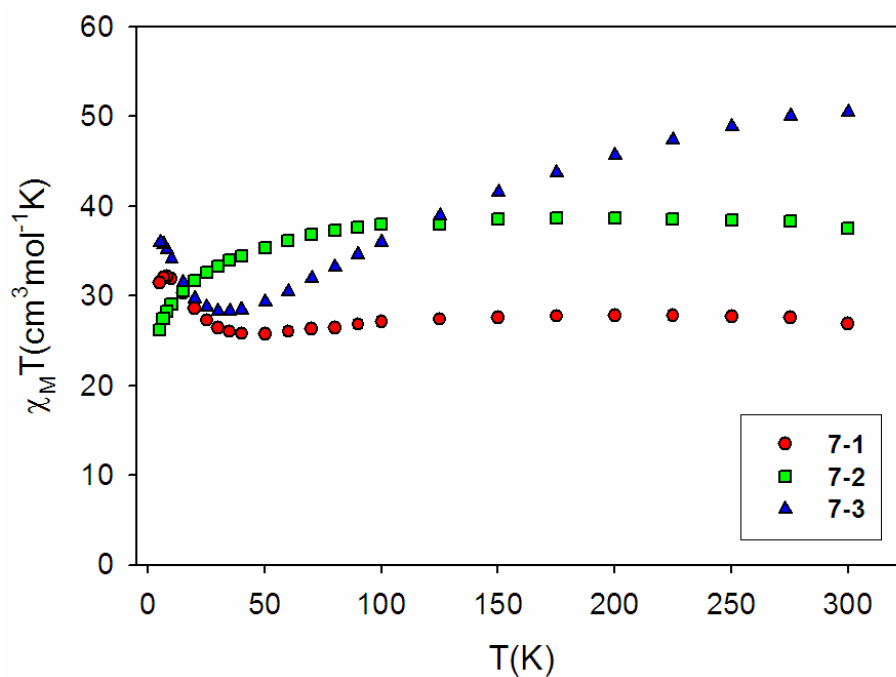


Figure 7-12. Plots of $\chi_M T$ vs T for complexes **7-1**·2H₂O (●), **7-2** (■) and **7-3**·5H₂O (▲)

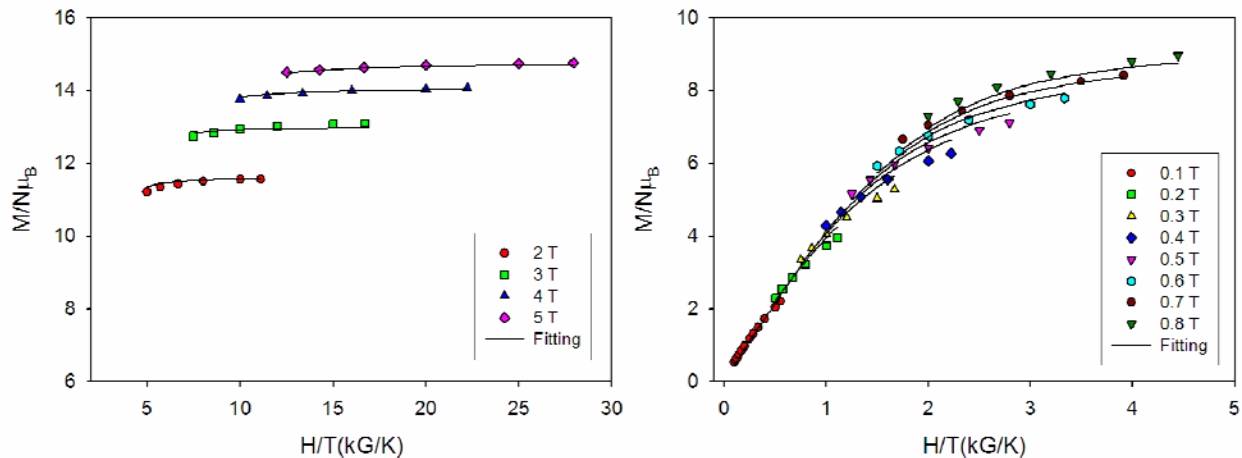


Figure 7-13. Plots of reduced magnetization ($M/N\mu_B$) vs H/T for complexes **7-1**·2H₂O (left) and **7-2** (right). The solid lines are the fits of the data; see the text for the fit parameters.

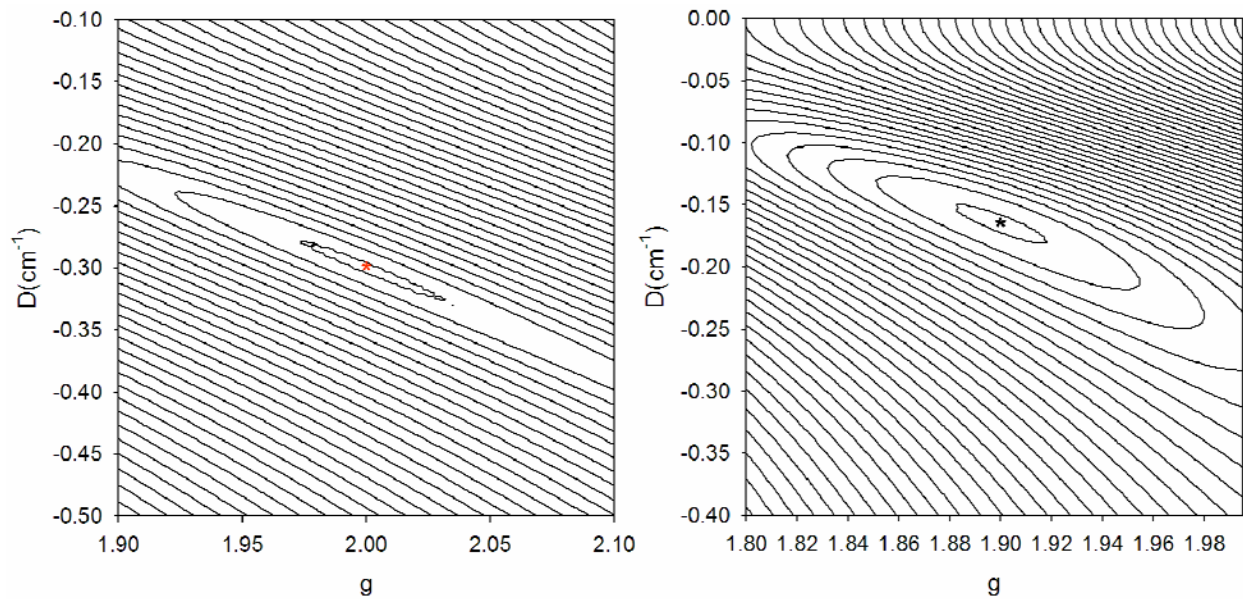


Figure. 7-14. Two-dimensional contour plot of the r.m.s. error surface vs D and g for the magnetization fit for **7-1**·2H₂O (left) and **7-2** (right).

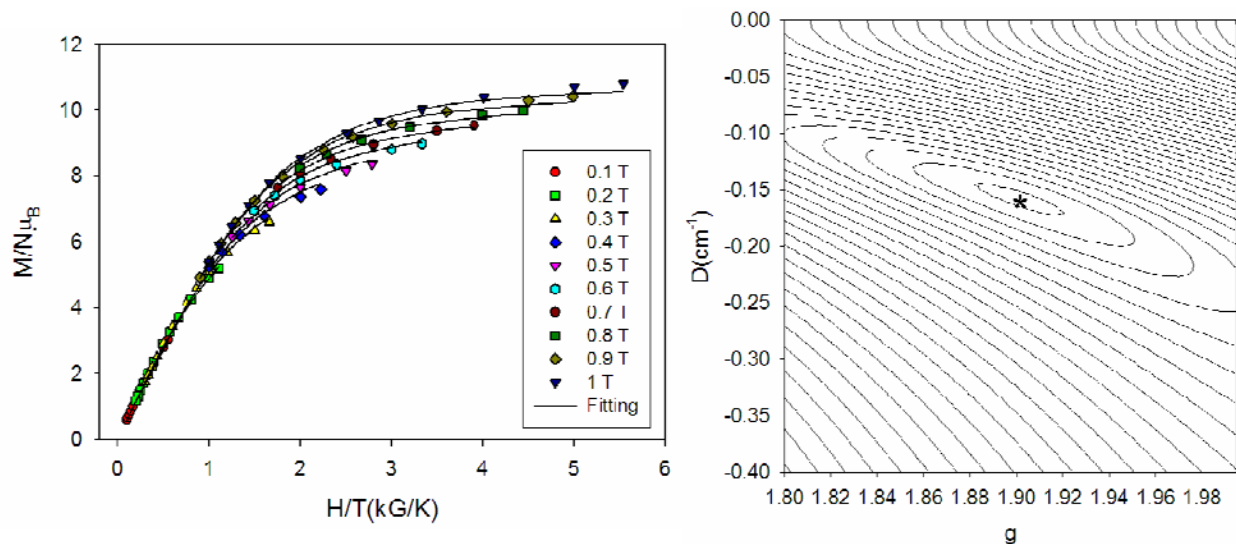


Figure 7-15. (left) Plots of reduced magnetization ($M/N\mu_B$) vs H/T for complex **7-3**·5H₂O. (right) Two-dimensional contour plot of the r.m.s. error surface vs D and g for the magnetization fit for **7-3**·5H₂O.

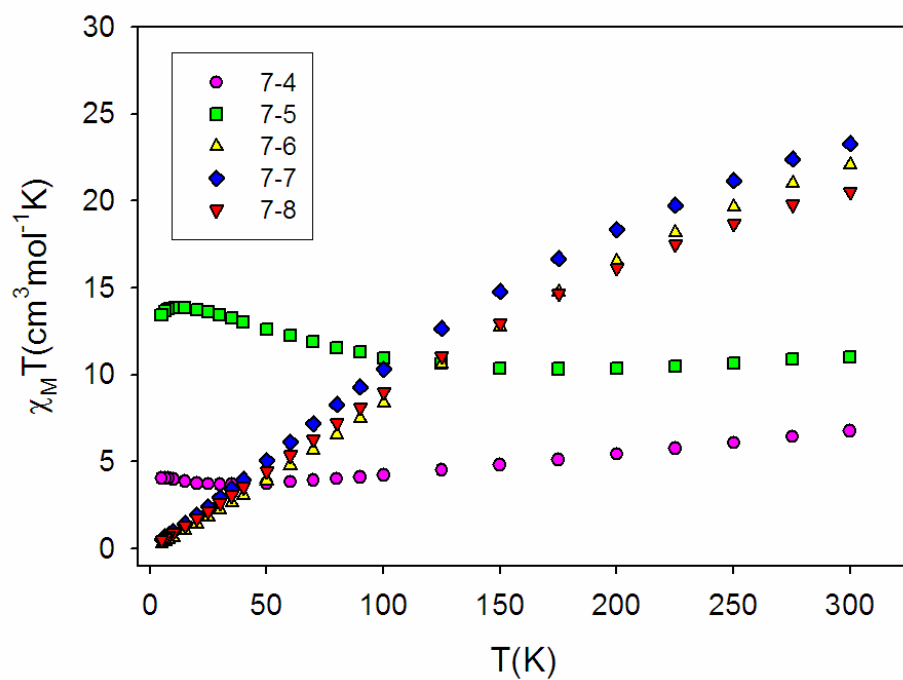


Figure 7-16. Plots of $\chi_M T$ vs T for complexes **7-4** to **7-8**.

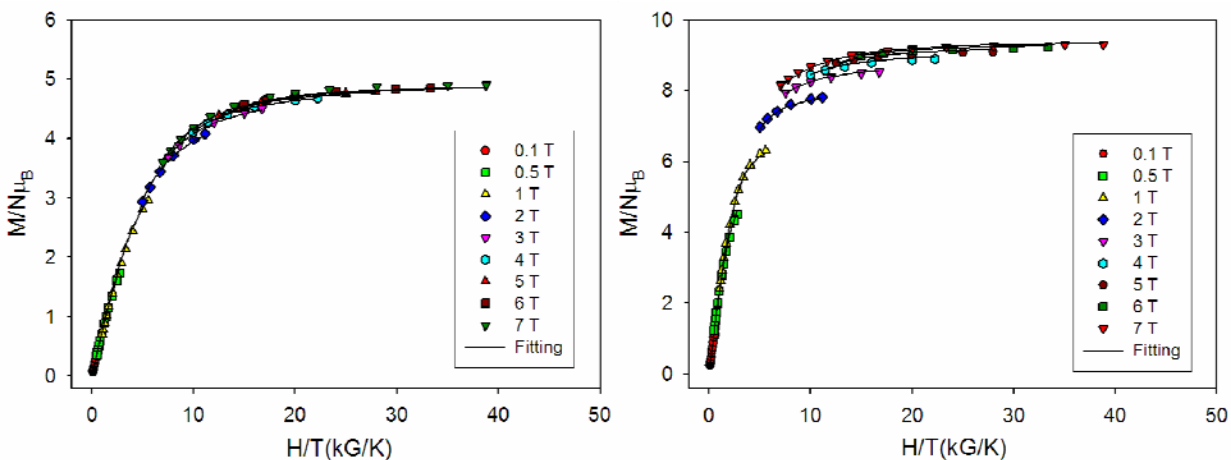


Figure 7-17. Plot of reduced magnetization ($M/N\mu_B$) vs H/T for complexes **7-4** (left) and **7-5·2CHCl₃·4H₂O** (right). The solid lines are the fit of the data; see the text for the fit parameters.

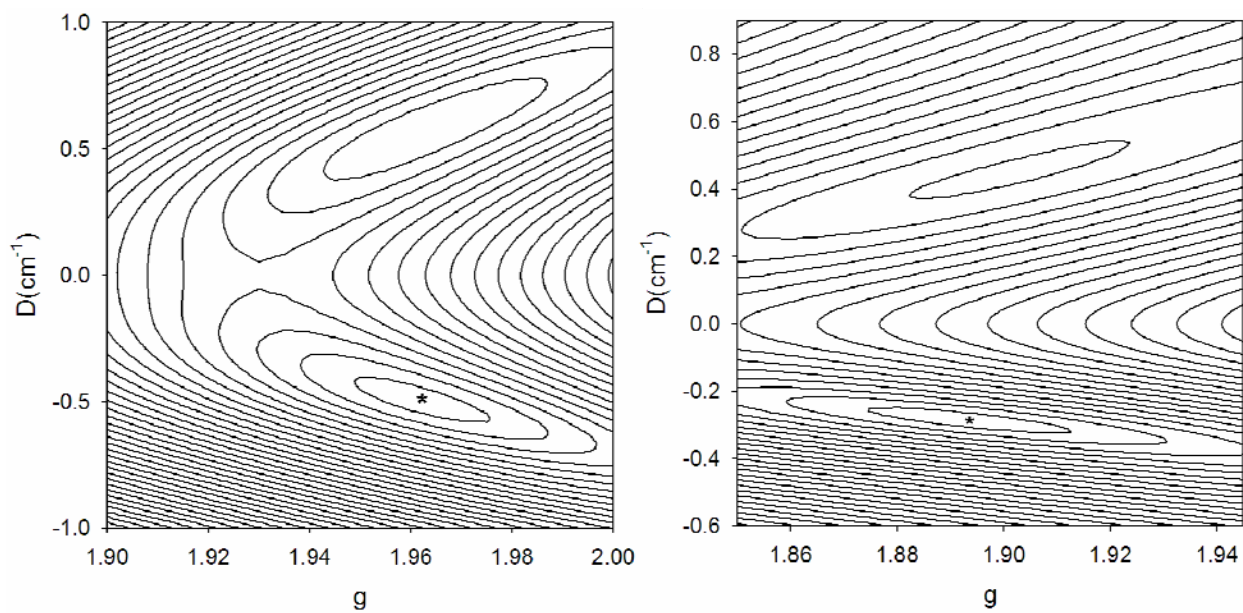


Figure 7-18. Two-dimensional contour plot of the fitting error surface vs D and g for **7-4** (left) and **7-5·2CHCl₃·4H₂O** (right).

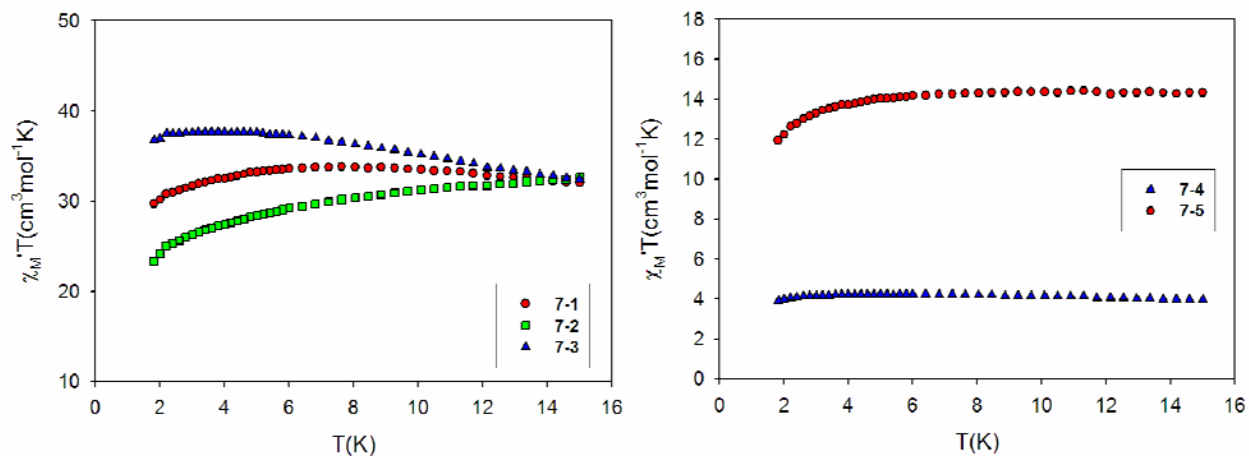


Figure 7-19. (left) Plot of $\chi_M T$ vs. T for complexes **7-1**·2H₂O (●), **7-2** (■) and **7-3**·5H₂O (▲) at 997 Hz. (right) Plot of $\chi_M T$ vs. T for complexes **7-4** (▲) and **7-5**·2CHCl₃·4H₂O (●) at 997 Hz.

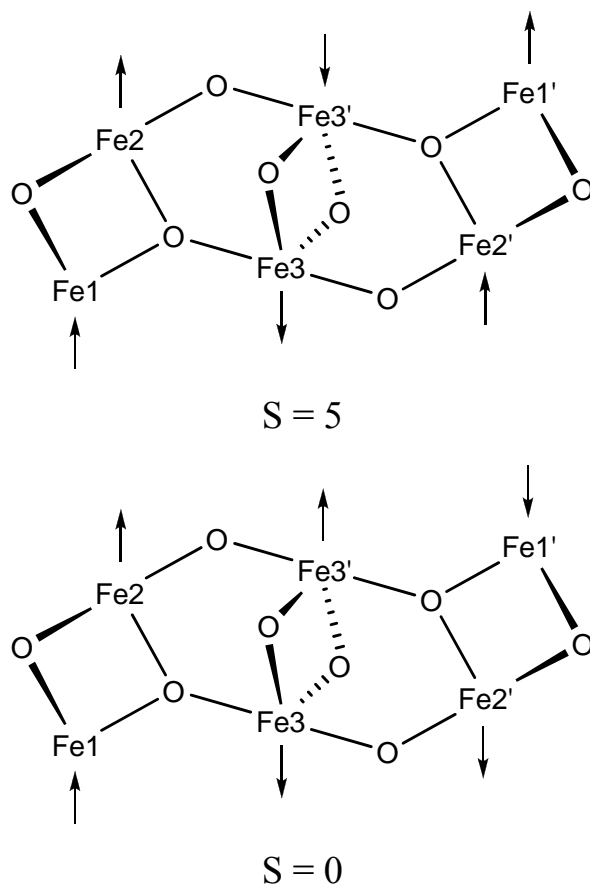


Figure 7-20. (top) Spin alignments at the six $S = 5/2$ Fe(III) atoms of **7-5** rationalizing its $S = 5$ ground state, based on the arguments given in the text. (bottom) Spin alignments if the strengths of the Fe2/Fe3' and Fe3/Fe3' couplings were reversed, showing that the wrong ground state would be obtained.

CHAPTER 8
SINGLE-MOLECULE MAGNETISM AND MAGNETOSTRUCTURAL CORRELATION
WITHIN A FAMILY OF $[\text{Mn}^{\text{III}}_{10}\text{Ln}^{\text{III}}_2]$ COMPLEXES

8.1 Introduction

Single-molecule magnets (SMMs) are individual molecules that can function as nanoscale magnetic particles below their blocking temperature (T_B). They thus represent a molecular (or bottom-up) approach to nanoscale magnetic materials, and one that retains all the advantages of molecular chemistry, particularly monodispersity, solubility, crystallinity, and a periphery of organic ligands.^{13,16,154,227} The SMM property results from a combination of a high-spin ground state (S) and an easy-axis type magnetoanisotropy (negative zero-field splitting parameter, D) and can be determined experimentally by the observation of frequency-dependent out-of-phase (χ'') signals in ac magnetic susceptibility measurements, and hysteresis loops in magnetization vs. dc field scans.^{13,15,19,228} Since the initial discovery of the Mn_{12} family of SMMs, a number of different structural types have been synthesized, the majority of which have been Mn clusters composed completely or partially of Mn^{III} atoms, since the Jahn-Teller distortion of high-spin Mn^{III} in near-octahedral geometry is the main source of the molecular anisotropy.^{21,22,171,213,228-232}

In order to develop new synthetic routes for the synthesis of new SMMs, we and others have recently been focusing on polynuclear 3d-4f complexes.²³³⁻²⁴⁵ The hope has been that the large anisotropy of most of the Ln^{III} ions, as well as their often large number of unpaired electrons, would enhance the SMM property by raising the barrier to magnetization relaxation. The initial success in 2004 in the synthesis of a mixed-metal, ferromagnetically-coupled Tb_2Cu_2 SMM complex with a slow magnetization relaxation rate,²⁴⁶ provided a proof-of-feasibility that amalgamation of transition metals with anisotropic Ln^{III} ions can have a major impact on the resulting relaxation barrier. Since then, this area has steadily built up momentum and there are now several types of 3d-4f SMMs, most of which are in Mn-Ln chemistry: $[\text{Mn}_{11}\text{Dy}_4]^{239}$,

$[\text{Mn}_2\text{Dy}_2]^{240}$ $[\text{Mn}_6\text{Dy}_6]^{241}$, $[\text{Mn}_6\text{Dy}_4]^{234}$ and $[\text{Mn}_{11}\text{Gd}_2]^{247}$. All these complexes display frequency-dependent out-of-phase ac susceptibility signals at low temperatures, but it was the $[\text{Mn}_{11}\text{Dy}_4]^{239}$ complex that first confirmed that such Mn-Ln SMMs can exhibit clear magnetization hysteresis and quantum tunneling of magnetization (QTM) through the anisotropy barrier. The first 3d-4f SMMs in Fe chemistry have also now been reported, $[\text{Fe}_2\text{Ho}_2(\text{OH})_2(\text{teaH})_2(\text{O}_2\text{CPh})_4(\text{NO}_3)_2]$ and $[\text{Fe}_2\text{Dy}_2(\text{OH})_2(\text{teaH})_2(\text{O}_2\text{CPh})_6]$ (teaH₃ = triethanolamine).²⁴⁵ The total number of examples of 3d-4f SMMs is thus still limited, and new synthetic methodologies to additional examples are of continuing interest, especially with the hope that some may have increased magnetization relaxation barriers, i.e. higher blocking temperatures, T_B . These points represent a major stimulus of this work.

As part of our continuing interest in the synthesis of new Mn-Ln SMMs, we have explored the use of 2-hydroxymethylpyridine (hmpH) in mixed-metal reactions. This alcohol containing group on deprotonation has been a common route to various homometallic Mn_x clusters in our previous work,^{34,63,211} and we expected that it might also prove a useful route to new Mn-Ln species. Indeed, we report in this paper our development of a synthetic procedure employing hmpH that has successfully led to a family of Mn^{III}₁₀Ln^{III}₂ isostructural complexes spanning most Ln^{III} ions: Ln = Pr (**8-1**), Nd (**8-2**), Sm (**8-3**), Gd (**8-4**), Tb (**8-5**), Dy (**8-6**), Ho (**8-7**) and Er (**8-8**). In addition to showing that some of these are new 3d-4f SMMs, we also take advantage of the availability of an isostructural series to map out the 3d-4f exchange coupling (and SMM properties) as a function of the Ln^{III} ion employed. It is rare to have such an opportunity in high nuclearity Ln-containing mixed-metal complexes.²³ In general, the large orbital angular momentum in Ln^{III} ions, except for Gd^{III}, prevents the convenient use of an isotropic (Heisenberg) spin Hamiltonian for interpretation of the magnetic properties of polynuclear 3d-4f

clusters. Costes *et al.* and Kahn *et al.* introduced an empirical approach of comparing a 3d-4f system with an isostructural one in which the Ln^{III} is replaced by a diamagnetic M^{III} ion, thus allowing the effect of the Ln^{III} to be factored out.²⁴⁸⁻²⁵⁰ In 2003, Figuerola *et al.* extended this to an Fe^{III}-Ln^{III} species by comparison with the isostructural Co^{III}-Ln^{III} and Fe^{III}-La^{III} complexes, thus factoring out both the individual Fe^{III} and Ln^{III} properties.²⁵¹ Since then, a variety of such studies have been carried out on dinuclear, trinuclear, tetranuclear, 1-D and 2-D cyanide-bridged 3d-4f assemblies.^{233,236,238,252-257} However, this strategy has not been employed as yet on polynuclear Mn-Ln oxide clusters relevant to the SMM field, and to the search for increased barriers to magnetization relaxation. In order to do so in the present work, we have also prepared the isostructural Mn^{III}₁₀Y^{III}₂ with diamagnetic Y^{III} for comparison with the Mn-Ln complexes, which has allowed characterization of the magnetic properties of the Mn^{III}₁₀ portion of the structure. We herein describe the combined results of this comparative investigation of the properties of this family of complexes.

8.2 Experimental Section

8.2.1 Syntheses

All preparations were performed under aerobic conditions using reagents and solvents as received. (NBuⁿ₄)[Mn₄O₂(O₂CPh)₉(H₂O)] was prepared as previously described.¹⁸⁵

[Mn₁₀Dy₂O₈(O₂CPh)₁₀(hmp)₆(NO₃)₄] (8-6). To a stirred solution of (NBuⁿ₄)[Mn₄O₂(O₂CPh)₉(H₂O)] (0.36 g, 0.23 mmol) in MeOH/MeCN (1/19 mL) was added Dy(NO₃)₃·5H₂O (0.10 g, 0.23 mmol) followed by hmpH (0.02 mL, 0.23 mmol). The mixture was stirred for an hour, filtered to remove undissolved solid, and the filtrate layered with Et₂O. X-ray quality red-brown crystals of **8-6**·3MeCN·MeOH were obtained over a period of one week. These were collected by filtration, washed with Et₂O, and dried *in vacuo*; the yield was 15%. The dried solid analyzed as solvent free. Anal. Calcd. (Found) for **8-6** (C₁₀₆H₈₆Dy₂Mn₁₀N₁₀O₄₆):

C, 40.93 (40.50); H, 2.79 (2.90); N, 4.50 (4.24)%. Selected IR data (cm⁻¹): 3434(br), 3063(w), 1707(w), 1605(m), 1566(s), 1487(m), 1385(s), 1308(w), 1228(w), 1175(w), 1157(w), 1069(m), 1051(w), 1027(w), 817(w), 765(w), 718(m), 668(m), 614(w), 548(m), 465(w), 429(w).

[Mn₁₀Pr₂O₈(O₂CPh)₁₀(hmp)₆(NO₃)₄] (8-1). Complex **8-1** was prepared following the same procedure as for **8-6** but with Pr(NO₃)₃·5H₂O (0.095 g, 0.23 mmol). The yield was 25%. Anal. Calcd. (Found) for **8-1** (C₁₀₆H₈₆N₁₀Mn₁₀O₄₆Pr₂): C, 41.51 (41.55); H, 2.83 (2.84); N, 4.57 (4.38)%. Selected IR data (cm⁻¹): 3434(br), 3063(w), 1707(w), 1606(m), 1566(m), 1403(s), 1290(w), 1176(w) 1069(m), 1051(w), 1027(w), 820(w), 763(w), 718(m), 661(m), 549(m), 429(w).

[Mn₁₀Nd₂O₈(O₂CPh)₁₀(hmp)₆(NO₃)₄] (8-2). Complex **8-2** was prepared following the same procedure as for **8-6** but with Nd(NO₃)₃·6H₂O (0.10 g, 0.23 mmol). The yield was 20%. Anal. Calcd. (Found) for **8-2** (C₁₀₆H₈₆N₁₀Mn₁₀O₄₆Nd₂): C, 41.42 (41.77); H, 2.82 (2.88); N, 4.56 (4.76)%. Selected IR data (cm⁻¹): 3446(br), 3063(w), 1698(w), 1607(m), 1566(s), 1473(m), 1401(s), 1315(w), 1291(w), 1175(w), 1157(w), 1069(m), 1050(w), 762(w), 718(m), 660(m), 612(w), 549(m), 460(w), 429(w).

[Mn₁₀Sm₂O₈(O₂CPh)₁₀(hmp)₆(NO₃)₄] (8-3). Complex **8-3** was prepared following the same procedure as for **8-6** but with Sm(NO₃)₃·6H₂O (0.10 g, 0.23 mmol). The yield was 12%. Anal. Calcd. (Found) for **8-3** (C₁₀₆H₈₆N₁₀Mn₁₀O₄₆Sm₂): C, 41.26 (41.36); H, 2.81 (2.73); N, 4.54 (4.21)%. Selected IR data (cm⁻¹): 3436(br), 3063(w), 1707(w), 1606(m), 1566(s), 1485(m), 1402(s), 1291(w), 1230(w), 1176(w), 1070(w), 1051(m), 1027(w), 819(w), 765(w), 718(m), 663(m), 614(w), 551(m), 468(w).

[Mn₁₀Gd₂O₈(O₂CPh)₁₀(hmp)₆(NO₃)₄] (8-4). Complex **8-4** was prepared following the same procedure as for **8-6** but with Gd(NO₃)₃·6H₂O (0.10 g, 0.23 mmol). X-ray crystallography

characterized the obtained crystals as **8-4**·3MeCN·MeOH. The yield was 10%. Anal. Calcd. (Found) for **8-4** (C₁₀₆H₈₆Gd₂Mn₁₀N₁₀O₄₆): C, 41.07 (41.35); H, 2.80 (2.81); N, 4.52 (4.22)%.

[Mn₁₀Tb₂O₈(O₂CPh)₁₀(hmp)₆(NO₃)₄] (8-5). Complex **8-5** was prepared following the same procedure as for **8-6** but with Tb(NO₃)₃·5H₂O (0.10 g, 0.23 mmol). The yield was 20%. Anal. Calcd. (Found) for **8-5** (C₁₀₆H₈₆N₁₀Mn₁₀O₄₆Tb₂): C, 41.03 (41.03); H, 2.79 (2.80); N, 4.51 (4.31)%. Selected IR data (cm⁻¹): 3432(br), 3062(w), 1710(w), 1605(m), 1566(s), 1487(m), 1401(s), 1291(w), 1175(w), 1157(w), 1070(m), 1051(w), 1026(w), 818(w), 765(w), 718(m), 665(m), 616(w), 550(m), 465(w).

[Mn₁₀Ho₂O₈(O₂CPh)₁₀(hmp)₆(NO₃)₄] (8-7). Complex **8-7** was prepared following the same procedure as for **8-6** but with Ho(NO₃)₃·5H₂O (0.10 g, 0.23 mmol). The yield was 15%. Anal. Calcd. (Found) for **8-7**·2H₂O (C₁₀₆H₉₀N₁₀Mn₁₀O₄₈Ho₂): C, 40.40 (40.11); H, 2.88 (2.79); N, 4.44 (4.23)%. Selected IR data (cm⁻¹): 3432(br), 3063(w), 1602(m), 1565(s), 1488(m), 1385(s), 1309(w), 1175(w), 1157(w), 1069(m), 1051(w), 1025(w), 765(w), 718(m), 670(m), 547(m), 466(w).

[Mn₁₀Er₂O₈(O₂CPh)₁₀(hmp)₆(NO₃)₄] (8-8). Complex **8-8** was prepared following the same procedure as for **8-6** but with Er(NO₃)₃·5H₂O (0.10 g, 0.23 mmol). The yield was 10%. Anal. Calcd. (Found) for **8-8**·3H₂O (C₁₀₆H₉₂N₁₀Mn₁₀O₄₈Er₂): C, 40.11 (39.85); H, 2.92 (2.84); N, 4.41 (4.23)%. Selected IR data (cm⁻¹): 3430(br), 3063(w), 1709(w), 1603(m), 1565(s), 1488(m), 1400(s), 1306(w), 1175(w), 1157(w), 1070(m), 1051(w), 1027(w), 817(w), 765(w), 717(m), 673(m), 612(w), 549(m).

[Mn₁₀Y₂O₈(O₂CPh)₁₀(hmp)₆(NO₃)₄] (8-9). Complex **8-9** was prepared following the same procedure as for **8-6** but with Y(NO₃)₃·6H₂O (0.087 g, 0.23 mmol). X-ray crystallography characterized the obtained crystals as **8-9**·4MeCN. The yield was 15%. Anal. Calcd. (Found) for

8-9 (C₁₀₆H₈₆N₁₀Mn₁₀O₄₆Y₂): C, 42.97 (42.69); H, 2.92 (2.83); N, 4.73 (5.17)%. Selected IR data (cm⁻¹): 3421(br), 3063(w), 1698(w), 1602(m), 1564(s), 1506(m), 1385(s), 1311(w), 1176(w), 1069(m), 1051(w), 765(w), 718(m), 667(m), 547(w), 467(w).

8.2.2 X-ray Crystallography

Data were collected by Dr. Khalil A. Abboud on a Siemens SMART PLATFORM equipped with a CCD area detector and a graphite monochromator utilizing Mo-K α radiation ($\lambda = 0.71073$ Å). Suitable crystals of **8-4**·3MeCN·MeOH, **8-6**·3MeCN·MeOH and **8-9**·4MeCN were attached to glass fibers using silicone grease and transferred to a goniostat where they were cooled to 173 K for data collection. Cell parameters were refined using up to 8192 reflections. A full sphere of data (1850 frames) was collected using the ω -scan method (0.3° frame width). The first 50 frames were re-measured at the end of the data collection to monitor instrument and crystal stability (maximum correction on I was <1 %). Absorption corrections by integration were applied based on measured indexed crystal faces. The structure was solved by the direct methods in *SHELXTL6*,²⁵⁸ and refined on F^2 using full-matrix least-squares. The non-H atoms were treated anisotropically, whereas the H atoms were placed in calculated, ideal positions and refined as riding on their respective C atoms.

For **8-4**·3MeCN·MeOH and **8-6**·3MeCN·MeOH, the asymmetric unit consists of a half Mn₁₀Gd₂ or Mn₁₀Dy₂ cluster, a disordered MeCN in a general position, and a half MeCN disordered against a half MeOH molecule about an inversion center. A total of 825 (**8-4**) or 817 (**8-6**) parameters were refined in the final cycle of refinement using 20616 (**8-4**) or 10817 (**8-6**) reflections with $I > 2\sigma(I)$ to give $R_1(wR_2)$ of 6.43(17.13) and 5.08(13.30)% for **8-4** and **8-6**, respectively.

For **8-9**·4MeCN, the asymmetric unit consists of a half Mn₁₀Y₂ cluster and two MeCN molecules. The latter are disordered and could not be modeled properly, thus program

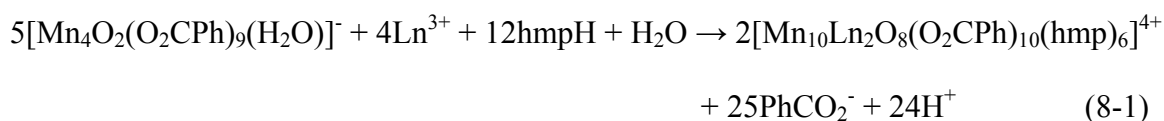
SQUEEZE,⁶⁸ a part of the PLATON package of crystallographic software, was used to calculate the solvent disorder area and remove its contribution to the overall intensity data. A total of 778 parameters were refined in the final cycle of refinement using 6197 reflections with $I > 2\sigma(I)$ to yield $R_1(wR_2)$ of 7.10(16.14)%, respectively.

Unit cell data and structure refinement details for **8-4**·3MeCN·MeOH, **8-6**·3MeCN·MeOH and **8-9**·4MeCN are listed in Table 8-1.

8.3 Results and Discussion

8.3.1 Syntheses

Many synthetic methods to high-nuclearity Mn^{III}-containing clusters and SMMs have involved the reaction of a chelate with preformed $[\text{Mn}_3\text{O}(\text{O}_2\text{CR})_6\text{L}_3]^{0,+}$ oxide-centered triangular complexes.^{32,259-262} The chelate has the dual function of encouraging molecular products rather than polymers, and fostering high-nuclearity products if good binding groups such as alkoxides are present. In the present work, the preformed tetranuclear Mn^{III}₄ complex (NBuⁿ₄)[Mn₄O₂(O₂CPh)₉(H₂O)] was employed.¹⁸⁵ This has also proven in the past to be a good stepping-stone to high nuclearity products.^{179,263,264} Reaction of (NBuⁿ₄)[Mn₄O₂(O₂CPh)₉(H₂O)] with 1 equiv each of hmpH and Ln(NO₃)₃ (Ln = Pr (**8-1**), Nd (**8-2**), Sm (**8-3**), Gd (**8-4**), Tb (**8-5**), Dy (**8-6**), Ho (**8-7**) and Er (**8-8**)) in MeCN:MeOH led to subsequent isolation of red-brown crystals of [Mn₁₀Ln₂O₈(O₂CPh)₁₀(hmp)₆(NO₃)₄] in fair yields of 10-30%. The yields are not optimized and we were happy to settle for lower yields of well-formed, pure material rather than add more Et₂O co-solvent, which would contaminate the products with by-products such as NBuⁿ₄NO₃ and others. The reaction is summarized in eq. 8-1.



We had hoped to make the complete series for every Ln (except Pm). However, the later lanthanides Tm, Yb and Lu gave products that were clearly not isostructural with **8-1** - **8-8**, and we assume this is related to their decreased size compared with the others. We were also unable to get the Eu analogue. The Ce reaction suffered from reactions that we assume involve redox reactions; we have seen elsewhere on multiple occasions that Ce favors the Ce^{IV} oxidation state in mixed-metal Mn-Ce chemistry involving high oxidation state Mn^{III}/Mn^{IV}.^{264,265}

To benefit the magnetism studies, as stated in the Introduction, we also attempted and succeeded in preparing the isostructural complex [Mn₁₀Y₂O₈(O₂CPh)₁₀(hmp)₆(NO₃)₄] (**8-9**), confirmed crystallographically (*vide infra*), by the same route. All these reactions were very sensitive to the Mn₄:hmpH:Ln^{III} ratio; other ratios were found to give poor crystallinity and/or mixtures of products. The mixed MeCN:MeOH solvent system is also very important to give clean products **8-1** – **8-9**. The structures of representative Ln^{III} complexes **8-4** and **8-6**, and the Y^{III} complex **8-9**, were determined by X-ray crystallography; all the complexes gave essentially superimposable IR spectra, and elemental analyses in agreement with the given formulations, and we conclude on these bases that the complexes are all isostructural. The compounds are air stable, but interstitial solvent molecules are easily lost during vacuum drying and the solids are slightly hygroscopic.

8.3.2 Description of Structures

The labeled structures of **8-4**, **8-6** and **8-9** are shown in Figure 8-1, and selected interatomic distances and angles for **8-4**, **8-6** and **8-9** are provided in Tables A-21, A-22 and A-23 respectively. The complexes all crystallize in triclinic space group *P* $\bar{1}$ with the Mn₁₀Ln₂ molecules lying on inversion centers, and their structures are essentially identical except for the identity of the Ln^{III} or Y^{III} atoms. Therefore, we will only describe the structure of complex **8-6** here. The complex contains a [Mn₁₀Dy₂(μ_3 -O²⁻)₄(μ_4 -O²⁻)₄]²⁰⁺ core that can be dissected into five

parallel layers of three types with an **ABCBA** arrangement (Figure 8-2). Layer **A** is the Dy1 atom, layer **B** consists of a triangular Mn^{III}₃ unit (Mn1, Mn2, Mn3), and layer **C** consists of a Mn^{III}₄ rhombus (Mn4, Mn4', Mn5, Mn5'). Each layer is held together and linked to its neighboring layers by a combination of four $\mu_3\text{-O}^{2-}$, two $\mu_4\text{-O}^{2-}$ and ten benzoate groups, six of which are in $\eta^1:\eta^1:\mu$ -bridging modes and four are in $\eta^2:\eta^1:\mu_3$ -bridging modes. Peripheral ligation is provided by four chelating NO₃⁻ groups, two on each Dy1 atom, and six chelating hmp⁻ groups, one each on the Dy1 atoms, and Mn2, Mn2', Mn3 and Mn3' of layer **B**; the hmp⁻ alkoxide arms also bridge Dy atoms with Mn atoms of layer **B**, or vice-versa. The Mn and Dy atoms are six and nine coordinate, respectively, and the Mn^{III} oxidation states were determined using a combination of charge-balance considerations, inspection of metric parameters and bond valence sum (BVS) calculations (Table 8-2).⁴⁸ As expected, the Mn^{III} centers exhibit a Jahn-Teller (JT) distortion, as expected for a high-spin d⁴ ion in near-octahedral geometry, and takes the form of the usual axial elongation. The JT elongation axes of the Mn^{III} atoms of layer **C** are approximately parallel to each other (thicker black bonds in Figure 8-2, bottom right). In layer **B**, the JT axes of Mn1 and Mn3 are approximately parallel but that of Mn2 is roughly perpendicular to them (Figure 8-2, bottom left).

The overall structure of these Mn₁₀Ln₂ complexes is unprecedented in 3d-4f chemistry, but that of the central **BCB** Mn₁₀ subunit is similar to that in the homometallic complexes [Mn₁₀O₈(O₂CPh)₆L₈] (L is the anion of picolinic acid or dibenzoylmethane),²⁶⁶ which also comprises two Mn₃ triangular units above and below a central Mn₄ planar unit; however, there are significant differences in the exact disposition of the three units and in the resulting metric parameters.

8.3.3 Magnetochemistry

Solid-state variable-temperature dc magnetic susceptibility data were collected on powdered microcrystalline samples of complexes **8-1** – **8-9** in the 5.0 - 300 K range and in a 0.1 T magnetic field. We will first discuss the data for [Mn₁₀Y₂] (**8-9**) and [Mn₁₀Gd₂] (**8-4**): the first will allow characterization of the magnetic properties of the Mn₁₀ sub-unit alone, and the second will show the resultant of its exchange coupling with isotropic Gd³⁺ ions ($S = 7/2$, ⁸S_{7/2} free-ion term). This will assist the interpretation of the data for the other complexes, which contain strongly anisotropic Ln^{III} ions.

8.3.3.1 Complexes **8-9** (Mn₁₀Y₂) and **8-4** (Mn₁₀Gd₂)

The plots of $\chi_M T$ vs T for **8-4** and **8-9** are shown in Figure 8-3. For **8-9**, the value of $\chi_M T$ smoothly decreases from 28.4 cm³Kmol⁻¹ at 300 K to 10.7 cm³Kmol⁻¹ at 5 K. The 300 K value is slightly less than the spin-only ($g = 2$) value of 30 cm³Kmol⁻¹ for ten Mn^{III} ions with non-interacting metal centers and decreases with decrease in temperature, indicating the presence of dominant intramolecular antiferromagnetic exchange interactions. The 5.0 K value suggests an $S = 4$ ground state. For **8-4**, the value of $\chi_M T$ decreases from 37.9 cm³Kmol⁻¹ at 300 K to 32.4 cm³Kmol⁻¹ at 50 K, stays roughly constant down to 15 K, and then decreases rapidly to 27.4 cm³Kmol⁻¹ at 5 K. The 300 K value is much less than the spin-only value of 45.7 cm³Kmol⁻¹ for ten Mn^{III} and two Gd^{III} non-interacting ions. The value of $\chi_M T$ at 5 K suggests an $S = 7$ ground state.

To confirm the above ground state spin estimates, magnetization (M) data were collected at various fields up to 7 T and in the 1.8-10 K temperature range. The resulting data are plotted in Figure 8-4 as reduced magnetization ($M/N\mu_B$) vs H/T , where N is Avogadro's number and μ_B is the Bohr magneton. The data were fit, using the program MAGNET,⁵³ by diagonalization of the spin Hamiltonian matrix assuming only the ground state is populated, incorporating axial

anisotropy ($D\hat{S}_z^2$) and Zeeman terms, and employing a full powder average. The corresponding spin Hamiltonian is given by eq 8-2, where S_z is the z-axis spin operator, g is the electronic g

$$\mathcal{H} = D\hat{S}_z^2 + g\mu_B\mu_0\hat{S}\cdot H \quad (8-2)$$

factor, μ_0 is the vacuum permeability, and H is the applied field. The last term in eq 8-2 is the Zeeman energy associated with the applied magnetic field. An acceptable fit for **8-9** was obtained with $S = 4$, $g = 2.01$ and $D = -0.89 \text{ cm}^{-1}$ using data collected in the 0.1-0.8 T field range; this fit is shown as the solid lines in Figure 8-4 (left). Alternative fits with $S = 3$ or 5 were rejected because they gave unreasonable values of g of 2.67 and 1.65, respectively. We could not get a good fit when we included data collected at fields higher than 0.8 T, as is often the case for such polynuclear complexes where there are low-lying excited states as a result of weak interactions and/or spin frustration effects.^{62,267} To assess the hardness of the fit and the resulting uncertainties in g and D , a root-mean square D vs g error surface for the fit was generated for **8-9** using the program GRID,⁷¹ which calculates the difference between the experimental $M/N\mu_B$ data and those calculated for various combinations of D and g . The corresponding D vs g 2-D contour plot for **8-9** is provided in Figure 8-5 and shows a soft minimum from which we estimate the uncertainties in the fit parameters to be $S = 4$, $g = 2.01(1)$, and $D = -0.89(5) \text{ cm}^{-1}$.

For $\text{Mn}_{10}\text{Gd}_2$ complex **8-4**, even more difficulty was encountered in obtaining a good fit of the data, which makes sense given that exchange couplings involving lanthanide ions are very weak as a result of the buried nature of f orbitals, and thus there will be an even greater number of very low-lying excited states. The best fit was with $S = 7$, $g = 2.00$ and $D = -0.11 \text{ cm}^{-1}$, and this is shown as the solid lines in Figure 8-4 (right). The overestimation by the fit of the experimental data at the lower fields of the plot suggests that the true ground state may be $S = 6$ with a very low-lying $S = 7$ excited state that is stabilized below the true ground state by the

applied field. Thus, the only safe conclusion to be drawn for the magnetization fit is that the ground state of **8-4** is probably either $S = 6$ or $S = 7$. We shall return to this point below. The corresponding D vs g 2-D contour plot for **8-4** is provided in Figure 8-5 (right) and also shows a soft minimum from which we estimate the uncertainties in the fit parameters to be $S = 7$, $g = 2.00(2)$, and $D = -0.11(1) \text{ cm}^{-1}$.

To probe the ground states of **8-4** and **8-9** further, and to assess their magnetization relaxation dynamics, ac susceptibility data were collected in the 1.8-10 K range under a 3.5 G ac field oscillating at frequencies in the 50-1000 Hz range. The obtained in-phase ac susceptibility (χ_M') signals are plotted as $\chi_M'T$ vs T in Figure 8-3 (right) and are invaluable as an additional and independent means to determine the ground state spin of a molecule without any complications from a dc field.^{69,224} $\chi_M'T$ for **8-9** steadily decreases with decreasing T , consistent with depopulation of low-lying excited states, and extrapolates to just under $10 \text{ cm}^3\text{Kmol}^{-1}$ at 0 K; this indicates an $S = 4$ ground state and $g \sim 2$, in agreement with the dc magnetization fit. $\chi_M'T$ for **8-4** again decreases steadily down to 8 K and then more rapidly, appearing to be heading for $\sim 19 \text{ cm}^3\text{Kmol}^{-1}$. Assuming the latter decrease is due to depopulation of excited states, the extrapolation indicates an $S = 6$ ground state and a very low-lying excited state(s). The ac data thus confirm the conclusions of the dc magnetization fit that **8-4** has a greater ground state S value than **8-9**; in any case, the precise ground state spin value of **8-4** is not essential for the analyses described below.

8.3.3.2 Comparison of 8-9 (Mn₁₀Y₂) with 8-4 (Mn₁₀Gd₂), 8-5 (Mn₁₀Tb₂), 8-6 (Mn₁₀Dy₂), 8-7 (Mn₁₀Ho₂), and 8-8 (Mn₁₀Er₂)

The study of 3d-4f complexes has been of increased interest to magnetochemists since the discovery of intrinsic ferromagnetic coupling in the Cu^{II}-Gd^{III} pair.^{268,269} In the present work, we have similarly sought to identify the nature of the interactions between the Mn₁₀ unit and the

Ln^{III} atoms of **8-1** – **8-8**. The availability of [Mn₁₀Y₂] (**8-9**) allows an empirical approach analogous to that introduced by Costas *et al* and Kahn *et al*.^{249,250} The magnetic properties of a [Mn₁₀Ln₂] complex are governed by (i) the magnetic properties of the central Mn₁₀ unit resulting from its many Mn^{III}...Mn^{III} interactions; (ii) Mn^{III}...Ln^{III} interactions between the Mn₁₀ unit and the Ln^{III} atoms; and (iii) the thermal population of the spin-orbit (Stark) components of the Ln^{III} ion. Complex **8-9** has allowed point (i) to be separately elucidated. Insights into the nature of the Mn^{III}...Ln^{III} interactions can now be obtained by comparing the $\chi_M T$ vs T data for [Mn₁₀Ln₂] and [Mn₁₀Y₂] (assuming that the three separate Mn^{III}...Ln^{III} interactions at each end of the molecule are insignificantly different, which is reasonable given that they are all bridged by a μ_4 -O²⁻ and an hmp⁻ alkoxide arm (Figures 8-1 and 8-2). This is carried out by determining the difference $\Delta(\chi_M T)$ between $\chi_M T$ for a [Mn₁₀Ln₂] cluster and [Mn₁₀Y₂] (eq 8-3). $\Delta(\chi_M T)$ will thus reflect both points (ii) and (iii), except for isotropic Gd^{III} (**8-4**) where it directly probes point (ii).

$$\Delta(\chi_M T) = (\chi_M T)_{\text{MnLn}} - (\chi_M T)_{\text{MnY}} \quad (8-3)$$

We do not have access to the analogous Co^{III}₁₀Ln₂ complexes, i.e. containing diamagnetic Co^{III} in place of the Mn^{III} of **8-1** – **8-8**, and thus cannot therefore separately determine the exact Ln^{III} $\chi_M T$ vs T behavior in these complexes, i.e. point (iii). However, the latter is available in the literature for Ln^{III} ions in a variety of coordination environments similar to **8-1** – **8-8**, and thus eq 8-3 can be employed to obtain important insights into the nature of the Mn^{III}...Ln^{III} interactions in these [Mn₁₀Ln₂] complexes.

Application of eq 8-3 to **8-4** and **8-9** gives the $\Delta(\chi_M T)$ shown as a dashed line in Figure 8-3 (left). $\Delta(\chi_M T)$ increases from 9.5 cm³Kmol⁻¹ at 300 K to 18.7 cm³Kmol⁻¹ at 10 K, and then drops to 16.6 cm³Kmol⁻¹ at 5 K. Since $\chi_M T$ vs T for Gd^{III} is essentially temperature-independent⁴ (Figure 8-6), the steady increase in $\Delta(\chi_M T)$ with decreasing T suggests the Mn^{III}...Ln^{III} exchange

interactions to be weakly ferromagnetic. This is consistent with the increase in ground state spin between **8-9** ($S = 4$) and **8-4** ($S = 6$ or 7). Note that it is not expected that an $S = 11$ ground state should result for **8-4** from weak ferromagnetic $\text{Mn}^{\text{III}}\cdots\text{Gd}^{\text{III}}$ interactions; there will be extensive spin frustration within the many triangular units of the Mn_{10} core, and resulting intermediate spin alignments, so weak ferromagnetic $\text{Mn}^{\text{III}}\cdots\text{Gd}^{\text{III}}$ interactions (likely comparable in strength to some $\text{Mn}^{\text{III}}\cdots\text{Mn}^{\text{III}}$ interactions), are by no means expected to give a simple spin summation. Indeed, it is even possible that the Mn_{10} portion of **8-4** may not still be effectively $S = 4$ once the extra $\text{Mn}^{\text{III}}\cdots\text{Gd}^{\text{III}}$ interactions are introduced.

The $\chi_{\text{M}}T$ for **8-5** ($\text{Mn}_{10}\text{Tb}_2$) increases from $46.7 \text{ cm}^3\text{Kmol}^{-1}$ at 300 K to $64.3 \text{ cm}^3\text{Kmol}^{-1}$ at 5 K (Figure 8-7, left). The 300 K value is slightly less than the spin only value of $53.6 \text{ cm}^3\text{Kmol}^{-1}$ expected for ten Mn^{III} ions and two Tb^{III} ($4f^8$, 7F_6 , $23.6 \text{ cm}^3\text{Kmol}^{-1}$) non-interacting ions (using the free-ion approximation for Tb) owing to the antiferromagnetic interactions within the Mn_{10} unit. The difference $\Delta(\chi_{\text{M}}T)$ increases sharply with decreasing temperature, from $18.2 \text{ cm}^3\text{Kmol}^{-1}$ at 300 K to $53.5 \text{ cm}^3\text{Kmol}^{-1}$ at 5 K. This indicates ferromagnetic $\text{Mn}^{\text{III}}\cdots\text{Tb}^{\text{III}}$ interactions. The $\chi_{\text{M}}T$ for **8-6** ($\text{Mn}_{10}\text{Dy}_2$) decreases slightly from $52.3 \text{ cm}^3\text{Kmol}^{-1}$ at 300 K to $48.0 \text{ cm}^3\text{Kmol}^{-1}$ at 50 K and then increases again reaching $51.9 \text{ cm}^3\text{Kmol}^{-1}$ at 5 K (Figure 8-7, right). The 300 K value is slightly less than the spin only value of $58.3 \text{ cm}^3\text{Kmol}^{-1}$ expected for ten Mn^{III} ions and two Dy^{III} ions ($4f^9$, $^6H_{15/2}$, $28.3 \text{ cm}^3\text{Kmol}^{-1}$). The difference $\Delta(\chi_{\text{M}}T)$ again increases sharply as the temperature is lowered, from $23.8 \text{ cm}^3\text{Kmol}^{-1}$ at 300 K to $41.1 \text{ cm}^3\text{Kmol}^{-1}$ at 5 K, again indicating ferromagnetic $\text{Mn}^{\text{III}}\cdots\text{Dy}^{\text{III}}$ interactions. Note that $\chi_{\text{M}}T$ vs T plots for isolated Dy^{III} (and Tb^{III}) complexes show decreases with decreasing T ,^{236,246,249-251,270} and thus they by themselves (i.e. point (iii) above) cannot be responsible for the increasing $\Delta(\chi_{\text{M}}T)$. The $\chi_{\text{M}}T$ for **8-7** decreases from $51.9 \text{ cm}^3\text{Kmol}^{-1}$ at 300 K to $40.5 \text{ cm}^3\text{Kmol}^{-1}$ at 5 K (Figure 8-8, left). The 300 K value is

again slightly less than the spin only value of $58.1 \text{ cm}^3\text{Kmol}^{-1}$ expected for ten Mn^{III} ions and two Ho^{III} ions ($4f^{10}$, $^5\text{I}_8$, $28.1 \text{ cm}^3\text{Kmol}^{-1}$). The $\Delta(\chi_{\text{M}}T)$ increases from $23.5 \text{ cm}^3\text{Kmol}^{-1}$ at 300 K to only $30.0 \text{ cm}^3\text{Kmol}^{-1}$ at 5 K. Thus, the increase in $\Delta(\chi_{\text{M}}T)$ is much smaller than those for **8-5** and **8-6**, and this makes it difficult to conclude with safety the nature of the $\text{Mn}^{\text{III}}\cdots\text{Ho}^{\text{III}}$ interactions. The $\chi_{\text{M}}T$ for **8-8** decreases continuously from $49.5 \text{ cm}^3\text{Kmol}^{-1}$ at 300 K to $21.3 \text{ cm}^3\text{Kmol}^{-1}$ at 5 K (Figure 6d). The 300 K value is less than the spin only value of $52.9 \text{ cm}^3\text{Kmol}^{-1}$ expected for ten Mn^{III} ions and two Er^{III} ions ($4f^{11}$, $^4\text{I}_{15/2}$, $22.9 \text{ cm}^3\text{Kmol}^{-1}$). The $\Delta(\chi_{\text{M}}T)$ stays approximately constant at $21.1 \text{ cm}^3\text{Kmol}^{-1}$ from 300 K to 100 K and then drops to $10.5 \text{ cm}^3\text{Kmol}^{-1}$ suggesting weak antiferromagnetic $\text{Mn}^{\text{III}}\cdots\text{Er}^{\text{III}}$ interactions in this complex.

8.3.3.3 Comparison of **8-9** (Mn_{10}Y_2) with **8-1** ($\text{Mn}_{10}\text{Pr}_2$), **8-2** ($\text{Mn}_{10}\text{Nd}_2$), **8-3** ($\text{Mn}_{10}\text{Sm}_2$)

For these three complexes with early lanthanides, the $\chi_{\text{M}}T$ vs T plots were essentially identical (Figure 8-9). The $\chi_{\text{M}}T$ at 300 K is 27.4, 28.4, and $26.8 \text{ cm}^3\text{Kmol}^{-1}$ for **8-1**, **8-2** and **8-3**, respectively. In each case, $\chi_{\text{M}}T$ then decreases with decreasing temperature to 14.6, 15.2, and $16.0 \text{ cm}^3\text{Kmol}^{-1}$, respectively, at 5 K. The $\chi_{\text{M}}T$ vs T behaviors of **8-1** – **8-3** are thus essentially parallel to that of **8-9**, except at the lowest temperatures. Consequently, $\Delta(\chi_{\text{M}}T)$ is small and negative at higher temperatures, and then slightly positive at lower temperatures. Since we do not know the exact $\chi_{\text{M}}T$ vs T behaviors of the Ln^{III} ions in the absence of the Mn^{III} , we cannot draw any safe conclusions from these small magnitudes of $\Delta(\chi_{\text{M}}T)$ about the exact sign of $\text{Mn}^{\text{III}}\cdots\text{Ln}^{\text{III}}$. In other work, the interactions of these early lanthanide ions with transition metals have been found to be typically antiferromagnetic.^{248-251,254,271}

The combined results suggest that complex **8-5** contains ferromagnetic $\text{Mn}^{\text{III}}\cdots\text{Tb}^{\text{III}}$ interactions, as is likely also the case in **8-4** and **8-6**, but the data are not clear enough to come to safe conclusions for the other complexes. It would require access to the corresponding M_{10}Ln_2 complexes with $\text{M} = \text{Co}^{\text{III}}$ or other diamagnetic ion to probe this point further. It should also be

reiterated that the exchange interactions within the Mn_{10} unit may be slightly altered as the Ln^{III} changes (as a result of small changes to bond distances and angles), and that this and the introduction of $\text{Mn}^{\text{III}}\cdots\text{Ln}^{\text{III}}$ interactions will complicate further the spin frustration effects. Thus, small changes to $\Delta(\chi_M T)$ are not considered reliable indicators of the sign of the $\text{Mn}^{\text{III}}\cdots\text{Ln}^{\text{III}}$ interactions.

8.3.3.4 Out-of-Phase ac Susceptibility Signals and Magnetization Hysteresis Loops

As stated in the Introduction, one of the objectives of the present work was to obtain new SMMs. We have thus explored all complexes by ac susceptibility studies. The in-phase signals for **8-4** and **8-9** were shown in Figure 8-3 (right); their out-of-phase (χ_M'') signals are shown in Figure 8-10. Complex **8-9** shows only the merest hint of a frequency-dependent signal down to 1.8 K, the operating minimum of our SQUID. Complex **8-4** shows a stronger but still very weak signal. Since the upper limit (U) to the magnetization relaxation barrier is given by $S^2|D|$ and $(S^2 - \frac{1}{4})|D|$ for integer and half-integer spin, respectively, the difference between **8-4** and **8-9** must reflect a bigger barrier as a result of the former's increased ground state spin - isotropic Gd^{III} is not expected to significantly increase the anisotropy. Similarly very weak signals were also observed for **8-1** – **8-3** (Figure 8-11). Thus, these complexes are at best only poor SMMs with very small relaxation barriers. However, much more encouraging results were observed for **8-5** – **8-7**, where the Ln^{III} ions bring both a large spin and large anisotropy to the molecules. In Figure 8-12 are shown the $\chi_M' T$ vs T and χ_M'' vs T plots for these complexes, and two points should be noted: (a) in each case, the $\chi_M' T$ at 5K is essentially identical to that in the corresponding dc $\chi_M T$ vs T plot (Figure 8-7) showing that the latter was not unduly affected by the dc field used; and (b) in each case, below ~ 3 K there is a frequency-dependent drop in $\chi_M' T$ and a strong and frequency-dependent χ_M'' peak, approximately one order of magnitude larger than those in **8-4**.

These data suggest that **8-5** – **8-7** are SMMs with significant relaxation barriers, and thus their magnetization vector cannot relax fast enough to stay in phase with the oscillating ac field.

The ac χ_M'' vs T plots can be used as a source of relaxation rate vs T kinetic data for determining the true or effective energy barrier (U_{eff}) to magnetization relaxation, because at the χ_M'' peak maximum the relaxation rate ($1/\tau$, where τ is the relaxation time) is equal to the angular frequency ($2\pi\nu$) of the ac field. The obtained data for **8-5** – **8-7** are shown as Arrhenius plots in Figure 8-13, based on the Arrhenius Law of eq 8-4, where k is the Boltzmann constant and τ_0 is the pre-exponential factor. The fit of the data for **8-6** to eq 8-4 (solid line in Figure 8-13) gave

$$\tau = \tau_0 \exp(U_{\text{eff}}/kT) \quad (8-4)$$

$U_{\text{eff}} \sim 39$ K and $\tau_0 \sim 1 \times 10^{-11}$ s. A similar analysis for **8-7** gave $U_{\text{eff}} \sim 41$ K and $\tau_0 \sim 3 \times 10^{-12}$ s.

Because the ac χ_M'' vs T data were over a small temperature range (~ 0.4 K), these values must be considered only approximations. The χ_M'' peaks for **8-5** are at lower temperatures and thus over too small a range for a meaningful plot, but its U_{eff} was comparable with those for **8-6** and **8-7**. Nevertheless, the τ_0 values appear smaller than those typically seen for transition metal SMMs (10^{-7} - 10^{-9} s) but are comparable with other 3d-4f ones.²⁴⁷

Because we were worried that the above U_{eff} and τ_0 values were not very accurate owing to the small T range employed, we carried out a more accurate analysis for representative complex **8-6** by supplementing the ac data with additional relaxation rate vs T data down to 0.04 K obtained from dc magnetization decay vs time measurements on a single crystal of **8-6**·3MeCN·MeOH. The sample's magnetization was first saturated in one direction at ~ 5 K with a large applied dc field, the T was then decreased to a chosen value in the 0.04 – 1.6 K range, the field removed, and the magnetization decay monitored with time. The obtained magnetization vs time plots are characteristic of a distribution of relaxation barriers, and are shown in Figure 8-14

(left). The dc decay and ac χ_M'' data were combined and used to construct an Arrhenius plot over a wider T range (Figure 8-14, right). Fitting of the data in the thermally activated region gave $U_{eff} = 30$ K and $\tau_0 = 6 \times 10^{-10}$ s. Below ~ 0.5 K, the τ vs $1/T$ plot deviates from linearity as the thermally activated relaxation rate diminishes and the relaxation via quantum tunneling through the anisotropy barrier becomes more dominant. Eventually at $T < 0.2$ K, it becomes essentially temperature-independent, as expected for the relaxation now being exclusively by quantum tunneling through the lowest lying M_S (M_J) levels. Such quantum tunneling was first observed for a 3d-4f complex in a $[\text{Mn}_{11}\text{Dy}_4]$ complex.²¹ The U_{eff} value of 30 K for **8-6** is the highest yet reported for a Mn-Ln SMM. Previous examples of $[\text{Mn}_{11}\text{Dy}_4]$,²³⁹ $[\text{Mn}_2\text{Dy}_2]$,²⁴⁰ $[\text{Mn}_6\text{Dy}_4]$,²³⁴ and $[\text{Mn}_{11}\text{Gd}_2]$ ²⁴⁷ SMMs have been reported to have U_{eff} values of 9.3, 15, 16 and 18.4 K respectively.

It should be noted that the U_{eff} value of 39 K obtained for **8-6** using just the ac χ_M'' data is very different from the more reliable 30 K obtained from the combined dc and ac data. These results thus represent an important caveat that inaccuracies of a large magnitude can be introduced by determining the barrier U_{eff} from too small a temperature range. Inversely, it should be accepted that when there is indeed no choice but to determine U_{eff} values over a limited T range, then large inaccuracies are likely.

To confirm whether these complexes are truly SMMs, magnetization vs dc field sweeps were carried out on single crystals of representative complex **8-6**·3MeCN·MeOH.¹⁵³ Hysteresis loops were observed below 1.6 K (Figure 8-15), whose coercivity increases with decreasing temperature and increasing scan rate, as expected for the superparamagnet-like properties of a SMM. The loops are dominated by a large step at zero field due to quantum tunneling of magnetization (QTM) through the anisotropy barrier. The large step is indicative of fast QTM

rates, as is typical of low symmetry molecules. Steps at other field positions are barely visible, and such smearing out is typical of broadening effects from a distribution of molecular environments, as already concluded to be present in the magnetization decay vs time plots mentioned above. Such distributions are due to solvent and/or ligand disorder, and the presence of low-lying excited states.

8.4 Conclusions

The reaction of a preformed Mn_4 cluster, hmpH and simple Ln^{III} salts has provided entry into a new family of 3d-4f $[Mn_{10}Ln_2]$ clusters for most of the Ln ions. Three representative crystal structures have shown the complexes to be isostructural, including the corresponding $[Mn_{10}Ln_2]$ analogue with diamagnetic Y^{III} . Comparisons of the combined dc and ac magnetic susceptibility studies have allowed important insights into the effect of the Ln^{III} ions on the magnetic properties. Complex **8-4**, containing isotropic Gd^{III} with $S = 7/2$ has demonstrated an increase in the spin compared with $[Mn_{10}Y_2]$ complex **8-9** as a result of net ferromagnetic interactions with the Mn_{10} core. This is reflected in the appearance of out-of-phase ac signals indicating the slow relaxation of a SMM. The result demonstrates that as long as the anisotropy of a Mn^{III}_x unit is sufficient, the large spin of Gd^{III} can boost the spin S if couplings are ferromagnetic and thus improve the SMM properties. The other Ln^{III} ions also bring significant anisotropy to the table, but the couplings for early lanthanide ions Pr, Nd and Sm do not improve the SMM properties above those of **8-9**, presumably due to their small spins and possibly antiferromagnetic couplings. The later lanthanide ions Tb, Dy and Ho give much more encouraging results, however, with all three compounds exhibiting strong out-of-phase signals above 1.8 K. This can be attributed to both their significant spin and anisotropy, and the observance of ferromagnetic $Mn \cdots Ln$ coupling between them and the central Mn_{10} unit; the similar ac behavior between **8-7** and **8-5/8-6** suggests the coupling really is ferromagnetic in each

case. The calculated U_{eff} value of 30 K for representative complex **8-6** is the highest yet for a Mn-Ln SMM. Single-crystal studies using a micro-SQUID on representative complex **8-6** confirm the SMM property by the clear observation of hysteresis loops.

The present work thus emphasizes that synthesis of $Mn^{III}-Ln^{III}$ complexes incorporating Tb, Dy and Ho is a somewhat promising approach to higher-barrier SMMs. We have reported elsewhere preliminary results on a related family of $Mn_{11}Ln_4$ complexes, and showed there that the Dy analogue again is an SMM exhibiting magnetization hysteresis. However, the barrier U_{eff} in that case was only 9.3 K, ~30% of that in **8-6**. This and related reports of Mn-Ln complexes^{234,239-241} serve to emphasize that merely incorporating one or more anisotropic Ln^{III} ions into a Mn^{III} -containing cluster, SMM or otherwise, will not automatically increase barriers and thus switch on or improve the SMM property. The nature of the Mn-Ln coupling, the presence of low-lying excited states, the QTM rates, the symmetry of the molecule, and other factors, all impact the observed magnetization relaxation barrier. Nevertheless, the present work does emphasize that it is possible to get barriers from Mn-Ln species that are fairly high, akin to those of two-electron reduced versions of the prototypical SMM family, $[Mn_{12}O_{12}(O_2CR)_{16}(H_2O)_4]^{2-}$, which also show out-of-phase ac peaks in the 2-4 K range.^{203,272}

Table 8-1. Crystallographic data for **8-4**·3MeCN·MeOH, **8-6**·3MeCN·MeOH and **8-9**·4MeCN.

	8-4	8-6	8-9
Formula ^a	C ₁₁₃ H ₉₉ Mn ₁₀ Gd ₂ N ₁₃ O ₄₇	C ₁₁₃ H ₉₉ Mn ₁₀ Dy ₂ N ₁₃ O ₄₇	C ₁₁₄ H ₉₈ Mn ₁₀ Y ₂ N ₁₄ O ₄₆
FW, g/mol ^a	3245.94	3265.46	3127.28
Space group	<i>P</i> $\bar{1}$	<i>P</i> $\bar{1}$	<i>P</i> $\bar{1}$
<i>a</i> , Å	14.7083(7)	14.7358(11)	14.737(3)
<i>b</i> , Å	15.2173(7)	15.2150(12)	15.080(3)
<i>c</i> , Å	16.7604(8)	16.6441(13)	16.569(3)
α , °	67.414(2)	67.6290(10)	67.175(4)
β , °	65.549(2)	65.6580(10)	65.668(4)
γ , °	87.627(2)	87.6360(10)	87.374(4)
<i>V</i> , Å ³	3122.0(3)	3114.3(4)	3063.9(10)
<i>Z</i>	1	1	1
<i>T</i> , K	173(2)	173(2)	173(2)
λ , Å ^b	0.71073	0.71073	0.71073
ρ_{calc} , g/cm ³	1.726	1.741	1.712
μ , mm ⁻¹	2.112	2.252	2.024
<i>R</i> 1 ^{c,d}	0.0643	0.0508	0.0710
<i>wR</i> 2 ^e	0.1713	0.1330	0.1614

^a Including solvate molecules. ^b Graphite monochromator. ^c $I > 2\sigma(I)$. ^d $R1 = \Sigma(|F_o| - |F_c|) / \Sigma|F_o|$. ^e $wR2 = [\Sigma[w(F_o^2 - F_c^2)^2] / \Sigma[w(F_o^2)^2]]^{1/2}$, $w = 1/[\sigma^2(F_o^2) + [(ap)^2 + bp]]$, where $p = [\max(F_o^2, O) + 2F_c^2]/3$.

Table 8-2. Bond-valence sums for the Mn atoms of complex **8-4**, **8-6** and **8-9**^a

	8-4			8-6			8-9		
	Mn ^{II}	Mn ^{III}	Mn ^{IV}	Mn ^{II}	Mn ^{III}	Mn ^{IV}	Mn ^{II}	Mn ^{III}	Mn ^{IV}
Mn1	3.09	<u>2.83</u>	2.97	3.05	<u>2.79</u>	2.93	3.13	<u>2.87</u>	3.01
Mn2	3.33	<u>3.08</u>	3.18	3.32	<u>3.07</u>	3.17	3.33	<u>3.08</u>	3.18
Mn3	3.31	<u>3.06</u>	3.16	3.31	<u>3.06</u>	3.16	3.34	<u>3.09</u>	3.18
Mn4	3.15	<u>2.88</u>	3.03	3.16	<u>2.89</u>	3.03	3.22	<u>2.95</u>	3.09
Mn5	3.06	<u>2.80</u>	2.94	3.07	<u>2.81</u>	2.94	3.09	<u>2.83</u>	2.97

^a The underlined value is the one closest to the charge for which it was calculated. The oxidation state of a particular atom can be taken as the nearest whole number to the underlined value

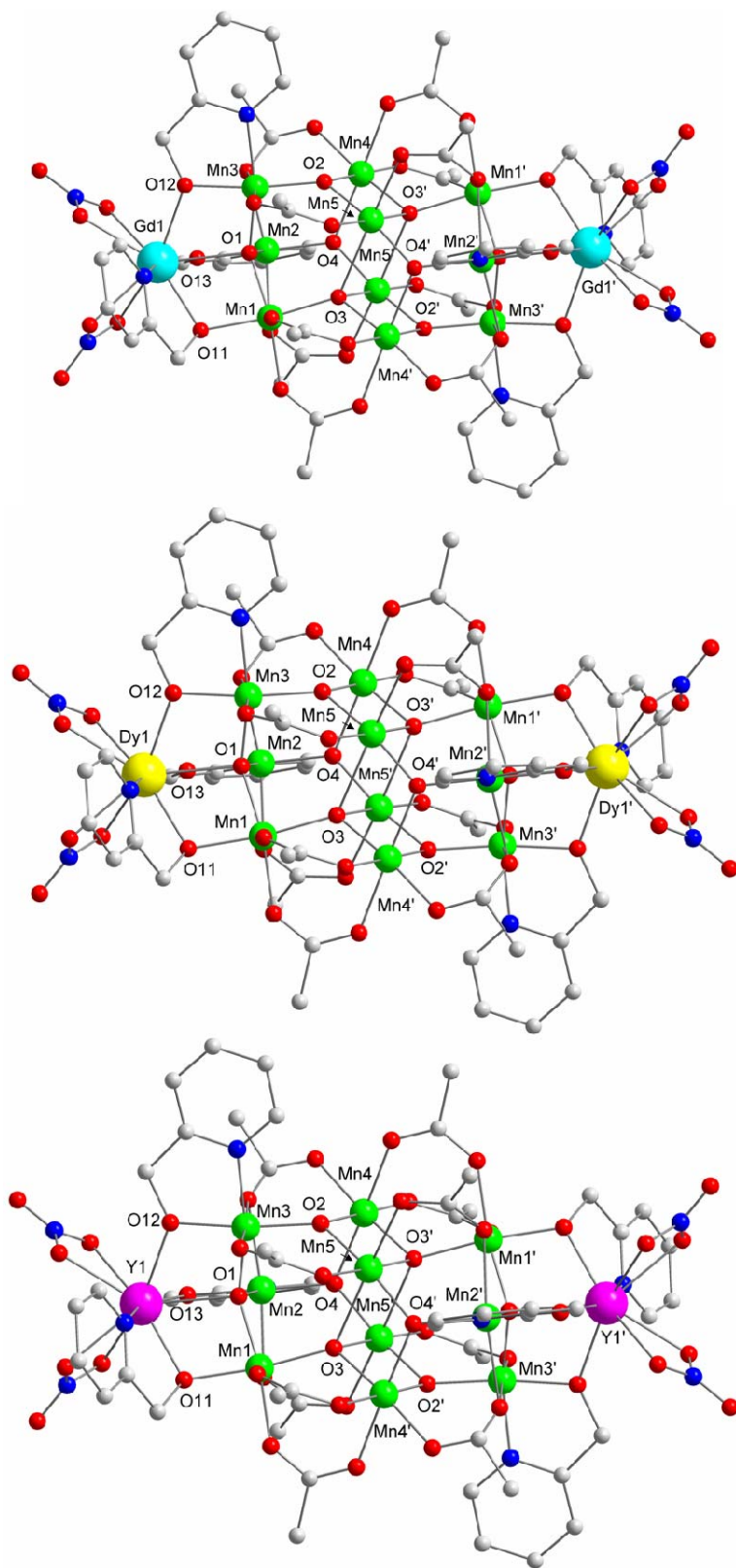


Figure 8-1. The structures of **8-4** (top), **8-6** (middle), and **8-9** (bottom). Hydrogen atoms and phenyl rings (except for the *ipso* carbon atoms) have been omitted for clarity. Color code: Gd, cyan; Dy, yellow; Y, pink; Mn, green; O, red; N, blue; C, grey.

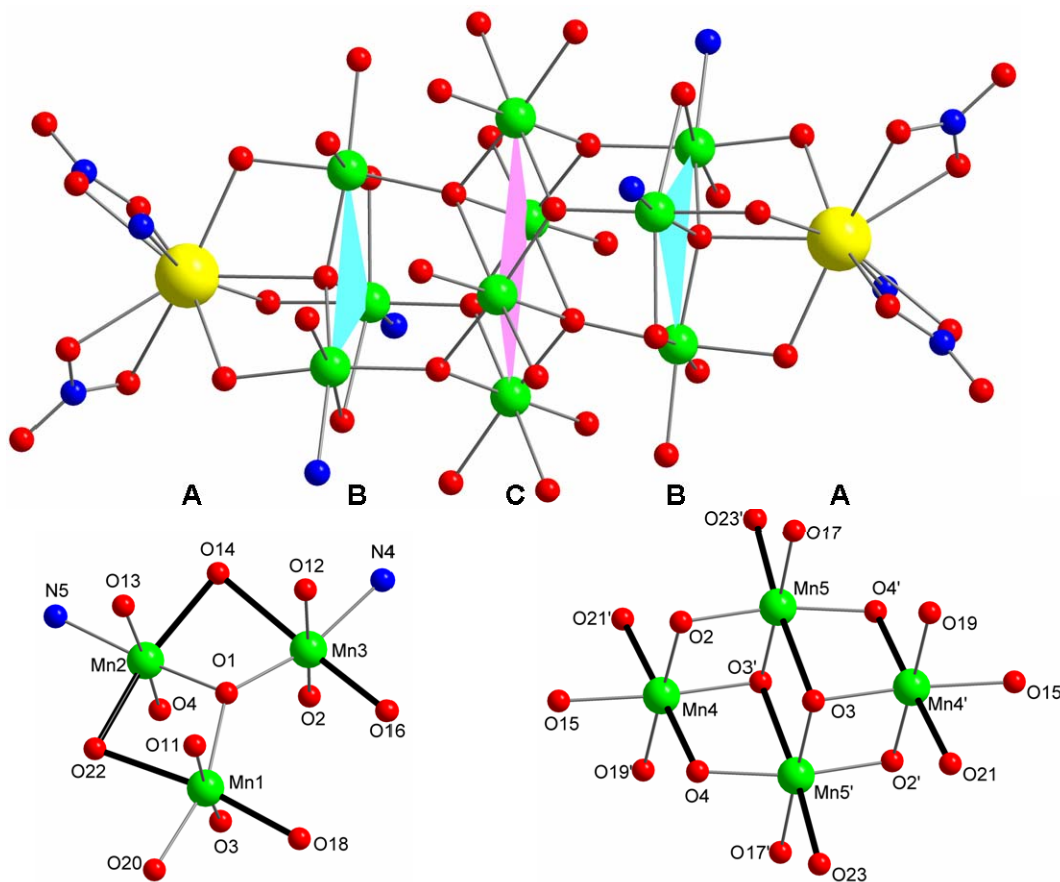


Figure 8-2. (top) Centrosymmetric core of **8-6** emphasizing the **ABCBA** layer structure. (bottom) The **B** (left) and **C** (right) layers showing the Jahn-Teller elongation axes as thicker black bonds. Color code: Dy, yellow; Mn, green; O, red; N, blue; C, grey.

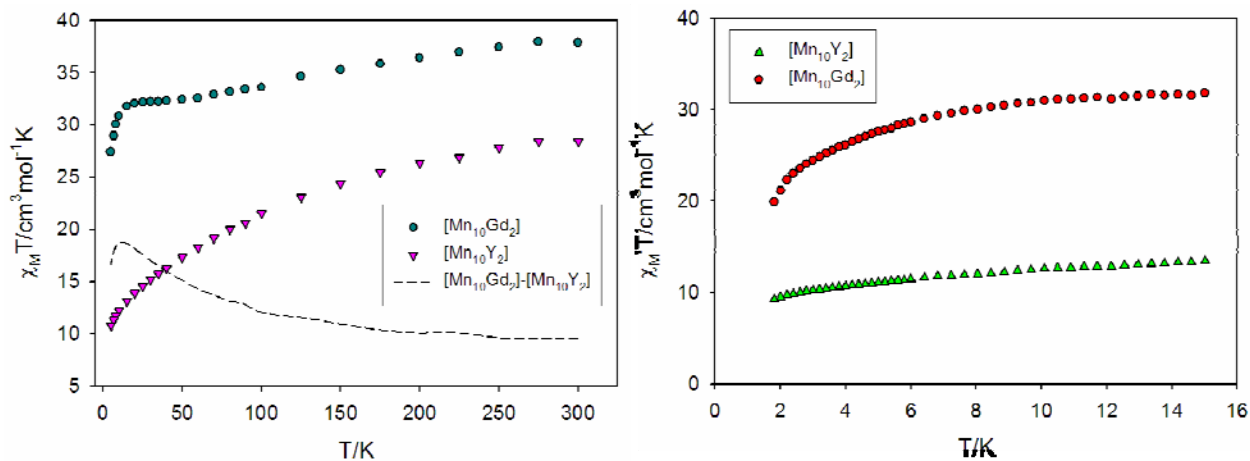


Figure 8-3. (left) Plot of $\chi_M T$ vs T for complexes **8-4** and **8-9** at 0.1 T. The difference, $\Delta(\chi_M T)$, is shown as the dashed line. (right) Plot of in-phase ac susceptibility (χ_M') as $\chi_M' T$ vs T for complexes **8-4** and **8-9**.

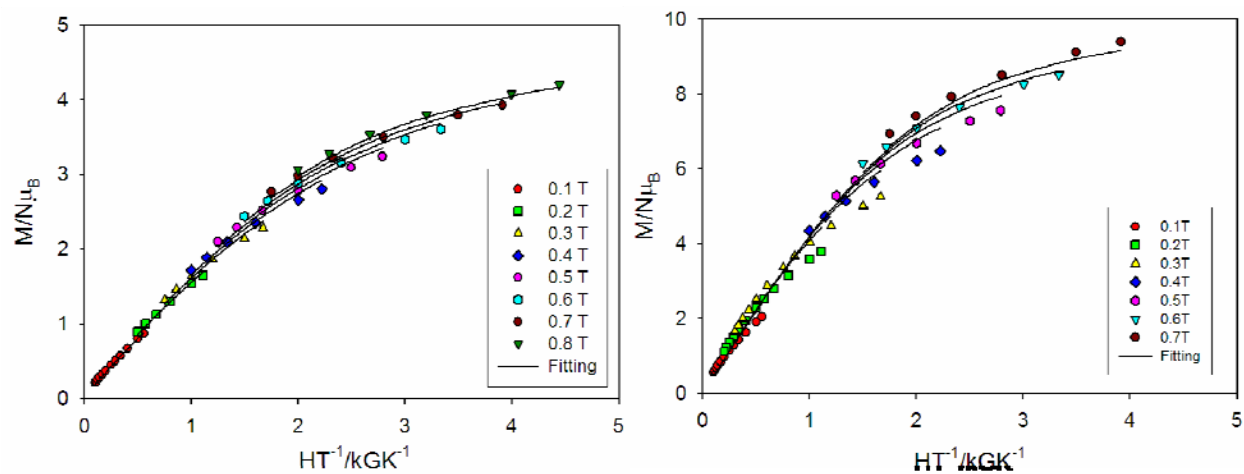


Figure 8-4. Plot of reduced magnetization ($M/N\mu_B$) vs H/T for complexes (left) **8-9** and (right) **8-4**. See the text for the fit parameters.

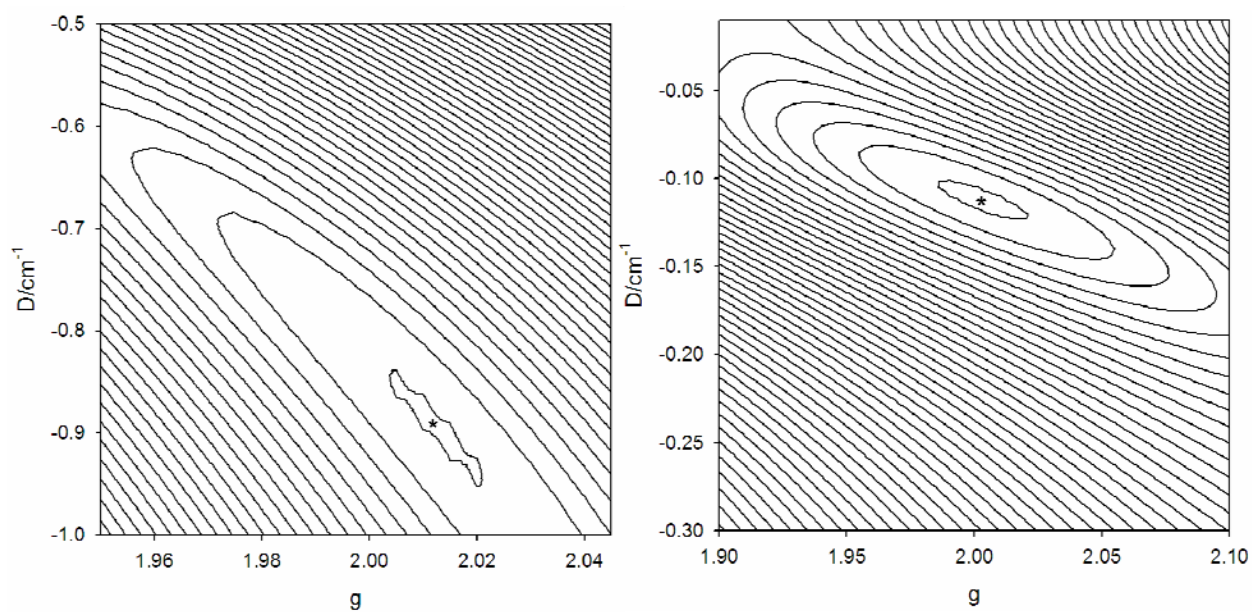


Figure 8-5. Two-dimensional contour plot of the error surface for the D vs g fit for (left) **8-9** and (right) **8-4**. The asterisk indicates the point of minimum error (best fit).

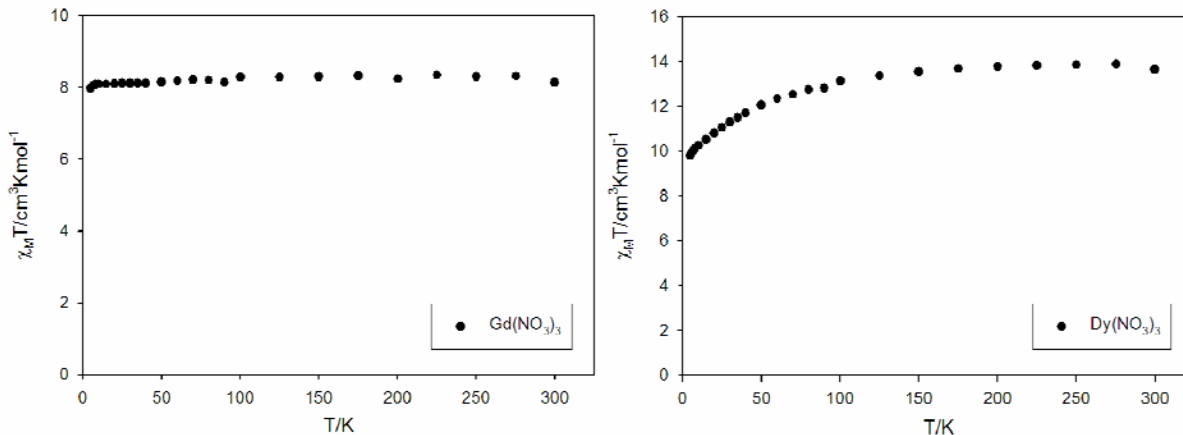


Figure 8-6. Plots of dc $\chi_M T$ vs T for (left) $\text{Gd}(\text{NO}_3)_3 \cdot 6\text{H}_2\text{O}$ and (right) $\text{Dy}(\text{NO}_3)_3 \cdot 5\text{H}_2\text{O}$.

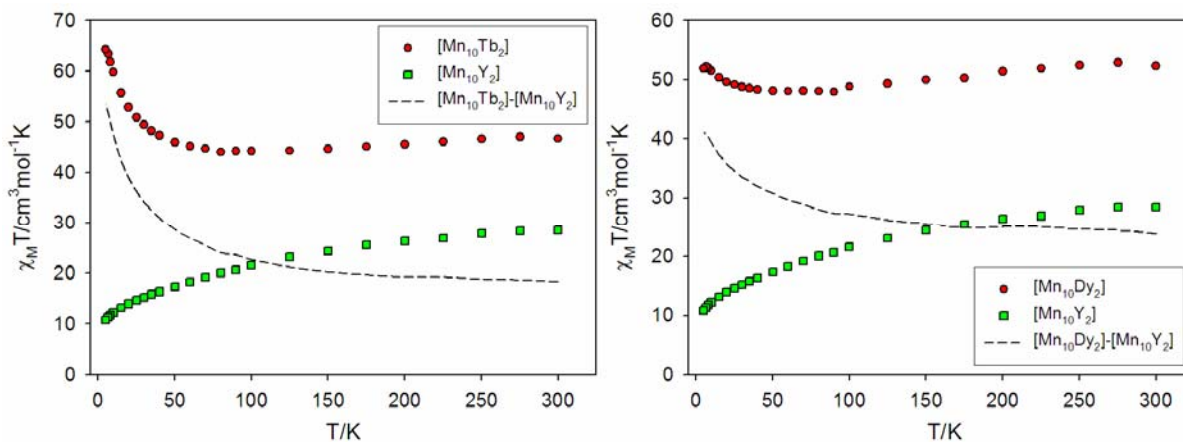


Figure 8-7. Plots of $\chi_M T$ vs T for **8-9** and (left) **8-5** and (right) **8-6**. In each case, the difference, $\Delta(\chi_M T)$, is shown as a dashed line.

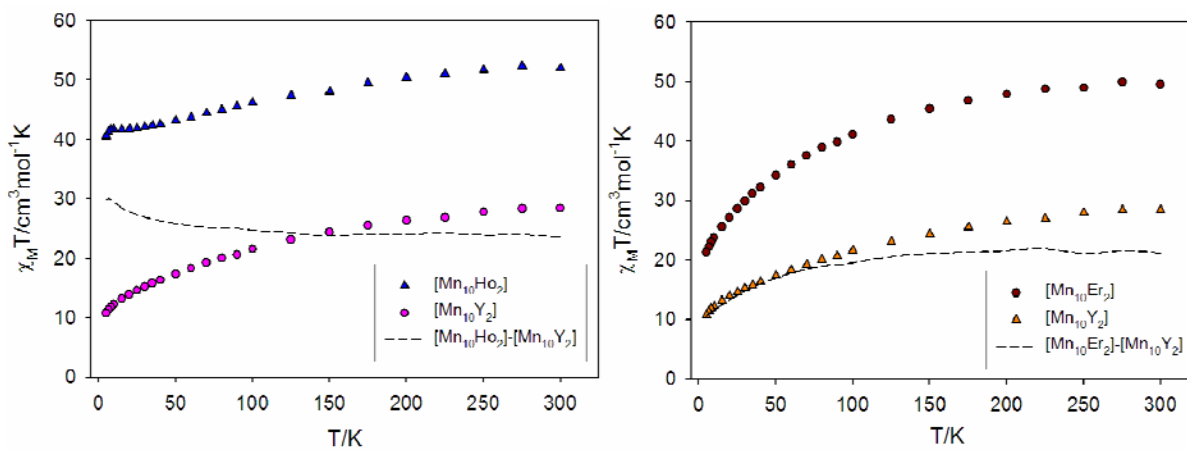


Figure 8-8. Plots of $\chi_M T$ vs T for **8-9** and (left) **8-7** and (right) **8-8**. In each case, the difference, $\Delta(\chi_M T)$, is shown as a dashed line.

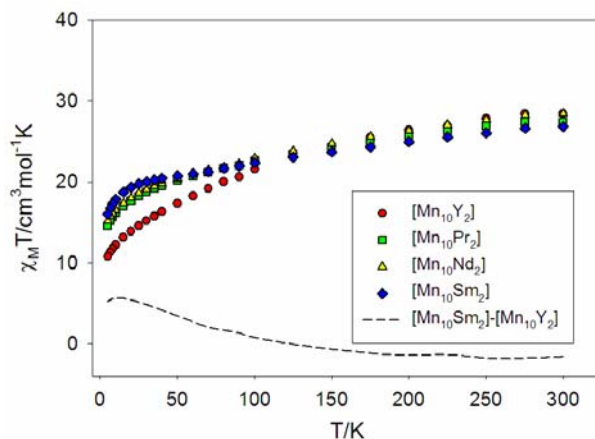


Figure 8-9. Plots of $\chi_M T$ vs T for **8-1**, **8-2**, **8-3** and **8-9**. The dashed line is the difference, $\Delta(\chi_M T)$, between **8-3** and **8-9**; the others are similar.

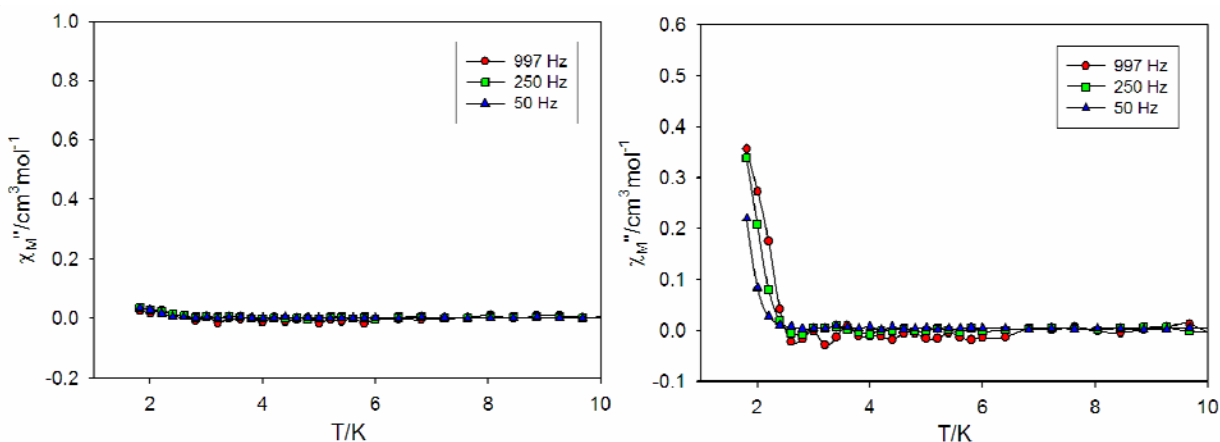


Figure 8-10. Plots of out-of-phase χ_M'' vs T ac susceptibility data for (left) **8-9** (Mn_{10}Y_2), and (right) **8-4** ($\text{Mn}_{10}\text{Gd}_2$).

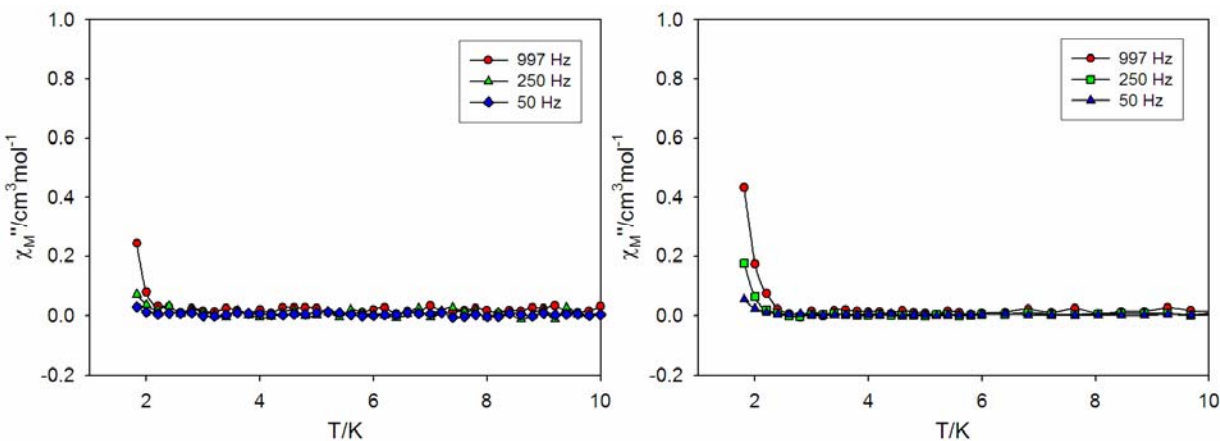


Figure 8-11. Plots of out-of-phase χ_M'' vs T ac susceptibility data for (left) **8-1** ($\text{Mn}_{10}\text{Pr}_2$), and (right) **8-2** ($\text{Mn}_{10}\text{Nd}_2$).

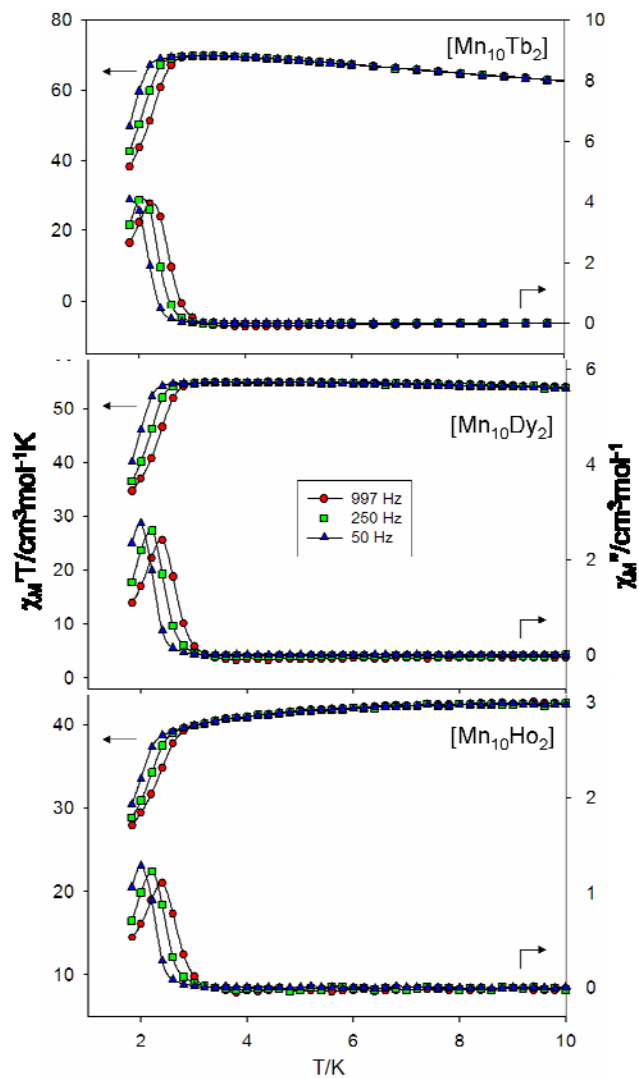


Figure 8-12. Plots of in-phase, $\chi_M' T$ vs T , and out-of-phase χ_M'' vs T ac susceptibility data for (top) **8-5** ($\text{Mn}_{10}\text{Tb}_2$), (middle) **8-6** ($\text{Mn}_{10}\text{Dy}_2$), and (bottom) **8-7** ($\text{Mn}_{10}\text{Ho}_2$).

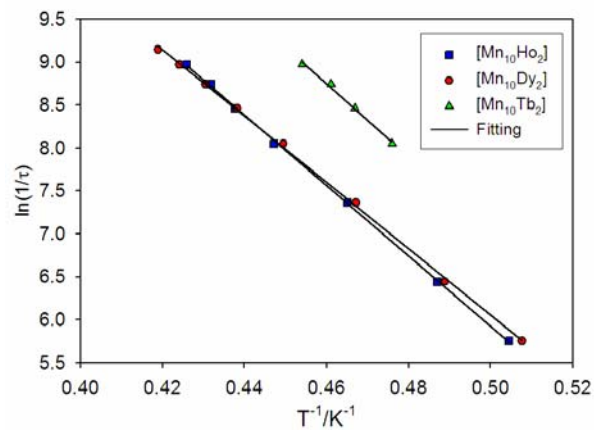


Figure 8-13. Plot of relaxation rate vs reciprocal temperature for **8-5** – **8-7**.

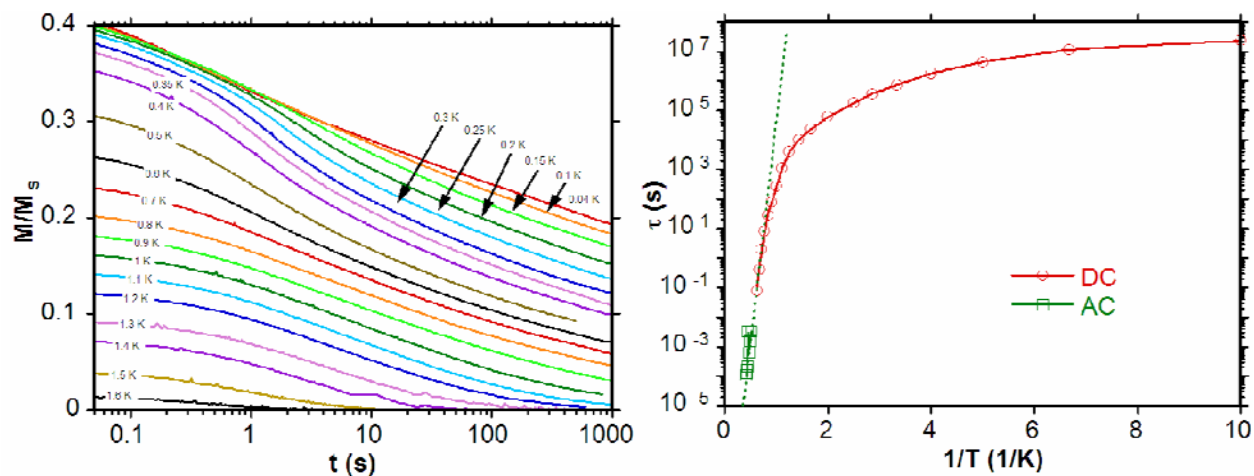


Figure 8-14. (left) Magnetization (M) vs. time decay plots in zero dc field for **8-6**·3MeCN·MeOH. The magnetization is normalized to its saturation value, M_s (right) Plot of relaxation time vs $1/T$ for **8-6** using combined ac χ_M'' and magnetization decay data.

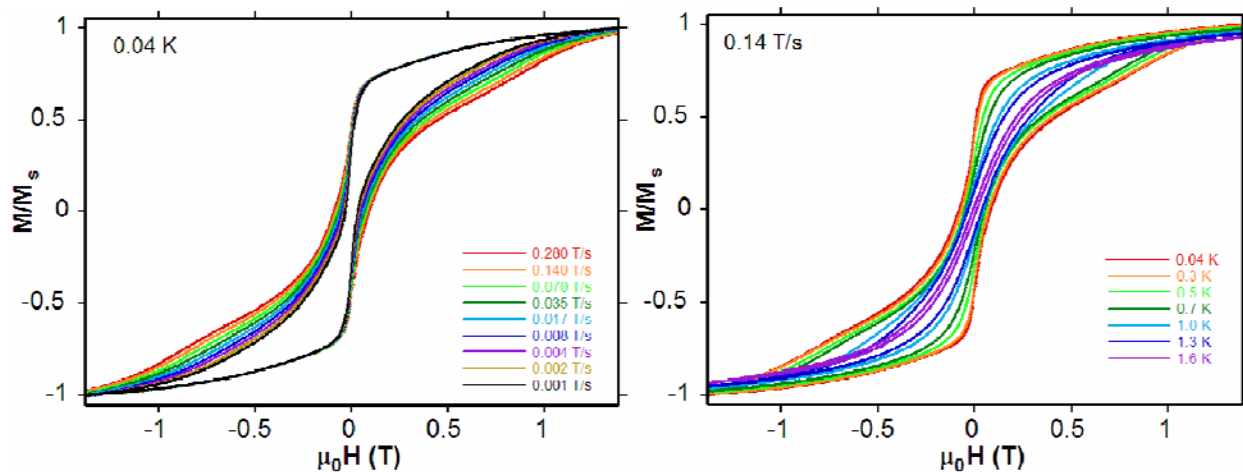


Figure 8-15. Single-crystal magnetization (M) vs dc field (H) hysteresis loops for a single crystal of **8-6**·3MeCN·MeOH at different scan rates (left) and temperatures (right).

CHAPTER 9
A FOURTH ISOLATED OXIDATION LEVEL OF THE $[\text{Mn}_{12}\text{O}_{12}(\text{O}_2\text{CR})_{16}(\text{H}_2\text{O})_4]$ FAMILY
OF SINGLE MOLECULE MAGNETS

9.1 Introduction

Single-molecule magnets (SMMs) are molecules that possess a significant barrier (vs kT) to reorientation of their magnetization (magnetic moment) vector as a result of the combination of a large ground state spin (S) and Ising (easy-axis) magnetoanisotropy (negative axial zero-field splitting parameter (D)).¹³ As such, they represent a molecular (bottom-up) approach to nanomagnetism. The first SMM was $[\text{Mn}_{12}\text{O}_{12}(\text{O}_2\text{CMe})_{16}(\text{H}_2\text{O})_4] \cdot 2\text{HO}_2\text{CMe} \cdot 4\text{H}_2\text{O}$ ^{15,273,274} ($\text{Mn}_{12}\text{-Ac}$; $4\text{Mn}^{\text{IV}}, 8\text{Mn}^{\text{III}}$) and many more have since been synthesized.^{21,22,231,275} Although complexes displaying SMM behavior are known for a variety of 3d, 4d, 4f and mixed-metal complexes,^{9,20,58,79,86,118,162,163,173,190,271,276-282} manganese carboxylate clusters have proven to be the most fruitful source of SMMs.^{21,22,32} Using only a limited palette of ligands and starting materials, a wide range of Mn SMMs has been obtained with their nuclearities ranging from 2 to 84.^{164,172,283} Amongst the known Mn SMMs, the Mn_{12} family continues to be attractive for study as a result of its ease of preparation, stability, ready modification in a variety of ways, high ground state spin ($S = 10$) and anisotropy, and the access to derivatives that crystallize in high symmetry (tetragonal) space groups.^{14,284,285}

The various modifications of the Mn_{12} family of SMMs that have been accomplished to date have proven extremely useful for a myriad of reasons and studies, and have permitted great advances in our knowledge and understanding of Mn_{12} complexes and the SMM phenomenon in general. In this regard, carboxylate substitution^{273,286-288} represented a big step forward because it provided an extremely useful and convenient means of accessing other carboxylate analogues, which provided benefits such as isotopic labeling, tunability of redox properties and increased solubility in a variety of organic solvents. One of the most informative impacts of the latter two

points was the observation of multiple, reversible redox processes and the subsequent generation and isolation of one-electron reduced complexes i.e. salts of the $[\text{Mn}_{12}\text{O}_{12}(\text{O}_2\text{CR})_{16}(\text{H}_2\text{O})_4]^-$ anion, abbreviated $[\text{Mn}_{12}]^-$. The crystal structures of such salts revealed minimal change to the structure on reduction, with the added electron localized on an outer, formerly Mn^{III} atom giving a trapped-valence $\text{Mn}^{\text{IV}}_4\text{Mn}^{\text{III}}_7\text{Mn}^{\text{II}}$ situation.²⁰² The $[\text{Mn}_{12}]^-$ salts allowed an assessment of the structural, magnetic and spectroscopic consequences of changing the electron count, as well as allowing the study of the differences in quantum properties due to the integer vs half-integer *S* value, since $[\text{Mn}_{12}]^-$ salts have an $S = 9\frac{1}{2}$ ground state.^{202,289-291} The subsequent introduction of carboxylates with more electron-withdrawing substituents into the Mn_{12} complexes made two-electron reduction easier and led to the successful generation and isolation of two-electron reduced $[\text{Mn}_{12}\text{O}_{12}(\text{O}_2\text{CR})_{16}(\text{H}_2\text{O})_4]^{2-}$ complexes, $[\text{Mn}_{12}]^{2-}$, such as salts of $[\text{Mn}_{12}\text{O}_{12}(\text{O}_2\text{CCHCl}_2)_{16}(\text{H}_2\text{O})_4]^{2-}$.²⁰³ The $[\text{Mn}_{12}]^{2-}$ anion was again found to be trapped-valence, with a $\text{Mn}^{\text{IV}}_4\text{Mn}^{\text{III}}_6\text{Mn}^{\text{II}}_2$ oxidation state description, and the spin was found to be $S = 10$, the same as the Mn_{12} parent compound.

The above efforts had thus provided the Mn_{12} family of SMMs in three oxidation states, providing a wealth of comparative chemical and physical data. So much so that it was clearly desirable to extend this family to a fourth oxidation level if at all possible. The three-electron reduction of Mn_{12} complexes is in fact observable in the cyclic voltammetry,²⁰³ and so we decided to pursue the generation and isolation of this oxidation state. Indeed, this effort has been successful, and we herein report the synthesis and characterization of the $[\text{Mn}_{12}]^{3-}$ salts $(\text{NPr}^n)_3[\text{Mn}_{12}\text{O}_{12}(\text{O}_2\text{CCHCl}_2)_{16}(\text{H}_2\text{O})_4]$ and $(\text{NMe}_4)_3[\text{Mn}_{12}\text{O}_{12}(\text{O}_2\text{CCHCl}_2)_{16}(\text{H}_2\text{O})_4]$.²⁰⁷

9.2 Experimental Section

9.2.1 Syntheses

All manipulations were performed under aerobic conditions using materials as received, except if otherwise noted. $[\text{Mn}_{12}\text{O}_{12}(\text{O}_2\text{CCHCl}_2)_{16}(\text{H}_2\text{O})]$ (**9-1**) was prepared as described elsewhere.²⁰³

$(\text{NPr}^n)_4[\text{Mn}_{12}\text{O}_{12}(\text{O}_2\text{CCHCl}_2)_{16}(\text{H}_2\text{O})_4]$ (**9-2**). Solid NPr^nI (0.03 g, 0.1 mmol) was added to a stirred dark brown solution of complex **9-1** (0.30 g, 0.10 mmol) in MeCN (15 mL). The resulting solution was stirred for 4 hours with no noticeable color change. After 4 hours, hexanes (20 mL) were added causing the formation of two phases, and the mixture shaken to facilitate extraction of I_2 into the hexanes phase. The hexanes layer was then removed, and the extraction process repeated a few more times until the hexanes layer was colorless. The two layers were then separated and the MeCN solution evaporated to dryness. The residue was dissolved in MeCN (10 mL), and Et_2O /hexanes (1:1 v/v, 20 mL) added. The resulting microcrystalline product was isolated and dried in vacuo. Yield, 70 %. Anal. Calcd (Found) for **9-2**·MeCN ($\text{C}_{46}\text{H}_{55}\text{N}_2\text{Mn}_{12}\text{O}_{48}\text{Cl}_{32}$): C, 17.28 (17.60); H, 1.73 (1.62); N, 0.87 (0.53) %.

$(\text{NPr}^n)_2[\text{Mn}_{12}\text{O}_{12}(\text{O}_2\text{CCHCl}_2)_{16}(\text{H}_2\text{O})_4]$ (**9-3**). Complex **9-3** was synthesized following the same procedure as for complex **9-2**, except that two equivalents of NPr^nI (0.06 g, 0.2 mmol) were employed and the reaction mixture was stirred for 10 hours. Yield, 65 %. Anal. Calcd (Found) for **9-3**·MeCN ($\text{C}_{58}\text{H}_{83}\text{N}_3\text{Mn}_{12}\text{O}_{48}\text{Cl}_{32}$): C, 20.59(20.82); H, 2.47(2.26); N, 1.24(0.88) %.

$(\text{NPr}^n)_3[\text{Mn}_{12}\text{O}_{12}(\text{O}_2\text{CCHCl}_2)_{16}(\text{H}_2\text{O})_4]$ (**9-4**). Complex **9-4** was synthesized following the same procedure as for complex **9-2**, except that three equivalents of NPr^nI (0.09 g, 0.3 mmol) were employed. The reaction mixture was stirred for 40 hours and the product was not recrystallized. Yield, 85 %. Anal. Calcd (Found) for **9-4** ($\text{C}_{68}\text{H}_{108}\text{N}_3\text{Mn}_{12}\text{O}_{48}\text{Cl}_{32}$): C, 23.14 (22.85); H, 3.08 (2.78); N, 1.19 (1.16) %.

(NMe₄)₃[Mn₁₂O₁₂(O₂CCHCl₂)₁₆(H₂O)₄] (**9-5**). Complex **9-5** was synthesized following the same procedure as for complex **9-4**, except that three equivalents of NMe₄I (0.06 g, 0.3 mmol) were employed and the reaction mixture was stirred for 48 hours. Yield, 80 %. Anal. Calcd (Found) for **9-5**·MeCN (C₄₆H₆₃N₄Mn₁₂O₄₈Cl₃₂): C, 17.08(16.92); H, 1.96(1.90); N, 1.73(1.78) %.

9.3 Results and Discussion

9.3.1 Syntheses

Electrochemical studies on various [Mn₁₂O₁₂(O₂CR)₁₆(H₂O)] complexes have revealed a rich redox chemistry involving several quasi-reversible oxidation and reduction processes.^{202,203,292} In addition, the redox potentials are, as expected, very sensitive to the electron-withdrawing and -donating ability of the carboxylate ligand. For example, E_{1/2} (vs ferrocene) for the first reduction varies by almost a volt from 0.91 V for the R = CHCl₂ complex to 0.00 V for the R = *p*-C₆H₄OMe complex. The particularly high electron-withdrawing capability of the R = CHCl₂ group, as reflected in the very low pK_a of 1.48 for CHCl₂CO₂H, brought the second reduction potential to 0.61 V (Figure 9-1), well within the reducing capability of our preferred reducing agent, iodide (0.14 V vs ferrocene in MeCN),²⁹³ and this led to the subsequent successful generation and isolation of (PPh₄)₂[Mn₁₂O₁₂(O₂CCHCl₂)₁₆(H₂O)₄] reported elsewhere.²⁰³ Similarly for the R = C₆F₅ substituent, which has also been used for the synthesis of the two-electron reduced complex (NMe₄)₂[Mn₁₂O₁₂(O₂CC₆F₅)₁₆(H₂O)₄]²⁷² from the reaction of [Mn₁₂O₁₂(O₂CC₆F₅)₁₆(H₂O)₄] with two equivalents of I⁻.

For the present work, we chose to employ the R = CHCl₂ carboxylate complex because it has a particularly well resolved third one-electron reduction in the cyclic voltammogram (CV) and differential pulse voltammogram (DPV) (Figure 9-1), and one that is still within the reducing capability of I⁻. A fourth, clearly irreversible reduction at ~0.1 V represented a potential problem, so we avoided the use of an excess of reducing agent beyond the stoichiometric three

equivalents. Thus, complex **9-1** was treated with three equivalents of NMe₄I, NPrⁿ₄I, NBuⁿ₄I and PPh₄I in MeCN for different lengths of time; the formation of I₂ was confirmed by its extraction into a hexane phase. It was found that longer reaction time of ≥40 h were required to give complete conversion of [Mn₁₂] to [Mn₁₂]³⁻, as established by subsequent characterization of the product; these are much longer times than routinely employed for the [Mn₁₂]⁻ and [Mn₁₂]²⁻ complexes.^{203,272} Samples of [Mn₁₂]³⁻ salts that were analytically pure (and subsequently shown by magnetism studies to be pure [Mn₁₂]³⁻) were obtained with the NMe₄⁺ and NPrⁿ₄⁺ cations, but we were not satisfied with the purity of the NBuⁿ₄⁺ and PPh₄⁺ salts or their prolonged stability in the solid state (vide infra). Thus, we used the NMe₄⁺ and NPrⁿ₄⁺ salts for the detailed studies below. In addition, for better comparisons of [Mn₁₂]^{z-} (z = 0 - 3) complexes with the same cation, we also prepared the NPrⁿ₄⁺ salts of the [Mn₁₂]⁻ and [Mn₁₂]²⁻ complexes. The transformations of **9-1** into **9-2** to **9-4** are summarized by general eq. 9-1, where z = 1, 2 or 3.



It soon became apparent that the [Mn₁₂]³⁻ anion is far less stable in solution than [Mn₁₂]⁻ and [Mn₁₂]²⁻. Numerous attempts to grow crystals of a [Mn₁₂]³⁻ salt with a variety of cations and under various crystallization conditions were all unsuccessful, giving amorphous powders and/or crystals that turned out to be the [Mn₁₂]²⁻ salt on analysis and magnetic examination. However, in reality a crystal structure would not have told us anything that we did not feel we already knew about the [Mn₁₂]³⁻ anion from previous observations of what happens to the structure of a Mn₁₂ complex on one- and two-electron reduction. The most important structural question in these other complexes had been where does(do) the added electron(s) go, and the answer was on the outer ring of Mn^{III} atoms. This is summarized in Figure 9-2, which shows the distribution of Mn oxidation states within the [Mn₁₂O₁₂] cores of these compounds. The neutral Mn₁₂ (Figure 9-2,

top) has four central Mn^{IV} atoms within a non-planar ring of eight outer Mn^{III} atoms. The latter divide by symmetry into two classes, and addition of one or two extra electrons leads to localization of these electrons onto Mn^{III} atoms of only one class leading to their conversion to Mn^{II}, giving Mn^{IV}₄Mn^{III}₇Mn^{II} and Mn^{IV}₄Mn^{III}₆Mn^{II}₂ oxidation state descriptions, respectively. This was established from the crystal structures of multiple [Mn₁₂]²⁻ complexes,^{202,203,272,291} and is shown in the two central figures of Figure 9-2. This counter-intuitive preferential reduction of a Mn^{III} rather than a Mn^{IV} was rationalized on the basis that reduction of a central Mn^{IV} would convert it into a Mn^{III} atom that would show a characteristic Jahn-Teller distortion, as expected for a high-spin d⁴ configuration (and exhibited by the outer Mn^{III} atoms). This would introduce strain into the relatively rigid central Mn₄O₄ cubane, and so reduction of an outer Mn^{III} becomes thermodynamically preferred since it causes no significant structural perturbation. We are thus certain that the third added electron in the [Mn₁₂]³⁻ complexes also has added to a formerly Mn^{III} atom of the same symmetry class, giving the Mn^{IV}₄Mn^{III}₅Mn^{II}₃ situation depicted in Figure 9-2, bottom.

On the basis of the above arguments, the decreased stability of the [Mn₁₂]³⁻ anion in solution compared with the [Mn₁₂]^{z-} (z = 0 - 2) is perhaps not surprising given the now high content of Mn^{II} in a complex that still contains four Mn^{IV} atoms. It is reasonable that such a species would be unstable to structural degradation initiated perhaps by the lability of the Mn^{II} centers and/or intramolecular redox transitions. This would also rationalize that observation in Figure 9-1 that the four-electron reduced species [Mn₁₂]⁴⁻, which would be expected to be Mn^{IV}₄Mn^{III}₄Mn^{II}₄, rapidly degrades even on the electrochemical timescale and thus does not show a well-formed peak in the DPV or even a reversible CV wave on the faster CV timescale.

9.3.2 Magnetochemistry

9.3.2.1 Dc Studies

Solid-state, variable-temperature dc magnetic susceptibility data in a 0.1 T field and in the 5.0-300 K range were collected on powdered crystalline samples of complexes **9-2** to **9-5**, restrained in eicosane to prevent torquing. The obtained data are plotted as $\chi_M T$ vs T in Figure 9-3. The $\chi_M T$ values for **9-2**, **9-3**, **9-4** and **9-5** slowly increase from 22.7, 21.8, 21.5 and 22.3 cm³ K mol⁻¹ at 300 K to a maximum of 46.2, 50.1, 38.8, and 38.1 cm³ K mol⁻¹ at 10 K, respectively, and then decrease at lower temperatures due to Zeeman effects from the applied field, any weak intermolecular interactions, etc. The $\chi_M T$ vs T profiles of **9-2** and **9-3** are essentially identical to those of previously reported [Mn₁₂]⁻ and [Mn₁₂]²⁻ complexes.^{203,272,291} Their maxima of 46.2 and 50.1 cm³ K mol⁻¹ at 10 K are in agreement with $S = 19/2$ and $S = 10$ ground states, respectively, and $g < 2$ as expected for Mn. This is in agreement with the ground states found in previous work for [Mn₁₂]⁻ and [Mn₁₂]²⁻ complexes.^{203,272,291} The calculated, spin-only ($g = 2$) values are 49.9 and 55.0 cm³ K mol⁻¹ for $S = 19/2$ and $S = 10$, respectively.

The $\chi_M T$ vs T profiles of **9-4** and **9-5** are essentially superimposable with each other throughout the whole temperature range, and with those of **9-2** and **9-3** in the 100-300 K range. Below 100 K, they diverge from those of the latter, and reach maxima significantly below those of **9-2** and **9-3**. This shows that **9-2** and **9-5** are indeed at a different oxidation level from either **9-2** or **9-3**, and also that they have a smaller ground state S value than them. Remembering that a Mn^{IV}₄Mn^{III}₅Mn^{II}₃ complex must have a half-integer ground state, then the $\chi_M T$ maxima at 10 K of 38.8 and 38.1 cm³ K mol⁻¹ suggest that **9-4** and **9-5** have an $S = 17/2$ ground state with $g < 2$; the spin-only ($g = 2$) value is 40.4 cm³ K mol⁻¹.

Confirmation of the above preliminary conclusion was sought from fits of magnetization (M) data collected on complexes **9-4** and **9-5** in the 0.1 - 4 T and 1.8 - 10 K ranges. The obtained

data are shown as reduced magnetization ($M/N\mu_B$) vs H/T plots in Figure 9-4, where N is Avogadro's number and μ_B is the Bohr magneton. The data were fit using the program *MAGNET*,⁵³ described elsewhere.⁵⁶ The best fits for **9-4** and **9-5** are shown as the solid lines in Figure 9-4, and the fit parameters were $S = 17/2$, $D = -0.25 \text{ cm}^{-1}$, $g = 1.91$ for **9-4**, and $S = 17/2$, $D = -0.23 \text{ cm}^{-1}$, $g = 1.90$ for **9-5**. Fits of the data with $S = 15/2$ or $19/2$ gave unreasonable g values of 2.21 and 1.72, respectively, and were therefore discounted. For a comparison of data for complexes with different degrees of reduction but with the same cation, we also collected variable-temperature and -field magnetization data for complexes **9-2** and **9-3**; the corresponding ($M/N\mu_B$) vs H/T plots and fits are provided in Figure 9-5. The fit parameters were $S = 19/2$, $D = -0.35 \text{ cm}^{-1}$, $g = 1.95$ for **9-2**, and $S = 10$, $D = -0.28 \text{ cm}^{-1}$, $g = 1.98$ for **9-3**. The obtained ground state S values of **9-2** and **9-3** are the same as those previously found for several other $[\text{Mn}_{12}]^z$ and $[\text{Mn}_{12}]^{2-}$ complexes.^{203,272,291}

To confirm that the obtained fit minima were the true global minima and to assess the hardness of the fit, a root-mean square D vs g error surface for the fit was generated for representative complex **9-4** using the program *GRID*,⁷¹ which calculates the relative difference between the experimental ($M/N\mu_B$) data and those calculated for various combinations of D and g . This is shown as a 2-D contour plot in Figure 9-6 covering the $D = -0.10$ to -0.50 cm^{-1} and $g = 1.86$ to 1.98 ranges. Only one minimum was observed, and this was a relatively soft minimum; we thus estimate the fitting uncertainties as $D = -0.25 \pm 0.01 \text{ cm}^{-1}$ and $g = 1.91 \pm 0.01$.

9.3.2.2 Comparison of the Magnetic Properties of the $[\text{Mn}_{12}]^z$ ($z = 0 - 3$) Family

The combined results for complexes **9-2** to **9-5**, as well as those for neutral complex **9-1**,²⁰³ are collected in Table 9-1. Considering first the S values, it is well known that the spin ground state changes very little on one- and two-electron reduction, from $S = 10$ to $S = 19/2$ and then back to $S = 10$ along the series **9-1** ($z = 0$), **9-2** ($z = 1$) and **9-3** ($z = 2$), respectively. Thus,

the Mn_{12} core acts almost as a ‘spin buffer’, picking up electrons with little change to the ground state S value. However, on three-electron reduction to complexes **9-4** and **9-5**, there is a more significant change to $S = 17/2$. This is no doubt due to the increased Mn^{II} content and the general weakening of many of the exchange interactions in the core. However, the $[\text{Mn}_{12}\text{O}_{12}]$ core is a complicated one with many symmetry inequivalent exchange interactions, many of them competing and it is thus not easy to provide a rationalization of the $S = 17/2$ ground state, as indeed it has not been possible in the past to rationalize those of the $[\text{Mn}_{12}]^{\cdot-}$ and $[\text{Mn}_{12}]^{2-}$ complexes either.

The g values given in Table 9-1 are provided only for completeness and should not be taken as particularly accurate. It is well known that fits of bulk magnetization data are not a good way to obtain accurate g values. While we prefer to quote the actual values obtained by having the g value as a free parameter, rather than fixing it at a more realistic value at or near 2.0, we do not attempt to draw any conclusions from resulting differences in g . It would require studies with a more sensitive technique such as EPR spectroscopy to provide more accurate g values.

In contrast to the S value, the axial zero-field splitting parameter D does exhibit a monotonic change with the extent of reduction; there is a clear decrease in $|D|$ with progressive one-electron reduction. This is exactly as expected because the molecular anisotropy, as gauged by the magnitude of $|D|$, is the projection of the single-ion Mn anisotropies onto the molecular anisotropy axis. Mn^{IV} and Mn^{II} are relatively isotropic ions, and the primary contributions to the molecular D are thus the Mn^{III} ions, which are significantly Jahn-Teller distorted. Since reduction involves addition of electrons onto formerly Mn^{III} centers converting them to Mn^{II} , the greater the extent of reduction, the fewer will be the remaining Mn^{III} ions, and the smaller will thus be the molecular anisotropy $|D|$. This assumes other factors remain the same, such as the

overall structure of the Mn_{12} complex, and the relative orientation of the Mn^{III} JT axes essentially parallel to the molecular z axis. It should be added that D values in Table 9-1 have been obtained by fitting the magnetization data with the rhombic (transverse) zero-field splitting parameter (E) fixed at $E = 0$. In fact, these complexes do not have axial symmetry, and E is unlikely to be exactly zero. In our experience, however, magnetization fits are usually not very sensitive to E , and the D values in Table 9-1 are therefore expected to be reasonable, especially for assessment of relative magnitudes within a series, as here. Nevertheless, for information purposes, we provide in Figure 9-6, the fit of the magnetization data of **9-4** as a function of D and E , with g held constant at 2.0; the fit is shown as a contour plot of the error surface. The best-fit parameters are $D = -0.24 \text{ cm}^{-1}$ and $|E| = 0.065 \text{ cm}^{-1}$. The D value changes very slightly (from 0.25 cm^{-1} obtained with $E = 0$), while the non-zero E is consistent with the low symmetry of a three-electron reduced $[\text{Mn}_{12}]^{3-}$ complex.

The final entries in Table 9-1 for each compound are the values of the U , the anisotropy barrier to magnetization relaxation, whose upper limit is given by $S^2|D|$. In practice, the true or effective barrier (U_{eff}) is smaller than this upper limit because the magnetization vector need not go over the top of the barrier but can tunnel through its upper regions via higher-lying M_S levels. This quantum tunneling of magnetization (QTM) is a characteristic of all SMMs. Since $|D|$ monotonically decreases with reduction, whereas the S stays roughly the same or decreases, then it would be expected that U would decrease with reduction, and this is what is indeed seen. The U for $[\text{Mn}_{12}]^{3-}$ complexes **9-4** and **9-5**, coming from their $S = 17/2$ spin and a $|D|$ value that has been decreased but is still reasonable, is still relatively large, and even decreased by QTM might still be sufficient for them to function as SMMs. In order to explore whether these $[\text{Mn}_{12}]^{3-}$

complexes might indeed exhibit slow relaxation; we investigated their magnetization dynamics using ac susceptibility.

9.3.2.3 Ac Studies

In ac studies, a weak field (1 - 5 G) oscillating at a particular frequency, typically up to 1500 Hz, is applied to a sample to probe the dynamics of the magnetization relaxation. If the magnetization vector can relax fast enough to keep up with the oscillating field, then there is no imaginary (out-of-phase) susceptibility signal (χ_M''), and the real (in-phase) susceptibility (χ_M') is equal to the dc susceptibility. However, if the barrier to magnetization relaxation is significant compared to thermal energy (kT), then there is a non-zero χ_M'' signal and the in-phase signal decreases. In addition, the χ_M'' signal will be frequency-dependent. The ac susceptibilities of $[\text{Mn}_{12}]^{z-}$ ($z = 0 - 2$) complexes **9-1** to **9-3** have been previously reported, but they were re-measured here for better comparison with those of **9-4** and **9-5** under identical conditions.

The ac susceptibilities for complexes **9-1** to **9-5** were collected on microcrystalline samples in a 3.5 G ac field, and the obtained data for complexes **9-4** and **9-5** at representative frequencies of 50, 250 and 1000 Hz are shown in Figures 9-7 and 9-8, respectively, as $\chi_M'T$ vs T and χ_M'' vs T plots. The in-phase ($\chi_M'T$) ac signal is invaluable as an additional and independent means to determine the ground state spin of a molecule, without any complications from a dc field.^{62,69,224} Inspection of Figures 9-7 and 9-8 shows that the $\chi_M'T$ values are essentially temperature independent down to ~ 5 K, below which they show decreases due to slow relaxation (vide infra). The temperature independent $\chi_M'T$ shows that only the spin ground state of the molecule is populated at these temperatures, and can be used to calculate its S value. The $\chi_M'T$ values of $40.5 \text{ cm}^3 \text{ K mol}^{-1}$ and $39.5 \text{ cm}^3 \text{ K mol}^{-1}$ for **9-4** and **9-5**, respectively, correspond to $S = 17/2$, $g = 2.00$, and $S = 17/2$, $g = 1.98$, in very satisfying agreement with the conclusions from the fits of the dc magnetization data discussed above. Note that for $S = 15/2$ or $19/2$ states, a $\chi_M'T$ value of ~ 40

$\text{cm}^3 \text{ K mol}^{-1}$ would require g values of 2.24 and 1.79, which are unreasonable for Mn. We conclude that $[\text{Mn}_{12}]^{3-}$ complexes **9-4** and **9-5** are confirmed to possess $S = 17/2$ ground states.

Below $\sim 5\text{K}$, the in-phase $\chi_M' T$ signals for **9-4** and **9-5** in Figures 9-7 and 9-8 exhibit a frequency-dependent decrease concomitant with the appearance of frequency-dependent out-of-phase (χ_M'') signals. This is indicative of the onset of slow magnetization relaxation relative to the ac field, i.e. the magnetization vector can no longer relax fast enough to stay in-phase with the oscillating field. This is the characteristic superparamagnet-like behavior of a SMM, and parallels that previously observed for the other oxidation levels of the $[\text{Mn}_{12}]^{z-}$ ($z = 0 - 2$) family. On the basis of the comparative data presented in Table 9-1, the appearance of the χ_M'' signals at very low temperatures of $\sim 2.5 \text{ K}$ and below are as expected for a barrier to magnetization relaxation in $[\text{Mn}_{12}]^{3-}$ complexes **9-4** and **9-5** being smaller than those in $[\text{Mn}_{12}]^{z-}$ ($z = 0 - 2$) complexes. This is emphasized by the comparative ac data presented in Figure 9-9, which shows the χ_M'' signals for complexes **9-1** to **9-4** at equivalent frequencies of 50, 250 and 1000 Hz. In each case, the χ_M'' signals are frequency-dependent and exhibit a monotonic shift to lower temperatures with increasing reduction: 6 - 8 K for **9-1** $[\text{Mn}_{12}]$; 4 - 6 K for **9-2** $[\text{Mn}_{12}]$; 2 - 4 K for **9-3** $[\text{Mn}_{12}]^{2-}$; and $\leq 2.5 \text{ K}$ for **9-4** $[\text{Mn}_{12}]^{3-}$. For better comparisons at identical ac frequencies, the χ_M'' signals for **9-1** to **9-4** at 50 and 1000 Hz are plotted together in Figure 9-10, bottom and top, respectively. A clear shift to lower temperature is seen with each reduction step. The combined data in Figures 9-9 and 9-10 are thus perfectly consistent with the conclusions from the data in Table 9-1 and the discussion above, since the barrier to magnetization relaxation scales with $S^2|D|$, and either one or both of these quantities decrease with each one-electron increase in the extent of reduction.

Note that it is not expected that there should be a linear decrease in barrier with reduction, since there are so many factors that determine the actual magnitude of the true or effective barrier, U_{eff} , including S , D , the rhombic ZFS parameter (E), fourth order spin Hamiltonian parameters, precise QTM rate and tunneling channel (i.e., which M_s levels are involved), spin-phonon coupling strengths, and others. Thus, there are too many parameters that contribute to the observed U_{eff} to permit a more quantitative comparison between different oxidation levels. Since we have not been able to obtain single-crystals, micro-SQUID hysteresis measurements could not be performed. Note also that the χ_M'' signals for complex **9-1** in Figures 9-9 and 9-10 also exhibit a weaker signal at lower temperatures, which is due to a faster-relaxing form arising from a different Jahn-Teller isomer, i.e. a form in which one of the Mn^{III} Jahn-Teller isomers is abnormally oriented towards a bridging oxide ion in the molecule.^{205,294,295} These isomeric forms are known to possess smaller barriers to magnetization relaxation and thus to exhibit their χ_M'' signals at lower temperatures.

9.4 Conclusions

The Mn_{12} family of SMMs has been successfully extended to four isolated oxidation states by the three-electron reduction of $[\text{Mn}_{12}\text{O}_{12}(\text{O}_2\text{CCHCl}_2)_{16}(\text{H}_2\text{O})_4]$ to $(\text{NR}_4)_3[\text{Mn}_{12}\text{O}_{12}(\text{O}_2\text{CCHCl}_2)_{16}(\text{H}_2\text{O})_4]$ ($\text{R} = \text{Me}, \text{Pr}^n$) with NR_4I . The $[\text{Mn}_{12}]^{3-}$ complexes are unstable in solution, which has prevented us from obtaining crystals suitable for X-ray crystallography, but this is not unduly disappointing, because it is clear on the basis of the structural characterization of the three other Mn_{12} oxidation states that the third electron will have added to an outer, formerly Mn^{III} ion giving a $\text{Mn}^{\text{IV}}_4\text{Mn}^{\text{III}}_5\text{Mn}^{\text{II}}_3$ trapped-valence situation. We do not believe it will be possible to extend the Mn_{12} family of SMMs to five members by four-electron reduction, given the instability demonstrated by the putative $[\text{Mn}_{12}]^{4-}$ species in the electrochemical studies.

The $[\text{Mn}_{12}]^{3-}$ complexes **9-4** and **9-5** both possess a half-integer $S = 17/2$ ground state, and a $|D|$ value smaller than that for the $[\text{Mn}_{12}]^{3-}$ complex **9-4**, which supports the above assertion that the third added electron is localized on a formerly Mn^{III} ion, since the Jahn-Teller distorted Mn^{III} ions are the primary source of the molecular anisotropy. As a result of the decreased S and D relative to the other Mn_{12} oxidation states, the barrier to magnetization relaxation U is also smaller than for the other oxidation states, but is still sufficient to yield out-of-phase (χ_M'') ac susceptibility signals indicative of slow magnetization relaxation. Thus, we conclude that the $[\text{Mn}_{12}]^{3-}$ complexes **9-4** and **9-5** are SMMs. Note that the observation of χ_M'' signals is indicative of a SMM but not normally sufficient proof of one. In this case, however, the well-established fact that the χ_M'' ac signals for the other Mn_{12} oxidation states are correctly identifying SMMs, as proven by single-crystal hysteresis studies, leaves little doubt that these same signals for the $[\text{Mn}_{12}]^{3-}$ complexes **9-4** and **9-5** are also due to SMMs. Thus, although we do not have single crystals with which to carry out micro-SQUID studies down to 0.04 K in order to observe magnetization hysteresis loops for **9-4** and **9-5**, there seems little doubt that the available data are indicating that the Mn_{12} family of SMMs now spans four oxidation levels.

Table 9-1. Magnetism Data for $[\text{Mn}_{12}]^{z-}$ ($z = 0 - 3$) Complexes **9-1** to **9-5**.

	$z = 0$ (9-1)	$z = 1-$ (9-2)	$z = 2-$ (9-3)	$z = 3-$ (9-4)	$z = 3-$ (9-5)
S	10	19/2	10	17/2	17/2
g	1.86	1.95	1.98	1.91	1.90
D/cm^{-1}	-0.45	-0.35	-0.28	-0.25	-0.23
D/K	-0.65	-0.50	-0.40	-0.35	-0.33
U/K^a	65	45	40	25	24

^a Calculated as $S^2|D|$ for **9-1** and **9-3**, and as $(S^2-1/4)|D|$ for **9-2**, **9-4** and **9-5**.

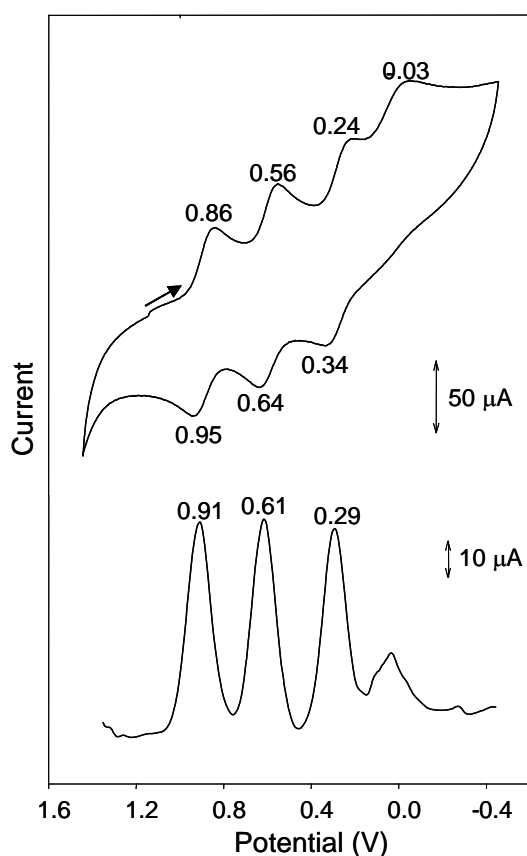


Figure 9-1. Cyclic voltammogram at 100 mV/s (top) and differential pulse voltammogram at 20 mV/s (bottom) for complex **9-1** in MeCN containing 0.1 M $\text{NBu}^n_4\text{PF}_6$ as supporting electrolyte. The indicated potentials are vs ferrocene.

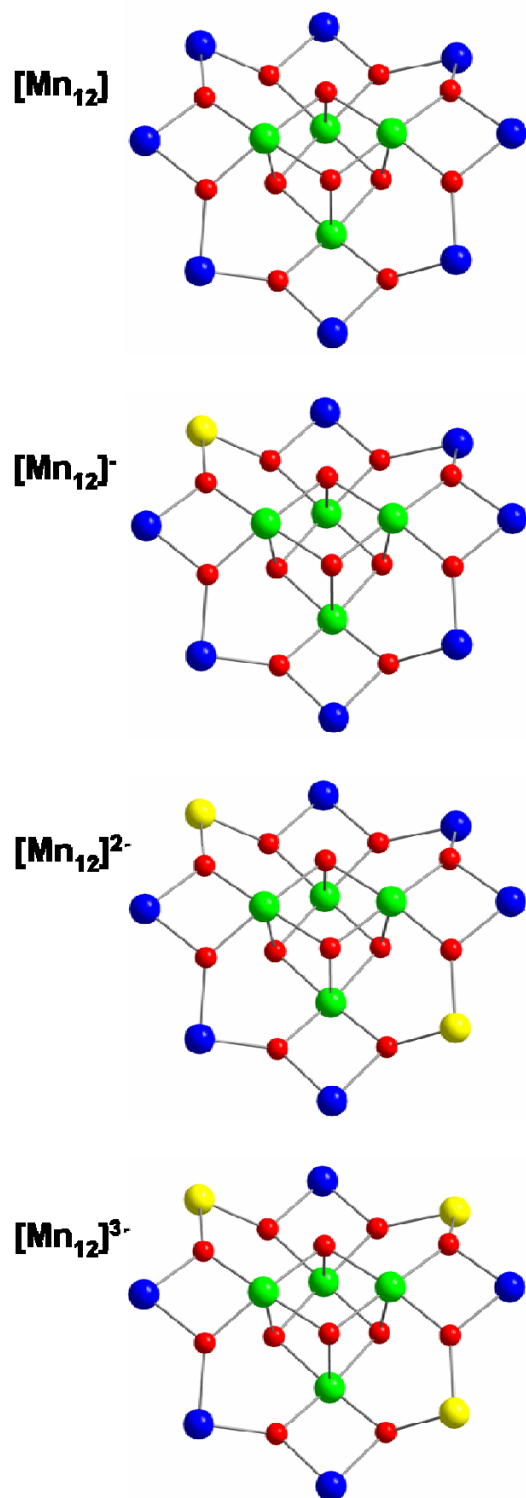


Figure 9-2. Proposed structural core of **9-1**, **9-2**, **9-3** and **9-4**. Color code: Mn^{IV}, green; Mn^{III}, blue; Mn^{II}, yellow, O, red.

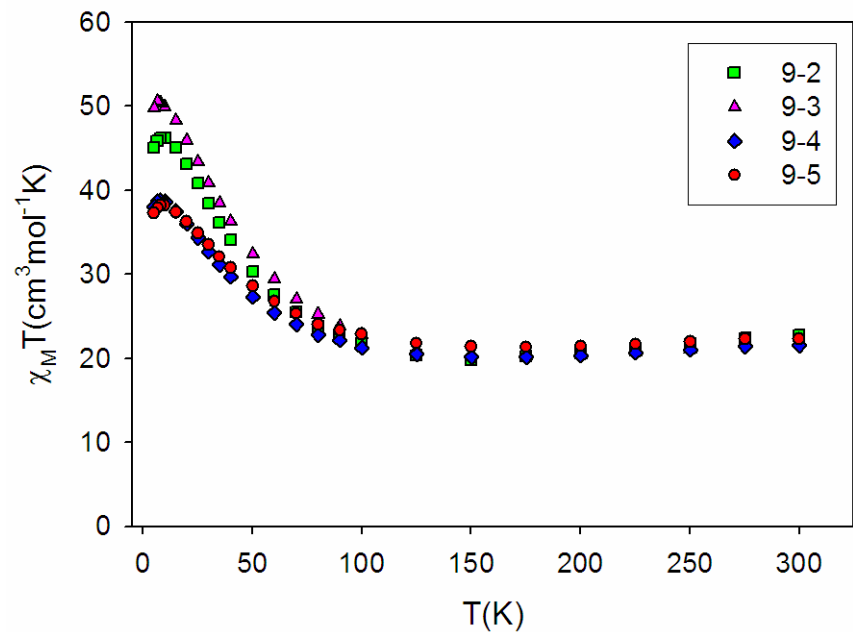


Figure 9-3. Plot of $\chi_M T$ vs T for **9-2** to **9-5**.

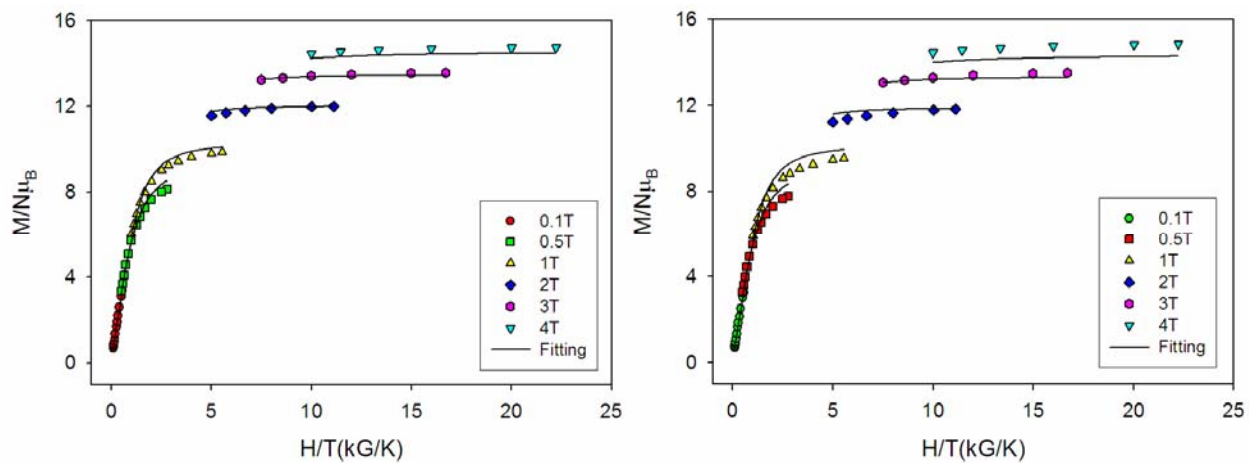


Figure 9-4. Plot of reduced magnetization ($M/N\mu_B$) vs H/T for **9-4** (left) and **9-5** (right). The solid lines are the fit of the data; see the text for the fit parameters.

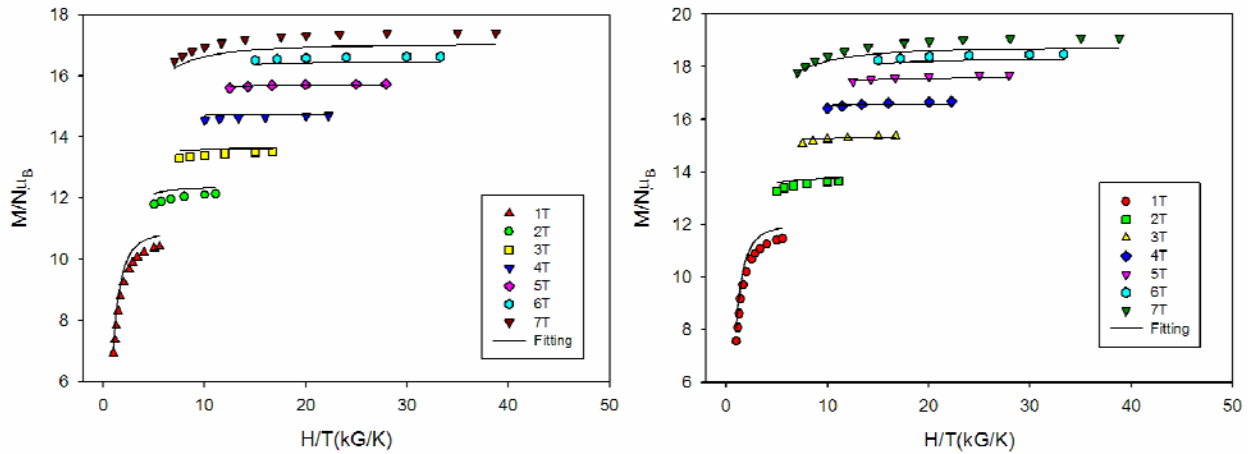


Figure 9-5. Plot of reduced magnetization ($M/N\mu_B$) vs H/T for **9-2** (left) and **9-3** (right).

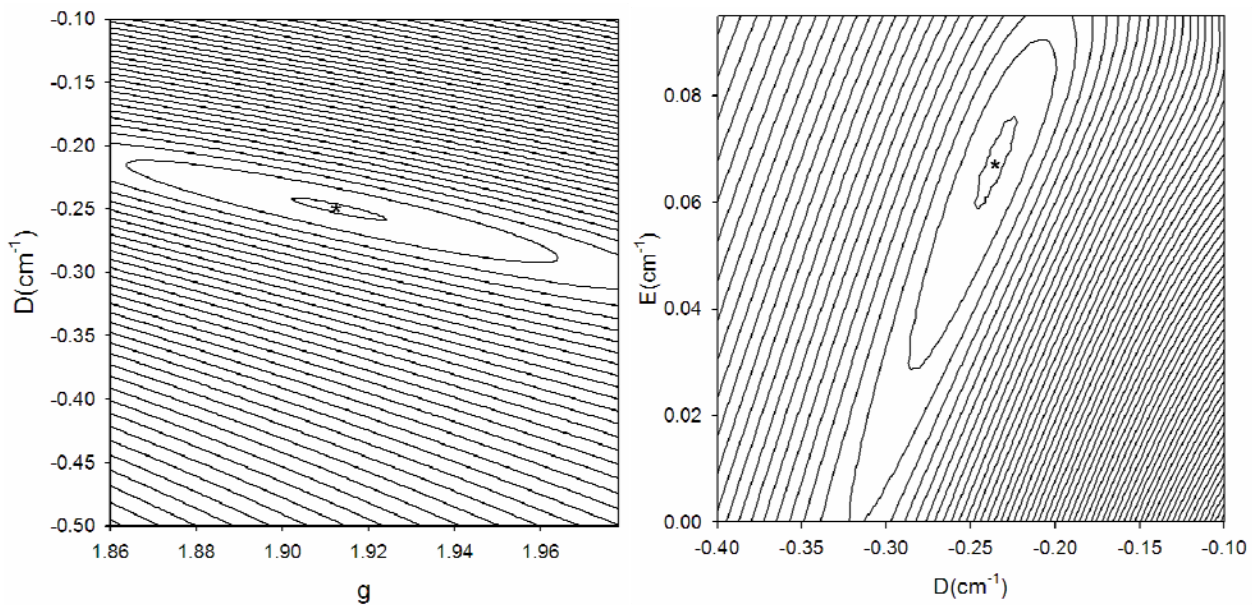


Figure 9-6. (left) Two-dimensional contour plot of the error surface for the D vs g fit for complex **9-4**. (right) Two-dimensional contour plot of the root-mean-square error surface for the D vs E fit for complex **9-4**.

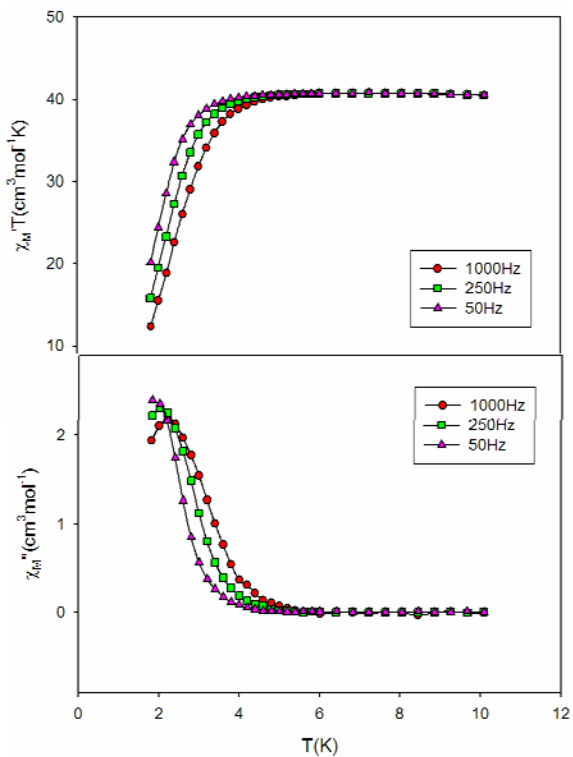


Figure 9-7. Plot of the in-phase ($\chi_M' T$) and out-of-phase (χ_M'') ac susceptibility data for **9-4**.

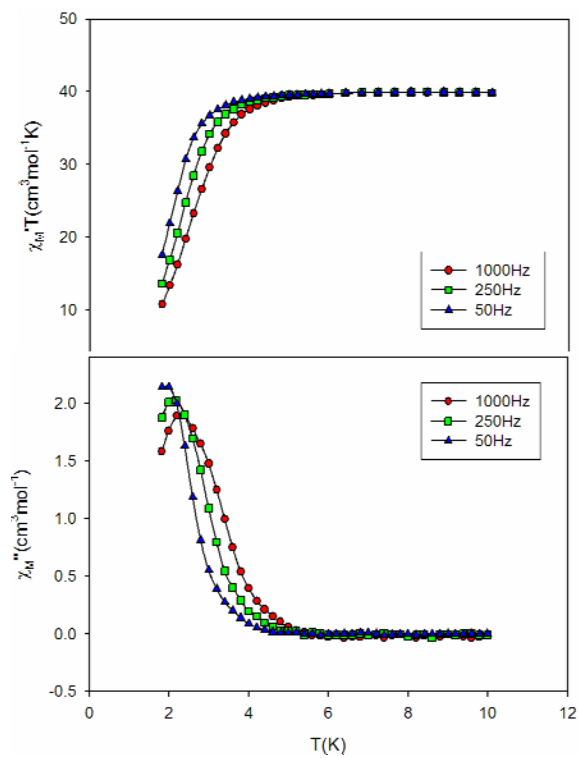


Figure 9-8. Plot of the in-phase ($\chi_M' T$) and out-of-phase (χ_M'') ac susceptibility data for **9-5**.

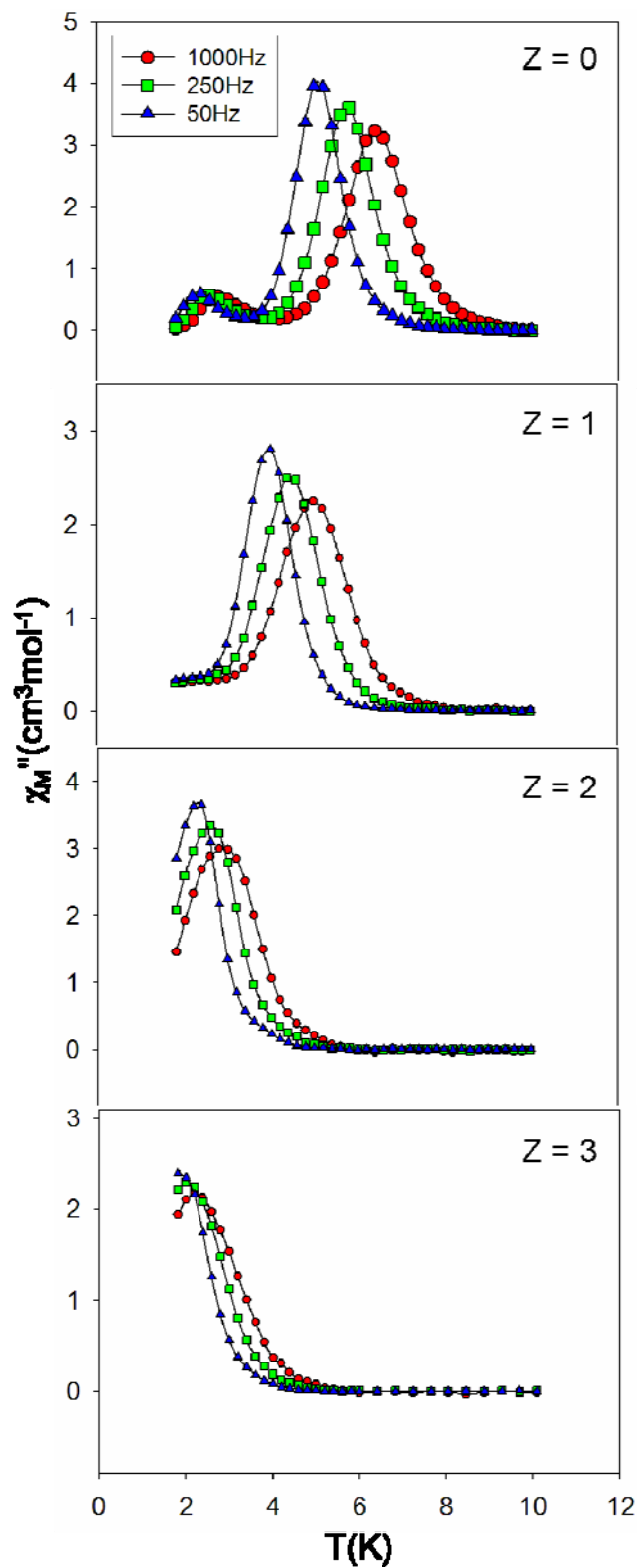


Figure 9-9. χ_M'' vs T plots for vacuum-dried complexes $[\text{Mn}_{12}]^{Z-}$ ($Z = 0, 1, 2, 3$) at the indicated frequencies.

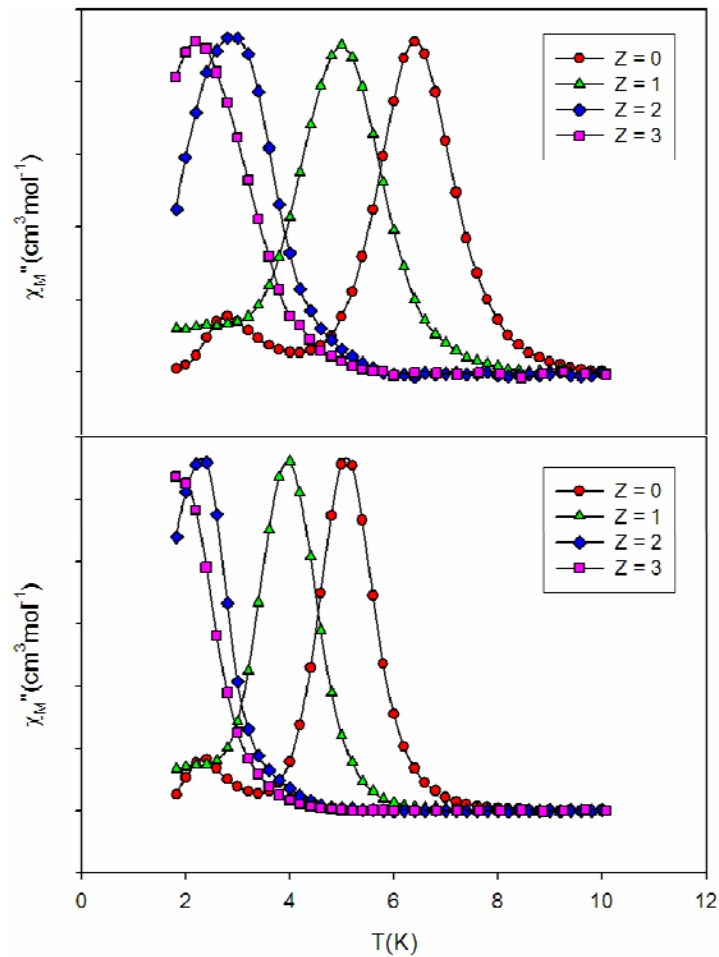


Figure 9-10. Comparison of the χ_M'' vs T plots for vacuum-dried complexes $[\text{Mn}_{12}]^{z-}$ ($z = 0, 1, 2, 3$) at 1000 Hz (top) and 50 Hz (bottom).

APPENDIX A
BOND DISTANCES AND ANGLES

Table A-1. Selected interatomic distances (Å) and angles (°) for [Mn₄O₂(O₂CMe)₅(salpro)]
·MeCN (**2-1**·MeCN)

Mn1-O3	1.8859(19)	Mn2-Mn3	3.1763(6)
Mn1-O2	1.8906(18)	Mn3-O2	1.8884(19)
Mn1-O4	1.946(2)	Mn3-O3	1.9062(18)
Mn1-O6	1.956(2)	Mn3-O12	1.9452(19)
Mn1-O5	2.0768(19)	Mn3-O10	1.950(2)
Mn1-Mn3	2.7704(6)	Mn3-O11	2.085(2)
Mn1-Mn2	3.1713(6)	Mn3-Mn4	3.1803(6)
Mn2-O8	1.864(2)	Mn4-O14	1.8768(19)
Mn2-O2	1.9090(18)	Mn4-O3	1.9145(18)
Mn2-N1	1.972(2)	Mn4-N2	1.972(2)
Mn2-O1	1.9905(18)	Mn4-O1	1.9776(18)
Mn2-O7	2.206(2)	Mn4-O15	2.222(2)
Mn2-O9	2.238(2)	Mn4-O13	2.271(2)
O3-Mn1-O2	81.26(8)	O3-Mn4-O1	94.64(8)
O3-Mn1-O4	168.79(9)	N2-Mn4-O1	82.55(9)
O2-Mn1-O4	93.60(8)	O3-Mn4-O15	86.21(8)
O2-Mn3-O3	80.79(8)	N2-Mn4-O15	98.94(9)
O2-Mn3-O12	170.65(8)	O1-Mn4-O15	88.57(8)
O3-Mn3-O12	91.79(8)	Mn4-O1-Mn2	133.88(9)
O2-Mn3-O10	94.91(8)	Mn3-O2-Mn1	94.30(8)
O3-Mn3-O10	165.26(8)	Mn3-O2-Mn2	113.53(9)
O12-Mn3-O10	90.87(8)	Mn1-O2-Mn2	113.16(9)
O14-Mn4-O3	92.81(8)	Mn1-O3-Mn3	93.87(8)
O14-Mn4-N2	90.08(9)	Mn1-O3-Mn4	114.47(9)
O3-Mn4-N2	174.03 (9)	Mn3-O3-Mn4	112.69(9)

Table A-2. Selected interatomic distances (Å) and angles (°) for [Mn₄O₂(O₂CBu')₅(salpro)]·MeOH·2CH₂Cl₂·C₇H₁₆ (**2-3**·MeOH·2CH₂Cl₂·C₇H₁₆)

Mn1-O2	1.887(2)	Mn2-Mn4	3.1932(7)
Mn1-O5	1.910(2)	Mn3-O11	1.877(2)
Mn1-O1	1.955(2)	Mn3-O2	1.9096(19)
Mn1-O3	1.956(2)	Mn3-N1	1.966(3)
Mn1-O4	2.110(2)	Mn3-O9	1.970(2)
Mn1-Mn4	2.7942(6)	Mn3-O12	2.181(2)
Mn1-Mn3	3.1688(6)	Mn3-O10	2.224(2)
Mn2-O8	1.884(2)	Mn3-Mn4	3.1361(7)
Mn2-O5	1.907(2)	Mn4-O5	1.888(2)
Mn2-N2	1.978(3)	Mn4-O2	1.904(2)
Mn2-O9	1.984(2)	Mn4-O13	1.946(2)
Mn2-O7	2.183(2)	Mn4-O14	1.949(2)
Mn2-O6	2.196(2)	Mn4-O15	2.081(2)
Mn1-O2-Mn4	94.97(9)	Mn4-O5-Mn1	94.74(9)
Mn1-O2-Mn3	113.17(10)	Mn2-O5-Mn1	111.16(10)
Mn4-O2-Mn3	110.64(9)	Mn3-O9-Mn2	134.10(10)
Mn4-O5-Mn2	114.58(10)		

Table A-3. Selected interatomic distances (Å) and angles (°) for
 NBu₄[Mn(O₂CPh)₂(salproH)]·CH₂Cl₂ (**2-4**·CH₂Cl₂)

Mn1-O5	1.8927(18)	Mn2-O13	1.8955(19)
Mn1-O6	1.9031(19)	Mn2-O12	1.9062(19)
Mn1-N1	2.019(2)	Mn2-N3	2.025(2)
Mn1-N2	2.043(2)	Mn2-N4	2.040(2)
Mn1-O2	2.1392(19)	Mn2-O9	2.118(2)
Mn1-O4	2.2005(19)	Mn2-O11	2.1862(19)
O5-Mn1-O6	91.53(8)	O13-Mn2-O12	91.10(8)
O5-Mn1-N1	88.77(9)	O13-Mn2-N3	88.66(9)
O6-Mn1-N1	176.05(9)	O12-Mn2-N3	177.79(9)
O5-Mn1-N2	174.10(9)	O13-Mn2-N4	175.42(9)
O6-Mn1-N2	88.20(9)	O12-Mn2-N4	88.51(9)
N1-Mn1-N2	91.10(9)	N3-Mn2-N4	91.56(9)
O5-Mn1-O2	98.88(8)	O13-Mn2-O9	98.21(8)
O6-Mn1-O2	92.15(8)	O12-Mn2-O9	90.70(8)
N1-Mn1-O2	91.69(9)	N3-Mn2-O9	91.51(9)
N2-Mn1-O2	87.02(8)	N4-Mn2-O9	86.36(9)
O5-Mn1-O4	87.08(7)	O13-Mn2-O11	88.57(8)
O6-Mn1-O4	88.89(8)	O12-Mn2-O11	90.04(8)
N1-Mn1-O4	87.19(8)	N3-Mn2-O11	87.76(8)
N2-Mn1-O4	87.02(8)	N4-Mn2-O11	86.87(8)
O2-Mn1-O4	173.91(7)	O9-Mn2-O11	173.16(8)

Table A-4. Selected interatomic distances (Å) and angles (°) for
 $[\text{Mn}_4(\text{hmp})_2(\text{pdmH})_2(\text{MeCN})_4](\text{ClO}_4)_4$ (**3-1**)

Mn1-O2	1.876(3)	Mn2-O1	2.157(2)
Mn1-O1	1.898(3)	Mn2-O2'	2.215(2)
Mn1-O4'	1.968(2)	Mn2-N3	2.267(3)
Mn1-N2	2.064(3)	Mn2-N4	2.272(3)
Mn1-N1	2.205(3)	Mn2-O3	2.303(3)
Mn1-O4	2.254(2)	Mn2-N5	2.310(4)
Mn1...Mn1'	3.2092(10)	Mn2-O4	2.363(2)
Mn1-O1-Mn2	112.43(11)	Mn1'-O4-Mn2	100.45(10)
Mn1-O2-Mn2'	109.12(11)	Mn1-O4-Mn2	93.85(9)
Mn1'-O4-Mn1	98.73(10)		

Table A-5. Selected interatomic distances (Å) and angles (°) for
 $[\text{Mn}_{25}\text{O}_{18}(\text{OH})_2(\text{hmp})_6(\text{pdm})_8(\text{pdmH})_2(\text{L})_2](\text{ClO}_4)_6 \cdot 8\text{MeCN} \cdot 4\text{MeOH}$ (**3-2**·8MeCN·4MeOH)

Mn(1)-O(26)'	2.130(5)	Mn(6)-O(22)	2.133(4)
Mn(1)-O(18)	2.180(5)	Mn(6)-O(7)	2.259(5)
Mn(1)-O(1)	2.215(7)	Mn(6)-O(8)	2.297(5)
Mn(2)-O(4)	1.874(5)	Mn(7)-O(25)	1.884(4)
Mn(2)-O(19)	1.904(5)	Mn(7)-O(22)	1.889(4)
Mn(2)-O(18)	1.918(4)	Mn(7)-O(14)	1.939(5)
Mn(3)-O(18)	1.887(5)	Mn(8)-O(20)	1.874(4)
Mn(3)-O(21)	1.901(5)	Mn(8)-O(19)	1.885(4)
Mn(3)-O(3)	1.928(5)	Mn(8)-O(22)	2.105(5)
Mn(4)-O(20)'	1.887(4)	Mn(9)-O(27)	1.879(5)
Mn(4)-O(23)	1.889(4)	Mn(9)-O(27)'	1.879(5)
Mn(4)-O(27)	2.109(4)	Mn(9)-O(22)'	1.892(4)
Mn(4)-O(21)	2.112(5)	Mn(10)-O(11)	1.883(5)
Mn(4)-N(3)	2.140(6)	Mn(10)-O(20)	1.908(5)
Mn(4)-O(6)	2.241(5)	Mn(10)-O(25)	1.909(5)
Mn(4)-O(5)	2.331(5)	Mn(11)-O(26)	2.116(5)
Mn(5)-O(24)	1.866(5)	Mn(11)-O(25)	2.205(4)
Mn(5)-O(27)	1.890(5)	Mn(11)-O(11)	2.223(6)
Mn(5)-O(16)	1.936(5)	Mn(11)-O(14)	2.493(5)
Mn(6)-O(19)	1.875(5)	Mn(12)-O(26)	2.112(5)
Mn(6)-O(23)	1.877(5)	Mn(13)-O(17)	1.887(5)
Mn(6)-O(21)	2.109(4)	Mn(13)-O(23)	1.903(5)
Mn(12)-O(17)	2.182(5)	Mn(13)-O(24)	1.919(4)
Mn(12)-O(24)	2.207(5)	Mn(13)-N(9)	2.027(6)
Mn(12)-N(8)	2.258(8)	Mn(13)-O(6)	2.258(5)
Mn(3)-O(3)-Mn(11)'	99.8(2)	Mn(13)-O(17)-Mn(12)	103.7(2)
Mn(2)-O(4)-Mn(1)	102.2(2)	Mn(3)-O(18)-Mn(2)	108.5(2)
Mn(3)-O(5)-Mn(10)'	96.68(17)	Mn(6)-O(19)-Mn(8)	110.7(2)
Mn(4)-O(6)-Mn(13)	88.63(19)	Mn(4)'-O(20)-Mn(10)	115.8(2)
Mn(2)-O(7)-Mn(3)	86.92(16)	Mn(9)-O(21)-Mn(3)	136.2(2)
Mn(7)-O(8)-Mn(13)	95.5(2)	Mn(8)-O(22)-Mn(6)	93.69(19)
Mn(5)'-O(9)-Mn(8)	97.1(2)	Mn(6)-O(23)-Mn(4)	109.6(2)
Mn(8)-O(10)-Mn(10)	88.12(16)	Mn(7)-O(24)-Mn(12)	100.21(18)

Table A-6. Selected interatomic distances (Å) and angles (°) for
 $[\text{Fe}_7\text{O}_4(\text{O}_2\text{CPh})_{11}(\text{dmem})_2]\cdot 4\text{MeCN}$ (**4-1**·4MeCN)

Fe1-O10'	1.8276(18)	Fe2-Fe4	2.9287(5)
Fe1-O2	1.9966(18)	Fe3-O9	1.8436(18)
Fe1-O4'	2.0424(18)	Fe3-O8	2.0092(19)
Fe1-O1	2.0519(19)	Fe3-O6	2.027(2)
Fe1-N2	2.248(2)	Fe3-O13	2.038(2)
Fe1-N1	2.269(3)	Fe3-O11	2.0547(19)
Fe2-O9	1.9234(17)	Fe3-O12	2.200(2)
Fe2-O10	1.941(2)	Fe3-C34	2.470(3)
Fe2-O5	2.051(2)	Fe4-O9	1.989(2)
Fe2-O2	2.0534(17)	Fe4-O10	1.9915(17)
Fe2-O3	2.0537(18)	Fe4-O14'	2.0680(17)
Fe2-O7	2.1053(18)	Fe4-O14	2.0681(18)
O10'-Fe1-O2	98.25(8)	O9-Fe3-O6	95.81(9)
O10'-Fe1-O4'	95.05(8)	O9-Fe4-O9'	176.62(10)
O2-Fe1-O4'	166.09(8)	O9-Fe4-O10	80.88(7)
O10'-Fe1-O1	103.89(8)	O9'-Fe4-O10	101.66(7)
O2-Fe1-O1	90.28(8)	O9-Fe4-O10'	101.66(7)
O9-Fe2-O10	83.84(8)	O9'-Fe4-O10'	80.87(7)
O9-Fe2-O5	94.27(8)	O10-Fe4-O10'	84.82(10)
O10-Fe2-O5	176.11(8)	O9-Fe4-O14'	87.48(7)
O9-Fe2-O2	94.30(7)	O9-Fe4-O14	90.19(8)
O10-Fe2-O2	97.13(7)	O10-Fe4-O14	92.39(7)
O9-Fe2-O3	174.58(8)	O10'-Fe4-O14	167.19(8)
O10-Fe2-O3	94.32(8)	Fe1-O2-Fe2	125.76(10)
O2-Fe2-O3	90.99(7)	Fe3-O9-Fe2	120.44(9)
O9-Fe2-O7	94.97(7)	Fe3-O9-Fe4	125.57(10)
O10-Fe2-O7	91.06(8)	Fe2-O9-Fe4	96.92(8)
O2-Fe2-O7	168.24(8)	Fe1'-O10-Fe2	124.59(9)
O3-Fe2-O7	79.95(7)	Fe1'-O10-Fe4	134.38(10)
O9-Fe3-O8	102.13(8)	Fe2-O10-Fe4	96.25(8)

Table A-7. Selected interatomic distances (Å) and angles (°) for
 $[\text{Fe}_7\text{O}_4(\text{O}_2\text{CMe})_{11}(\text{dmem})_2]\cdot\text{MeCN}$ (**4-2**·MeCN)

Fe1-O1	1.8783(17)	Fe4-O16	1.9894(18)
Fe1-O6	1.9992(19)	Fe4-O17	2.0107(18)
Fe1-O8	2.0106(18)	Fe4-O15	2.057(2)
Fe1-O5	2.0147(17)	Fe4-N3	2.246(2)
Fe1-N2	2.191(2)	Fe5-O2	1.9402(17)
Fe1-N1	2.282(2)	Fe5-O3	1.9568(17)
Fe1-Fe2	2.9585(5)	Fe5-O4	2.0141(17)
Fe2-O3	1.8672(17)	Fe5-O19	2.0554(19)
Fe2-O1	1.9833(18)	Fe5-O21	2.0590(19)
Fe2-O12	2.0291(18)	Fe5-O18	2.0922(18)
Fe2-O11	2.0413(19)	Fe5-Fe6	2.9066(5)
Fe2-O5	2.0541(18)	Fe6-O4	1.9053(18)
Fe2-O7	2.1647(18)	Fe6-O3	1.9579(17)
Fe3-O1	1.8621(17)	Fe6-O13	2.0416(18)
Fe3-O2	1.9900(17)	Fe6-O23	2.0525(19)
Fe3-O16	2.0380(18)	Fe6-O22	2.055(2)
Fe3-O10	2.0658(19)	Fe6-O25	2.0619(19)
Fe3-O14	2.094(2)	Fe7-O4	1.8175(18)
Fe3-O9	2.0976(18)	Fe7-O24	2.011(2)
Fe3-Fe4	2.9540(5)	Fe7-O20	2.057(2)
Fe4-O2	1.8787(17)	Fe7-O27	2.0623(19)
Fe3-O1-Fe1	133.53(10)	Fe2-O3-Fe6	129.56(9)
Fe3-O1-Fe2	123.22(9)	Fe5-O3-Fe6	95.88(7)
Fe1-O1-Fe2	99.98(8)	Fe7-O4-Fe6	121.04(9)
Fe4-O2-Fe5	127.18(9)	Fe7-O4-Fe5	132.30(10)
Fe4-O2-Fe3	99.52(8)	Fe6-O4-Fe5	95.69(7)
Fe5-O2-Fe3	130.01(9)	Fe1-O5-Fe2	93.29(7)
Fe2-O3-Fe5	128.04(9)	Fe4-O16-Fe3	94.35(7)

Table A-8. Selected interatomic distances (Å) and angles (°) for
 $[\text{Fe}_6\text{O}_2(\text{OH})_4(\text{O}_2\text{CBu}')_8(\text{dmem})_2]\cdot 2\text{MeCN} (\mathbf{4}\cdot 3\cdot 2\text{MeCN})$

Fe1-O5'	1.9366(16)	Fe2-O8'	2.0448(18)
Fe1-O5	1.9382(17)	Fe2-O6	2.0662(19)
Fe1-O1	2.0251(18)	Fe2-O7	2.2189(19)
Fe1-O2	2.0457(17)	Fe2-C11	2.481(3)
Fe1-O10'	2.0471(17)	Fe3-O10	1.9420(17)
Fe1-O3	2.0504(18)	Fe3-O9	1.9651(18)
Fe1-Fe1'	2.8651(7)	Fe3-O2	2.0181(18)
Fe2-O5	1.8441(17)	Fe3-O11	2.0331(19)
Fe2-O9	1.9580(18)	Fe3-N1	2.231(2)
Fe2-O4	2.0412(18)	Fe3-N2	2.272(2)
O5'-Fe1-O5	84.64(7)	O9-Fe2-O8'	89.35(8)
O5'-Fe1-O1	94.52(7)	O5-Fe2-O6	99.44(8)
O5-Fe1-O1	178.33(8)	O9-Fe2-O6	157.16(8)
O5'-Fe1-O2	95.30(7)	O5-Fe2-O7	160.49(7)
O5-Fe1-O2	88.98(7)	O9-Fe2-O7	96.06(7)
O1-Fe1-O2	89.67(7)	O10-Fe3-O9	99.75(8)
O5'-Fe1-O10'	87.64(7)	O10-Fe3-O2	96.45(7)
O5-Fe1-O10'	91.72(7)	O9-Fe3-O2	90.25(8)
O1-Fe1-O10'	89.68(7)	O10-Fe3-O11	93.63(8)
O2-Fe1-O10'	177.02(7)	O9-Fe3-O11	89.97(8)
O5'-Fe1-O3	171.93(7)	O2-Fe3-O11	169.73(7)
O5-Fe1-O3	93.52(7)	Fe3-O2-Fe1	125.40(8)
O2-Fe1-O3	92.51(7)	Fe2-O5-Fe1'	128.19(9)
O10'-Fe1-O3	84.56(7)	Fe2-O5-Fe1	126.51(9)
O5-Fe2-O9	103.36(8)	Fe1'-O5-Fe1	95.36(7)
O5-Fe2-O4	96.43(7)	Fe2-O9-Fe3	117.76(9)
O9-Fe2-O4	91.06(8)	Fe3-O10-Fe1'	129.75(9)
O5-Fe2-O8'	96.06(7)		

Table A-9. Selected interatomic distances (Å) and angles (°) for
 $[\text{Fe}_3\text{O}(\text{O}_2\text{CBu}^t)_2(\text{N}_3)_3(\text{dmem})_2] \cdot 4\text{CH}_2\text{Cl}_2$ (**4-4**·2CH₂Cl₂)

Fe1-O1	1.8716(19)	Fe2-O4	2.0469(19)
Fe1-N8	2.007(2)	Fe2-O6	2.0605(19)
Fe1-O3	2.0291(18)	Fe2-O1	2.0700(19)
Fe1-O7	2.0608(19)	Fe3-O1	1.8647(19)
Fe1-N4	2.220(2)	Fe3-N5	2.020(2)
Fe1-N3	2.243(2)	Fe3-O2	2.0245(19)
Fe2-O3	1.9787(19)	Fe3-O5	2.066(2)
Fe2-O2	1.9834(19)	Fe3-N2	2.211(2)
Fe2-N11	2.007(2)	Fe3-N1	2.241(2)
O1-Fe1-O3	80.87(8)	O2-Fe2-O1	77.73(7)
O1-Fe1-O7	96.21(8)	O4-Fe2-O1	93.04(8)
O3-Fe1-O7	88.65(8)	O6-Fe2-O1	90.70(7)
O1-Fe1-N4	97.88(9)	O1-Fe3-N5	106.84(10)
O3-Fe1-N4	95.48(8)	O1-Fe3-O2	81.60(8)
O7-Fe1-N4	165.78(9)	O1-Fe3-O5	95.92(8)
O1-Fe1-N3	157.25(8)	O2-Fe3-O5	88.49(8)
N8-Fe1-N3	95.53(10)	O1-Fe3-N2	98.10(9)
O3-Fe1-N3	76.70(8)	O2-Fe3-N2	95.09(9)
O7-Fe1-N3	87.04(9)	O5-Fe3-N2	165.89(9)
N4-Fe1-N3	80.71(9)	O1-Fe3-N1	157.93(8)
O3-Fe2-O2	155.14(8)	O2-Fe3-N1	76.51(8)
O3-Fe2-O4	92.88(8)	O5-Fe3-N1	86.38(9)
O2-Fe2-O4	88.52(8)	N2-Fe3-N1	81.21(9)
O3-Fe2-O6	89.19(8)	Fe3-O1-Fe1	162.82(11)
O2-Fe2-O6	91.02(8)	Fe3-O1-Fe2	98.34(8)
O4-Fe2-O6	176.04(8)	Fe1-O1-Fe2	98.85(8)
O3-Fe2-O1	77.41(7)	Fe2-O2-Fe3	96.07(8)
		Fe2-O2-Fe1	96.77(8)

Table A-10. Selected interatomic distances (Å) and angles (°) for
 $[\text{Fe}_5\text{O}_2(\text{OH})(\text{O}_2\text{CMe})_5(\text{hmbp})_3](\text{ClO}_4)_2 \cdot 5\text{MeCN}$ (**5-1**·5MeCN)

Fe1-O16	1.825(3)	Fe3-O9	2.063(3)
Fe1-O3	2.021(3)	Fe3-N5	2.094(4)
Fe1-O15	2.058(3)	Fe3-N6	2.189(4)
Fe1-O1	2.075(3)	Fe4-O16	1.951(3)
Fe1-N2	2.104(3)	Fe4-O11	1.956(3)
Fe1-N1	2.190(3)	Fe4-O14	2.003(3)
Fe2-O4	1.933(3)	Fe4-O10	2.017(3)
Fe2-O5	1.980(3)	Fe4-O12	2.039(3)
Fe2-O3	2.023(3)	Fe4-O5	2.058(3)
Fe2-O6	2.052(3)	Fe5-O11	1.951(3)
Fe2-N4	2.116(4)	Fe5-O16	1.951(3)
Fe2-N3	2.155(5)	Fe5-O2	2.017(3)
Fe3-O11	1.826(3)	Fe5-O8	2.021(3)
Fe3-O6	2.008(3)	Fe5-O4	2.031(3)
Fe3-O7	2.048(3)	Fe5-O13	2.041(3)
O16-Fe1-O3	100.08(12)	O11-Fe5-O16	84.45(11)
O16-Fe1-O15	93.21(12)	O11-Fe5-O8	91.98(12)
O16-Fe1-O1	94.68(12)	O16-Fe5-O8	176.20(12)
O4-Fe2-O5	111.55(12)	O11-Fe5-O4	88.95(12)
O4-Fe2-O3	90.87(13)	O16-Fe5-O4	87.62(11)
O5-Fe2-O3	89.21(13)	O2-Fe5-O4	91.79(13)
O4-Fe2-O6	88.51(13)	O8-Fe5-O4	93.62(12)
O5-Fe2-O6	88.59(13)	O11-Fe5-O13	88.85(11)
O11-Fe3-O6	104.43(12)	O16-Fe5-O13	89.14(11)
O11-Fe3-O9	93.41(13)	O4-Fe5-O13	176.24(12)
O16-Fe4-O11	84.34(11)	Fe1-O3-Fe2	114.99(14)
O16-Fe4-O14	92.60(11)	Fe2-O4-Fe5	119.95(15)
O11-Fe4-O14	176.42(12)	Fe2-O5-Fe4	118.09(14)
O16-Fe4-O10	176.14(12)	Fe3-O6-Fe2	112.45(14)
O11-Fe4-O12	88.83(11)	Fe3-O11-Fe5	125.89(15)
O16-Fe4-O5	88.71(12)	Fe3-O11-Fe4	127.03(14)
O11-Fe4-O5	87.71(11)	Fe5-O11-Fe4	94.45
O14-Fe4-O5	90.36(12)	O10-Fe4-O5	91.81(13)

Table A-11. Selected interatomic distances (Å) and angles (°) for
 $[\text{Fe}_6\text{O}_2(\text{OH})_2(\text{O}_2\text{CPh})_6(\text{hmbp})_4](\text{NO}_3)_2 \cdot 3\text{MeCN} \cdot \text{H}_2\text{O}$ (**5-2**·3MeCN·H₂O)

Fe1-O7'	1.912(2)	Fe2-O4	2.033(2)
Fe1-O3	1.974(2)	Fe2-O3	2.063(2)
Fe1-O9'	2.046(2)	Fe2-Fe2'	2.9430(8)
Fe1-O1	2.059(2)	Fe3-O8	1.832(2)
Fe1-N2	2.097(3)	Fe3-O9	2.015(2)
Fe1-N1	2.186(3)	Fe3-O6	2.031(2)
Fe2-O8	1.938(2)	Fe3-O10	2.049(2)
Fe2-O8'	1.978(2)	Fe3-N3	2.095(3)
Fe2-O7	2.011(2)	Fe3-N4	2.183(3)
Fe2-O5	2.029(2)	O4-Fe2-O3	90.14(9)
O7'-Fe1-O3	105.96(9)	O8-Fe3-O9	99.68(9)
O7'-Fe1-O9'	94.49(9)	O8-Fe3-O6	98.96(9)
O3-Fe1-O9'	91.67(10)	O9-Fe3-O6	93.29(10)
O7'-Fe1-O1	89.85(10)	O8-Fe3-O10	93.08(9)
O3-Fe1-O1	96.07(10)	O9-Fe3-O10	95.63(10)
O9'-Fe1-O1	169.75(10)	O6-Fe3-O10	163.60(10)
O8-Fe2-O8'	82.56(9)	O8-Fe3-N3	173.82(10)
O8-Fe2-O7	88.09(9)	O9-Fe3-N3	77.43(10)
O8'-Fe2-O7	94.18(9)	O6-Fe3-N3	86.72(10)
O8-Fe2-O5	97.21(9)	O10-Fe3-N3	81.85(10)
O8'-Fe2-O5	176.80(9)	O8-Fe3-N4	109.05(10)
O7-Fe2-O5	89.00(9)	O9-Fe3-N4	151.19(10)
O8-Fe2-O4	175.77(9)	O6-Fe3-N4	80.31(10)
O8'-Fe2-O4	94.14(9)	O10-Fe3-N4	85.27(11)
O7-Fe2-O4	89.52(9)	Fe1'-O7-Fe2	125.85(11)
O5-Fe2-O4	86.24(9)	Fe3-O8-Fe2	124.38(11)
O8-Fe2-O3	92.59(9)	Fe3-O8-Fe2'	129.12(11)
O8'-Fe2-O3	91.68(9)	Fe2-O8-Fe2'	97.44(9)
O7-Fe2-O3	174.13(9)	Fe3-O9-Fe1'	116.32(10)
O5-Fe2-O3	85.13(9)		

Table A-12. Selected interatomic distances (Å) and angles (°) for
 $[\text{Fe}_{18}\text{O}_8(\text{OH})_2(\text{O}_2\text{CBu}^t)_{28}(\text{heen})_4] \cdot 4\text{C}_5\text{H}_{12} \cdot 4\text{CH}_2\text{Cl}_2$ (**6-1**·4C₅H₁₂·4CH₂Cl₂)

Fe1-O6	1.848(2)	Fe5-N4	2.175(3)
Fe1-O5'	1.981(3)	Fe5-N3	2.202(3)
Fe1-O5	2.022(3)	Fe6-O23	1.943(2)
Fe1-O1	2.046(3)	Fe6-O30	1.978(2)
Fe1-O3	2.055(3)	Fe6-O31	2.030(3)
Fe1-O7	2.102(3)	Fe6-O21	2.032(3)
Fe2-O6	1.923(2)	Fe6-O18	2.034(2)
Fe2-O11	1.993(2)	Fe6-O29	2.042(3)
Fe2-O12	1.994(3)	Fe6-Fe7	2.9008(8)
Fe2-O4	2.019(3)	Fe7-O23	1.941(2)
Fe2-O2	2.028(3)	Fe7-O30	1.949(2)
Fe2-O9	2.083(3)	Fe7-O24	2.024(3)
Fe3-O6	1.894(2)	Fe7-O35	2.042(2)
Fe3-O11	1.937(3)	Fe7-O19	2.048(2)
Fe3-O8	2.019(3)	Fe7-O33	2.073(3)
Fe3-O10	2.060(2)	Fe8-O23	1.849(2)
Fe3-N2	2.163(3)	Fe8-O28	1.994(3)
Fe3-N1	2.220(3)	Fe8-O25	2.036(3)
Fe4-O11	1.819(3)	Fe8-O22	2.037(3)
Fe4-O14	1.872(4)	Fe8-O27	2.108(3)
Fe4-O17	1.974(3)	Fe8-O26	2.140(3)
Fe4-O13	2.013(3)	Fe9-O30	1.843(2)
Fe4-O16	2.029(3)	Fe9-O34	1.980(3)
Fe5-O18	1.954(2)	Fe9-O32	2.018(3)
Fe5-O16	1.966(3)	Fe9-O36	2.084(3)
Fe5-O19	2.000(2)	Fe9-O37	2.114(3)
Fe5-O17	2.011(2)	Fe9-O38	2.123(3)
Fe1'-O5-Fe1	104.35(11)	Fe5-O18-Fe6	127.19(13)
Fe1-O6-Fe3	132.53(13)	Fe5-O19-Fe7	126.89(12)
Fe1-O6-Fe2	122.96(12)	Fe8-O23-Fe7	126.05(13)
Fe3-O6-Fe2	96.22(11)	Fe8-O23-Fe6	120.88(12)
Fe4-O11-Fe3	138.87(13)	Fe7-O23-Fe6	96.64(11)
Fe4-O11-Fe2	125.23(13)	Fe9-O30-Fe7	120.39(13)
Fe3-O11-Fe2	92.62(11)	Fe9-O30-Fe6	126.41(13)

Table A-13. Selected interatomic distances (Å) and angles (°) for
 $[\text{Fe}_9\text{O}_4(\text{OH})_4(\text{O}_2\text{CPh})_{13}(\text{heehH})_2] \cdot 9\text{MeCN}$ (**6-2·9MeCN**)

Fe1-O7	1.939(4)	Fe5-O23	2.098(6)
Fe1-O1	1.984(4)	Fe5-N3	2.189(6)
Fe1-O8	1.985(4)	Fe5-N4	2.205(6)
Fe1-O5	2.013(4)	Fe6-O14	1.905(4)
Fe1-O3	2.088(4)	Fe6-O27	1.961(4)
Fe1-O6	2.145(4)	Fe6-O24	2.027(4)
Fe2-O7	1.912(4)	Fe6-O16	2.035(4)
Fe2-O12	1.990(4)	Fe6-O5	2.058(4)
Fe2-O4	2.017(4)	Fe6-O28	2.093(4)
Fe2-O9	2.045(4)	Fe7-O27	1.960(4)
Fe2-O11	2.057(4)	Fe7-O31	1.963(4)
Fe2-O6	2.076(4)	Fe7-O36	2.010(4)
Fe3-O14	1.887(4)	Fe7-O26	2.012(4)
Fe3-O15	1.989(4)	Fe7-O5	2.086(4)
Fe3-O17	2.010(4)	Fe7-O21	2.141(4)
Fe3-O10	2.049(4)	Fe8-O7	1.889(4)
Fe3-O6	2.069(4)	Fe8-O31	1.968(4)
Fe3-O11	2.093(4)	Fe8-O34	2.008(4)
Fe4-O14	1.964(4)	Fe8-O32	2.044(4)
Fe4-O22	1.979(4)	Fe8-O21	2.048(4)
Fe4-O19	2.000(4)	Fe8-O13	2.071(4)
Fe4-O21	2.048(4)	Fe9-O31	1.850(4)
Fe4-O18	2.067(4)	Fe9-O8	2.016(4)
Fe4-O11	2.115(4)	Fe9-O37	2.032(4)
Fe5-O27	1.853(4)	Fe9-O35	2.071(4)
Fe5-O22	1.986(4)	Fe9-N1	2.195(5)
Fe5-O25	2.038(5)	Fe9-N2	2.223(5)
Fe1-O5-Fe6	130.80(18)	Fe3-O14-Fe6	125.3(2)
Fe1-O5-Fe7	121.71(18)	Fe3-O14-Fe4	101.98(17)
Fe6-O5-Fe7	92.87(14)	Fe6-O14-Fe4	129.7(2)
Fe3-O6-Fe2	97.96(15)	Fe8-O21-Fe4	127.88(19)
Fe3-O6-Fe1	133.2(2)	Fe8-O21-Fe7	93.22(15)
Fe2-O6-Fe1	90.39(15)	Fe4-O21-Fe7	122.76(19)
Fe8-O7-Fe2	125.50(19)	Fe4-O22-Fe5	120.5(2)

Table A-14. Selected interatomic distances (Å) and angles (°) for
 $4[\text{Fe}_7\text{O}_3(\text{OMe})_3(\text{MeOH})_{1.5}(\text{heen})_3\text{Cl}_{4.5}(\text{H}_2\text{O})]\text{Cl}_5[\text{FeCl}_4]\cdot 6\text{MeOH}\cdot\text{H}_2\text{O}$
(6-3·6MeOH·H₂O)

Fe1-O2	1.844(4)	Fe4-Cl3	2.3995(15)
Fe1-O3	1.848(3)	Fe4-Cl4	2.458(4)
Fe1-O1	1.856(4)	Fe5-O3	1.944(3)
Fe1-Cl1	2.2564(15)	Fe5-O8	1.960(4)
Fe2-O1	1.955(4)	Fe5-O10	2.000(4)
Fe2-O6	1.973(4)	Fe5-O9	2.022(4)
Fe2-O14	1.993(4)	Fe5-N3	2.157(5)
Fe2-O5	2.028(4)	Fe5-N4	2.195(4)
Fe2-O4	2.128(4)	Fe6-O3	1.949(4)
Fe2-Cl2	2.3670(15)	Fe6-O13	1.972(4)
Fe3-O2	1.947(4)	Fe6-O10	1.981(4)
Fe3-O5	1.970(4)	Fe6-O12	2.025(4)
Fe3-O7	1.996(4)	Fe6-O11	2.131(4)
Fe3-O6	2.015(4)	Fe6-Cl5	2.3727(15)
Fe3-N1	2.175(6)	Fe7-O1	1.941(4)
Fe3-N2	2.180(6)	Fe7-O12	1.960(4)
Fe4-O9	1.964(4)	Fe7-O14	1.998(4)
Fe4-O7	1.987(4)	Fe7-O13	2.018(4)
Fe4-O2	1.987(4)	Fe7-N6	2.169(5)
Fe4-O8	2.037(4)	Fe7-N5	2.183(5)
Fe4-O4"	2.043(13)	Fe8-Cl8	2.2078(15)
Cl8'-Fe8-Cl8	109.79(8)	Fe5-O3-Fe6	102.64(15)
Cl8"-Fe8-Cl8	110.36(8)	Fe3-O5-Fe2	102.14(18)
Cl8-Fe8-Cl8'''	108.27(9)	Fe2-O6-Fe3	102.49(17)
Fe1-O1-Fe7	123.50(18)	Fe4-O7-Fe3	100.48(17)
Fe1-O1-Fe2	128.89(19)	Fe5-O8-Fe4	102.71(17)
Fe7-O1-Fe2	102.33(17)	Fe4-O9-Fe5	103.09(17)
Fe1-O2-Fe4	128.2(2)	Fe6-O10-Fe5	99.53(15)
Fe3-O2-Fe4	102.21(17)	Fe7-O12-Fe6	102.13(16)
Fe1-O3-Fe5	124.31(19)	Fe6-O13-Fe7	101.98(16)
Fe1-O3-Fe6	128.29(19)	Fe2-O14-Fe7	99.01(16)

Table A-15. Selected interatomic distances (Å) and angles (°) for
 $[\text{Fe}_6\text{O}_2(\text{O}_2\text{CPh})_5(\text{heen})_3(\text{heenH})](\text{ClO}_4)_2 \cdot 2\text{EtOH} \cdot 1.5\text{H}_2\text{O}$ (**6-4**·2EtOH·1.5H₂O)

Fe1-O7'	1.918(3)	Fe2-O3	2.053(3)
Fe1-O10	1.957(3)	Fe2-N1	2.171(4)
Fe1-O7	1.980(3)	Fe2-N2	2.200(4)
Fe1-O1	2.027(3)	Fe3-O11	1.853(10)
Fe1-O8	2.044(3)	Fe3-O8	1.984(4)
Fe1-O4'	2.116(3)	Fe3-O9	1.995(3)
Fe1-Fe1'	2.9113(11)	Fe3-O10	1.997(3)
Fe2-O7	1.846(3)	Fe3-O5	2.025(6)
Fe2-O9	2.022(3)	Fe3-N3	2.187(6)
Fe2-O2'	2.048(3)	Fe3-N4	2.212(5)
Fe2-O7-Fe1'	120.52(15)	Fe3-O8-Fe1	101.62(16)
Fe2-O7-Fe1	130.32(16)	Fe3-O9-Fe2	121.73(16)
Fe1'-O7-Fe1	96.63(12)	Fe1-O10-Fe3	104.30(16)

Table A-16. Selected interatomic distances (Å) and angles (°) for
 $[\text{Mn}_8\text{O}_3(\text{OH})(\text{OMe})(\text{O}_2\text{CPh})_7(\text{edte})(\text{edteH}_2)](\text{O}_2\text{CPh})\cdot 2\text{CH}_2\text{Cl}_2\cdot \text{MeOH}$
(7-1·2CH₂Cl₂·MeOH)

Mn1-O3	1.8836(19)	Mn5-O14	1.8923(18)
Mn1-O25	1.8844(17)	Mn5-O22	1.8941(17)
Mn1-O4	1.9492(18)	Mn5-O16	1.9467(18)
Mn1-O17	1.9591(17)	Mn5-O12	1.9517(19)
Mn1-O27	2.176(2)	Mn5-O19	2.195(2)
Mn1-O18	2.3097(18)	Mn5-O15	2.3662(18)
Mn2-O7	1.8554(18)	Mn6-O1	2.2242(17)
Mn2-O25	1.9105(18)	Mn6-O16	2.2495(18)
Mn2-O18	1.9424(17)	Mn6-O18	2.2606(17)
Mn2-O6	1.9566(17)	Mn6-O15	2.2617(18)
Mn2-O5	2.1596(18)	Mn6-O17	2.2647(18)
Mn2-O1	2.4368(17)	Mn6-N4	2.279(2)
Mn3-O10	2.1431(17)	Mn6-N3	2.285(2)
Mn3-O7	2.1543(18)	Mn7-O22	1.8957(18)
Mn3-O8	2.180(2)	Mn7-O1	1.8997(17)
Mn3-O9	2.239(2)	Mn7-O20	1.9505(19)
Mn3-N2	2.330(2)	Mn7-O21	1.9565(18)
Mn3-N1	2.359(2)	Mn7-O23	2.1235(19)
Mn3-O6	2.4054(17)	Mn7-O16	2.3692(18)
Mn4-O10	1.8661(17)	Mn8-O25	1.8937(17)
Mn4-O22	1.9136(18)	Mn8-O1	1.9079(17)
Mn4-O15	1.9297(17)	Mn8-O21	1.9517(18)
Mn4-O6	1.9652(17)	Mn8-O26	1.9571(19)
Mn4-O11	2.1725(19)	Mn8-O24	2.1360(19)
Mn4-O1	2.4695(18)	Mn8-O17	2.3122(18)
Mn7-O1-Mn8	97.12(8)	Mn2-O7-Mn3	109.95(9)
Mn8-O1-Mn2	88.95(6)	Mn4-O10-Mn3	110.16(8)
Mn6-O1-Mn2	92.52(6)	Mn6-O15-Mn5	97.48(7)
Mn7-O1-Mn4	89.31(6)	Mn5-O16-Mn6	111.83(8)
Mn6-O1-Mn4	92.09(6)	Mn8-O21-Mn7	93.83(8)
Mn2-O1-Mn4	80.05(5)	Mn5-O22-Mn7	105.86(8)
Mn2-O6-Mn4	107.14(8)	Mn1-O25-Mn8	104.91(8)
Mn2-O6-Mn3	97.31(7)	Mn4-O6-Mn3	97.19(7)

Table A-17. Selected interatomic distances (Å) and angles (°) for
 $[\text{Mn}_{12}\text{O}_4(\text{OH})_2(\text{edte})_4\text{Cl}_6(\text{H}_2\text{O})_2]\cdot 6\text{MeCN}\cdot \frac{1}{2}\text{H}_2\text{O}$ (**7-2**·6MeCN·½H₂O)

Mn1-O6'	2.065(3)	Mn2-O1'	2.033(3)
Mn1-O3	2.088(3)	Mn2-Cl2	2.5255(14)
Mn1-O1	2.138(3)	Mn3-O6	1.882(3)
Mn1-O2'	2.306(3)	Mn3-O3	1.905(3)
Mn1-Cl1	2.4050(13)	Mn3-O5	2.107(2)
Mn1-Cl2	2.5813(14)	Mn3-O1	2.163(3)
Mn2-O1	1.841(2)	Mn3-O2	2.209(3)
Mn2-O5'	1.910(2)	Mn3-N2	2.275(3)
Mn2-O4	2.0098(15)	Mn3-N1	2.320(3)
Mn2-O2	2.015(3)	O2-Mn2-Cl2	92.62(8)
Mn2-O4-Mn2'	133.9(2)	O2-Mn2-Cl2	92.62(8)
O6'-Mn1-O3	168.16(11)	O1'-Mn2-Cl2	171.93(8)
O2'-Mn1-Cl1	108.95(7)	O6-Mn3-O5	87.60(11)
O1-Mn1-Cl2	82.17(7)	O5-Mn3-O1	72.73(9)
O2'-Mn1-Cl2	147.38(7)	O3-Mn3-O2	105.80(11)
O1-Mn2-O5'	172.08(12)	O5-Mn3-N2	75.17(10)
O1-Mn2-O4	92.17(10)	O6-Mn3-N1	100.89(12)

Table A-18. Selected interatomic distances (Å) and angles (°) for
 $[\text{Mn}_{20}\text{O}_8(\text{OH})_4(\text{O}_2\text{CMe})_6(\text{edte})_6](\text{ClO}_4)_2 \cdot 10\text{MeOH}$ (**7-3**·10MeOH)

Mn1-O2	2.111(7)	Mn6-O22	1.890(6)
Mn1-O7	2.116(7)	Mn6-O20	1.900(5)
Mn1-O14	2.148(11)	Mn6-O10'	1.927(6)
Mn1-O13	2.258(9)	Mn6-O12'	1.944(5)
Mn1-O6	2.293(7)	Mn6-O17	2.132(6)
Mn1-O4	2.333(6)	Mn6-O24	2.523(5)
Mn2-O2	1.874(6)	Mn7-O19	1.856(6)
Mn2-O3	1.903(5)	Mn7-O16	1.919(6)
Mn2-O1	1.926(7)	Mn7-O1	1.979(7)
Mn2-N2	2.165(7)	Mn7-O8'	2.002(8)
Mn2-O4	2.175(6)	Mn7-O11	2.142(8)
Mn2-N1	2.308(8)	Mn7-O9	2.177(7)
Mn3-O20	1.882(6)	Mn8-O21	1.990(6)
Mn3-O22	1.895(6)	Mn8-O20	1.999(6)
Mn3-O6	1.973(6)	Mn8-O11	2.039(7)
Mn3-O4	1.988(6)	Mn8-O5	2.121(6)
Mn3-O19	2.227(6)	Mn8-O24	2.498(5)
Mn4-O5	1.892(7)	Mn9-O23	1.916(6)
Mn4-O7	1.910(7)	Mn9-O21'	1.929(6)
Mn4-O8'	1.934(8)	Mn9-O24'	1.939(5)
Mn4-N3	2.159(9)	Mn9-O24	1.946(5)
Mn4-O6	2.228(6)	Mn9-O10	2.270(5)
Mn4-N4'	2.35(2)	Mn9-O12'	2.270(5)
Mn4-N4	2.356(16)	Mn10-O9	2.229(6)
Mn5-O22	1.986(6)	Mn10-O12	2.246(6)
Mn5-O23	1.994(5)	Mn10-O11	2.260(6)
Mn5-O9	2.040(6)	Mn10-O10	2.264(6)
Mn5-O19	2.085(7)	Mn10-N6	2.303(8)
Mn5-O3	2.145(6)	Mn10-N5	2.304(8)
Mn2-O1-Mn7	128.2(4)	Mn10-O10-Mn9	93.0(2)
Mn2-O2-Mn1	110.8(3)	Mn8-O11-Mn7	95.2(3)
Mn2-O3-Mn5	110.8(3)	Mn6'-O12-Mn9'	99.1(2)

Table A-19. Selected interatomic distances (Å) and angles (°) for
 $[\text{Fe}_6\text{O}_2(\text{O}_2\text{CBu}')_8(\text{edteH})_2] \cdot 2\text{CHCl}_3$ (**7-5**·2CHCl₃)

Fe1-O12	1.931(2)	Fe2-O2	2.050(3)
Fe1-O6	1.957(3)	Fe2-N2	2.251(3)
Fe1-O10	2.025(3)	Fe2-N1	2.289(3)
Fe1-O8	2.026(3)	Fe3-O12	1.858(2)
Fe1-O1	2.037(3)	Fe3-O13'	2.019(3)
Fe1-O3	2.051(2)	Fe3-O13	2.033(2)
Fe2-O12	1.907(2)	Fe3-O4'	2.034(2)
Fe2-O4	1.965(3)	Fe3-O11	2.039(3)
Fe2-O3	2.030(3)	Fe3-O9	2.040(3)
Fe3-O12-Fe2	123.25(13)	Fe3'-O13-Fe3	102.33(11)
Fe3-O12-Fe1	123.83(13)	Fe2-O3-Fe1	94.06(10)
Fe2-O12-Fe1	102.16(11)	Fe2-O4-Fe3'	118.77(12)

Table A-20. Selected interatomic distances (Å) and angles (°) for
 $[\text{Fe}_{12}\text{O}_4(\text{OH})_2(\text{O}_2\text{CMe})_6(\text{edte})_4(\text{H}_2\text{O})_2](\text{ClO}_4)_4 \cdot 4\text{MeCN}$ (**7-6**·4MeCN)

Fe1-O2	1.977(6)	Fe6-O4	2.074(6)
Fe1-O3	1.985(6)	Fe7-O17	1.926(6)
Fe1-O1	2.040(6)	Fe7-O33	1.969(6)
Fe1-O7	2.187(6)	Fe7-O13	1.982(6)
Fe1-O4	2.223(6)	Fe7-O29	2.037(6)
Fe2-O2	1.964(6)	Fe7-O12	2.092(6)
Fe2-O11	1.984(7)	Fe8-O19	1.972(7)
Fe2-O5	2.010(7)	Fe8-O10	1.976(7)
Fe2-O13	2.053(6)	Fe8-O31	2.001(7)
Fe2-O4	2.104(6)	Fe8-O29	2.068(6)
Fe3-O10	1.972(7)	Fe8-O12	2.098(7)
Fe3-O11	1.988(7)	Fe9-O21	1.959(6)
Fe3-O9	2.038(6)	Fe9-O24	1.979(6)
Fe3-O13	2.160(6)	Fe9-O22	2.031(7)
Fe3-O12	2.239(6)	Fe9-O37	2.186(6)
Fe4-O3	1.975(6)	Fe9-O23	2.237(7)
Fe4-O21	1.981(7)	Fe10-O32	1.954(6)
Fe4-O7	2.004(6)	Fe10-O24	1.974(6)
Fe4-O16	2.080(6)	Fe10-O26	1.995(8)
Fe4-O23	2.098(6)	Fe10-O37	2.031(6)
Fe5-O17	1.944(6)	Fe10-O27	2.032(7)
Fe5-O1	1.968(7)	Fe10-O30	2.103(7)
Fe5-O37	1.971(6)	Fe11-O18	1.952(6)
Fe5-O7	2.032(6)	Fe11-O29	1.963(6)
Fe5-O23	2.104(6)	Fe11-O22	1.980(6)
Fe6-O18	1.939(6)	Fe11-O37	2.026(6)
Fe6-O9	1.967(6)	Fe11-O30	2.093(6)
Fe6-O7	1.980(6)	Fe12-O32	1.962(6)
Fe6-O13	2.013(6)	Fe12-O31	1.976(7)
Fe12-O29	2.156(6)	Fe12-O30	2.236(7)
Fe7-O17-Fe5	135.1(3)	Fe6-O18-Fe11	134.1(3)

Table A-21. Selected interatomic distances (Å) and angles (°) for
 $[\text{Mn}_{10}\text{Gd}_2\text{O}_8(\text{O}_2\text{CPh})_{10}(\text{hmp})_6(\text{NO}_3)_4] \cdot 3\text{MeCN} \cdot \text{MeOH}$ (**8-4**·3MeCN·MeOH)

Gd1-O13	2.312(5)	Mn2-N5	2.030(6)
Gd1-O11	2.325(5)	Mn2-O22	2.190(5)
Gd1-O12	2.360(5)	Mn2-O14	2.223(5)
Gd1-O8	2.469(7)	Mn2-Mn3	3.1327(13)
Gd1-N3	2.504(7)	Mn3-O2	1.882(4)
Gd1-O1	2.509(4)	Mn3-O12	1.905(4)
Gd1-O6	2.512(9)	Mn3-O1	1.915(4)
Gd1-O5	2.535(8)	Mn3-N4	2.026(5)
Gd1-O9	2.567(7)	Mn3-O16	2.086(5)
Gd1-N2	2.949(8)	Mn3-O14	2.380(6)
Gd1-N1	2.951(10)	Mn4-O2	1.912(4)
Gd1-Mn2	3.4185(10)	Mn4-O3'	1.947(4)
Mn1-O11	1.916(5)	Mn4-O19'	1.954(5)
Mn1-O3	1.931(4)	Mn4-O15	1.994(6)
Mn1-O1	1.942(4)	Mn4-O4	2.125(4)
Mn1-O20	1.973(5)	Mn4-O21'	2.151(6)
Mn1-O18	2.137(5)	Mn5-O4'	1.885(4)
Mn1-O22	2.308(5)	Mn5-O2	1.907(4)
Mn1-Mn2	3.1104(14)	Mn5-O3'	1.938(4)
Mn2-O4	1.841(4)	Mn5-O17	1.962(4)
Mn2-O13	1.908(5)	Mn5-O23'	2.211(5)
Mn3-O1-Mn1	133.2(2)	Mn5-O3	2.476(4)
Mn3-O1-Mn2	108.5(2)	Mn1-O3-Mn5	124.90(19)
Mn1-O1-Mn2	106.31(19)	Mn5'-O3-Mn5	93.99(17)
Mn3-O1-Gd1	101.54(16)	Mn4'-O3-Mn5	90.99(16)
Mn1-O1-Gd1	102.50(18)	Mn2-O4-Mn5'	124.6(2)
Mn2-O1-Gd1	99.50(17)	Mn2-O4-Mn4	118.7(2)
Mn3-O2-Mn5	125.8(2)	Mn5'-O4-Mn4	104.62(19)
Mn3-O2-Mn4	125.3(2)	Mn1-O11-Gd1	110.4(2)
Mn5-O2-Mn4	98.54(18)	Mn3-O12-Gd1	107.37(19)
Mn1-O3-Mn5'	124.1(2)	Mn2-O13-Gd1	107.8(2)
Mn1-O3-Mn4'	118.5(2)	Mn2-O14-Mn3	85.71(18)
Mn5'-O3-Mn4'	96.31(18)	Mn2-O22-Mn1	87.45(16)

Table A-22. Selected interatomic distances (Å) and angles (°) for
 $[\text{Mn}_{10}\text{Dy}_2\text{O}_8(\text{O}_2\text{CPh})_{10}(\text{hmp})_6(\text{NO}_3)_4] \cdot 3\text{MeCN} \cdot \text{MeOH}$ (**8-6**·3MeCN·MeOH)

Dy1-O13	2.301(4)	Mn2-N5	2.039(5)
Dy1-O11	2.315(4)	Mn2-O22	2.186(4)
Dy1-O12	2.341(4)	Mn2-O14	2.217(5)
Dy1-O6	2.454(6)	Mn3-O2	1.878(3)
Dy1-O8	2.477(4)	Mn3-O12	1.904(3)
Dy1-O1	2.478(3)	Mn3-O1	1.911(3)
Dy1-N3	2.495(5)	Mn3-N4	2.027(5)
Dy1-O5	2.500(5)	Mn3-O16	2.092(4)
Dy1-O9	2.515(5)	Mn3-O14	2.384(5)
Dy1-N1	2.901(6)	Mn4-O2	1.919(3)
Dy1-N2	2.921(5)	Mn4-O19'	1.949(4)
Mn1-O11	1.915(4)	Mn4-O3'	1.949(3)
Mn1-O3	1.940(3)	Mn4-O15	1.995(5)
Mn1-O1	1.952(3)	Mn4-O4	2.117(3)
Mn1-O20	1.977(4)	Mn4-O21'	2.143(5)
Mn1-O18	2.139(4)	Mn5-O4'	1.887(3)
Mn1-O22	2.301(4)	Mn5-O2	1.905(3)
Mn1-Mn2	3.1220(11)	Mn5-O3'	1.939(3)
Mn2-O4	1.842(3)	Mn5-O17	1.961(3)
Mn2-O13	1.902(4)	Mn5-O23'	2.212(4)
Mn3-O1-Mn1	132.96(18)	Mn5-O3	2.466(3)
Mn3-O1-Mn2	108.24(17)	Mn5'-O3-Mn5	94.11(13)
Mn1-O1-Mn2	106.15(15)	Mn1-O3-Mn5	124.33(15)
Mn3-O1-Dy1	101.87(13)	Mn4'-O3-Mn5	91.20(13)
Mn1-O1-Dy1	102.70(15)	Mn2-O4-Mn5'	124.77(19)
Mn2-O1-Dy1	100.00(13)	Mn2-O4-Mn4	118.35(16)
Mn3-O2-Mn5	126.65(18)	Mn5'-O4-Mn4	104.75(15)
Mn3-O2-Mn4	124.95(18)	Mn1-O11-Dy1	110.13(18)
Mn5-O2-Mn4	98.51(14)	Mn3-O12-Dy1	107.18(14)
Mn5'-O3-Mn1	124.39(17)	Mn2-O13-Dy1	108.13(17)
Mn5'-O3-Mn4'	96.34(14)	Mn2-O14-Mn3	85.69(16)
Mn1-O3-Mn4'	118.47(17)	Mn2-O22-Mn1	88.14(13)

Table A-23. Selected interatomic distances (Å) and angles (°) for
 $[\text{Mn}_{10}\text{Y}_2\text{O}_8(\text{O}_2\text{CPh})_{10}(\text{hmp})_6(\text{NO}_3)_4] \cdot 4\text{MeCN}$ (**8-9**·4MeCN)

Y1-O11	2.290(5)	Mn2-O14	2.285(7)
Y1-O13	2.296(6)	Mn3-O2	1.869(4)
Y1-O12	2.334(4)	Mn3-O12	1.892(4)
Y1-O6	2.432(7)	Mn3-O1	1.911(4)
Y1-O8	2.450(5)	Mn3-N5	2.015(5)
Y1-O1	2.450(4)	Mn3-O16	2.091(5)
Y1-N3	2.465(7)	Mn3-O14	2.470(8)
Y1-O5	2.475(7)	Mn4-O2	1.917(4)
Y1-O9	2.497(6)	Mn4-O19'	1.948(5)
Y1-N1	2.885(8)	Mn4-O3'	1.962(4)
Y1-N2	2.910(7)	Mn4-O15	1.998(7)
Mn1-O11	1.908(5)	Mn4-O4	2.081(4)
Mn1-O3	1.921(4)	Mn4-O21'	2.100(6)
Mn1-O1	1.947(4)	Mn5-O4'	1.895(4)
Mn1-O20	1.967(5)	Mn5-O2	1.910(4)
Mn1-O18	2.137(5)	Mn5-O3'	1.933(4)
Mn1-O22	2.291(5)	Mn5-O17	1.945(5)
Mn2-O4	1.843(4)	Mn5-O23'	2.213(5)
Mn2-O13	1.895(5)	Mn5-O3	2.439(4)
Mn2-O1	1.947(5)	Mn5-Mn4'	3.1527(14)
Mn2-N4	2.014(6)	Mn5-Mn5'	3.2167(19)
Mn2-O22	2.181(5)	O3-Mn5'	1.933(4)
Mn3-O1-Mn2	107.8(2)	Mn1-O3-Mn5	124.78(18)
Mn3-O1-Mn1	132.9(2)	Mn5'-O3-Mn5	94.02(17)
Mn2-O1-Mn1	105.72(18)	Mn4'-O3-Mn5	90.85(16)
Mn3-O1-Y1	102.26(16)	Mn2-O4-Mn5'	124.5(2)
Mn2-O1-Y1	100.61(17)	Mn2-O4-Mn4	118.21(19)
Mn1-O1-Y1	103.05(19)	Mn5'-O4-Mn4	104.82(19)
Mn3-O2-Mn5	126.5(2)	Mn1-O11-Y1	110.5(2)
Mn3-O2-Mn4	124.8(2)	Mn3-O12-Y1	107.22(17)
Mn5-O2-Mn4	98.53(17)	Mn2-O13-Y1	108.0(2)
Mn1-O3-Mn5'	124.1(2)	Mn2-O14-Mn3	81.8(3)
Mn1-O3-Mn4'	118.8(2)	Mn2-O22-Mn1	87.87(16)

APPENDIX B
LIST OF COMPOUNDS

[Mn₄O₂(O₂CMe)₅(salpro)] (2-1)

[Mn₄O₂(O₂CEt)₅(salpro)] (2-2)

[Mn₄O₂(O₂CBu^t)₅(salpro)] (2-3)

NMe₄[Mn(O₂CPh)₂(salproH)] (2-4)

[Mn₄(hmp)₄(pdmH)₂(MeCN)₄](ClO₄)₄ (3-1)

[Mn₂₅O₁₈(OH)₂(hmp)₆(pdm)₈(pdmH)₂(L)₂](ClO₄)₆ (3-2)

[Fe₇O₄(O₂CPh)₁₁(dmem)₂] (4-1)

[Fe₇O₄(O₂CMe)₁₁(dmem)₂] (4-2)

[Fe₆O₂(OH)₄(O₂CCBu^t)₈(dmem)₂] (4-3)

[Fe₃O(O₂CBu^t)₂(N₃)₃(dmem)₂] (4-4)

[Fe₅O₂(OH)(O₂CMe)₅(hmbp)₃](ClO₄)₂ (5-1)

[Fe₆O₂(OH)₂(O₂CPh)₆(hmbp)₄](NO₃)₂ (5-2)

[Fe₆O₂(OH)₂(O₂CMe)₆(hmbp)₄](NO₃)₂ (5-3)

[Fe₆O₂(OH)₂(O₂CBu^t)₆(hmbp)₄](NO₃)₂ (5-4)

[Fe₁₈O₈(OH)₂(O₂CBu^t)₂₈(heen)₄] (6-1)

[Fe₉O₄(OH)₄(O₂CPh)₁₃(heenH)₂] (6-2)

4[Fe₇O₃(OMe)₃(MeOH)_{1.5}(heen)₃Cl_{4.5}(H₂O)]Cl₅[FeCl₄] (6-3)

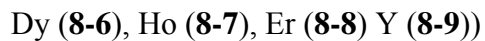
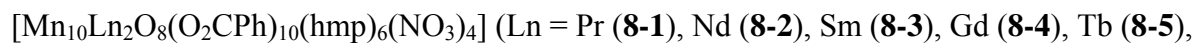
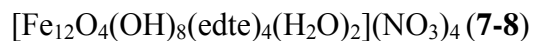
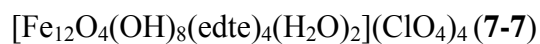
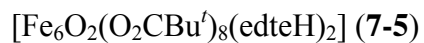
[Fe₆O₂(O₂CPh)₅(heen)₃(heenH)](ClO₄)₂ (6-4)

[Mn₈O₃(OH)(OMe)(O₂CPh)₇(edte)(edteH₂)](O₂CPh) (7-1)

[Mn₁₂O₄(OH)₂(edte)₄Cl₆(H₂O)₂] (7-2)

[Mn₂₀O₈(OH)₄(O₂CMe)₆(edte)₆](ClO₄)₂ (7-3)

[Fe₅O₂(O₂CPh)₇(edte)(H₂O)] (7-4)



APPENDIX C PHYSICAL MEASUREMENTS

Infrared spectra were recorded in the solid state (KBr pellets) on a Nicolet Nexus 670 FTIR spectrometer in the 400 - 4000 cm^{-1} range. Elemental analyses (C, H and N) were performed by the in-house facilities of the University of Florida, Chemistry Department. Cl analysis was performed by Complete Analysis Laboratories, Inc. in Parsippany, New Jersey. Variable-temperature dc and ac magnetic susceptibility data were collected at the University of Florida using a Quantum Design MPMS-XL SQUID susceptometer equipped with a 7 T magnet and operating in the 1.8 – 300 K range. Samples were embedded in solid eicosane to prevent torquing. Magnetization vs. field and temperature data was fit using the program *MAGNET*.⁵³ Pascal's constants were used to estimate the diamagnetic correction, which was subtracted from the experimental susceptibility to give the molar paramagnetic susceptibility (χ_M). Double-axis angle- dependent high-frequency electron paramagnetic resonance (HFEPR) studies were performed on single crystals using a rotating cavity²⁹⁶ and a 7 T transverse magnetic field, which can be rotated about an axis perpendicular to the axis of the rotating cavity. In addition, a 17 T axial magnet was employed for some single-axis measurements. The experiments were carried out over a wide range of frequencies (50-200 GHz) and with the sample at temperatures in the 1.8-20 K range.

APPENDIX D
VAN VLECK EQUATIONS

p = paramagnetic impurity

$$c = N\mu_B^2/3k$$

N = Avogadro's number

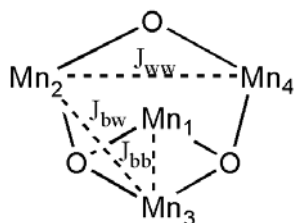
g = Lande's factor

k = Boltzmann constant

T = Temperature

TIP = Temperature independent paramagnetism

D-1[Mn₄O₂(O₂CMe)₅(salpro)] (2-1)



$$\chi_M = (c g^2)/T (\text{Num/Den}) + \text{TIP}$$

$$l = J_{bb}/k/T$$

$$m = J_{bw}/k/T$$

$$n = J_{ww}/k/T$$

$$\begin{aligned} \text{Num} = &+ 300.0000 * \exp(0.0000 * l + 0.0000 * m + 0.0000 * n) \\ &+ 6.0000 * \exp(2.0000 * l + 0.0000 * m + 0.0000 * n) \\ &+ 0.0000 * \exp(2.0000 * l + -4.0000 * m + 2.0000 * n) \\ &+ 300.0000 * \exp(2.0000 * l + -2.0000 * m + 2.0000 * n) \\ &+ 30.0000 * \exp(2.0000 * l + 2.0000 * m + 2.0000 * n) \\ &+ 6.0000 * \exp(2.0000 * l + -6.0000 * m + 6.0000 * n) \\ &+ 84.0000 * \exp(2.0000 * l + 4.0000 * m + 6.0000 * n) \\ &+ 30.0000 * \exp(2.0000 * l + -8.0000 * m + 12.0000 * n) \\ &+ 180.0000 * \exp(2.0000 * l + 6.0000 * m + 12.0000 * n) \\ &+ 84.0000 * \exp(2.0000 * l + -10.0000 * m + 20.0000 * n) \\ &+ 330.0000 * \exp(2.0000 * l + 8.0000 * m + 20.0000 * n) \\ &+ 114.0000 * \exp(6.0000 * l + 0.0000 * m + 0.0000 * n) \\ &+ 300.0000 * \exp(6.0000 * l + -6.0000 * m + 2.0000 * n) \\ &+ 30.0000 * \exp(6.0000 * l + -2.0000 * m + 2.0000 * n) \\ &+ 414.0000 * \exp(6.0000 * l + 4.0000 * m + 2.0000 * n) \\ &+ 30.0000 * \exp(6.0000 * l + -12.0000 * m + 6.0000 * n) \\ &+ 6.0000 * \exp(6.0000 * l + -10.0000 * m + 6.0000 * n) \\ &+ 180.0000 * \exp(6.0000 * l + 8.0000 * m + 6.0000 * n) \\ &+ 6.0000 * \exp(6.0000 * l + -16.0000 * m + 12.0000 * n) \\ &+ 180.0000 * \exp(6.0000 * l + 2.0000 * m + 12.0000 * n) \\ &+ 330.0000 * \exp(6.0000 * l + 12.0000 * m + 12.0000 * n) \end{aligned}$$

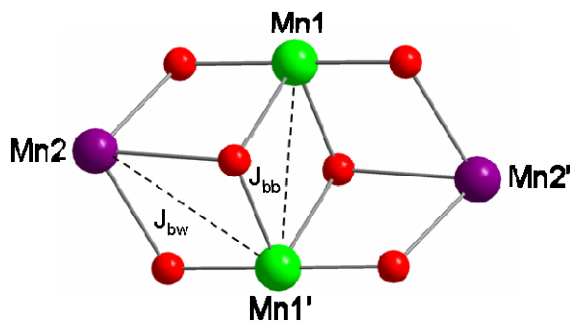
$$\begin{aligned}
& + 30.0000 * \exp(6.0000 * l + -20.0000 * m + 20.0000 * n) \\
& + 84.0000 * \exp(6.0000 * l + -14.0000 * m + 20.0000 * n) \\
& + 546.0000 * \exp(6.0000 * l + 16.0000 * m + 20.0000 * n) \\
& + 84.0000 * \exp(12.0000 * l + 0.0000 * m + 0.0000 * n) \\
& + 30.0000 * \exp(12.0000 * l + -8.0000 * m + 2.0000 * n) \\
& + 414.0000 * \exp(12.0000 * l + -2.0000 * m + 2.0000 * n) \\
& + 510.0000 * \exp(12.0000 * l + 6.0000 * m + 2.0000 * n) \\
& + 6.0000 * \exp(12.0000 * l + -16.0000 * m + 6.0000 * n) \\
& + 294.0000 * \exp(12.0000 * l + -12.0000 * m + 6.0000 * n) \\
& + 84.0000 * \exp(12.0000 * l + -6.0000 * m + 6.0000 * n) \\
& + 180.0000 * \exp(12.0000 * l + 2.0000 * m + 6.0000 * n) \\
& + 330.0000 * \exp(12.0000 * l + 12.0000 * m + 6.0000 * n) \\
& + 0.0000 * \exp(12.0000 * l + -24.0000 * m + 12.0000 * n) \\
& + 6.0000 * \exp(12.0000 * l + -22.0000 * m + 12.0000 * n) \\
& + 30.0000 * \exp(12.0000 * l + -18.0000 * m + 12.0000 * n) \\
& + 180.0000 * \exp(12.0000 * l + -4.0000 * m + 12.0000 * n) \\
& + 546.0000 * \exp(12.0000 * l + 18.0000 * m + 12.0000 * n) \\
& + 6.0000 * \exp(12.0000 * l + -30.0000 * m + 20.0000 * n) \\
& + 30.0000 * \exp(12.0000 * l + -26.0000 * m + 20.0000 * n) \\
& + 84.0000 * \exp(12.0000 * l + -20.0000 * m + 20.0000 * n) \\
& + 546.0000 * \exp(12.0000 * l + 10.0000 * m + 20.0000 * n) \\
& + 840.0000 * \exp(12.0000 * l + 24.0000 * m + 20.0000 * n) \\
& + 180.0000 * \exp(20.0000 * l + 0.0000 * m + 0.0000 * n) \\
& + 414.0000 * \exp(20.0000 * l + -10.0000 * m + 2.0000 * n) \\
& + 510.0000 * \exp(20.0000 * l + -2.0000 * m + 2.0000 * n) \\
& + 330.0000 * \exp(20.0000 * l + 8.0000 * m + 2.0000 * n) \\
& + 294.0000 * \exp(20.0000 * l + -20.0000 * m + 6.0000 * n) \\
& + 84.0000 * \exp(20.0000 * l + -14.0000 * m + 6.0000 * n) \\
& + 180.0000 * \exp(20.0000 * l + -6.0000 * m + 6.0000 * n) \\
& + 330.0000 * \exp(20.0000 * l + 4.0000 * m + 6.0000 * n) \\
& + 1386.0000 * \exp(20.0000 * l + 16.0000 * m + 6.0000 * n) \\
& + 6.0000 * \exp(20.0000 * l + -30.0000 * m + 12.0000 * n) \\
& + 30.0000 * \exp(20.0000 * l + -26.0000 * m + 12.0000 * n) \\
& + 180.0000 * \exp(20.0000 * l + -12.0000 * m + 12.0000 * n) \\
& + 546.0000 * \exp(20.0000 * l + 10.0000 * m + 12.0000 * n) \\
& + 840.0000 * \exp(20.0000 * l + 24.0000 * m + 12.0000 * n) \\
& + 0.0000 * \exp(20.0000 * l + -40.0000 * m + 20.0000 * n) \\
& + 6.0000 * \exp(20.0000 * l + -38.0000 * m + 20.0000 * n) \\
& + 30.0000 * \exp(20.0000 * l + -34.0000 * m + 20.0000 * n) \\
& + 84.0000 * \exp(20.0000 * l + -28.0000 * m + 20.0000 * n) \\
& + 546.0000 * \exp(20.0000 * l + 2.0000 * m + 20.0000 * n) \\
& + 1224.0000 * \exp(20.0000 * l + 32.0000 * m + 20.0000 * n)
\end{aligned}$$

$$\begin{aligned}
\text{Den} = & + 25.0000 * \exp(0.0000 * l + 0.0000 * m + 0.0000 * n) \\
& + 3.0000 * \exp(2.0000 * l + 0.0000 * m + 0.0000 * n) \\
& + 1.0000 * \exp(2.0000 * l + -4.0000 * m + 2.0000 * n)
\end{aligned}$$

+ 24.0000 *exp(2.0000 *l+ -2.0000 *m+ 2.0000 *n)
 + 5.0000 *exp(2.0000 *l+ 2.0000 *m+ 2.0000 *n)
 + 3.0000 *exp(2.0000 *l+ -6.0000 *m+ 6.0000 *n)
 + 7.0000 *exp(2.0000 *l+ 4.0000 *m+ 6.0000 *n)
 + 5.0000 *exp(2.0000 *l+ -8.0000 *m+ 12.0000 *n)
 + 9.0000 *exp(2.0000 *l+ 6.0000 *m+ 12.0000 *n)
 + 7.0000 *exp(2.0000 *l+ -10.0000 *m+ 20.0000 *n)
 + 11.0000 *exp(2.0000 *l+ 8.0000 *m+ 20.0000 *n)
 + 12.0000 *exp(6.0000 *l+ 0.0000 *m+ 0.0000 *n)
 + 24.0000 *exp(6.0000 *l+ -6.0000 *m+ 2.0000 *n)
 + 5.0000 *exp(6.0000 *l+ -2.0000 *m+ 2.0000 *n)
 + 18.0000 *exp(6.0000 *l+ 4.0000 *m+ 2.0000 *n)
 + 6.0000 *exp(6.0000 *l+ -12.0000 *m+ 6.0000 *n)
 + 3.0000 *exp(6.0000 *l+ -10.0000 *m+ 6.0000 *n)
 + 9.0000 *exp(6.0000 *l+ 8.0000 *m+ 6.0000 *n)
 + 3.0000 *exp(6.0000 *l+ -16.0000 *m+ 12.0000 *n)
 + 9.0000 *exp(6.0000 *l+ 2.0000 *m+ 12.0000 *n)
 + 11.0000 *exp(6.0000 *l+ 12.0000 *m+ 12.0000 *n)
 + 5.0000 *exp(6.0000 *l+ -20.0000 *m+ 20.0000 *n)
 + 7.0000 *exp(6.0000 *l+ -14.0000 *m+ 20.0000 *n)
 + 13.0000 *exp(6.0000 *l+ 16.0000 *m+ 20.0000 *n)
 + 7.0000 *exp(12.0000 *l+ 0.0000 *m+ 0.0000 *n)
 + 5.0000 *exp(12.0000 *l+ -8.0000 *m+ 2.0000 *n)
 + 18.0000 *exp(12.0000 *l+ -2.0000 *m+ 2.0000 *n)
 + 20.0000 *exp(12.0000 *l+ 6.0000 *m+ 2.0000 *n)
 + 3.0000 *exp(12.0000 *l+ -16.0000 *m+ 6.0000 *n)
 + 21.0000 *exp(12.0000 *l+ -12.0000 *m+ 6.0000 *n)
 + 7.0000 *exp(12.0000 *l+ -6.0000 *m+ 6.0000 *n)
 + 9.0000 *exp(12.0000 *l+ 2.0000 *m+ 6.0000 *n)
 + 11.0000 *exp(12.0000 *l+ 12.0000 *m+ 6.0000 *n)
 + 1.0000 *exp(12.0000 *l+ -24.0000 *m+ 12.0000 *n)
 + 3.0000 *exp(12.0000 *l+ -22.0000 *m+ 12.0000 *n)
 + 5.0000 *exp(12.0000 *l+ -18.0000 *m+ 12.0000 *n)
 + 9.0000 *exp(12.0000 *l+ -4.0000 *m+ 12.0000 *n)
 + 13.0000 *exp(12.0000 *l+ 18.0000 *m+ 12.0000 *n)
 + 3.0000 *exp(12.0000 *l+ -30.0000 *m+ 20.0000 *n)
 + 5.0000 *exp(12.0000 *l+ -26.0000 *m+ 20.0000 *n)
 + 7.0000 *exp(12.0000 *l+ -20.0000 *m+ 20.0000 *n)
 + 13.0000 *exp(12.0000 *l+ 10.0000 *m+ 20.0000 *n)
 + 15.0000 *exp(12.0000 *l+ 24.0000 *m+ 20.0000 *n)
 + 9.0000 *exp(20.0000 *l+ 0.0000 *m+ 0.0000 *n)
 + 18.0000 *exp(20.0000 *l+ -10.0000 *m+ 2.0000 *n)
 + 20.0000 *exp(20.0000 *l+ -2.0000 *m+ 2.0000 *n)
 + 11.0000 *exp(20.0000 *l+ 8.0000 *m+ 2.0000 *n)
 + 21.0000 *exp(20.0000 *l+ -20.0000 *m+ 6.0000 *n)
 + 7.0000 *exp(20.0000 *l+ -14.0000 *m+ 6.0000 *n)

$$\begin{aligned}
&+ 9.0000 * \exp(20.0000 * 1 + -6.0000 * m + 6.0000 * n) \\
&+ 11.0000 * \exp(20.0000 * 1 + 4.0000 * m + 6.0000 * n) \\
&+ 28.0000 * \exp(20.0000 * 1 + 16.0000 * m + 6.0000 * n) \\
&+ 3.0000 * \exp(20.0000 * 1 + -30.0000 * m + 12.0000 * n) \\
&+ 5.0000 * \exp(20.0000 * 1 + -26.0000 * m + 12.0000 * n) \\
&+ 9.0000 * \exp(20.0000 * 1 + -12.0000 * m + 12.0000 * n) \\
&+ 13.0000 * \exp(20.0000 * 1 + 10.0000 * m + 12.0000 * n) \\
&+ 15.0000 * \exp(20.0000 * 1 + 24.0000 * m + 12.0000 * n) \\
&+ 1.0000 * \exp(20.0000 * 1 + -40.0000 * m + 20.0000 * n) \\
&+ 3.0000 * \exp(20.0000 * 1 + -38.0000 * m + 20.0000 * n) \\
&+ 5.0000 * \exp(20.0000 * 1 + -34.0000 * m + 20.0000 * n) \\
&+ 7.0000 * \exp(20.0000 * 1 + -28.0000 * m + 20.0000 * n) \\
&+ 13.0000 * \exp(20.0000 * 1 + 2.0000 * m + 20.0000 * n) \\
&+ 17.0000 * \exp(20.0000 * 1 + 32.0000 * m + 20.0000 * n)
\end{aligned}$$

D-2 [Mn₄(hmp)₄(pdmH)₂(MeCN)₄](ClO₄)₄ (3-1)



$$\chi_M = (c g^2)/T (\text{Num/Den}) + \text{TIP}$$

$$l = J_{bb}/k/T$$

$$m = J_{bw}/k/T$$

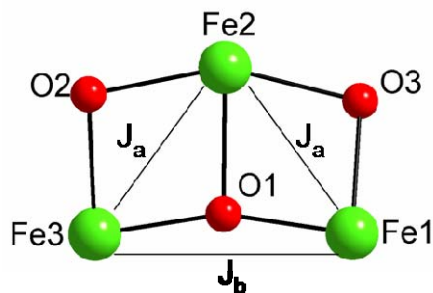
$$\begin{aligned}
\text{Num} = &+ 630.0000 * \exp(0.0000 * 1 + 0.0000 * m) + 6.0000 * \exp(2.0000 * 1 + 0.0000 * m) \\
&+ 0.0000 * \exp(2.0000 * 1 + -4.0000 * m) + 630.0000 * \exp(2.0000 * 1 + -2.0000 * m) \\
&+ 30.0000 * \exp(2.0000 * 1 + 2.0000 * m) + 6.0000 * \exp(2.0000 * 1 + -6.0000 * m) \\
&+ 84.0000 * \exp(2.0000 * 1 + 4.0000 * m) + 30.0000 * \exp(2.0000 * 1 + -8.0000 * m) \\
&+ 180.0000 * \exp(2.0000 * 1 + 6.0000 * m) + 84.0000 * \exp(2.0000 * 1 + -10.0000 * m) \\
&+ 330.0000 * \exp(2.0000 * 1 + 8.0000 * m) + 180.0000 * \exp(2.0000 * 1 + -12.0000 * m) \\
&+ 546.0000 * \exp(2.0000 * 1 + 10.0000 * m) + 114.0000 * \exp(6.0000 * 1 + 0.0000 * m) \\
&+ 630.0000 * \exp(6.0000 * 1 + -6.0000 * m) + 30.0000 * \exp(6.0000 * 1 + -2.0000 * m) \\
&+ 414.0000 * \exp(6.0000 * 1 + 4.0000 * m) + 30.0000 * \exp(6.0000 * 1 + -12.0000 * m) \\
&+ 6.0000 * \exp(6.0000 * 1 + -10.0000 * m) + 180.0000 * \exp(6.0000 * 1 + 8.0000 * m) \\
&+ 186.0000 * \exp(6.0000 * 1 + -16.0000 * m) + 180.0000 * \exp(6.0000 * 1 + 2.0000 * m) \\
&+ 330.0000 * \exp(6.0000 * 1 + 12.0000 * m) + 30.0000 * \exp(6.0000 * 1 + -20.0000 * m) \\
&+ 84.0000 * \exp(6.0000 * 1 + -14.0000 * m) + 546.0000 * \exp(6.0000 * 1 + 16.0000 * m) \\
&+ 84.0000 * \exp(6.0000 * 1 + -24.0000 * m) + 546.0000 * \exp(6.0000 * 1 + 6.0000 * m)
\end{aligned}$$

$$\begin{aligned}
& + 840.0000 * \exp(6.0000 * 1 + 20.0000 * m) + 630.0000 * \exp(12.0000 * 1 + 0.0000 * m) \\
& + 30.0000 * \exp(12.0000 * 1 + -8.0000 * m) + 414.0000 * \exp(12.0000 * 1 + -2.0000 * m) \\
& + 510.0000 * \exp(12.0000 * 1 + 6.0000 * m) + 6.0000 * \exp(12.0000 * 1 + -16.0000 * m) \\
& + 624.0000 * \exp(12.0000 * 1 + -12.0000 * m) + 84.0000 * \exp(12.0000 * 1 + -6.0000 * m) \\
& + 180.0000 * \exp(12.0000 * 1 + 2.0000 * m) + 330.0000 * \exp(12.0000 * 1 + 12.0000 * m) \\
& + 0.0000 * \exp(12.0000 * 1 + -24.0000 * m) + 186.0000 * \exp(12.0000 * 1 + -22.0000 * m) \\
& + 30.0000 * \exp(12.0000 * 1 + -18.0000 * m) + 180.0000 * \exp(12.0000 * 1 + -4.0000 * m) \\
& + 546.0000 * \exp(12.0000 * 1 + 18.0000 * m) + 90.0000 * \exp(12.0000 * 1 + -30.0000 * m) \\
& + 30.0000 * \exp(12.0000 * 1 + -26.0000 * m) + 84.0000 * \exp(12.0000 * 1 + -20.0000 * m) \\
& + 546.0000 * \exp(12.0000 * 1 + 10.0000 * m) + 840.0000 * \exp(12.0000 * 1 + 24.0000 * m) \\
& + 30.0000 * \exp(12.0000 * 1 + -36.0000 * m) + 840.0000 * \exp(12.0000 * 1 + 14.0000 * m) \\
& + 1224.0000 * \exp(12.0000 * 1 + 30.0000 * m) + 180.0000 * \exp(20.0000 * 1 + 0.0000 * m) \\
& + 414.0000 * \exp(20.0000 * 1 + -10.0000 * m) + 510.0000 * \exp(20.0000 * 1 + -2.0000 * m) \\
& + 330.0000 * \exp(20.0000 * 1 + 8.0000 * m) + 624.0000 * \exp(20.0000 * 1 + -20.0000 * m) \\
& + 84.0000 * \exp(20.0000 * 1 + -14.0000 * m) + 180.0000 * \exp(20.0000 * 1 + -6.0000 * m) \\
& + 330.0000 * \exp(20.0000 * 1 + 4.0000 * m) + 1386.0000 * \exp(20.0000 * 1 + 16.0000 * m) \\
& + 186.0000 * \exp(20.0000 * 1 + -30.0000 * m) + 30.0000 * \exp(20.0000 * 1 + -26.0000 * m) \\
& + 180.0000 * \exp(20.0000 * 1 + -12.0000 * m) + 546.0000 * \exp(20.0000 * 1 + 10.0000 * m) \\
& + 840.0000 * \exp(20.0000 * 1 + 24.0000 * m) + 0.0000 * \exp(20.0000 * 1 + -40.0000 * m) \\
& + 90.0000 * \exp(20.0000 * 1 + -38.0000 * m) + 30.0000 * \exp(20.0000 * 1 + -34.0000 * m) \\
& + 84.0000 * \exp(20.0000 * 1 + -28.0000 * m) + 546.0000 * \exp(20.0000 * 1 + 2.0000 * m) \\
& + 1224.0000 * \exp(20.0000 * 1 + 32.0000 * m) + 6.0000 * \exp(20.0000 * 1 + -48.0000 * m) \\
& + 30.0000 * \exp(20.0000 * 1 + -44.0000 * m) + 546.0000 * \exp(20.0000 * 1 + -8.0000 * m) \\
& + 840.0000 * \exp(20.0000 * 1 + 6.0000 * m) + 1224.0000 * \exp(20.0000 * 1 + 22.0000 * m) \\
& + 1710.0000 * \exp(20.0000 * 1 + 40.0000 * m)
\end{aligned}$$

$$\begin{aligned}
\text{Den} = & + 36.0000 * \exp(0.0000 * 1 + 0.0000 * m) + 3.0000 * \exp(2.0000 * 1 + 0.0000 * m) \\
& + 1.0000 * \exp(2.0000 * 1 + -4.0000 * m) + 35.0000 * \exp(2.0000 * 1 + -2.0000 * m) \\
& + 5.0000 * \exp(2.0000 * 1 + 2.0000 * m) + 3.0000 * \exp(2.0000 * 1 + -6.0000 * m) \\
& + 7.0000 * \exp(2.0000 * 1 + 4.0000 * m) + 5.0000 * \exp(2.0000 * 1 + -8.0000 * m) \\
& + 9.0000 * \exp(2.0000 * 1 + 6.0000 * m) + 7.0000 * \exp(2.0000 * 1 + -10.0000 * m) \\
& + 11.0000 * \exp(2.0000 * 1 + 8.0000 * m) + 9.0000 * \exp(2.0000 * 1 + -12.0000 * m) \\
& + 13.0000 * \exp(2.0000 * 1 + 10.0000 * m) + 12.0000 * \exp(6.0000 * 1 + 0.0000 * m) \\
& + 35.0000 * \exp(6.0000 * 1 + -6.0000 * m) + 5.0000 * \exp(6.0000 * 1 + -2.0000 * m) \\
& + 18.0000 * \exp(6.0000 * 1 + 4.0000 * m) + 6.0000 * \exp(6.0000 * 1 + -12.0000 * m) \\
& + 3.0000 * \exp(6.0000 * 1 + -10.0000 * m) + 9.0000 * \exp(6.0000 * 1 + 8.0000 * m) \\
& + 12.0000 * \exp(6.0000 * 1 + -16.0000 * m) + 9.0000 * \exp(6.0000 * 1 + 2.0000 * m) \\
& + 11.0000 * \exp(6.0000 * 1 + 12.0000 * m) + 5.0000 * \exp(6.0000 * 1 + -20.0000 * m) \\
& + 7.0000 * \exp(6.0000 * 1 + -14.0000 * m) + 13.0000 * \exp(6.0000 * 1 + 16.0000 * m) \\
& + 7.0000 * \exp(6.0000 * 1 + -24.0000 * m) + 13.0000 * \exp(6.0000 * 1 + 6.0000 * m) \\
& + 15.0000 * \exp(6.0000 * 1 + 20.0000 * m) + 20.0000 * \exp(12.0000 * 1 + 0.0000 * m) \\
& + 5.0000 * \exp(12.0000 * 1 + -8.0000 * m) + 18.0000 * \exp(12.0000 * 1 + -2.0000 * m) \\
& + 20.0000 * \exp(12.0000 * 1 + 6.0000 * m) + 3.0000 * \exp(12.0000 * 1 + -16.0000 * m) \\
& + 32.0000 * \exp(12.0000 * 1 + -12.0000 * m) + 7.0000 * \exp(12.0000 * 1 + -6.0000 * m) \\
& + 9.0000 * \exp(12.0000 * 1 + 2.0000 * m) + 11.0000 * \exp(12.0000 * 1 + 12.0000 * m) \\
& + 1.0000 * \exp(12.0000 * 1 + -24.0000 * m) + 12.0000 * \exp(12.0000 * 1 + -22.0000 * m)
\end{aligned}$$

$$\begin{aligned}
& + 5.0000 * \exp(12.0000 * 1 + -18.0000 * m) + 9.0000 * \exp(12.0000 * 1 + -4.0000 * m) \\
& + 13.0000 * \exp(12.0000 * 1 + 18.0000 * m) + 10.0000 * \exp(12.0000 * 1 + -30.0000 * m) \\
& + 5.0000 * \exp(12.0000 * 1 + -26.0000 * m) + 7.0000 * \exp(12.0000 * 1 + -20.0000 * m) \\
& + 13.0000 * \exp(12.0000 * 1 + 10.0000 * m) + 15.0000 * \exp(12.0000 * 1 + 24.0000 * m) \\
& + 5.0000 * \exp(12.0000 * 1 + -36.0000 * m) + 15.0000 * \exp(12.0000 * 1 + 14.0000 * m) \\
& + 17.0000 * \exp(12.0000 * 1 + 30.0000 * m) + 9.0000 * \exp(20.0000 * 1 + 0.0000 * m) \\
& + 18.0000 * \exp(20.0000 * 1 + -10.0000 * m) + 20.0000 * \exp(20.0000 * 1 + -2.0000 * m) \\
& + 11.0000 * \exp(20.0000 * 1 + 8.0000 * m) + 32.0000 * \exp(20.0000 * 1 + -20.0000 * m) \\
& + 7.0000 * \exp(20.0000 * 1 + -14.0000 * m) + 9.0000 * \exp(20.0000 * 1 + -6.0000 * m) \\
& + 11.0000 * \exp(20.0000 * 1 + 4.0000 * m) + 28.0000 * \exp(20.0000 * 1 + 16.0000 * m) \\
& + 12.0000 * \exp(20.0000 * 1 + -30.0000 * m) + 5.0000 * \exp(20.0000 * 1 + -26.0000 * m) \\
& + 9.0000 * \exp(20.0000 * 1 + -12.0000 * m) + 13.0000 * \exp(20.0000 * 1 + 10.0000 * m) \\
& + 15.0000 * \exp(20.0000 * 1 + 24.0000 * m) + 1.0000 * \exp(20.0000 * 1 + -40.0000 * m) \\
& + 10.0000 * \exp(20.0000 * 1 + -38.0000 * m) + 5.0000 * \exp(20.0000 * 1 + -34.0000 * m) \\
& + 7.0000 * \exp(20.0000 * 1 + -28.0000 * m) + 13.0000 * \exp(20.0000 * 1 + 2.0000 * m) \\
& + 17.0000 * \exp(20.0000 * 1 + 32.0000 * m) + 3.0000 * \exp(20.0000 * 1 + -48.0000 * m) \\
& + 5.0000 * \exp(20.0000 * 1 + -44.0000 * m) + 13.0000 * \exp(20.0000 * 1 + -8.0000 * m) \\
& + 15.0000 * \exp(20.0000 * 1 + 6.0000 * m) + 17.0000 * \exp(20.0000 * 1 + 22.0000 * m) \\
& + 19.0000 * \exp(20.0000 * 1 + 40.0000 * m)
\end{aligned}$$

D.3 [Fe₃O(O₂CBu^t)₂(N₃)₃(dmem)₂ (4-4)



$$\chi_M = (c g^2)/T \text{ (Num/Den)}$$

$$m = J_a/k/T$$

$$n = J_b/k/T$$

$$\begin{aligned}
\text{Num} = & + 52.5000 \exp(8.7500 m + 0.0000 n) + 15.0000 \exp(1.7500 m + 2.0000 n) \\
& + 52.5000 \exp(6.7500 m + 2.0000 n) + 126.0000 \exp(13.7500 m + 2.0000 n) \\
& + 1.5000 \exp(-5.2500 m + 6.0000 n) + 15.0000 \exp(-2.2500 m + 6.0000 n) \\
& + 52.5000 \exp(2.7500 m + 6.0000 n) + 126.0000 \exp(9.7500 m + 6.0000 n) \\
& + 247.5000 \exp(18.7500 m + 6.0000 n) + 1.5000 \exp(-11.2500 m + 12.0000 n) \\
& + 15.0000 \exp(-8.2500 m + 12.0000 n) + 52.5000 \exp(-3.2500 m + 12.0000 n) \\
& + 126.0000 \exp(3.7500 m + 12.0000 n) + 247.5000 \exp(12.7500 m + 12.0000 n) \\
& + 429.0000 \exp(23.7500 m + 12.0000 n) + 15.0000 \exp(-16.2500 m + 20.0000 n) \\
& + 52.5000 \exp(-11.2500 m + 20.0000 n) + 126.0000 \exp(-4.2500 m + 20.0000 n)
\end{aligned}$$

$$\begin{aligned}
&+ 247.5000 \exp(4.7500 m+ 20.0000 n)+ 429.0000 \exp(15.7500 m+ 20.0000 n) \\
&+ 682.5000 \exp(28.7500 m+ 20.0000 n)+ 52.5000 \exp(-21.2500 m+ 30.0000 n) \\
&+ 126.0000 \exp(-14.2500 m+ 30.0000 n)+ 247.5000 \exp(-5.2500 m+ 30.0000 n) \\
&+ 429.0000 \exp(5.7500 m+ 30.0000 n)+ 682.5000 \exp(18.7500 m+ 30.0000 n) \\
&+ 1020.0000 \exp(33.7500 m+ 30.0000 n)
\end{aligned}$$

$$\begin{aligned}
\text{Den} = &+ 6.0000 \exp(8.7500 m+ 0.0000 n)+ 4.0000 \exp(1.7500 m+ 2.0000 n) \\
&+ 6.0000 \exp(6.7500 m+ 2.0000 n)+ 8.0000 \exp(13.7500 m+ 2.0000 n) \\
&+ 2.0000 \exp(-5.2500 m+ 6.0000 n)+ 4.0000 \exp(-2.2500 m+ 6.0000 n) \\
&+ 6.0000 \exp(2.7500 m+ 6.0000 n)+ 8.0000 \exp(9.7500 m+ 6.0000 n) \\
&+ 10.0000 \exp(18.7500 m+ 6.0000 n)+ 2.0000 \exp(-11.2500 m+ 12.0000 n) \\
&+ 4.0000 \exp(-8.2500 m+ 12.0000 n)+ 6.0000 \exp(-3.2500 m+ 12.0000 n) \\
&+ 8.0000 \exp(3.7500 m+ 12.0000 n)+ 10.0000 \exp(12.7500 m+ 12.0000 n) \\
&+ 12.0000 \exp(23.7500 m+ 12.0000 n)+ 4.0000 \exp(-16.2500 m+ 20.0000 n) \\
&+ 6.0000 \exp(-11.2500 m+ 20.0000 n)+ 8.0000 \exp(-4.2500 m+ 20.0000 n) \\
&+ 10.0000 \exp(4.7500 m+ 20.0000 n)+ 12.0000 \exp(15.7500 m+ 20.0000 n) \\
&+ 14.0000 \exp(28.7500 m+ 20.0000 n)+ 6.0000 \exp(-21.2500 m+ 30.0000 n) \\
&+ 8.0000 \exp(-14.2500 m+ 30.0000 n)+ 10.0000 \exp(-5.2500 m+ 30.0000 n) \\
&+ 12.0000 \exp(5.7500 m+ 30.0000 n)+ 14.0000 \exp(18.7500 m+ 30.0000 n) \\
&+ 16.0000 \exp(33.7500 m+ 30.0000 n)
\end{aligned}$$

LIST OF REFERENCES

- (1) Stohr, J.; Siegmann, H. C. *Magnetism: From Fundamentals to Nanoscale Dynamics*; Springer 2006; Vol. 152.
- (2) Jiles, D. *Introduction to Magnetism and Magnetic Materials*; Chapman & Hall: New York, 1991.
- (3) Huheey, J. E.; Keiter, E. A.; Keiter, R. L. *Inorganic Chemistry: Principles of Structure and Reactivity*; 4th ed.; HarperCollin College: New York, 1993.
- (4) Kahn, O. *Molecular Magnetism*; VCH: Weinheim, Germany, 1993.
- (5) Smart, L.; Moore, E. *Solid State Chemistry*; Chapman & Hall: New York, 1993.
- (6) Miller, J. S.; Epstein, A. J. *Angew. Chem. Int. Ed.* **1994**, *33*, 385.
- (7) Epstein, A. J. *MRS Bulletin* **2000**, *25*, 33.
- (8) Drago, R. S. *Physical Methods for Chemists*; 2nd ed.; Surfside Scientific Publishers, 1992.
- (9) Aromi, G.; Aubin, S. M. J.; Bolcar, M. A.; Christou, G.; Eppley, H. J.; Folting, K.; Hendrickson, D. N.; Huffman, J. C.; Squire, R. C.; Tsai, H. L.; Wang, S.; Wemple, M. W. *Polyhedron* **1998**, *17*, 3005.
- (10) Miller, J. S.; Epstein, A. J. *MRS Bulletin* **2000**, *25*, 21.
- (11) *Magnetism: A Supramolecular Function*; Kahn, O., Ed.; Kluwer: Dordrecht, 1996.
- (12) Lis, T. *Acta Crystallogr., Sect. B: Struct. Sci.* **1980**, *36*, 2042.
- (13) Christou, G.; Gatteschi, D.; Hendrickson, D. N.; Sessoli, R. *MRS Bulletin* **2000**, *25*, 66.
- (14) Chakov, N. E.; Lee, S. C.; Harter, A. G.; Kuhns, P. L.; Reyes, A. P.; Hill, S. O.; Dalal, N. S.; Wernsdorfer, W.; Abboud, K. A.; Christou, G. *J. Am. Chem. Soc.* **2006**, *128*, 6975.
- (15) Sessoli, R.; Gatteschi, D.; Caneschi, A.; Novak, M. A. *Nature* **1993**, *365*, 141.
- (16) Leuenberger, M. N.; Loss, D. *Nature* **2001**, *410*, 789.
- (17) Ritter, S. K. In *Chem. Eng. News* 2004; Vol. 82, p 29.
- (18) Chudnovsky, E. M. *Science* **1996**, *274*, 938.
- (19) Gatteschi, D.; Sessoli, R. *Angew. Chem. Int. Ed.* **2003**, *42*, 268.
- (20) Gatteschi, D.; Sessoli, R.; Cornia, A. *Chem. Commun.* **2000**, 725.

- (21) Christou, G. *Polyhedron* **2005**, *24*, 2065.
- (22) Aromi, G.; Brechin, E. K. *Struct. Bonding* **2006**, *122*, 1.
- (23) Benelli, C.; Gatteschi, D. *Chem. Rev.* **2002**, *102*, 2369.
- (24) Christou, G. *Acc. Chem. Res.* **1989**, *22*, 328.
- (25) Kurtz, D. M. *Chem. Rev.* **1990**, *90*, 585.
- (26) Bertini, I.; Gray, H. B.; Lippard, S. J.; Valentine, J. S. *Bioinorganic Chemistry*; University Science Books: Mill Valley, CA, 1994.
- (27) *Manganese Redox Enzymes*; Pecoraro, V. L., Ed.; VCH Publishers, Inc., 1992.
- (28) Wu, A. J.; Penner-Hahn, J. E.; Pecoraro, V. L. *Chem. Rev.* **2004**, *104*, 903.
- (29) Mukhopadhyay, S.; Mandal, S. K.; Bhaduri, S.; Armstrong, W. H. *Chem. Rev.* **2004**, *104*, 3981.
- (30) Gorun, S. M.; Papaefthymiou, G. C.; Frankel, R. B.; Lippard, S. J. *J. Am. Chem. Soc.* **1987**, *109*, 3337.
- (31) Taft, K. L.; Papaefthymiou, G. C.; Lippard, S. J. *Science* **1993**, *259*, 1302.
- (32) Brechin, E. K. *Chem. Commun.* **2005**, 5141.
- (33) Yachandra, V. K.; Sauer, K.; Klein, M. P. *Chem. Rev.* **1996**, *96*, 2927.
- (34) Stamatatos, T. C.; Abboud, K. A.; Wernsdorfer, W.; Christou, G. *Angew. Chem. Int. Ed.* **2007**, *46*, 884.
- (35) Ako, A. M.; Hewitt, I. J.; Mereacre, V.; Clerac, R.; Wernsdorfer, W.; Anson, C. E.; Powell, A. K. *Angew. Chem. Int. Ed.* **2006**, *45*, 4926.
- (36) Vincent, J. B.; Christmas, C.; Chang, H. R.; Li, Q. Y.; Boyd, P. D. W.; Huffman, J. C.; Hendrickson, D. N.; Christou, G. *J. Am. Chem. Soc.* **1989**, *111*, 2086.
- (37) Libby, E.; McCusker, J. K.; Schmitt, E. A.; Folting, K.; Hendrickson, D. N.; Christou, G. *Inorg. Chem.* **1991**, *30*, 3486.
- (38) Brechin, E. K.; Boskovic, C.; Wernsdorfer, W.; Yoo, J.; Yamaguchi, A.; Sanudo, E. C.; Concolino, T. R.; Rheingold, A. L.; Ishimoto, H.; Hendrickson, D. N.; Christou, G. *J. Am. Chem. Soc.* **2002**, *124*, 9710.

- (39) Bertocello, K.; Fallon, G. D.; Murray, K. S.; Tiekink, E. R. T. *Inorg. Chem.* **1991**, *30*, 3562.
- (40) Bonadies, J. A.; Kirk, M. L.; Lah, M. S.; Kessissoglou, D. P.; Hatfield, W. E.; Pecoraro, V. L. *Inorg. Chem.* **1989**, *28*, 2037.
- (41) Gelasco, A.; Pecoraro, V. L. *J. Am. Chem. Soc.* **1993**, *115*, 7928.
- (42) Mikuriya, M.; Yamato, Y.; Tokii, T. *Bull. Chem. Soc. Jpn.* **1992**, *65*, 1466.
- (43) Bagai, R.; Abboud, K. A.; Christou, G. *Dalton Trans.* **2006**, 3306.
- (44) Nishida, Y.; Kida, S. *J. Chem. Soc., Dalton Trans.* **1986**, 2633.
- (45) Vincent, J. B.; Chang, H. R.; Folting, K.; Huffman, J. C.; Christou, G.; Hendrickson, D. N. *J. Am. Chem. Soc.* **1987**, *109*, 5703.
- (46) SHELXTL6; Bruker-AXS:Madison, WI - 2000.
- (47) Schake, A. R.; Vincent, J. B.; Li, Q. Y.; Boyd, P. D. W.; Folting, K.; Huffman, J. C.; Hendrickson, D. N.; Christou, G. *Inorg. Chem.* **1989**, *28*, 1915.
- (48) Liu, W. T.; Thorp, H. H. *Inorg. Chem.* **1993**, *32*, 4102.
- (49) Palenik, G. J. *Inorg. Chem.* **1997**, *36*, 4888.
- (50) Kambe, K. *J. Phys. Soc. Jpn.* **1950**, *5*, 48.
- (51) VanVleck, J. H. *The Theory of Electrical and Magnetic Susceptibilities*; Oxford Press, London, 1932.
- (52) Aromi, G.; Bhaduri, S.; Artus, P.; Huffman, J. C.; Hendrickson, D. N.; Christou, G. *Polyhedron* **2002**, *21*, 1779.
- (53) Davidson, E. R. *MAGNET; Indiana University: Bloomington, IN.* **1999**.
- (54) Yoo, J.; Yamaguchi, A.; Nakano, M.; Krzystek, J.; Streib, W. E.; Brunel, L. C.; Ishimoto, H.; Christou, G.; Hendrickson, D. N. *Inorg. Chem.* **2001**, *40*, 4604.
- (55) Hendrickson, D. N.; Christou, G.; Schmitt, E. A.; Libby, E.; Bashkin, J. S.; Wang, S. Y.; Tsai, H. L.; Vincent, J. B.; Boyd, P. D. W.; Huffman, J. C.; Folting, K.; Li, Q. Y.; Streib, W. E. *J. Am. Chem. Soc.* **1992**, *114*, 2455.
- (56) Aliaga-Alcalde, N.; Edwards, R. S.; Hill, S. O.; Wernsdorfer, W.; Folting, K.; Christou, G. *J. Am. Chem. Soc.* **2004**, *126*, 12503.

- (57) Brockman, J. T.; Huffman, J. C.; Christou, G. *Angew. Chem. Int. Ed.* **2002**, *41*, 2506.
- (58) Boudalis, A. K.; Donnadieu, B.; Nastopoulos, V.; Clemente-Juan, J. M.; Mari, A.; Sanakis, Y.; Tuchagues, J. P.; Perlepes, S. P. *Angew. Chem. Int. Ed.* **2004**, *43*, 2266.
- (59) Papaefstathiou, G. S.; Perlepes, S. P.; Escuer, A.; Vicente, R.; Font-Bardia, M.; Solans, X. *Angew. Chem. Int. Ed.* **2001**, *40*, 884.
- (60) Papaefstathiou, G. S.; Escuer, A.; Vicente, R.; Font-Bardia, M.; Solans, X.; Perlepes, S. P. *Chem. Commun.* **2001**, 2414.
- (61) Stamatatos, T. C.; Foguet-Albiol, D.; Lee, S. C.; Stoumpos, C. C.; Raptopoulou, C. P.; Terzis, A.; Wernsdorfer, W.; Hill, S. O.; Perlepes, S. P.; Christou, G. *J. Am. Chem. Soc.* **2007**, *129*, 9484.
- (62) Murugesu, M.; Habrych, M.; Wernsdorfer, W.; Abboud, K. A.; Christou, G. *J. Am. Chem. Soc.* **2004**, *126*, 4766.
- (63) Stamatatos, T. C.; Abboud, K. A.; Wernsdorfer, W.; Christou, G. *Angew. Chem. Int. Ed.* **2006**, *45*, 4134.
- (64) Brechin, E. K.; Yoo, J.; Nakano, M.; Huffman, J. C.; Hendrickson, D. N.; Christou, G. *Chem. Commun.* **1999**, 783.
- (65) Yoo, J.; Brechin, E. K.; Yamaguchi, A.; Nakano, M.; Huffman, J. C.; Maniero, A. L.; Brunel, L. C.; Awaga, K.; Ishimoto, H.; Christou, G.; Hendrickson, D. N. *Inorg. Chem.* **2000**, *39*, 3615.
- (66) Brechin, E. K.; Soler, M.; Davidson, J.; Hendrickson, D. N.; Parsons, S.; Christou, G. *Chem. Commun.* **2002**, 2252.
- (67) Brechin, E. K.; Soler, M.; Christou, G.; Helliwell, M.; Teat, S. J.; Wernsdorfer, W. *Chem. Commun.* **2003**, 1276.
- (68) Vandersluis, P.; Spek, A. L. *Acta Crystallogr.; Sect. A* **1990**, *46*, 194.
- (69) Sanudo, E. C.; Wernsdorfer, W.; Abboud, K. A.; Christou, G. *Inorg. Chem.* **2004**, *43*, 4137.
- (70) Boskovic, C.; Wernsdorfer, W.; Folting, K.; Huffman, J. C.; Hendrickson, D. N.; Christou, G. *Inorg. Chem.* **2002**, *41*, 5107.
- (71) Davidson, E. R. *GRID; Indiana University: Bloomington, IN.* **1999**.
- (72) Goodwin, J. C.; Sessoli, R.; Gatteschi, D.; Wernsdorfer, W.; Powell, A. K.; Heath, S. L. *J. Chem. Soc., Dalton Trans.* **2000**, 1835.

- (73) Gorun, S. M.; Papaefthymiou, G. C.; Frankel, R. B.; Lippard, S. J. *J. Am. Chem. Soc.* **1987**, *109*, 4244.
- (74) Jones, L. F.; Brechin, E. K.; Collison, D.; Helliwell, M.; Mallah, T.; Piligkos, S.; Rajaraman, G.; Wernsdorfer, W. *Inorg. Chem.* **2003**, *42*, 6601.
- (75) Powell, A. K.; Heath, S. L.; Gatteschi, D.; Pardi, L.; Sessoli, R.; Spina, G.; Del Giallo, F.; Pieralli, F. *J. Am. Chem. Soc.* **1995**, *117*, 2491.
- (76) Canada-Vilalta, C.; O'Brien, T. A.; Brechin, E. K.; Pink, M.; Davidson, E. R.; Christou, G. *Inorg. Chem.* **2004**, *43*, 5505.
- (77) McCusker, J. K.; Vincent, J. B.; Schmitt, E. A.; Mino, M. L.; Shin, K.; Coggin, D. K.; Hagen, P. M.; Huffman, J. C.; Christou, G.; Hendrickson, D. N. *J. Am. Chem. Soc.* **1991**, *113*, 3012.
- (78) Kahn, O. *Chem. Phys. Lett.* **1997**, *265*, 109.
- (79) Barra, A. L.; Caneschi, A.; Cornia, A.; de Biani, F. F.; Gatteschi, D.; Sangregorio, C.; Sessoli, R.; Sorace, L. *J. Am. Chem. Soc.* **1999**, *121*, 5302.
- (80) Powell, G. W.; Lancashire, H. N.; Brechin, E. K.; Collison, D.; Heath, S. L.; Mallah, T.; Wernsdorfer, W. *Angew. Chem. Int. Ed.* **2004**, *43*, 5772.
- (81) Delfs, C.; Gatteschi, D.; Pardi, L.; Sessoli, R.; Wieghardt, K.; Hanke, D. *Inorg. Chem.* **1993**, *32*, 3099.
- (82) Sangregorio, C.; Ohm, T.; Paulsen, C.; Sessoli, R.; Gatteschi, D. *Phys. Rev. Lett.* **1997**, *78*, 4645.
- (83) Caneschi, A.; Cornia, A.; Lippard, S. J. *Angew. Chem. Int. Ed.* **1995**, *34*, 467.
- (84) Murugesu, M.; Abboud, K. A.; Christou, G. *Dalton Trans.* **2003**, 4552.
- (85) Jones, L. F.; Batsanov, A.; Brechin, E. K.; Collison, D.; Helliwell, M.; Mallah, T.; McInnes, E. J. L.; Piligkos, S. *Angew. Chem. Int. Ed.* **2002**, *41*, 4318.
- (86) Moragues-Canovas, M.; Riviere, P.; Ricard, L.; Paulsen, C.; Wernsdorfer, W.; Rajaraman, G.; Brechin, E. K.; Mallah, T. *Adv. Mater.* **2004**, *16*, 1101.
- (87) Foguet-Albiol, D.; Abboud, K. A.; Christou, G. *Chem. Commun.* **2005**, 4282.
- (88) Saalfrank, R. W.; Bernt, I.; Uller, E.; Hampel, F. *Angew. Chem. Int. Ed.* **1997**, *36*, 2482.
- (89) King, P.; Stamatatos, T. C.; Abboud, K. A.; Christou, G. *Angew. Chem. Int. Ed.* **2006**, *45*, 7379.

- (90) Ammala, P.; Cashion, J. D.; Kepert, C. M.; Moubaraki, B.; Murray, K. S.; Spiccia, L.; West, B. O. *Angew. Chem. Int. Ed.* **2000**, *39*, 1688.
- (91) Murugesu, M.; Abboud, K. A.; Christou, G. *Polyhedron* **2004**, *23*, 2779.
- (92) Taft, K. L.; Lippard, S. J. *J. Am. Chem. Soc.* **1990**, *112*, 9629.
- (93) Bagai, R.; Datta, S.; Betancur-Rodriguez, A.; Abboud, K. A.; Hill, S.; Christou, G. *Inorg. Chem.* **2007**, *46*, 4535.
- (94) Duncan, J. F.; Kanekar, C. R.; Mok, K. F. *J. Chem. Soc. A* **1969**, 480.
- (95) Earnshaw, A.; Figgis, B. N.; Lewis, J. *J. Chem. Soc. A* **1966**, 1656.
- (96) Bond, A. M.; Clark, R. J. H.; Humphrey, D. G.; Panayiotopoulos, P.; Skelton, B. W.; White, A. H. *J. Chem. Soc., Dalton Trans.* **1998**, 1845 and references there in.
- (97) Armstrong, W. H.; Lippard, S. J. *Inorg. Chem.* **1985**, *24*, 981.
- (98) Tolis, E. I.; Helliwell, M.; Langley, S.; Raftery, J.; Winpenny, R. E. P. *Angew. Chem. Int. Ed.* **2003**, *42*, 3804.
- (99) Yao, H. C.; Li, Y. Z.; Zheng, L. M.; Xin, X. Q. *Inorg. Chim. Acta* **2005**, *358*, 2523.
- (100) Datta, S.; Betancur-Rodriguez, A.; Lee, S. C.; Hill, S.; Foguet-Albiol, D.; Bagai, R.; Christou, G. *Polyhedron* **2007**, *26*, 2243.
- (101) Jones, L. F.; Jensen, P.; Moubaraki, B.; Berry, K. J.; Boas, J. F.; Pilbrow, J. R.; Murray, K. S. *J. Mater. Chem.* **2006**, *16*, 2690.
- (102) Ako, A. M.; Waldmann, O.; Mereacre, V.; Klower, F.; Hewitt, I. J.; Anson, C. E.; Gudel, H. U.; Powell, A. K. *Inorg. Chem.* **2007**, *46*, 756.
- (103) Brown, I. D.; Wu, K. K. *Acta Crystallogr., Sect. B: Struct. Sci.* **1976**, *32*, 1957.
- (104) Taguchi, T.; Stamatatos, T. C.; Abboud, K. A.; Jones, C. M.; O'Brien, T. A.; Christou, G. *Inorg. Chem.* **2007**, In Press and references there in.
- (105) Nair, V. S.; Hagen, K. S. *Inorg. Chem.* **1992**, *31*, 4048.
- (106) Ammala, P. S.; Batten, S. R.; Cashion, J. D.; Kepert, C. M.; Moubaraki, B.; Murray, K. S.; Spiccia, L.; West, B. O. *Inorg. Chim. Acta* **2002**, *331*, 90.
- (107) Cotton, F. A.; Wilkinson, G. *Advanced Inorganic Chemistry*; Wiley: New York, 1980.
- (108) Gorun, S. M.; Lippard, S. J. *J. Am. Chem. Soc.* **1985**, *107*, 4568.

- (109) Wemple, M. W.; Coggin, D. K.; Vincent, J. B.; McCusker, J. K.; Streib, W. E.; Huffman, J. C.; Hendrickson, D. N.; Christou, G. *J. Chem. Soc., Dalton Trans.* **1998**, 719.
- (110) Boudalis, A. K.; Tangoulis, V.; Raptopoulou, C. P.; Terzis, A.; Tuchagues, J. P.; Perlepes, S. P. *Inorg. Chim. Acta* **2004**, 357, 1345.
- (111) Boudalis, A. K.; Lalioti, N.; Spyroulias, G. A.; Raptopoulou, C. P.; Terzis, A.; Bousseksou, A.; Tangoulis, V.; Tuchagues, J. P.; Perlepes, S. P. *Inorg. Chem.* **2002**, 41, 6474.
- (112) Gorun, S. M.; Lippard, S. J. *Inorg. Chem.* **1991**, 30, 1625.
- (113) Dziobkowski, C. T.; Wroblewski, J. T.; Brown, D. B. *Inorg. Chem.* **1981**, 20, 671.
- (114) Armstrong, W. H.; Lippard, S. J. *J. Am. Chem. Soc.* **1983**, 105, 4837.
- (115) Armstrong, W. H.; Spool, A.; Papaefthymiou, G. C.; Frankel, R. B.; Lippard, S. J. *J. Am. Chem. Soc.* **1984**, 106, 3653.
- (116) Armstrong, W. H.; Lippard, S. J. *J. Am. Chem. Soc.* **1985**, 107, 3730.
- (117) Lee, S. C.; Stamatatos, T. C.; Hill, S.; Perlepes, S. P.; Christou, G. *Polyhedron* **2007**, 26, 2225.
- (118) Oshio, H.; Hoshino, N.; Ito, T.; Nakano, M. *J. Am. Chem. Soc.* **2004**, 126, 8805.
- (119) Benelli, C.; Parsons, S.; Solan, G. A.; Winpenny, R. E. P. *Angew. Chem. Int. Ed.* **1996**, 35, 1825.
- (120) Barra, A. L.; Gatteschi, D.; Sessoli, R. *Chem. Eur. J.* **2000**, 6, 1608.
- (121) Bacsa, J.; Zhao, H.; Dunbar, K. R. *Acta Crystallogr. Sect. C* **2003**, C59, m561.
- (122) Canada-Vilalta, C.; O'Brien Ted, A.; Pink, M.; Davidson Ernest, R.; Christou, G. *Inorg. Chem.* **2003**, 42, 7819.
- (123) Yan, B.; Chen, Z. D. *Inorg. Chem. Commun.* **2001**, 4, 138.
- (124) Seddon, E. J.; Huffman, J. C.; Christou, G. *Dalton* **2000**, 4446.
- (125) Brechin, E. K.; Knapp, M. J.; Huffman, J. C.; Hendrickson, D. N.; Christou, G. *Inorg. Chim. Acta* **2000**, 297, 389.
- (126) Christmas, C. A.; Tsai, H. L.; Pardi, L.; Kesselman, J. M.; Gantzel, P. K.; Chadha, R. K.; Gatteschi, D.; Harvey, D. F.; Hendrickson, D. N. *J. Am. Chem. Soc.* **1993**, 115, 12483.
- (127) Bagai, R.; Abboud, K. A.; Christou, G. *Inorg. Chem.* **2007**, 46, 5567.

- (128) Demnitz, F. W. J.; D'Henri, M. B. *Org. Prep. Proced. Int.* **1998**, *30*, 467.
- (129) Heirtzler, F. R. *Synlett* **1999**, 1203.
- (130) Norrby, T.; Borje, A.; Zhang, L.; Akermark, B. *Acta Chem. Scand.* **1998**, *52*, 77.
- (131) Brown, I. D.; Altermatt, D. *Acta Crystallogr., Sect. B: Struct. Sci.* **1985**, *B41*, 244.
- (132) Tabernor, J.; Jones, L. F.; Heath, S. L.; Muryn, C.; Aromi, G.; Ribas, J.; Brechin, E. K.; Collison, D. *Dalton Trans.* **2004**, 975.
- (133) Boskovic, C.; Sieber, A.; Chaboussant, G.; Guedel, H. U.; Ensling, J.; Wernsdorfer, W.; Neels, A.; Labat, G.; Stoeckli-Evans, H.; Janssen, S. *Inorg. Chem.* **2004**, *43*, 5053.
- (134) Boskovic, C.; Labat, G.; Neels, A.; Gudel, H. U. *Dalton Trans.* **2003**, 3671.
- (135) Lachicotte, R. J.; Hagen, K. S. *Inorg. Chim. Acta* **1997**, *263*, 407.
- (136) Reynolds, R. A.; Coucouvanis, D. *Inorg. Chem.* **1998**, *37*, 170.
- (137) O'Keefe, B. J.; Monnier, S. M.; Hillmyer, M. A.; Tolman, W. B. *J. Am. Chem. Soc.* **2001**, *123*, 339.
- (138) Mikuriya, M.; Nakadera, K. *Chem. Lett.* **1995**, 213.
- (139) Mikuriya, M.; Hashimoto, Y.; Nakashima, S. *Chem. Commun.* **1996**, 295.
- (140) Herold, S.; Lippard, S. J. *Inorg. Chem.* **1997**, *36*, 50.
- (141) Krishnamurthy, D.; Sarjeant, A. N.; Goldberg, D. P.; Caneschi, A.; Totti, F.; Zakharov, L. N.; Rheingold, A. L. *Chem. Eur. J.* **2005**, *11*, 7328.
- (142) Overgaard, J.; Hibbs, D. E.; Rentschler, E.; Timco, G. A.; Larsen, F. K. *Inorg. Chem.* **2003**, *42*, 7593.
- (143) Chaudhuri, P.; Rentschler, E.; Birkelbach, F.; Krebs, C.; Bill, E.; Weyhermuller, T.; Florke, U. *Eur. J. Inorg. Chem.* **2003**, 541.
- (144) Taft, K. L.; Papaefthymiou, G. C.; Lippard, S. J. *Inorg. Chem.* **1994**, *33*, 1510.
- (145) Bagai, R.; Abboud, K. A.; Christou, G. *Chem. Commun.* **2007**, 3359.
- (146) Bagai, R.; Wernsdorfer, W.; Abboud, K. A.; Christou, G. *J. Am. Chem. Soc.* **2007**, *129*, 12918.

- (147) Affronte, M.; Carretta, S.; Timco, G. A.; Winpenny, R. E. P. *Chem. Commun.* **2007**, 1789.
- (148) Watton, S. P.; Fuhrmann, P.; Pence, L. E.; Caneschi, A.; Cornia, A.; Abbati, G. L.; Lippard, S. J. *Angew. Chem. Int. Ed.* **1997**, *36*, 2774.
- (149) Schmitt, W.; Anson, C. E.; Wernsdorfer, W.; Powell, A. K. *Chem. Commun.* **2005**, 2098.
- (150) Jones, L. F.; Low, D. M.; Helliwell, M.; Raftery, J.; Collison, D.; Aromi, G.; Cano, J.; Mallah, T.; Wernsdorfer, W.; Brechin, E. K.; McInnes, E. J. L. *Polyhedron* **2006**, *25*, 325.
- (151) Yao, H. C.; Wang, J. J.; Ma, Y. S.; Waldmann, O.; Du, W. X.; Song, Y.; Li, Y. Z.; Zheng, L. M.; Decurtins, S.; Xin, X. Q. *Chem. Commun.* **2006**, 1745.
- (152) Bino, A.; Shweky, I.; Cohen, S.; Bauminger, E. R.; Lippard, S. J. *Inorg. Chem.* **1998**, *37*, 5168.
- (153) Wernsdorfer, W. *Adv. Chem. Phys.* **2001**, *118*, 99.
- (154) Wernsdorfer, W.; Aliaga-Alcalde, N.; Hendrickson, D. N.; Christou, G. *Nature* **2002**, *416*, 406.
- (155) Tiron, R.; Wernsdorfer, W.; Aliaga-Alcalde, N.; Christou, G. *Phys. Rev. B* **2003**, *68*, 140407.
- (156) Hill, S.; Edwards, R. S.; Aliaga-Alcalde, N.; Christou, G. *Science* **2003**, *302*, 1015.
- (157) Tiron, R.; Wernsdorfer, W.; Foguet-Albiol, D.; Aliaga-Alcalde, N.; Christou, G. *Phys. Rev. Lett.* **2003**, *91*, 227203.
- (158) Sun, Z. M.; Grant, C. M.; Castro, S. L.; Hendrickson, D. N.; Christou, G. *Chem. Commun.* **1998**, 721.
- (159) Yang, E. C.; Hendrickson, D. N.; Wernsdorfer, W.; Nakano, M.; Zakharov, L. N.; Sommer, R. D.; Rheingold, A. L.; Ledezma-Gairaud, M.; Christou, G. *J. Appl. Phys.* **2002**, *91*, 7382.
- (160) Andres, H.; Basler, R.; Blake, A. J.; Cadiou, C.; Chaboussant, G.; Grant, C. M.; Gudel, H. U.; Murrie, M.; Parsons, S.; Paulsen, C.; Semadini, F.; Villar, V.; Wernsdorfer, W.; Winpenny, R. E. P. *Chem. Eur. J.* **2002**, *8*, 4867.
- (161) Aubin, S. M. J.; Wemple, M. W.; Adams, D. M.; Tsai, H. L.; Christou, G.; Hendrickson, D. N. *J. Am. Chem. Soc.* **1996**, *118*, 7746.
- (162) Dendrinou-Samara, C.; Alexiou, M.; Zaleski, C. M.; Kampf, J. W.; Kirk, M. L.; Kessissoglou, D. P.; Pecoraro, V. L. *Angew. Chem. Int. Ed.* **2003**, *42*, 3763.

- (163) Milios, C. J.; Raptopoulou, C. P.; Terzis, A.; Lloret, F.; Vicente, R.; Perlepes, S. P.; Escuer, A. *Angew. Chem. Int. Ed.* **2004**, *43*, 210.
- (164) Miyasaka, H.; Clerac, R.; Wernsdorfer, W.; Lecren, L.; Bonhomme, C.; Sugiura, K.; Yamashita, M. *Angew. Chem. Int. Ed.* **2004**, *43*, 2801.
- (165) Hundal, G.; Hundal, M. S.; Obrai, S.; Poonia, N. S.; Kumar, S. *Inorg. Chem.* **2002**, *41*, 2077.
- (166) Plass, W. *Eur. J. Inorg. Chem.* **1998**, 799.
- (167) de Sousa, A. S.; Fernandes, M. A. *Polyhedron* **2002**, *21*, 1883.
- (168) Bagai, R.; Abboud, K. A.; Christou, G. *Inorg. Chem.* **2007**, In Press.
- (169) Bagai, R.; Daniels, M. R.; Abboud, K. A.; Christou, G. *Inorg. Chem.*, **2008**, In Press.
- (170) Wu, R. W.; Poyraz, M.; Sowrey, F. E.; Anson, C. E.; Wocadlo, S.; Powell, A. K.; Jayasooriya, U. A.; Cannon, R. D.; Nakamoto, T.; Katada, M.; Sano, H. *Inorg. Chem.* **1998**, *37*, 1913.
- (171) Milios, C. J.; Vinslava, A.; Wernsdorfer, W.; Prescimone, A.; Wood, P. A.; Parsons, S.; Perlepes, S. P.; Christou, G.; Brechin, E. K. *J. Am. Chem. Soc.* **2007**, *129*, 6547.
- (172) Tasiopoulos, A. J.; Vinslava, A.; Wernsdorfer, W.; Abboud, K. A.; Christou, G. *Angew. Chem. Int. Ed.* **2004**, *43*, 2117.
- (173) Maheswaran, S.; Chastanet, G.; Teat, S. J.; Mallah, T.; Sessoli, R.; Wernsdorfer, W.; Winpenny, R. E. P. *Angew. Chem. Int. Ed.* **2005**, *44*, 5044.
- (174) Godbole, M. D.; Roubeau, O.; Clerac, R.; Kooijman, H.; Spek, A. L.; Bouwman, E. *Chem. Commun.* **2005**, 3715.
- (175) Rajaraman, G.; Murugesu, M.; Sanudo, E. C.; Soler, M.; Wernsdorfer, W.; Helliwell, M.; Murn, C.; Raftery, J.; Teat, S. J.; Christou, G.; Brechin, E. K. *J. Am. Chem. Soc.* **2004**, *126*, 15445.
- (176) Murugesu, M.; Wernsdorfer, F.; Abboud, K. A.; Christou, G. *Angew. Chem. Int. Ed.* **2005**, *44*, 892.
- (177) Brechin, E. K.; Christou, G.; Soler, M.; Helliwell, M.; Teat, S. J. *Dalton Trans.* **2003**, 513.
- (178) Jones, L. F.; Brechin, E. K.; Collison, D.; Raftery, J.; Teat, S. J. *Inorg. Chem.* **2003**, *42*, 6971.

- (179) Tsai, H. L.; Wang, S. Y.; Folting, K.; Streib, W. E.; Hendrickson, D. N.; Christou, G. *J. Am. Chem. Soc.* **1995**, *117*, 2503.
- (180) Tanase, S.; Aromi, G.; Bouwman, E.; Kooijman, H.; Spek, A. L.; Reedijk, J. *Chem. Commun.* **2005**, 3147.
- (181) Milios, C. J.; Kefalloniti, E.; Raptopoulou, C. P.; Terzis, A.; Vicente, R.; Lalioti, N.; Escuer, A.; Perlepes, S. P. *Chem. Commun.* **2003**, 819.
- (182) Alvarez, C. S.; Bond, A. D.; Cave, D.; Mosquera, M. E. G.; Harron, E. A.; Layfield, R. A.; McPartlin, M.; Rawson, J. M.; Wood, P. T.; Wright, D. S. *Chem. Commun.* **2002**, 2980.
- (183) Boskovic, C.; Huffman, J. C.; Christou, G. *Chem. Commun.* **2002**, 2502.
- (184) Saalfrank, R. W.; Low, N.; Demleitner, B.; Stalke, D.; Teichert, M. *Chem. Eur. J.* **1998**, *4*, 1305.
- (185) Wemple, M. W.; Tsai, H. L.; Wang, S. Y.; Claude, J. P.; Streib, W. E.; Huffman, J. C.; Hendrickson, D. N.; Christou, G. *Inorg. Chem.* **1996**, *35*, 6437.
- (186) Tasiopoulos, A. J.; Abboud, K. A.; Christou, G. *Chem. Commun.* **2003**, 580.
- (187) Milios, C. J.; Fabbiani, F. P. A.; Parsons, S.; Murugesu, M.; Christou, G.; Brechin, E. K. *Dalton Trans.* **2006**, 351.
- (188) Saalfrank, R. W.; Low, N.; Trummer, S.; Sheldrick, G. M.; Teichert, M.; Stalke, D. *Eur. J. Inorg. Chem.* **1998**, 559.
- (189) Murugesu, M.; Wernsdorfer, W.; Abboud, K. A.; Brechin, E. K.; Christou, G. *Dalton Trans.* **2006**, 2285.
- (190) Li, Y. G.; Wernsdorfer, W.; Clerac, R.; Hewitt, I. J.; Anson, C. E.; Powell, A. K. *Inorg. Chem.* **2006**, *45*, 2376.
- (191) Masello, A.; Murugesu, M.; Abboud, K. A.; Christou, G. *Polyhedron* **2007**, *26*, 2276.
- (192) Lampropoulos, C.; Murugesu, M.; Abboud, K. A.; Christou, G. *Polyhedron* **2007**, *26*, 2129.
- (193) Sun, Z. M.; Gantzel, P. K.; Hendrickson, D. N. *Inorg. Chem.* **1996**, *35*, 6640.
- (194) Caneschi, A.; Ferraro, F.; Gatteschi, D.; Melandri, M. C.; Rey, P.; Sessoli, R. *Angew. Chem. Int. Ed.* **1989**, *28*, 1365.
- (195) Yu, S. B.; Lippard, S. J.; Shweky, I.; Bino, A. *Inorg. Chem.* **1992**, *31*, 3502.

- (196) Ye, B. H.; Mak, T.; Williams, I. D.; Li, X. Y. *Chem. Commun.* **1997**, 1813.
- (197) Coucouvanis, D.; Reynolds, R. A.; Dunham, W. R. *J. Am. Chem. Soc.* **1995**, *117*, 7570.
- (198) Cheng, B. S.; Fries, P. H.; Marchon, J. C.; Scheidt, W. R. *Inorg. Chem.* **1996**, *35*, 1024.
- (199) Komatsuzaki, H.; Ichikawa, S.; Hikichi, S.; Akita, M.; Moro-oka, Y. *Inorg. Chem.* **1998**, *37*, 3652.
- (200) Biswas, S.; Mitra, K.; Adhikary, B.; Lucas, C. R. *Transition Met. Chem.* **2005**, *30*, 586.
- (201) Zhou, A. J.; Qin, L. J.; Beedle, C. C.; Ding, S.; Nakano, M.; Leng, J. D.; Tong, M. L.; Hendrickson, D. N. *Inorg. Chem.* **2007**, *46*, 8111.
- (202) Eppley, H. J.; Tsai, H. L.; Devries, N.; Folting, K.; Christou, G.; Hendrickson, D. N. *J. Am. Chem. Soc.* **1995**, *117*, 301.
- (203) Soler, M.; Wernsdorfer, W.; Abboud, K. A.; Huffman, J. C.; Davidson, E. R.; Hendrickson, D. N.; Christou, G. *J. Am. Chem. Soc.* **2003**, *125*, 3576.
- (204) Bian, G. Q.; Kuroda-Sowa, T.; Konaka, H.; Hatano, M.; Maekawa, M.; Munakata, M.; Miyasaka, H.; Yamashita, M. *Inorg. Chem.* **2004**, *43*, 4790.
- (205) Zhao, H. H.; Berlinguette, C. P.; Bacsá, J.; Prosvirin, A. V.; Bera, J. K.; Tichy, S. E.; Schelter, E. J.; Dunbar, K. R. *Inorg. Chem.* **2004**, *43*, 1359.
- (206) Coronado, E.; Torment-Aliaga, A.; Gaita-Arino, A.; Gimenez-Saiz, C.; Romero, F. M.; Wernsdorfer, W. *Angew. Chem. Int. Ed.* **2004**, *43*, 6152.
- (207) Bagai, R.; Christou, G. *Inorg. Chem.* **2007**, *46*, 10810.
- (208) Tasiopoulos, A. J.; Wernsdorfer, W.; Abboud, K. A.; Christou, G. *Inorg. Chem.* **2005**, *44*, 6324.
- (209) King, P.; Wernsdorfer, W.; Abboud, K. A.; Christou, G. *Inorg. Chem.* **2005**, *44*, 8659.
- (210) Foguet-Albiol, D.; O'Brien, T. A.; Wernsdorfer, W.; Moulton, B.; Zaworotko, M. J.; Abboud, K. A.; Christou, G. *Angew. Chem. Int. Ed.* **2005**, *44*, 897.
- (211) Boskovic, C.; Brechin, E. K.; Streib, W. E.; Folting, K.; Hendrickson, D. N.; Christou, G. *Chem. Commun.* **2001**, 467.
- (212) Boskovic, C.; Brechin, E. K.; Streib, W. E.; Folting, K.; Bollinger, J. C.; Hendrickson, D. N.; Christou, G. *J. Am. Chem. Soc.* **2002**, *124*, 3725.

- (213) Rumberger, E. M.; Shah, S. J.; Beedle, C. C.; Zakharov, L. N.; Rheingold, A. L.; Hendrickson, D. N. *Inorg. Chem.* **2005**, *44*, 2742.
- (214) Yao, H. C.; Li, Y. Z.; Song, Y.; Ma, Y. S.; Zheng, L. M.; Xin, X. Q. *Inorg. Chem.* **2006**, *45*, 59.
- (215) Dendrinou-Samara, C.; Zaleski, C. M.; Evagorou, A.; Kampf, J. W.; Pecoraro, V. L.; Kessissoglou, D. P. *Chem. Commun.* **2003**, 2668.
- (216) Cavaluzzo, M.; Chen, Q.; Zubieta, J. *Chem. Commun.* **1993**, 131.
- (217) Koo, B. K.; Lee, U. *Bull. Korean Chem. Soc.* **2001**, *22*, 103.
- (218) Brechin, E. K.; Clegg, W.; Murrie, M.; Parsons, S.; Teat, S. J.; Winpenny, R. E. P. *J. Am. Chem. Soc.* **1998**, *120*, 7365.
- (219) Abu-Nawwas, A. A. H.; Cano, J.; Christian, P.; Mallah, T.; Rajaraman, G.; Teat, S. J.; Winpenny, R. E. P.; Yukawa, Y. *Chem. Commun.* **2004**, 314.
- (220) Sellmann, D.; Geipel, F.; Heinemann, F. W. *Chem. Eur. J.* **2002**, *8*, 958.
- (221) Caneschi, A.; Cornia, A.; Fabretti, A. C.; Gatteschi, D. *Angew. Chem. Int. Ed.* **1999**, *38*, 1295.
- (222) Boskovic, C.; Gudel, H. U.; Labat, G.; Neels, A.; Wernsdorfer, W.; Moubaraki, B.; Murray, K. S. *Inorg. Chem.* **2005**, *44*, 3181.
- (223) Soler, M.; Wernsdorfer, W.; Foltling, K.; Pink, M.; Christou, G. *J. Am. Chem. Soc.* **2004**, *126*, 2156.
- (224) Brechin, E. K.; Sanudo, E. C.; Wernsdorfer, W.; Boskovic, C.; Yoo, J.; Hendrickson, D. N.; Yamaguchi, A.; Ishimoto, H.; Concolino, T. E.; Rheingold, A. L.; Christou, G. *Inorg. Chem.* **2005**, *44*, 502.
- (225) Weihe, H.; Gudel, H. U. *J. Am. Chem. Soc.* **1997**, *119*, 6539.
- (226) Werner, R.; Ostrovsky, S.; Griesar, K.; Haase, W. *Inorg. Chim. Acta* **2001**, *326*, 78.
- (227) Bogani, L.; Wernsdorfer, W. *Nature Mat.* **2008**, *7*, 179.
- (228) Oshio, H.; Nihei, M.; Yoshida, A.; Nojiri, H.; Nakano, M.; Yamaguchi, A.; Karki, Y.; Ishimoto, H. *Chem. Eur. J.* **2005**, *11*, 843.
- (229) Li, Y. G.; Wernsdorfer, W.; Clerac, R.; Hewitt, I. J.; Anson, C. E.; Powell, A. K. *Inorg. Chem.* **2006**, *45*, 2376-2378.

- (230) Maheswaran, S.; Chastanet, G.; Teat, S. J.; Mallah, T.; Sessoli, R.; Wernsdorfer, W.; Winpenny, R. E. P. *Angew. Chem. Int. Ed.* **2005**, *44*, 5044-5048.
- (231) Beltran, L. M. C.; Long, J. R. *Acc. Chem. Res.* **2005**, *38*, 325.
- (232) Oshio, H.; Nakano, M. *Chem. Eur. J.* **2005**, *11*, 5178.
- (233) Hamamatsu, T.; Yabe, K.; Towatari, M.; Osa, S.; Matsumoto, N.; Re, N.; Pochaba, A.; Mrozinski, J.; Gallani, J. L.; Barla, A.; Imperia, P.; Paulsen, C.; Kappler, J. P. *Inorg. Chem.* **2007**, *46*, 4458-4468.
- (234) Zaleski, C. M.; Kampf, J. W.; Mallah, T.; Kirk, M. L.; Pecoraro, V. L. *Inorg. Chem.* **2007**, *46*, 1954-1956.
- (235) Li, D. F.; Clerac, R.; Wang, G. B.; Yee, G. T.; Holmes, S. M. *Eur. J. Inorg. Chem.* **2007**, 1341.
- (236) Pointillart, F.; Bernot, K.; Sessoli, R.; Gatteschi, D. *Chem. Eur. J.* **2007**, *13*, 1602.
- (237) Mori, F.; Nyui, T.; Ishida, T.; Nogami, T.; Choi, K. Y.; Nojiri, H. *J. Am. Chem. Soc.* **2006**, *128*, 1440-1441.
- (238) Costes, J. P.; Auchel, M.; Dahan, F.; Peyrou, V.; Shova, S.; Wernsdorfer, W. *Inorg. Chem.* **2006**, *45*, 1924-1934.
- (239) Mishra, A.; Wernsdorfer, W.; Abboud, K. A.; Christou, G. *J. Am. Chem. Soc.* **2004**, *126*, 15648.
- (240) Mishra, A.; Wernsdorfer, W.; Parsons, S.; Christou, G.; Brechin, E. K. *Chem. Commun.* **2005**, 2086.
- (241) Zaleski, C. M.; Depperman, E. C.; Kampf, J. W.; Kirk, M. L.; Pecoraro, V. L. *Angew. Chem. Int. Ed.* **2004**, *43*, 3912.
- (242) Ma, B. Q.; Gao, S.; Su, G.; Xu, G. X. *Angew. Chem. Int. Ed.* **2001**, *40*, 434.
- (243) Ferbinteanu, M.; Kajiwara, T.; Choi, K. Y.; Nojiri, H.; Nakamoto, A.; Kojima, N.; Cimpoesu, F.; Fujimura, Y.; Takaishi, S.; Yamashita, M. *J. Am. Chem. Soc.* **2006**, *128*, 9008.
- (244) Zaleski, C. M.; Depperman, E. C.; Kampf, J. W.; Kirk, M. L.; Pecoraro, V. L. *Inorg. Chem.* **2006**, *45*, 10022.
- (245) Murugesu, M.; Mishra, A.; Wernsdorfer, W.; Abboud, K. A.; Christou, G. *Polyhedron* **2006**, *25*, 613.

- (246) Osa, S.; Kido, T.; Matsumoto, N.; Re, N.; Pochaba, A.; Mrozinski, J. *J. Am. Chem. Soc.* **2004**, *126*, 420-421.
- (247) Mereacre, V. M.; Ako, A. M.; Clerac, R.; Wernsdorfer, W.; Filoti, G.; Bartolome, J.; Anson, C. E.; Powell, A. K. *J. Am. Chem. Soc.* **2007**, *129*, 9248.
- (248) Kahn, M. L.; Lecante, P.; Verelst, M.; Mathoniere, C.; Kahn, O. *Chem. Mater.* **2000**, *12*, 3073.
- (249) Kahn, M. L.; Mathoniere, C.; Kahn, O. *Inorg. Chem.* **1999**, *38*, 3692.
- (250) Costes, J. P.; Dahan, F.; Dupuis, A.; Laurent, J. P. *Chem. Eur. J.* **1998**, *4*, 1616.
- (251) Figuerola, A.; Diaz, C.; Ribas, J.; Tangoulis, V.; Granell, J.; Lloret, F.; Mahia, J.; Maestro, M. *Inorg. Chem.* **2003**, *42*, 641.
- (252) Zhao, H. H.; Lopez, N.; Prosvirin, A.; Chifotides, H. T.; Dunbar, K. R. *Dalton Trans.* **2007**, 878.
- (253) Chen, W. T.; Guo, G. C.; Wang, M. S.; Xu, G.; Cai, L. Z.; Akitsu, T.; Akita-Tanaka, M.; Matsushita, A.; Huang, J. S. *Inorg. Chem.* **2007**, *46*, 2105.
- (254) Estrader, M.; Ribas, J.; Tangoulis, V.; Solans, X.; Font-Bardia, M.; Maestro, M.; Diaz, C. *Inorg. Chem.* **2006**, *45*, 8239.
- (255) Figuerola, A.; Ribas, J.; Lluell, M.; Casanova, D.; Maestro, M.; Alvarez, S.; Diaz, C. *Inorg. Chem.* **2005**, *44*, 6939.
- (256) Figuerola, A.; Ribas, J.; Casanova, D.; Maestro, M.; Alvarez, S.; Diaz, C. *Inorg. Chem.* **2005**, *44*, 6949.
- (257) Figuerola, A.; Diaz, C.; Ribas, J.; Tangoulis, V.; Sangregorio, C.; Gatteschi, D.; Maestro, M.; Mahia, J. *Inorg. Chem.* **2003**, *42*, 5274.
- (258) Sheldrick, G. M. *SHELXL-97; University of Göttingen, Germany* **1997**.
- (259) Sanudo, E. C.; Brechin, E. K.; Boskovic, C.; Wernsdorfer, W.; Yoo, J.; Yamaguchi, A.; Concolino, T. R.; Abboud, K. A.; Rheingold, A. L.; Ishimoto, H.; Hendrickson, D. N.; Christou, G. *Polyhedron* **2003**, *22*, 2267.
- (260) Wittick, L. M.; Murray, K. S.; Moubaraki, B.; Batten, S. R.; Spiccia, L.; Berry, K. J. *Dalton Trans.* **2004**, 1003.
- (261) Ako, A. M.; Mereacre, V.; Hewitt, I. J.; Clerac, R.; Lecren, L.; Anson, C. E.; Powell, A. K. *J. Mater. Chem.* **2006**, *16*, 2579.

- (262) Shanmugam, M.; Chastanet, G.; Mallah, T.; Sessoli, R.; Teat, S. J.; Timco, G. A.; Winpenny, R. E. P. *Chem. Eur. J.* **2006**, *12*, 8777.
- (263) Mishra, A.; Tasiopoulos, A. J.; Wernsdorfer, W.; Abboud, K. A.; Christou, G. *Inorg. Chem.* **2007**, *46*, 3105-3115.
- (264) Tasiopoulos, A. J.; Mishra, A.; Christou, G. *Polyhedron* **2007**, *26*, 2183-2188.
- (265) Tasiopoulos, A. J.; O'Brien, T. A.; Abboud, K. A.; Christou, G. *Angew. Chem. Int. Ed.* **2004**, *43*, 345.
- (266) Eppley, H. J.; Aubin, S. M. J.; Streib, W. E.; Bollinger, J. C.; Hendrickson, D. N.; Christou, G. *Inorg. Chem.* **1997**, *36*, 109.
- (267) Bagai, R.; Abboud, K. A.; Christou, G. *Inorg. Chem.* **2008**, *47*, 621-631.
- (268) Bencini, A.; Benelli, C.; Caneschi, A.; Carlin, R. L.; Dei, A.; Gatteschi, D. *J. Am. Chem. Soc.* **1985**, *107*, 8128.
- (269) Bencini, A.; Benelli, C.; Caneschi, A.; Dei, A.; Gatteschi, D. *Inorg. Chem.* **1986**, *25*, 572.
- (270) Kido, T.; Ikuta, Y.; Sunatsuki, Y.; Ogawa, Y.; Matsumoto, N. *Inorg. Chem.* **2003**, *42*, 398-408.
- (271) Hamamatsu, T.; Yabe, K.; Towatari, M.; Osa, S.; Matsumoto, N.; Re, N.; Pochaba, A.; Mrozinski, J.; Gallani, J. L.; Barla, A.; Imperia, P.; Paulsen, C.; Kappler, J. P. *Inorg. Chem.* **2007**, *46*, 4458.
- (272) Chakov, N. E.; Soler, M.; Wernsdorfer, W.; Abboud, K. A.; Christou, G. *Inorg. Chem.* **2005**, *44*, 5304.
- (273) Sessoli, R.; Tsai, H. L.; Schake, A. R.; Wang, S. Y.; Vincent, J. B.; Folting, K.; Gatteschi, D.; Christou, G.; Hendrickson, D. N. *J. Am. Chem. Soc.* **1993**, *115*, 1804.
- (274) Caneschi, A.; Gatteschi, D.; Sessoli, R.; Barra, A. L.; Brunel, L. C.; Guillot, M. *J. Am. Chem. Soc.* **1991**, *113*, 5873.
- (275) Rebilly, J. N.; Mallah, T. *Struct. Bonding* **2006**, *122*, 103.
- (276) Berlinguette, C. P.; Vaughn, D.; Canada-Vilalta, C.; Galan-Mascaros, J. R.; Dunbar, K. R. *Angew. Chem. Int. Ed.* **2003**, *42*, 1523.
- (277) Benelli, C.; Cano, J.; Journaux, Y.; Sessoli, R.; Solan, G. A.; Winpenny, R. E. P. *Inorg. Chem.* **2001**, *40*, 188.
- (278) Price, D. J.; Batten, S. R.; Moubaraki, B.; Murray, K. S. *Chem. Commun.* **2002**, 762.

- (279) Koizumi, S.; Nihei, M.; Nakano, M.; Oshio, H. *Inorg. Chem.* **2005**, *44*, 1208.
- (280) Godbole, M. D.; Roubeau, O.; Mills, A. M.; Kooijman, H.; Spek, A. L.; Bouwman, E. *Inorg. Chem.* **2006**, *45*, 6713.
- (281) Ishikawa, N.; Sugita, M.; Wernsdorfer, W. *Angew. Chem. Int. Ed.* **2005**, *44*, 2931.
- (282) Costes, J. P.; Auchel, M.; Dahan, F.; Peyrou, V.; Shova, S.; Wernsdorfer, W. *Inorg. Chem.* **2006**, *45*, 1924.
- (283) Stamatatos, T. C.; Foguet-Albiol, D.; Stoumpos, C. C.; Raptopoulou, C. P.; Terzis, A.; Wernsdorfer, W.; Perlepes, S. P.; Christou, G. *J. Am. Chem. Soc.* **2005**, *127*, 15380.
- (284) Friedman, J. R.; Sarachik, M. P.; Tejada, J.; Ziolo, R. *Phys. Rev. Lett.* **1996**, *76*, 3830.
- (285) Hill, S.; Anderson, N.; Wilson, A.; Takahashi, S.; Chakov, N. E.; Murugesu, M.; North, J. M.; Dalal, N. S.; Christou, G. *J. Appl. Phys.* **2005**, *97*, 10M510.
- (286) Boskovic, C.; Pink, M.; Huffman, J. C.; Hendrickson, D. N.; Christou, G. *J. Am. Chem. Soc.* **2001**, *123*, 9914.
- (287) Artus, P.; Boskovic, C.; Yoo, J.; Streib, W. E.; Brunel, L. C.; Hendrickson, D. N.; Christou, G. *Inorg. Chem.* **2001**, *40*, 4199.
- (288) Soler, M.; Artus, P.; Folting, K.; Huffman, J. C.; Hendrickson, D. N.; Christou, G. *Inorg. Chem.* **2001**, *40*, 4902.
- (289) Kuroda-Sowa, T.; Lam, M.; Rheingold, A. L.; Frommen, C.; Reiff, W. M.; Nakano, M.; Yoo, J.; Maniero, A. L.; Brunel, L. C.; Christou, G.; Hendrickson, D. N. *Inorg. Chem.* **2001**, *40*, 6469.
- (290) Kuroda-Sowa, T.; Nogami, T.; Konaka, H.; Maekawa, M.; Munakata, M.; Miyasaka, H.; Yamashita, M. *Polyhedron* **2003**, *22*, 1795.
- (291) Aubin, S. M. J.; Sun, Z. M.; Pardi, L.; Krzystek, J.; Folting, K.; Brunel, L. C.; Rheingold, A. L.; Christou, G.; Hendrickson, D. N. *Inorg. Chem.* **1999**, *38*, 5329.
- (292) Chakov, N. E.; Zakharov, L. N.; Rheingold, A. L.; Abboud, K. A.; Christou, G. *Inorg. Chem.* **2005**, *44*, 4555.
- (293) Connelly, N. G.; Geiger, W. E. *Chem. Rev.* **1996**, *96*, 877.
- (294) Sun, Z. M.; Ruiz, D.; Dilley, N. R.; Soler, M.; Ribas, J.; Folting, K.; Maple, M. B.; Christou, G.; Hendrickson, D. N. *Chem. Commun.* **1999**, 1973.

(295) Aubin, S. M. J.; Sun, Z. M.; Eppley, H. J.; Rumberger, E. M.; Guzei, I. A.; Folting, K.; Gantzel, P. K.; Rheingold, A. L.; Christou, G.; Hendrickson, D. N. *Inorg. Chem.* **2001**, *40*, 2127.

(296) Takahashi, S.; Hill, S. *Rev. Sci. Instrum.* **2005**, *76*, 023114.

BIOGRAPHICAL SKETCH

Rashmi Bagai was born in Delhi, India in 1979. She entered Hindu College, Delhi University in 1995 and received Bachelor of Science degree in 1998. She then successfully qualified in the joint entrance exam of the Indian Institute of Technology, Delhi to pursue her masters in chemistry. During her masters, she worked in the research group of Prof. Jai Deo Singh on the preparation of tripodal ligands incorporating three aldehydic moieties interconnected by a rigid triazine spacer. After the completion of her Master of Science degree in 2000, she was awarded the prestigious Council of Scientific and Industrial Research - Junior Research Fellowship (CSIR-JRF) on the basis of a written competitive test conducted jointly by CSIR and UGC (University Grants Commission) at the national level. Thereafter, she joined the research group of Prof. Debkumar Bandyopadhyay at IIT, Delhi in July, 2000 as a CSIR-JRF research assistant. The research involved extensive kinetic studies and preparation of Iron(III) porphyrin based catalytic systems for the oxidation of various organic and organometallic compounds. She got married to Ranjan Mitra, her friend for nine years, in May 2003 in Delhi, India and moved to USA. In August 2003, she joined the research group of Prof. George Christou in the Department of Chemistry at the University of Florida. Her doctoral research primarily involves exploration of new ligands for the preparation and magnetic characterization of polynuclear oxo-bridged Mn and Fe clusters, some of which behave as single-molecule magnets.